Development of a Scintillator Based Coded-Aperture Neutron Imager for Nuclear Decommissioning Applications

Michał Jacek Cieślak
Department of Engineering
University of Lancaster

A thesis submitted for the degree of
Doctor of Philosophy

July 17, 2019

For my wife, Patrycja and my son, Ireneusz.

Acknowledgments

The PhD thesis you are holding in your hands would have never been completed, if it had not been for the support of many people. The idea for this project originated with my academic supervisor, Doctor Kelum Gamage whose unceasing enthusiasm for this project was an invaluable source of encouragement. I am very grateful for his openness, understanding, patience and support throughout this project. Through his scientific assistance and insightful comments he guided me to the successful completion of this project.

I would like to thank my industrial supervisor, Doctor Robert Glover for the fruitful scientific discussions and perceptive observations. I would like to thank my academic supervisor, Professor James Taylor for the support and providing reassurance during this project.

I wish to express my gratitude to the former and current staff, colleagues and friends in the Engineering Department, in particular; Jan Henschke, Peter Jones, Matthew Balmer, Ikechukwu Ukaegbu, Anita Crompton, Mauro Licata, Hajir Al Hamrashdi, Ashley Jones, Helen Parker, Vytautas Astromskas and Harald Schlegl.

I would have never had the courage to even consider this PhD, if it had not been for the caring support of my loving family. I would like to thank my parents, Barbara and Zdzisław for their prayers, patience and reassurance. I would like to thank my sister, Beata for her unconditional belief in my abilities to embark on this project. I am indebted to my wife, Patrycja whose faith in me was the biggest encouragement before I even begun this PhD and has never faded. My wife's love and support accompanied me at every stage of this project, for which I am ceaselessly grateful. I would like to thank my son, Ireneusz for his inexhaustible amounts of energy and the most endearing smile which were the sweetest distractions during this PhD.

Finally, I would like to gratefully acknowledge the financial support from the Engineering and Physical Sciences Research Council (EPSRC), Sellafield Ltd, UK and the Faculty of Science and Technology of Lancaster University, UK.

Abstract

This thesis documents a proof-of-concept study of a novel, scintillator based, coded-aperture approach to neutron detection. Developments presented in this document suggest that coded-aperture approach, previously mainly associated with photon detectors, can be adapted for a small scale neutron detector. This work represents an innovative, scintillator based approach for small scale radiation detector aimed at nuclear decommissioning applications.

A novel pixelated plastic scintillator was designed and built in this work. Scintillator cells (2.8 × 2.8 × 15 mm each), build of EJ-299-34 plastic were manufactured and arranged into a 13 × 13 array. The plastic scintillator which was used in this research was sensitive to both gamma and neutron fields. Experimental data were obtained for various solid scintillator samples and a comparison of a number of pulse shape discrimination techniques was performed. Prior to the experimental work, a simulation based study identified potential candidates for the scintillation material, as well as characterised the mixed-field environment, provided by ^{252}Cf at Lancaster University, UK. Suitable coded-aperture materials were also computationally identified, and were subsequently used to manufacture a tungsten coded aperture, based on modified uniformly redundant array design technique.

Pixelated nature of the coded-aperture based approach to radiation imaging allows the lateral resolution of the image to be improved, without affecting the signal-to-noise ratio. The focal point of this technique is located in the coded-aperture design and the scintillator. Modulation properties of the rank-7 coded aperture, made of tungsten using additive manufacturing techniques, were investigated. The experiment was performed using ^{137}Cs gamma-ray calibration source at Lancaster University. Data obtained were subsequently used to perform the localisation of the point source used in this study. The idea of using tungsten coded aperture for dual-particle imaging was also simulated using Monte Carlo techniques (MCNPX) prior to the experimental work.

The pulse shape discrimination performance of the pixelated organic plastic scintillator was investigated. The scintillator was exposed to a mixed-field environment provided by ^{252}Cf and its performance was compared to that of a cylindrical plastic sample. Tests were also carried out in moderated neutron and gamma-ray fields of ^{252}Cf. Suitable pixelated photodetectors, together with associated readout electronics circuitry, were also identified.

Declarations

I, Michał Jacek Cieślak, hereby certify that this thesis has been written by me and has not been submitted in any previous application for a higher degree. The work presented here was carried out at the University of Lancaster between October 2015 and July 2019.

Signed M Cieślak ....

Date 24/07/2019 ....

I, Doctor Kelum Asanga Akurugoda Gamage, hereby certify that the candidate has fulfilled the conditions of the resolution and regulations appropriate for the degree of Doctor of Philosophy in the University of Lancaster and that the candidate is qualified to submit this thesis in application for that degree.

Signed ....

Date 17/07/2019 ....

Contents

List of Figures

List of Tables

Chapter 1

Introduction

1.1 Nuclear Decommissioning

As of April 2018 there are 449 commercial nuclear reactors operating worldwide. In the United Kingdom alone there are currently 15 operating nuclear reactors, 30 permanently shut down nuclear reactors, 26 in decommissioning process or decommissioned, with 2 reactors currently being built (Hinkley Point C-1 and C-2) [1]. Other sources list further 9 planned power plants, with the planned reactors for Sellafield and Moorside sites now cancelled [2]. The currently operating reactors account for approximately 21% UK's electricity production. However, 14 out of total 15 reactors are scheduled to be shut down within the next 10 years [2].

Regardless of the type of the nuclear reactor, large amounts of nuclear waste are produced in the process of power generation. Moreover, commercial facilities within the power station site become contaminated. The first, and crucial, step of the clean-up process of a nuclear facility is the radiological characterisation, which has a huge impact on the success and duration of the decommissioning process. It identifies the contamination level of the affected areas of a nuclear facility, enabling determination of the radiation fields and requirements for conditioning of the contaminated areas, as well as for the transportation of the radioactive waste [3]. Therefore, decommissioning process of nuclear power station can last for many decades, if the techniques used for characterisation (e.g. radiation detection, localisation and imaging) are not of sufficient quality. Sellafield alone (formerly Windscale and Calder Hall), which is currently undergoing decommissioning, is estimated to take over 100 years before the decommissioning process is completed [4]. Even when the decommissioning is deemed complete, it may take hundreds of years before the land can be used again in a reasonable way, as predicted for Dounreay site [5].

The enormity of the scale of the decommissioning issue at Sellafield has become clearer when a white paper was released by the government in the early 2000's. British nuclear legacy was identified therein. However, not much has been achieved due to delayed administration handling. Currently, the term Nuclear Legacy encompasses all nuclear waste, that was 'put away' before long term storage solution is found, predominantly at Sellafield where most of UK nuclear waste is currently stored [6]. Before the nuclear waste can be transported to a permanent storage places, type of radiation emitted must be identified.

Britain's commitment to nuclear power (the current deadline for the completion of Hinkley Point C-1 is 2026) ensures that nuclear waste management and identification of radioactive substances in the nuclear waste will remain essential for decades to come. Despite living in the period of *Nuclear Renaissance*, it is no longer viable to build new nuclear facilities without making provisions for the afterlife of the nuclear site. The aforementioned *Nuclear Legacy* in the UK is a result of the attitude, where what happens with the nuclear power plant after its operation is somebody else's problem [3].

In order to address the issue that has been neglected for many years, many technology branches have combined their efforts. For instance, robotic engineering is used to support radiological survey of the vast area. Recent advancements in robotic technology and artificial intelligence (AI) allow a controlled or an autonomous machine to perform a radiological assay in places difficult (or dangerous) to access for manual workers [7, 8]. Regardless of the immediate application area, at the heart of every detector technology, there is a type of sensitive medium which directly interacts with the particle(s) of interest. These can be directly detected by by the state-of-the-art analogue electronic devices, or further transduced before being digitised. The progress in the field of digital signal processing enables not only to perform detailed off-line analysis of detected signals, but also implement digital filtering with ease, which was previously restricted to the analogue domain.

1.2 Nuclear Detection and Imaging

The design complexity of a nuclear power plant requires that different detection techniques be employed to perform decommissioning tasks in various parts of the nuclear site. Moreover, the difficulty of the process is further increased in places such as Sellafield, whose role was changing in time - from a nuclear power plant producing Pu for nuclear weapons programme, through commercial nuclear power station, to eventually spent fuel reprocessing and nuclear decommissioning site. As a result, a range of radiation detectors for specific particle types needs to be utilised to address all the areas of the site. These include fast electron sources such as beta particles, heavy charged particles such as alpha particles as well as uncharged radiation sources such as gamma-ray photons and neutrons.

Since neutrons are at the heart of the chain reaction, the immediate area around the reactor is most likely to be affected by this type of radiation. However, transport of nuclear fuel can also leave traces of neutron radiation in other areas of the nuclear sites. Controversial reports suggest the level of negligence at Sellafield led to a situation where large amounts of contaminated material have overfilled the storage ponds. As the ponds are gradually cleaned of the radioactive sludge and contaminated equipment, it is of vital importance to have the radiation field fully characterised before a decision is made about active human involvement in the clean-up process.

Furthermore, neutrons pose a serious threat to the human life, as they can penetrate through many layers of protection clothing (even military degree) and attack the living tissue. Therefore, it is essential, from the safety viewpoint, that all the areas within a nuclear power site be accurately characterised. Different types of sensitive detectors can be used for such application, but detectors capable of detecting or rejecting strong gamma-ray fields (background, secondary gamma-radiation) are preferred.

For many years, ^{3}He based neutron detectors were the preferred choice. These are capable of detecting thermal neutrons and are virtually impervious to gamma-ray photons. As they are only capable of detecting thermal neutrons, H-rich material is required to modulate the energy spectrum of the surrounding field, so that the modulated neutrons can be detected by ^{3}He. However, since ^{3}He is obtained as a by-product of ^{3}H production for thermonuclear weapons, world's ^{3}He supply has dropped as a result of the ongoing global efforts to denuclearise. At the same time, the demand for ^{3}He based neutron detectors has been growing steadily following the terrorist attacks in the USA in September 2001 [9].

Following that, an ongoing search for a suitable replacement began. An extensive analysis of the available alternatives has been presented in 2010 by Kouzes et al. [10]. It considers different types of detectors (gas, liquid, solid), taking into account properties such as neutron detection capabilities, handling safety, operational safety, insusceptibility to other particle types, and target application. Another study performed in 2016, together with currently intensified efforts to develop safe, solid organic detectors represents current trends in the field of neutron detection [11, 12]. However, it should be noted that the primary effort in those studies was to identify a method providing best neutron detection performance for certain applications, such as nuclear proliferation and decommissioning.

Combining such detectors with conventional camera enabled nuclear imaging to be performed. It allowed nuclear sites to be characterised, providing an image of radioactive hotspot locations. However, there are certain drawbacks to the technologies currently used to perform site characterisation. Identification process may take a long time, as commonly used detectors and imagers require a slow process of scanning to be completed before the results are obtained. Further information about the differences between the numerous imaging techniques currently employed and future possibilities are presented in chapter 3.

1.3 A novel approach to neutron detection based on pixelated, organic plastic scintillator and tungsten coded aperture

The overall aim of the research described in this thesis was to present a proof-of-concept study of a novel scintillator based coded-aperture approach to neutron detection. The main focus of the work was placed on the design and testing of the key elements of a complete system, which can be built based on the concepts illustrated in this work.

The concept presented in this study encompasses a system based on an organic plastic scintillator capable of neutron identification by the means of pulse shape discrimination (PSD). Ongoing research into solid scintillators sees the material being constantly improved with regard to its neutron/gamma detection capabilities [13]. However, its adaptation as a pixelated very small scale detector has not been previously investigated. Based on numerous Monte Carlo simulation studies, presented in this thesis, a small scale pixelated scintillator was built and tested. It was developed using Eljen's EJ-299-34 (currently replaced by EJ-276 [14]) scintillator blocks. Each block was designed as 2.8 × 2.8 × 15 mm block, to allow easy size matching with available pixelated photodetectors - position sensitive photomultiplier tubes (PSPMTs) or silicon photomultipliers (SiPMs). Pixelated plastic scinitllator consists of 169 blocks arranged into a 13 × 13 array of single blocks, with the overall size of 39.52 × 39.22 mm. Each block is separated from one another with a ^{TM}3M reflective film, providing up to 98% cross-talk separation. For the purposes of this research, characterisation of this scintillator was performed within the fields produced by ^{137}Cs and ^{252}Cf radionuclides.

Neutron detectors currently used in nuclear decommissioning applications, utilising solid organic scintillators (plastic or crystal), tend to be built from a single block of the sensitive material. The localisation of the interaction within the scintillator is then achieved by methods such as time of flight (TOF), position sensitive detectors (PSPMTs, SiPMs) or exploitation of internal effects occurring in crystal scintillator. In any of the listed cases, there exists the possibility of misclassification of the interaction location, or more precisely, detection of the event within the scinitllation medium. Therefore, in this work the pixelated scintillator was developed, which provides an additional information about the localisation of interaction in two dimensions. This information can be used on its own, or as a primary method in multi-modal systems. The scintillator was built using Eljen Tehchonlogy's EJ-299-34 material.

Following an extensive literature review and number of Monte Carlo simulations (chapter 3 and 5), a material for the coded aperture, based on both W and Cd, was determined. However, due to health reasons associated with Cd exposure, as well as the small scale of the coded aperture, the machining of the part was very challenging and eventually using such composition for the coded aperture had to be avoided. As a result, it was decided to have the coded aperture build with only W. It was necessary to adjust the part's dimensions, as its original design was deemed not manufacturable. The outer dimensions of the coded aperture, as well as those of the single opening, were designed to match the scintillator's dimensions. However, due to manufacturing constraints the dimensions of the single opening were reduced from 2.8 mm to 2.5 mm. This novel part was produced using the latest additive manufacturing technologies. This type of apertures are only rarely used in neutron/gamma detection applications, as they are predominantly utilised in single particle detectors, where they are used to either modulate the energy spectrum of the particles (neutron detection application), or fully block the incoming particles on the opaque elements of the aperture (gamma-ray detectors). In this work, the potential of dual-particle detection using this method is presented.

A particle (neutron or gamma-ray photon), which managed to pass through the coded-aperture layer, is likely to interact within the scintillator, where it produces fluorescence (proportional to energy decay rate of the particle). The fluorescence is then collected via photo-detector and transduced into an electronic signal. Throughout the work completed in this research, ET Enterprises 9107B single channel photomultiplier tube (PMT) was used. Despite the continuous advancement and research into new photo-detection techniques (PSPMTs, SiPMs), there is always a trade-off between the factors such as the complexity of readout electronics required, electromagnetic interference immunity, light saturation level of the detector. Having extensively analysed the listed properties, it was decided to perform all the experimental work in this research using the ET Enterprises 9107B PMT.

The electronic signal generated from the PMT, as a result of an interaction of a neutron or gamma-ray photon within the scintillator, is then to be digitised. As a result various pulse shape discrimination (PSD) methods can be easily implemented in the digital domain. There are many variables that differentiate digitisers. However, there are two main factors often cited when digitisers are considered, which stay in close connection to the quality of the PSD obtained; these are sampling frequency and bit resolution. During the research completed for this thesis, two digitisers of different sampling rates as well as different bit resolutions have been tested.

Generally, the higher sampling rate results in better PSD quality (separation), which comes at cost of lower bit resolution. However, the higher effective sampling rate has far greater impact on the PSD performance of the detector system than the increased bit resolution. This is exemplified in this thesis, where initial scintillator testing (chapter 5) was performed with 150 MS/s 14-bit resolution digitiser, and all the following experimental work (chapter 7,8) was performed using 500 MS/s 12-bit digitiser. Initial testing of three scintillator samples suggests that if the intrinsic PSD capability of the scintillator is of sufficient quality, the sampling rate of the digitiser can be as low as the quoted 150 MS/s. However, if the intrinsic PSD capability of the scintillator is not of adequate quality, sampling rate of the digitiser needs to be increased to obtain the expected results. In this work, the initially tested samples (research sample of plastic scinitllator from Lawrence Livernmore National Laboratory and single stilbene crystal) present very good PSD performance across the entire energy spectrum of neutrons. The material of pixelated plastic scintillator (EJ-299-34) can be easily formed into blocks (due to higher solid content) at the cost of PSD performance. As a result, it was necessary to increase the sampling rate of the digitiser, because the 150 MS/s digitiser proved unable to separate neutrons from gamma-ray photons within the pixelated plastic scintillator.

Experimental work described in this thesis was fully performed at Lancaster University, Lancaster, UK (chapter 5,7,8). As described more extensively in chapter 5, because of the way ^{252}Cf source is stored at Lancaster University, the energy spectrum of the radionuclide is modulated. Given the nature of the experiments performed, the arrangement at Lancaster University makes the neutron detection somewhat more difficult, due to the modulation provided by the steel tank and water. It was considered during the PhD to perform the experiments at other locations where "bare" sources are available. However, it was concluded that more strenuous experimental conditions at Lancaster University will ensure optimal operation of the system in most demanding environment.

In summary, a novel scinitllator based coded-aperture neutron/gamma detection imaging system has been designed and its main components built and tested. This system shows a great potential to provide a much improved neutron/gamma-ray detection performance with regard to the resolution of the obtained image, owing to the pixelated nature of the plastic organic scintillator.

1.4 Peer-reviewed journal publications

1. Cieslak, M.J., Gamage, K.A.A. & Glover, R. 2019, *Critical review of scintillating crystals for neutron detection*, Crystals, vol 9, no. 480, DOI: 10.3390/cryst9090480
2. Cieslak, M.J., Gamage, K.A.A., Glover, R. & Taylor, C.J. 2019, *Pulse shape discrimination performance of a pixelated plastic scintillator (EJ-299-34) for a coded-aperture based dual particle imaging system*, Journal of Instrumentation, vol 14, no. 7, P07017, DOI: 10.1088/1748-0221/14/07/P07017
3. Cieslak, M.J., Gamage, K.A.A., Glover, R. & Taylor, C.J. 2019, *Gamma-ray modulation properties of tungsten coded apertures for a novel mixed-field imaging system*, Journal of Instrumentation, vol 14, no. 2, P02007. DOI: 10.1088/1748-0221/14/02/P02007
4. Cieslak, M.J., Gamage, K.A.A. & Glover, R. 2017, *Investigation into a suitable scintillator and coded-aperture material for a mixed-field radiation imaging system*, Journal of Instrumentation, vol 12, no. 12, P12007. DOI: 10.1088/1748-0221/12/12/P12007
5. Cieslak, M.J., Gamage, K.A.A. & Glover, R. 2017, *Pulse shape discrimination characteristics of stilbene crystal, pure and 6Li loaded plastic scintillators for a high resolution coded-aperture neutron imager*, Journal of Instrumentation, vol 12, no. 7, P07023. DOI: 10.1088/1748-0221/12/07/P07023
6. Cieslak, M.J., Gamage, K.A.A. & Glover, R. 2016, *Coded-aperture imaging*

systems: past, present and future development - a review, Radiation Measurements, vol 92, pp. 59-71. DOI: 10.1016/j.radmeas.2016.08.002

1.5 Conferences and Workshops

- *Study of modulation properties of tungsten based coded aperture.* 7th International Conference on Radiation in Various Fields of Research (RAD 2019) - Herceg Novi, Montenegro, 10-14 June 2019
- *Neutron Detection Instrumentation for Nuclear Decommissioning Applications.* NUPP 2019 - 3rd International Conference on Nuclear Power Plants: Structures, Risk and Decommissioning, London, 10-11 June 2019
- *Characterisation of a pixelated plastic scintillator for a coded aperture neutron/gamma imaging system.* 2018 IEEE Nuclear Science Symposium Medical Imaging Conference, Sydney, Australia, 10-17 November 2018
- *Development of a scintillator based coded-aperture neutron imaging system.* NDRA 2018 - SUMMER SCHOOL ON NEUTRON DETECTORS, Riva del Garda Centro Congressi, Riva del Garda - Trento, Italy, 2-5 July 2018
- *Development of a scintillator based coded-aperture mixed-field imaging system for nuclear decommissioning applications.* NUPP 2018 - 2nd International Conference on Nuclear Power Plants: Structures, Risk and Decommissioning, London, 11-12 June 2018
- *Localised Response Retrieval from Hamamatsu H9500 for a Coded-aperture Dual-particle Imaging System Based on an Organic Pixelated Plastic Scintillator (EJ-299-34).* 21st IEEE Real Time Conference (RT2018), Williamsburg, VA, USA, 9-15 Jun 2018
- *Digital Neutron-Gamma Discrimination Performance of Stilbene in Comparison with Plastic Scintillators.* International Topical Meeting on Industrial Radiation and Radioisotope Measurement Applications (IRRMA-X), Chicago, IL, USA, 9-13 July 2017

- *Comparison of Pulse Shape Discrimination Characteristics in Three Organic Scintillators for a High Resolution Coded-Aperture Neutron Imager.* 2016 European Nuclear Conference (ENC-2016), Warsaw, Poland, 9-13 October 2016

- *Design and development of a real-time readout electronics system to retrieve data from a square multi-anode photomultiplier tube for neutron gamma pulse shape discrimination.* 20th IEEE-NPSS Real Time Conference 2016 - Padova, Italy, 5-10 June 2016

1.6 Outline of each chapter

- **Chapter 2.** This chapter stipulates the underlying science of the research performed to complete this thesis. Concepts discussed include particle interactions with matter, neutron/gamma detection methods, digital imaging methods in nuclear applications.

- **Chapter 3.** This chapter presents an extensive literature review performed to identify the current methods and technologies utilised within the field of coded-aperture based neutron imaging systems. Initially, application areas of coded aperture imaging methods within nuclear detection research have been reviewed, with focus placed on neutron detection applications. Possible novel applications of coded aperture approach for neutron detection in nuclear decommissioning have been suggested through Monte Carlo simulations.

- **Chapter 4.** In this chapter a further review of scintillators capable of neutron detection is presented. Here the emphasis is placed on the scintillating crystals, including both organic and inorganic crystals. Mechanisms responsible for detection of neutrons scintillating crystals are defined, and promising candidates listed. A comparison between organic crystal and plastic scintillators, based on practical results, is also included in order to exemplify the superiority of organic crystals when fast neutrons are targeted.

- **Chapter 5.** This chapter describes a set of experiments performed with three different types of solid organic scintillators to identify the most suitable candidate for the overall system. Three scintillators were exposed to the same neutron/gamma field produced by ^{252}Cf at Lancaster University and their neutron/gamma separation performance assessed. Three PSD algorithms applied in the digital domain have been compared, and the suitability each algorithm was judged based on the results the separation quality obtained and computation time required to obtain the result.

- **Chapter 6.** In the similar way to the experiment performed in chapter 5, here the experimental set-up of the previous chapter was tested within the modelled environment using Monte Carlo simulation code. Comparably to chapter 4, three scintillators were tested to assess their neutron/gamma detection capabilities. Following that, simulation based investigation into the most suitable coded aperture material was performed. Following a brief literary review, three compositions of ^{113}Cd and W were investigated, and the most fitting identified.
- **Chapter 7.** Following on from the preceding chapter, in this part the results of a practical experiment aiming at investigating the modulation properties of a tungsten coded aperture are presented. The aperture was manufactured based on the simulation work described in chapter 6. Modulation capabilities of the aperture, as well as its source localisation potential, were assessed and thoroughly discussed.
- **Chapter 8.** In this chapter the final part of the system was practically tested. Pixelated plastic scintillator, comprising of 169 plastic blocks (2.8 × 2.8 × 15 mm each) arranged into 13 × 13 array, was investigated with regard to its neutron detection capabilities via pulse shape discrimination techniques. Two distinguished fast signal digitisers were utilised to collect the raw data. Digitisers' performance was compared in the context of the digitiser's sampling rate influence on the quality of the particle separation. Performance of the scintillator within modulated neutron/gamma-ray environment is also assessed.
- **Chapter 9.** In this chapter the aims of this project are revisited. Most

important achievements of this thesis are assessed and final conclusions are drawn.

- **Chapter 10.** This chapter is dedicated to the possible future directions of the project executed.

Chapter 2

Background

2.1 Particle interactions with matter

Neutrons, neutrinos, X-ray and gamma-ray photons are all classified as uncharged particle. As they are electrically neutral, they need to interact with matter and produce electrically charged particle, so that they can be detected. Therefore, in order to identify how uncharged particle of interest (neutron or gamma-ray photon) can be detected, charged particle interactions are described first, and followed by consideration of uncharged particles.

2.1.1 Charged particles interactions

Charged particles interactions with matter are primarily governed by coulomb forces, and are comprised of two main particle groups - fast electrons and heavy charged particles. The former are defined as particles, whose mass is equal to or greater than one atomic mass unit. Coulomb forces attract positively heavy charged particles (e.g. alpha particle) to the electrons orbiting the target atom when the two are in close proximity. As a result of coulomb forces interaction between the heavy charged particle and orbiting electrons, a pulse is sensed by one of the electrons and, depending on the proximity of the two interacting particles, the electron can be either raised to a higher orbit/shell (excitation) or struck of the atom completely (ionisation).

Detection of heavy charged particles is of particular importance for thermal neutron detection following neutron capture reactions (n,α) on isotopes with high thermal neutron cross-sections, such as ^{10}B and ^{6}Li. When organic scintillators are loaded with high thermal neutron cross-section isotopes (^{10}B,^{6}Li), α particles resulting from thermal neutron interactions are characterised by the energy decay rate, which is proportional to the kinetic energy of the interacting particle. The same property is responsible for fast neutron/gamma discrimination in organic scintillators. The differences in the rate of energy decay can therefore be used to separate slow neutrons, fast neutrons and gamma-rays, provided the intrinsic separation capability of the sensitive detector is sufficient. Neutron reactions utilised for neutron detection are further discussed in chapter 4.

2.1.2 X-ray and gamma-ray photons interactions

Both X-ray and gamma-ray photons could be described as massless, uncharged particles. The main difference between the two particles is the origin of the photon. X-rays are photons emitted from the electron shells, whereas gamma-rays are attributed to the interactions with the atomic nucleus. Also, lower energy photons (up to approx. 100 keV) are often classified as X-rays with higher energy particles being classified as gamma-rays [15]. Regardless of the classification of the photons, they interact with matter predominantly in three possible ways: *Photoelectric absorption, Compton scattering and Pair production.* Energy of the gamma-ray photon relates to the probability of the type of reaction the photon may undergo, as shown in Figure 2.1.

Photoelectric absorption - often also called Photoelectric effect - as the name suggests, causes the disappearance of the gamma-ray photon when it interacts with the target atom. The gamma-ray photon can either raise one of the bound electrons to a higher energy level in the atom or result in a photoelectron being ejected. The energy of the ejected photoelectron is given by Equation 2.1, where E_b is the binding energy of the photoelectron on its original shell.

$$E_{e^-} = hv - E_b \tag{2.1}$$

The photoelectric absorption is the dominant type of interaction for the low energy photons (X-ray photon region). However, typical gamma-ray photon energies of radioisotopes encountered in nuclear applications fall into Compton scattering

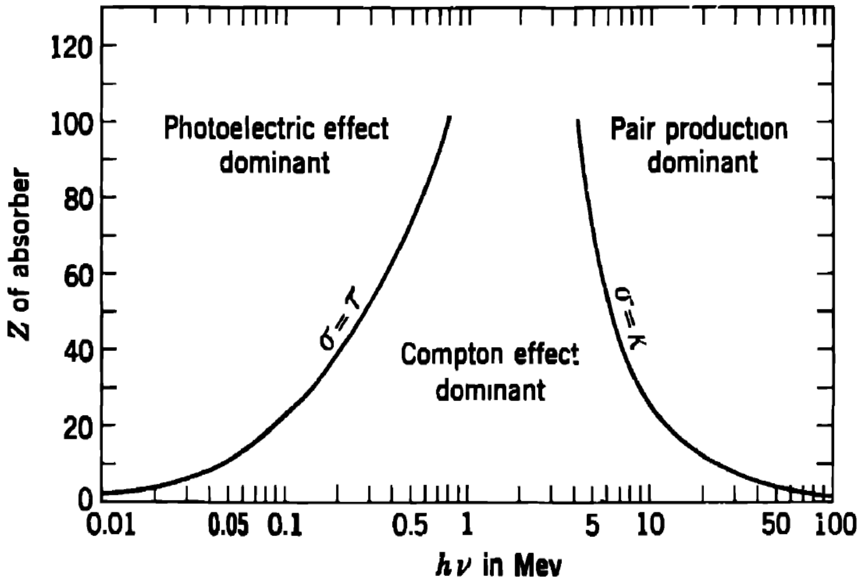

Figure 2.1: Relative importance of three main gamma-ray interaction types, presented as a function of energy [16, p. 712]

interaction region. In this effect, the incident gamma-ray photon undergoes an interaction with one of the electrons of the target material. Trajectories of the particles involved in the process are shown in Figure 2.2.

When the incident photon interacts with the atomic electron, some of the photon's energy is transferred to the Compton electron (often also called recoil electron). Energy of the Compton electron is dependant on the scattering angle, and can vary from zero to a very large part of the incident photon energy. It is impossible for the incident photon to transfer all its energy to the Compton electron. The relationship between energy of incident photon and the scattered photon is defined in Equation 2.2.

$$hv' = \frac{hv_0}{1 + \frac{hv_0}{m_0c^2}(1 - \cos\vartheta)} \tag{2.2}$$

The probability of the incident photon interacting with the target atom is proportional to the number of electrons available within the atom. Therefore, the higher the atomic number of the target, the higher the probability of interaction between the incident photon and target's electrons via Compton scattering. This is also the dominant type of gamma-ray photon interaction in organic

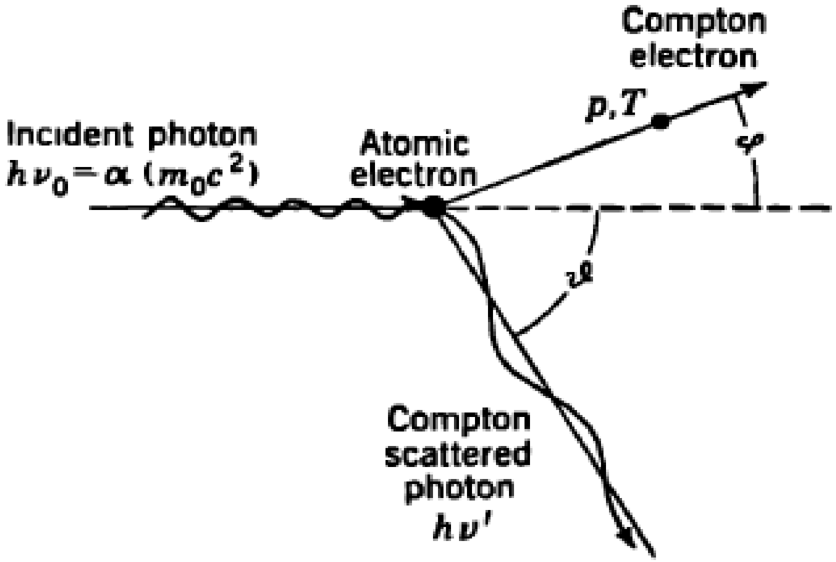

Figure 2.2: Trajectories for the incident photon, scattered photon, and the scattering electron [16, p. 675].

neutron/gamma scintillation detectors which are capable of PSD. As atoms of H interact mostly via Compton scattering with the incident gamma-ray photon above 10 keV, this type of interaction is exploited to infer the incident gamma-ray photons [17]. Compton scattering has also been applied to gamma-ray anisotropy studies in organic scintillators [18].

As presented in Figure 2.1, the highest energy range is dominated by Pair production effect. This interaction is only energetically impossible for gamma-ray photons, whose energy is lower than 1.02 MeV (double the rest-mass energy of an electron). The probability of pair production occurring is small at the photon energy only slightly exceeding 1.02 MeV. However, as the energy increases into hundreds of MeVs, Pair production becomes the dominant type of interaction. It is also more likely to occur in materials with higher atomic number. The incident gamma-ray photon of the sufficient energy disappears, and gives rise to an electron-positron pair. The excess energy (above 1.02 MeV) is transformed into kinetic energy and shared between the electron-positron pair. The two particles will eventually annihilate producing two annihilation photons [19].

2.2 Neutron interactions

Similarly to gamma-ray photons, neutron carries no charge. As such, neutron cannot interact with matter through coulomb forces. It is also the most penetrating form of radiation, which can travel through different types of material without any interaction. A comparison of penetration capabilities of all radiation types is shown in Figure 2.3. Neutrons can only undergo a strong interaction with a nucleus of an atom of the target material.

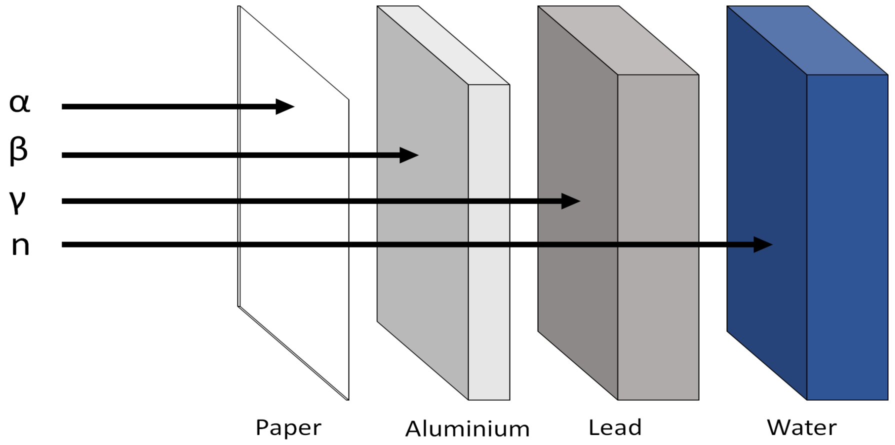

Figure 2.3: Material penetration capabilities of different radiation types with example stopping materials.

Neutron classification based on neutron energy differs between literary sources. Therefore, for clarity, classification presented in Table 2.1 will be used throughout this thesis. It should also be noted that this research focuses on fast neutron detection. However, significant emphasis is also placed on thermal neutrons, as these are often used to detect fast neutrons in applications where the latter ones are thermalised before being detected via thermal neutron sensitive detector.

Depending on the target material, as well as kinetic energy of the incident neutron, neutron interactions with matter can be split into scattering, absorption and transfer. Probability of the occurrence of the specific type of neutron interaction is defined by cross-section for every isotope. Neutron cross-section (e.g. elastic, capture) is measured in barns, where 1 barn equals 10^{-24} cm^2. As fast neutrons are more likely to undergo elastic scattering with light atoms, such as ^{1}H, their elastic cross-section will be greater than of those isotopes, such as ^{6}Li, which are

Table 2.1: Neutron classification based on its kinetic energy [20, p. 308].

Neutron class	**Neutron energy**
Cold neutrons	0.0–0.025 eV
Thermal neutrons	0.025 eV
Epithermal neutrons	0.025–0.4 eV
Cadmium neutrons	0.4–0.6 eV
EpiCadmium neutrons	0.6–1 eV
Slow neutrons	1–10 eV
Resonance neutrons	10–300 eV
Intermediate neutrons	300 eV–1 MeV
Fast neutrons	1–20 MeV
Ultrafast neutrons	> 20 MeV

more likely to capture thermal neutrons. It follows that neutron capture cross-section is greater for isotopes such as ^{6}Li than for lighter atoms, as the mentioned ^{1}H. Example total cross sections of some isotopes relevant to this work are shown in Figure 2.4.

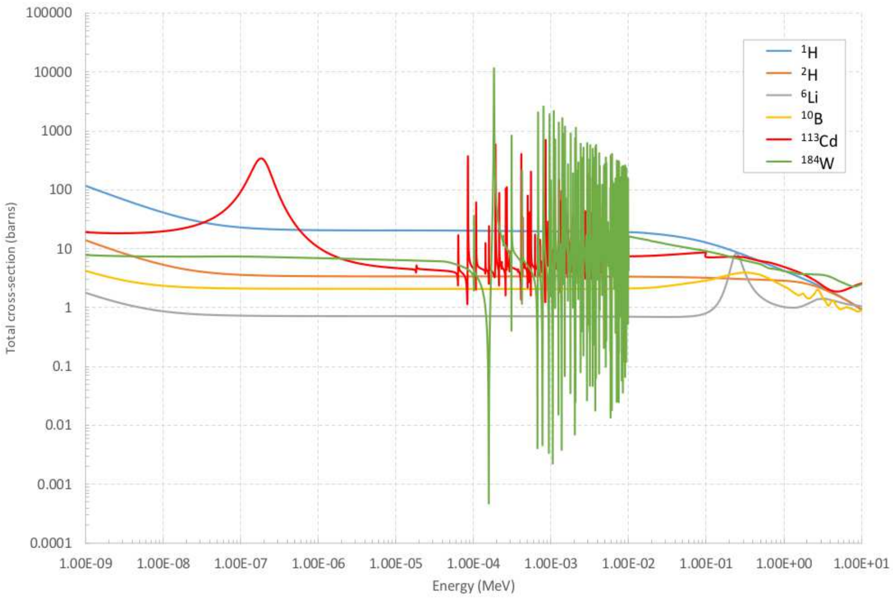

Figure 2.4: Total cross-sections of selected isotopes generated using ENDF/B-VIII.0 libraries.

Cross-sections presented in Figure 2.4 suggest that ^{113}Cd exhibits the highest interaction probability, in the region of thermal neutrons, of all the isotopes plotted. These interactions, predominantly radiative capture reactions, produce a large number of gamma-ray photons when a neutron interacts with ^{113}Cd nuclei. As organic scintillators are often sensitive to both neutrons and gamma-ray photons, it is undesirable to increase the gamma-ray field unnecessarily.

From the perspective of this research, ^{1,2}H and ^{184}W isotopes are of greatest interest. It can be observed that ^{1,2}H atoms present fairly consistent scattering probability across neutron energy spectrum, which is the most likely interaction that is going to take place in an organic scintillator. On the other hand, ^{184}W atoms are known for gamma-ray stopping due to its high atomic number. Its elastic cross-section suggests that it can also be utilised to scatter intermediate and fast neutrons (subject to the previously mentioned increased gamma-ray field).

2.2.1 Neutron scattering

There are two distinguishable types of neutron scattering. *Elastic scattering* is of particular importance for fast neutron detection. When an incident neutron undergoes elastic scattering (usually with light atom, such as hydrogen), it does not disappear, but is loses some of its energy as a result of a collision with nucleus of the target atom. The result of this interaction is normally *recoil nucleus* and the scattered neutron, as shown in Figure 2.5. Recoil nucleus are often referred to as *recoil protons*, and devices utilising this interaction type to detect fast neutrons *recoil proton detectors*.

The amount of kinetic energy transferred from the incident neutron to the recoil nucleus depends on the scattering angle θ between the direction of the incoming neutron and recoiling nucleus. If the incident neutron is deflected only slightly, the angle θ, between the incident neutron direction and the recoil nucleus, is close to 90°, and the transferred energy is close to zero. This is caused by only a slight interaction between the incident neutron and the target nucleus. In case of a direct collision, the scattering angle is close to zero and the transferred energy close to maximum. The energy of the recoil nucleus is defined in Equation 2.3.

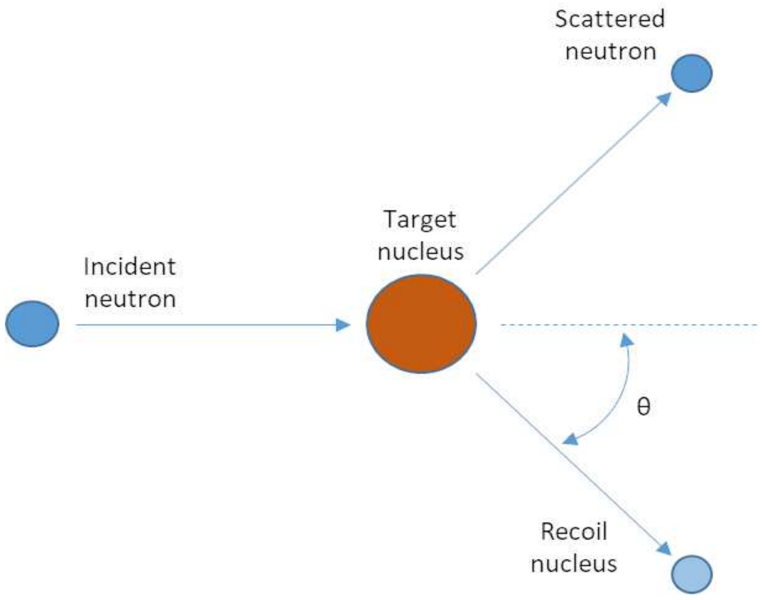

Figure 2.5: Elastic scattering diagram.

$$E_R = \frac{4A}{(1+A)^2}(cos^2\theta)E_n; \tag{2.3}$$

The other type of neutron scattering is referred to as *inelastic scattering* and is likely to occur when the incident neutron energy is sufficiently high. As a result of this interaction, the recoil nucleus is left in an excited state, which quickly returns to a stable state through the emission of gamma-ray photon. Therefore, this interaction is not desirable for PSD based detectors as it increases the number of gamma-ray photons that need to be separated.

2.2.2 Neutron absorption

In comparison to neutron scattering, there are also two types of neutron absorption interactions namely *nuclear fission* and *radiative capture*. The former constitutes the basis of nuclear power generation, where atoms with high fission cross-sections (such as ^{235}U, ^{239}Pu) are bombarded with thermal neutrons. These are captured by the target isotopes, briefly turned into excited state, and then split into two lighter isotopes, and thus initiating *chain reaction*. High fission cross-section for thermal neutrons of these isotopes can therefore be also utilised for thermal neutron detection. Pulses induced as a result of fission interactions can also be very easily detected, as Q-value for these interactions is very high (approx. 200 MeV) [19].

The other type of neutron capture interactions, when combined with specific *transfer reactions*, can be utilised to detect thermal neutrons. *Radiative capture* is often denoted as (n,γ) which results in a loss of the incident neutron, and is accompanied by a release of gamma-ray photons. In case of organic scintillator, the most likely scenario includes a radiative capture through hydrogen atom. The resulting gamma-ray photon of relatively high energy is likely to escape the scintillator without interaction. However, if the organic scintillator is loaded with one of high capture cross-section isotopes such as ^{10}B or ^{6}Li, energy of the incident neutron can be modulated to such level that virtually all thermal neutrons will be captured on the loading isotope. This type of neutron capture interaction is associated with a release of heavy charged particle (e.g. α particle, proton), which gives rise to another pulse of light in the organic scintillator, and thus can be detected.

2.2.3 Transfer reactions

As indicated in the previous paragraph, *transfer reactions* can be useful for neutron detection because they result in release of heavy charged particle. These then give rise to another pulse of light, which can be further used to infer the origin of the interaction. Some examples of *transfer reactions* are ^{10}B (n, α), ^{6}Li (n, α) and ^{3}He (n, p). Q-values for these reactions are considerably lower than for nuclear fission, and PSD still needs to be utilised to separate different types of particles. However, these reactions are preferred, when compared with *nuclear fission* based detectors, as the detection medium due to safety reasons.

2.3 Neutron detection methods

The most important classification related to neutron detection methods is the one based on the targeted neutron energy. The separation line is often drawn between slow and fast neutron detectors, as presented by Knoll [19]. Slow neutron detectors primarily exploit radiative capture reactions, whereas fast neutrons are detected predominantly through elastic scattering with a proton. Regardless of the type of reaction used to detect neutron of a specific energy, three main types of neutron detectors can be differentiated. These are gas-filled detectors, semiconductor devices and scintillators.

2.3.1 Gas-filled detectors

These detectors, which include ionisation chambers, proportional and Geiger-Mueller counters, exploit the ionisation of the gas particles within the detector. When radiation passes through a gas detector, ions are produced as a result. These can then be easily detected and counted, provided appropriate detection method was used.

Gas-filled detectors in neutron detection applications have targeted both slow and fast neutron energy regions. Given the neutral nature of neutrons, they can only be detected through an interaction where a charge particle is produced. The charged particle can be then multiplied in the gas and subsequently detected. Prime examples of gas-filled detectors include BF_3 and ^3He proportional counters, which utilise slow neutron reactions.

These devices have been highly popular due to their good neutron detection efficiency. However, efficiency of BF_3 based detectors is closely linked to the size of the detector, which is required to be large enough to avoid the *wall effect*. It occurs when the interaction takes place too close to the wall of the detector and not all of the reaction energy is deposited in the gas [19]. Moreover, problems with toxicity and temperature limitation (BF_3) and high production cost of ^3He, led to an ongoing search for alternative approaches [10].

Another approach has seen high efficiency proportional counters lined with high neutron cross-section isotopes. It allows the walls of the counter to be lined with e.g. ^{10}B. Although this approach addresses some of the issues associated with BF_3 detectors (toxicity, temperature limitations), neutron detection efficiency and gamma discrimination capabilities are reported to be inferior when compared to BF_3 devices [19]. Further discussions related to detectors, utilised reactions, gamma-ray sensitivity and associated problems are presented in chapters 3 and 4.

2.3.2 Semiconductor devices

In a similar way to the lined gas-filled detectors, isotopes with high thermal neutron cross-section, such as ^{10}B, can be used to cover standard charged particle detector, e.g. semiconductor device. As a result of an interaction, the incident particle causes a charged particle to arise, which then in turn deposits its energy in the semiconductor detector [19]. In order to target wider energy spectrum polyethylene lining can be used [21].

Semiconductor devices offer the advantage of requiring less energy to produce a pair of charge carriers in comparison to gas-detectors (approximately a factor of 10 less). They are also characterised by higher density (1000 larger than gas), which leads to a larger initial charge signal. However, there is no mechanism for internal multiplication in semiconductor devices [22]. As a result, the output signals are very small and very susceptible to external electronic noise. Therefore, dedicated electronics is required to extract the weak signal.

Most of semiconductor devices used to be based on silicon p-n junction diodes [23, 24]. Recent technological development led to broader adaptation of cadmium-zinc-telluride (CZT) detectors, which continues to improved [25]. However, semiconductor radiation detection devices remain expensive, due to the purity of the raw materials required, and can only be manufactured in small volumes [22].

2.3.3 Scintillation detectors

Scintillation detectors are an example of a well-established neutron detection methods and are perceived as viable alternatives for ^{3}He based devices [26]. The drawback of using scintillators for neutron detection is that many types are sensitive to both neutrons and gamma-ray photons. As a result, pulses induced by incident particles need to be discriminated so that they can be correctly classified. There are numerous methods allowing reliable particle separation, which can be applied both in time and frequency domain [27, 28, 29].

The most basic classification divides scintillators into organic and inorganic detectors. Inorganic scintillation detectors operate primarily in the area of slow neutron interactions (due to the content of high thermal neutron cross-section isotopes), whereas fast neutrons are mostly detected using pure organic scintillators. Some organic scintillators (both liquid and plastic) are loaded with high thermal neutron cross-section isotopes to address the difficulty of finding a suitable candidate for the complete energy spectrum. Different types of scintillation detectors are discussed in detail in chapter 3 and chapter 4.

This document focuses on fast neutron detection using solid organic scintillators, which are produced using a solution of carbon and hydrogen. Incident neutrons interact with hydrogen nucleus via elastic scattering resulting in recoil protons. These are capable of raising π-electrons in the scintillator to one of the excited electronic states. When a π-electron is excited, a pulse of visible light (often referred to as luminescence) is emitted when the π-electron returns to the ground electronic state. The length of the pulse varies depending on the type of the scintillator.

As organic scintillators are sensitive to both neutron and gamma-ray photons, the latter are responsible for the emission of light pulses resulting from Compton scattering interactions in the scintillator. The visible light emitted, from either neutron or gamma-ray interactions, can be converted into electronic pulses via suitable photodetector. These can be subsequently processed to exploit the differences in the shape of the pulse between neutrons and gamma-ray photons which originate in the dissimilar ionising densities of each particle type. This is described in more detail in chapter 5.

2.4 Neutron energy spectra of the chosen radioactive isotopes

Simulation and experimental work performed as a part of this PhD project uses two radioactive isotopes which produce mixed-field environments: ^{252}Cf and ^{241}AmBe. Since this study primarily focuses on neutron detection, modelled neutron energy spectra of ^{252}Cf and ^{241}AmBe are presented in Fig. 2.6. ^{252}Cf was modelled using Watt spectrum distribution, whereas ^{241}AmBe was based on source calibration specification from the Reference neutron radiations as presented by British Standard Institution [30]. Both spectra are shown as a function of neutron energy flux, as measured in MCNPX simulation package.

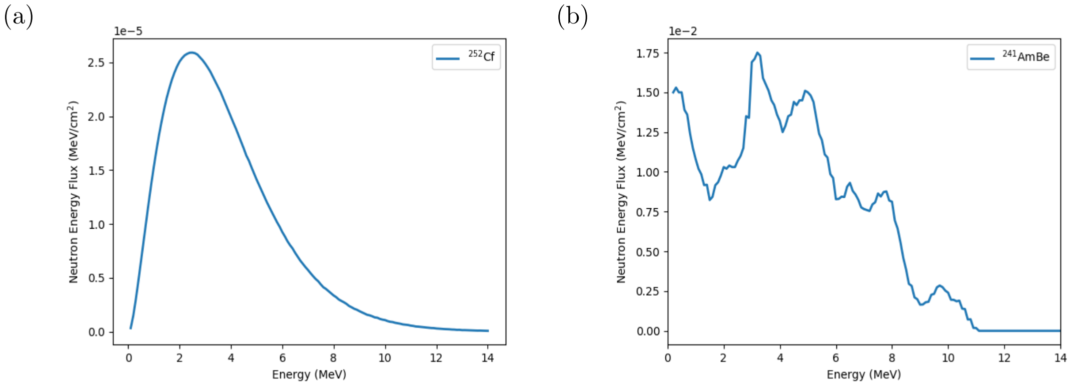

Figure 2.6: Neutron energy spectra of a) ^{252}Cf and b) ^{241}AmBe.

As can be observed from the neutron energy spectra presented in Fig. 2.6, neutron distribution and average energy values for each isotope are dissimilar. The average neutron energy for ^{252}Cf is approximately 2.1 - 2.5 MeV (Fig. 2.6a), whereas neutron energy spectrum of ^{241}AmBe averages at approximately 4.5 MeV (Fig. 2.6b). It should also be noted that neutron production process is different for each isotope.

2.4.1 Neutron production mechanism

^{252}Cf is a spontaneous fission source which is constantly in an excited state. Therefore, its atoms are constantly splitting, thus producing neutrons. Each fission event is accompanied by the release of gamma-rays when the atom splits. On average there are 3.767 neutrons and 7.980 gamma-rays produced in a single fission event [31, 32]. In a practical situation it may sometimes be required to focus the experiment on single particle emission/detection. This can be easily achieved through the application on the appropriate shielding.

The other radioactive isotope which was used in this study, ^{241}AmBe, produces neutrons as a result of an interaction between alpha particle emitting isotope, such as ^{241}Am, with a light isotope, such as Be. The reaction between the alpha particles emitted by ^{241}Am and ^{9}Be is presented in Equation 2.4.

$$^{4}_{2}\alpha + ^{9}_{4}\mathrm{Be} \longrightarrow ^{1}_{0}\mathrm{n} + ^{12}_{6}\mathrm{C}^{*} \longrightarrow ^{12}_{6}\mathrm{C} + 4.44\,\mathrm{MeV} \tag{2.4}$$

As a result of the interaction between ^{241}Am and ^{9}Be a fast neutron is produced, as well as ^{12}C* which de-excites through the release of a gamma-ray photon of 4.44 MeV. ^{241}AmBe source produces approximately 1.14×10^6 neutrons per second [33]. As expected, the lifetime of such neutron emitter is dependent upon the half-life of the alpha particle emitting isotope. Together with ^{252}Cf, ^{241}AmBe represent the most common, laboratory neutron sources.

2.4.2 Gamma-ray emission

There are approximately twice as many gamma-ray photons as there are neutrons released during a fission event occurring in the isotope of ^{252}Cf (3.767 neutrons and 7.980 gamma-rays). Energy of gamma-rays produced is measured in hundreds of keV. In contrast, ^{241}AmBe produces primarily 4.44 MeV gamma-ray photons, which accompany the reaction occurring between ^{241}Am and ^{9}Be.

2.4.3 ^{252}Cf at Lancaster University

Due to safety concerns, radioactive sources are normally stored in shielded environments to minimise their harmful influence on staff working with or in a close proximity of these sources. Since neutrons are best modulated through light atoms, such as hydrogen, hydrogen-rich materials are most suitable for such applications. Therefore, ^{252}Cf source at Lancaster University, when not used, is stored in the centre of a water-filled stainless steel tank. This is depicted in Fig. 2.7 where position 1 reflects the location of the source, when in stored position.

The radioactive source can be pneumatically moved to the exposed position, marked with position 2 in Fig. 2.7. This is the position which is normally used for experiments in order to maximise the number of neutrons unaffected by the shielding. However, a large number of neutrons reaching the detector will be modulated through the interactions with the water atoms in the tank. Therefore, the experimental set-up of Lancaster University was modelled and the resulting spectrum computationally measured. Graphs presenting the modulated spectrum of ^{252}Cf at Lancaster University are presented in Fig. 2.8.

It can be observed that the peak flux in the modulated environment has moved down the energy scale on the x-axis to approximately 0.7-0.8 MeV, as shown in

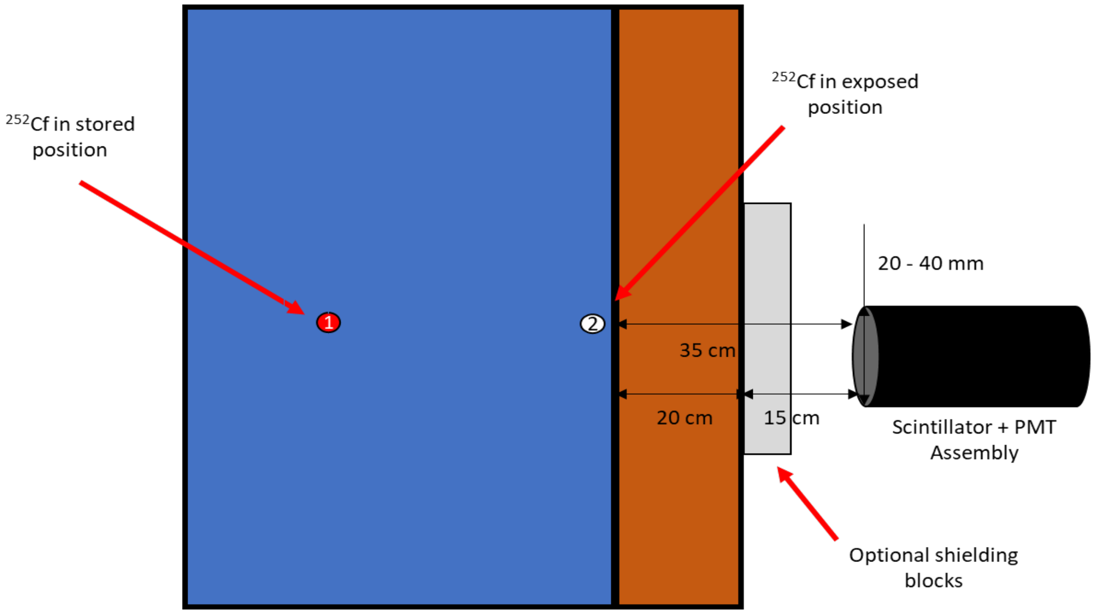

Figure 2.7: Side view of the water-filled steel tank with the radioactive source (^{252}Cf) at Lancaster University. A typical experimental set-up is also presented, with the distances used clearly marked. (Please note, the presented diagram is not to scale).

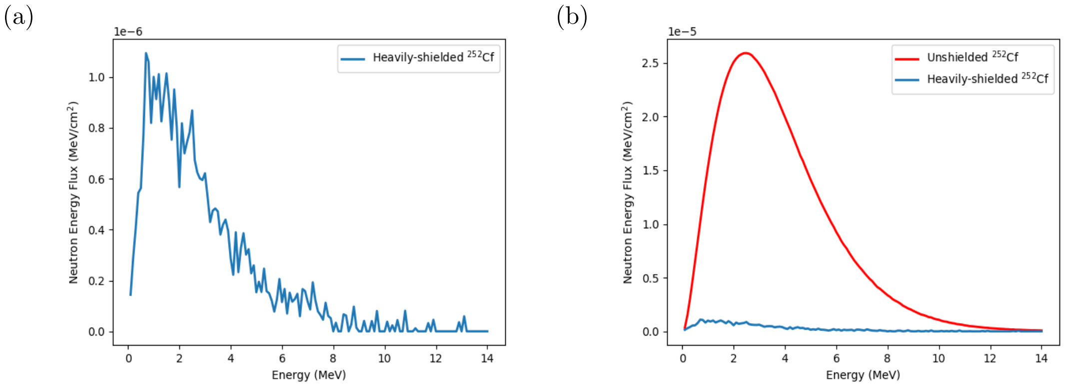

Figure 2.8: Modulated neutron energy spectra of ^{252}Cf at Lancaster University where a) presents the modulated spectrum, and b) a comparison to an unmodulated spectrum for equal number of total particle histories.

Fig. 2.8b. This can have a profound influence on the performance of an organic scintillating detector, as these are primarily targeting energy region of fast neutrons. In line with Table 2.1, neutrons of energy 1 MeV and higher are classed as fast neutrons. Moreover, the measured energy flux is approximately 20 times lower when compared with the unshielded source as shown in 2.8a.

2.5 Readout electronics

This thesis focuses on the work performed with solid organic scintillators. Solid organic scintillators, including single stilbene crystals and various types of plastics, were utilised in the experimental work performed in chapters 5, 7 and 8. As mentioned in the previous section, neutral particles must first undergo an interaction which produces charged particles that can be detected. These then need to be digitised to perform further processing. In this section the most important parts of typical readout electronic systems for scintillator based detectors are described.

2.5.1 Photomultiplier tubes

The weak light produced in a scintillator, as a result of an interaction between the incident particle and the scintillation medium, needs to be converted to an electrical signal. The most commonly used photodetector is a photomultiplier tube (PMT). A schematic of a PMT with a scintillator attached, and a path taken by an incident particle, is presented in Figure 2.9.

As presented in Figure 2.9, when an incident particle (neutron or gamma-ray photon) interacts within a scintillator, it gives rise to a very weak light signal (typically a few hundred photons). This weak beam of visible light is then converted to low energy electrons (sometimes referred to as photoelectrons) through the photocathode. The charge of the photoelectrons is insufficient to produce the required electrical signal and needs to be amplified. This is achieved through the electron multiplication stage of a PMT, where focusing electrodes direct the low energy electrons onto the first dynode and each electron is multiplied. Depending on the number of stages in a PMT, a scintillation pulse may produce between 10^7 and 10^{10} electrons.

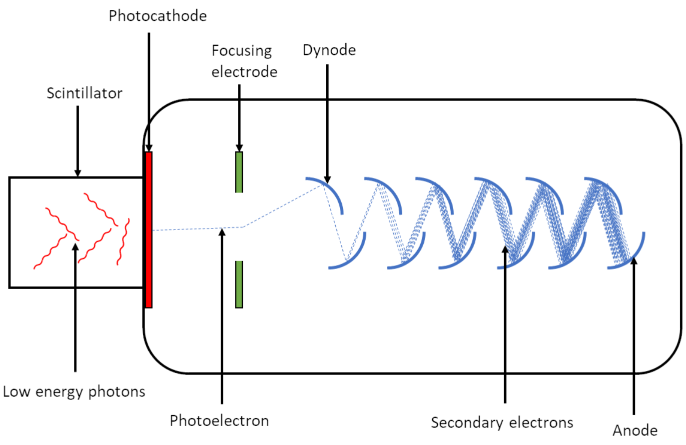

Figure 2.9: Schematic of a photomultiplier tube (PMT) with a scintillator attached.

When choosing a PMT for a specific scintillator, characteristics such as efficiency must be considered. Typical efficiency of a photocathode is 20-30%, which is also dependant on the wavelength of the incident photon. Therefore, wavelength characteristics of the scintillator and PMT must be matched to maximise efficiency.

2.5.2 Digitising electronic systems

Improvements in the field of digital electronics over the recent decades led to the development of fast semiconductor devices, such as digital signal processors (DSP) and field programmable gate arrays (FPGA). Both approaches have been successfully employed to process digital signals produced by organic scintillators [34, 35, 36]. Since these devices can operate at high frequencies, they can offer many benefits related to the reduction of data processing time, as initial pulse analysis can be performed on the processor.

Before the signals produced by a PMT can be processed on an FPGA or a DSP chip, they need to be converted from the analogue domain to discrete digital signals. This is typically achieved through analogue-to-digital converters (ADC), which sample the incoming analogue signal at a set frequency with a defined resolution. Both characteristics have a significant impact on the performance of the complete detector.

The minimum sampling rate of a digital signal is defined by Shannon-Nyquist Theorem, which says that the sampling rate should be at least twice the frequency of the waveform. The optimal sampling frequency for a detector based on organic scintillator has been closely studied in literature [37, 38], and is further discussed in chapter 8. Generally, there will be a low frequency cut-off point which is sufficient to transfer enough information about the pulse shape to perform necessary processing [37]. In a similar way, there will be a high sampling rate cut-off where further increase does not introduce any significant improvement to the system [38].

Other characteristics to be considered when searching for a suitable ADC are its bandwidth and resolution. Resolution of an ADC may have a significant impact on the performance of a digisiting system, if large energy ranges are to be investigated [39]. However, it is often the case that higher resolution of an ADC is achieved at the cost of a lower sampling rate. Literature suggests that on average sampling rates of between 250-1000 MS/s and resolutions between 8-12 bits offer good detector performance [37, 40].

2.5.3 Field Programmable Gate Arrays

Field Programmable Gate Arrays (FPGA) offer a significant advantage over typical microprocessor system, due to the way they execute instructions. Microprocessor systems, such as DSP, are examples of sequential execution with single instruction being executed per machine cycle. FPGAs allow parallel execution of multiple instructions on programmable parallel logic blocks. This allows fast processing of the data arriving from high sampling rate ADCs. As such, FPGAs propose a suitable solution for many real-time systems. Therefore, FPGAs find their place across many nuclear instrumentation applications [41, 42, 43].

One of the most important advantages of using an FPGA in a digitising system is that it can act as a buffer between a fast ADC and other electronic devices (e.g. microcontroller, PC) which perform further processing of the digitised data. The link between FPGA and further processing unit will normally be realised using slower communication protocols, so that the unit - such as PC - will be capable of handling the speed of the data transfer. Therefore, depending on the application and the choice of the unit for further data processing, overall system can either perform the data analysis in real time or store the data for off-line analysis.

A combined system comprising an ADC and FPGA chip samples the analogue signal arriving at the ADC input and the discrete digital value is compared to a trigger level set on the FPGA. If the new ADC value exceeds the trigger level, its value is stored in a buffer and transmitted for further processing. It is usually useful to store a number of samples before the trigger level is exceeded, in order to avoid pulse pile-up situation. Once triggered, FPGA will normally store a defined number of discrete values in one trigger window. In an organic scintillator, it is often approximately 200-300 ns, which normally covers a time period before and after the pulse.

For the purposes of the experimental work documented in this thesis two digitiser systems have been used. One was a standard single channel FPGA based digitiser operating at 150 MS/s, whereas the other one was sampling at 500 MS/s. In the case of the former, it was developed by Balmer [39] and was subsequently used for solid scintillator characterisation work documented in chapter 5. This digitiser system was further developed in the course of this project to allow dual-channel operation for a pixelated detector [44].

2.6 Digital signal and image processing

When working with digital signals, converted from the analogue domain, it is impossible to avoid electrical noise. Electrical noise can be defined as random and undesired changes in the electrical signal which occurs in all electronic circuits. As described in preceding sections, signals generated by radiation detectors are often weak and transient-like. Therefore, an exposure of the detector to low level of electrical noise can lead to an incorrect interpretation of the analysed data.

The most common and inevitable type of noise is Johnson-Nyquist noise. It is often referred to as thermal noise, because it is caused by random thermal motion of charged particles in an electrical conductor. It is an example of *white noise*, whose amplitude remains unchanged across the whole frequency spectrum (with an exception of very high frequency regions). In contrast to *white noise*, flicker noise (or 1/f noise) is an example of a *pink noise*, where the intensity of the noise is conversely proportional to the frequency. The final type of noise that should be noted in electrical signals is short noise. This type of noise does not depend of frequency and is caused by random current fluctuations. These changes originate in the way electrical charge carriers behave in a conductor. In a similar way, short noise can be observed in photon counting applications, when light is considered as a particle.

2.6.1 Digital signal filtering

The weak and transient-like pulses generated by radiation detectors carry a lot of information about the origin of the interaction of the incident particle. For instance, pulse height information can be used to obtain the energy spectrum of the investigated system. In the case of solid organic scintillators, the rate of the signal decay (in the tail of the pulse), can be exploited to classify the pulse as either produced by neutron or a gamma-ray interaction. Therefore, it is of vital importance that the noise levels are as low as possible to not distort the information therein. As noise influence is unavoidable, filtering techniques can be used to reduce the noise levels. However, these should be applied with care so that as much as possible of the original information is retained in the signal.

Filters applied in the analogue domain used to take a form of a low-pass filter which would stop high frequency noise from appearing on the output signal. Traditionally, such filters were built using resistor-capacitor integrator circuits whose charge collection time would be in the order of tens of microseconds. Owing to the advantages of technological advancement, the same techniques can now be implemented with ease in the digital domain.

Depending on the complexity of the filter implemented, filtering can be either implemented directly at first stage processing (FPGA or DSP) or at further processing stage (e.g. PC). The former is favourable for real-time applications, whereas the latter is confined to off-line processing. Although the computational overhead associated with complex techniques may have a profound impact on the choice of the processing platform, it is rarely directly related to significant quality improvements [45].

In this thesis the moving average filter was used to perform signal processing whenever digital signals were analysed. The main reason for the popularity of this filter in digital signal processing is its capability of random noise reduction, while maintaining a sharp step response. The moving average filter is a special example of a non-recursive finite impulse filter (FIR) whose output depends on the number of current and previous values (samples), as well as on the weight of the coefficients. It is also quite universal, as it can be applied to almost any frequency response characteristics. Its computational overhead is also low, permitting it to be easily incorporated directly into an FPGA chip.

2.6.2 Image processing techniques

Similarly to the electrical noise occurring on the output signals of the radiation detectors, optical noise can cause distortions in imaging applications. Subsequently, the location of the radioactive source can be incorrectly assessed and pose a serious threat in nuclear safety applications. Details of imaging devices typically used in nuclear safety applications are presented in chapter 3. Therein, an in-depth explanation of the term signal-to-noise-ratio (SNR) is presented, which is a relation of the signal measured and unwanted interference. Given that some noise is unavoidable, SNR of any imaging system should be kept as high as possible.

When coded-aperture based imaging systems are considered in general optical applications, the amount of noise appearing on the resulting image is primarily determined by the geometry of the coded aperture. It is assumed that the aperture is built of a material that is fully opaque to the particles emitted by the object being imaged (e.g. visible light). As such, the aperture can be designed using techniques based on two-dimensional convolution techniques, which enables the SNR to be improved in comparison to other techniques used in nuclear imaging applications, such as single opening collimators.

Standard two-dimensional convolution uses kernel, also called filter, which is utilised to, for instance, make the image smoother. Assuming that the object to be convoluted is represented as a two-dimensional array, the kernel is formed by another two-dimensional array of the same or smaller size which represents a delta function. An example of a kernel is presented in Figure 2.10, with the impulse of the delta function marked in the centre of the array. The result of the convolution is obtained by matrix multiplication of the object array with the kernel array. In Figure 2.10, an example 13 × 13 array is presented with a single opening in the centre of the array. Mathematically all but the centre cells would be filled with zeros, with the centre being one. The kernel array is moved cell by cell of the object array, with the impulse of the filter array always matching the currently filtered cell of the input array.

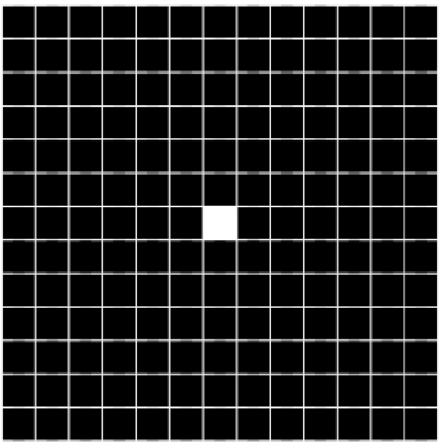

Figure 2.10: An example of a 13 × 13 kernel with a single opening in the centre.

The application of this simple kernel results in a higher resolution image, which allows more details of the object to be recognised. Depending on the application, the design of the filter can be different and reveal more details of the object (sharpen) or hide some details (blur). The effects of convolution can be easily reversed by using deconvolution. In the reverse process, the difference between the two arrays (object array and the resulting array) can be exploited, i.e. optical noise can be ignored, paving a way to a high resolution image of the object.

This concept has been successfully adopted in radiation imaging applications where different types of filters were investigated. In case of radiation imaging, convolution is realised through the coded aperture, which is built using a certain pattern defined for the filter used. There, filters consist of a defined pattern of transparent (ones) and opaque (zeros) cells, which either block or allow a particle to pass. Similarly to standard convolution, the resulting image can be deconvoluted where an impulse response is expected in ideal conditions. Further details about types of filters used in radiation imaging applications, as well as computational based examples in the field neutron detection, are discussed in chapter 3.

Chapter 3

Coded-aperture imaging systems: Past, present and future development - A review

Cieslak, M.J., Gamage, K.A.A., Glover, R.

Published in Radiation Measurements, 3rd August 2016

3.1 Abstract

Scintillator based coded-aperture imaging has proven to be effective when applied for X- and gamma-ray detection. Adaptation of the same method for neutron imaging has resulted in a number of propitious systems, which could be potentially employed for neutron detection in security and nuclear decommissioning applications. Recently developed scintillator based coded-aperture imagers reveal that localisation of neutron sources using this technique may be feasible, since pulse shape discrimination algorithms implemented in the digital domain can reliably separate gamma-rays from fast neutron interactions occurring within an organic scintillator. Moreover, recent advancements in the development of solid organic scintillators make them a viable solution for nuclear decommissioning applications as they present less hazardous characteristics than currently dominating liquid scintillation detectors. In this paper existing applications of coded apertures for radiation detection are critically reviewed, highlighting potential improvements

for coded-aperture based neutron source localisation. Further, the suitability of coded apertures for neutron imaging in nuclear decommissioning is also assessed using Monte-Carlo modelling.

3.2 Introduction

Accurate localisation of radioactive materials is crucial for nuclear safety and security. The growing threat of attacks using radioactive substances, as well as an increasing number of nuclear plants requiring characterisation to support decommissioning, necessitate development of a portable system capable of detecting radiation sources in real-time.

Radioactive substances are used in medicine, non-destructive testing, and power generation. For example, nuclear fuel used in power generation produces nuclear waste that needs to be carefully disposed of as it remains radioactive for a time period. If the source of radiation is not accurately identified and localised, radiation emitted by these materials can pose a health risk for personnel in close proximity to these materials. Localisation is particularly important during nuclear decommissioning and decontamination, since the actual location of the radioactive source within nuclear waste is often unknown.

Highly-penetrating radiation may be released in a form of X- or gamma-ray photons or free neutrons, emitted as a result of nuclear processes occurring within the atomic structure of radioisotopes. All three types of radiation mentioned can be detected using different gas filled tubes, which are sensitive to a specific type [46, 47]; examples are ionisation chambers, proportional counters and Geiger-Mueller counters. Scintillators can also be used in the same way as primary detectors to detect each type of radiation [48, 49, 50]. They transform energy detected into light pulses that can be counted by photosensitive electronic components e.g. photodiodes and photomultiplier tubes (PMTs).

Although the detectors mentioned above generally provide good radiation sensitivity, by themselves, they offer no specific information about the location of the radioactive source. Preliminary results of a recent study by Schuster and Brubaker [18] suggest that the anisotropic response of crystalline scintillation materials to neutron interactions may reveal some directional information about the source location. This type of information is of vital importance for nuclear decommissioning applications.

Substances used in the types of detectors mentioned can be difficult to source. ^{3}He, for instance, is mainly obtained as a byproduct from the radioactive decay of tritium; BF$_3$, on the other hand, is a hazardous gas and as such not desirable [10]. Radiographic film represents a safe implementation of radiation detector. For example, it has been employed in medical devices to perform skeletal body scanning with X-rays, successfully identifying fracture location [51]. A modification to the film detector, in the form of an imaging plate, allows detection of radioactive sources, where it is particularly useful for nuclear decommissioning applications [52, 53].

Radiation imaging methods do not only detect an occurrence of a radioactive event but also provide the location of the incident. As such their potential has led to the development of radiation cameras - based on the operation principle of a general pinhole camera [54]. Pinhole cameras, capable of identifying radioactive substances from a distance, are frequently used in nuclear decommissioning. CARTOGAM is an example of such gamma-ray pinhole imager [55, 56, 57]. The size of the pinhole determines the angular resolution and signal-to-noise ratio (SNR) of a specific camera; the former increases in a camera with a small opening, whereas the latter decreases when the diameter of a pinhole is decreased.

It follows that an ideal single pinhole camera, would require an infinitely small pinhole to obtain the highest angular resolution. Conversely, the highest SNR would be achieved in a camera with an infinitely long diameter of the opening. Hence, in practical applications, a compromise must always be found between SNR and the angular resolution for the single pinhole cameras. In order to address this problem scatter-hole cameras were developed, where multiple holes of small diameter were distributed randomly on the aperture offering significant improvements in SNR, while maintaining good angular resolution [58]. However, reconstruction of the original image was difficult due to the random distribution of the pinholes. The issue was addressed by coded-aperture imaging, which was introduced with ‘encoding‘ and ‘decoding‘ arrays to simplify the process of image reconstruction

[59].

Coded-aperture imaging is a technique adopted in X-ray cameras and telescopes, widely utilised in numerous space exploration missions [60, 61, 62, 63, 64]. Due to similar characteristics to X-rays, coded-aperture method has been incorporated into gamma-ray imagers for medical applications [65, 66], non-destructive testing [67], explosives detection [68], as well as for nuclear decommissioning and decontamination; these are GAMPIX [69], RADCAM [49] and High-Energy Radiation Visualiser (HREV) [70, 71]. Coded-aperture methods, for neutron source localisation, have been applied in the field of national security [72, 73] and nuclear material detection at fuel cycle facilities [74].

The scintillator based coded-aperture neutron imaging systems mentioned target fast neutron localisation. In each case pulse shape discrimination (PSD) methods are exploited to separate gamma-rays from neutron events. Multiple channel real-time PSD has been successfully implemented laying the foundations for high resolution (high number of pixels) organic scintillator based coded-aperture imagers [75]. However, identified neutron interactions must be localised within the scintillator so that the decoding process can be performed. The decoding process, which may contribute to the timing overhead of the localisation procedure, is required to infer the actual location of the radioactive substances.

In this paper existing coded-aperture imaging systems are critically reviewed with relevance to radiation detection and localisation. The advantages of the coded-aperture technique over other methods are recognised, when used for X- and gamma-ray detection, as well as its potential for neutron imaging. Additionally, the coded-mask itself, as well as sensitive neutron detectors for such an application are also highlighted. The potential of employing coded-aperture based techniques for neutron imaging in nuclear decommissioning is evidenced by a simple model generated in Monte Carlo N-Particle eXtended (MCNPX) simulation software package.

3.3 Radiation imaging and development of collimator-based detectors

Radiographic film was the original method of X-ray detection, used by Roentgen to discover X-rays, that was later adopted for gamma-radiography. Radiographic film has been successfully implemented in medical devices to perform skeletal body imaging with X-rays. It was possible due to the attenuation properties of X-rays for elements such as Ca [51]. A modification in a form of an imaging plate was introduced to the film detector to map ^{239}Pu in human lungs [52].

In medical applications, an X-ray radiation source is placed in front of an object to be imaged, whose shadow is cast on the photographic film, where the picture of the object is projected. Images generated using this method show good spatial resolution but low sensitivity. Replacing the film with a pixelated charge coupled device (CCD) offers a way of improving the low sensitivity issue. It allows an analogue to digital converter (ADC) to be connected to individual pixels on the device. The ADC can be adjusted to ignore signals below certain voltage threshold to reduce the amount of noise reconstructed, effectively increasing the sensitivity of such a device [76].

Semiconductor solid state detectors, such as cadmium zinc telluride (CdZnTe), may also be implemented (either independently or in conjunction with gas filled tubes, scintillators) for radiation localisation. When solid state detectors are exposed to radiation sources directly, they convert the pulses - emitted as a result of the interaction between the radiating particles and the detector - into electrical current, which can be easily measured. Although semiconductor solid state detectors are more susceptible to damages caused by radiation, they are sometimes preferred in spectrometry applications due to their superior energy resolution [19].

As an alternative to direct detection methods, ionising properties of specific gases prompted the development of detector tubes. The tubes filled with gas produce an electronic signal as a result of ionisation between the gas and radioactive particles [19]. Depending on the radiation type gases utilised include BF_3 and Xe for neutron and X-, gamma-ray detectors respectively. Alternatively, the scintillating properties of specific chemical compounds, for example CsI(Tl) and

CsI(Na), offer a way of transforming X- and gamma-ray energy to light photons that can be counted using photosensitive electronic components.

Scintillator, such as CsI(Tl), can be used as a sensitive detector for a single pinhole radiation camera [77]. Spatial resolution of the pinhole camera depends predominantly on the size of the single opening in the aperture and the performance of the sensitive detector used. However, it can be significantly improved if a collimator is used to narrow the path of the incoming radiation to the single opening of the aperture [78]. Replacing the single pinhole camera with a multi hole version, which was then followed by a new family of coded-aperture imaging systems, enhanced the quality of images obtained even further.

3.3.1 Coded-aperture based imaging

The coded-aperture approach for radiation detection has its roots in development of scatter-hole cameras for X- and gamma-rays. Introduction of a multi-hole mask improves the SNR while maintaining a good angular resolution of a small diameter, single hole imaging device [58]. In mathematical terms masks were represented as binary arrays with the ones corresponding to the pinholes, and the zeros to opaque elements in the aperture. In the early work on coded apertures, pinholes were randomly distributed on the mask and placed in front of a source to be analysed. The source casts multiple overlapping shadows on the detector through the mask as presented in Figure 3.1. Fourier convolution theorem is then used to reconstruct a single, high resolution image from the photons counted on the detector plane [79]. Since the pinholes were randomly distributed, a construction of a unique binary array was required for each specific application.

Random patterns pose difficulties with image reconstruction due to a lack of uniformity in pinholes distribution. An inherent noise appears as a result of small terms present in Fourier transform of large size random binary arrays. This problem was addressed by the development of uniformly redundant arrays (URAs). If the distribution of the transparent and opaque elements of the aperture can be represented as a binary encoding array A and the decoding array as G, then A and G can be chosen such that the reconstructed image (correlation of A and G with addition of some noise signal N) approximates a delta function. Delta function is

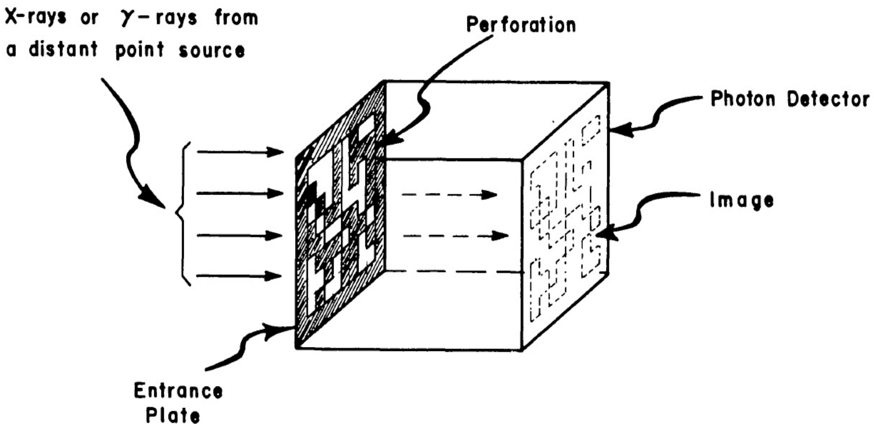

Figure 3.1: Scatter-hole camera aperture as proposed by Dicke [58].

represented by a single impulse located at the central point in signal analysis. In radiation detectors the impulse indicates the location of the reconstructed source [80].

Calculation of possible dimensions of the arrays is based on pseudo-noise arrays and previous research documents their implementation for URA based coded apertures. It has experimentally been shown that URAs offer significant improvements to SNR in comparison with randomly distributed arrays; the quality of reconstruction is improved if the exposure time is increased. URA based coded apertures are constructed by 2 × 2 arrangement of the basic design [81, 59]. Thus, the size of the detector can be kept small as only the basic array is required to fully recover the source distribution.

Despite its advantages the algorithm used for the construction of URAs restricts the shape of the aperture to a rectangle as vertical and horizontal sides dimensions, p and q, must satisfy the condition p - q = 2 [59]. This limitation was recognised and a modification to the original design was introduced in a form of a hexagonal URA (HURA). An algorithm, based on pseudo-noise (PN) sequences [82], for the realisation of URA on a hexagonal lattice was first presented by Finger and Prince [83]. It followed a previously proposed implementation of a rotating HURA for gamma-ray imaging [84]. In the new form HURA was successfully adopted for X- and gamma-ray imaging in high energy astronomy [85]. In addition a set of characteristics to assess the performance of the aperture was also proposed [86].

The limitation imposed on the physical dimensions of the coded-aperture designs based on URA algorithm led to the development of another class of coded-aperture arrays. Pseudo-Noise Product (PNP) arrays allowed a construction of coded apertures in previously unavailable dimensions. PNP array can be implemented in any dimensions, provided a corresponding PN sequence exists. However the transparency of PNP arrays is halved in comparison to URAs, because a two-dimensional PNP array is constructed through a direct product of two one-dimensional PN sequences. Although the resulting transparency of the coded aperture is reduced to 25%, SNR comparison with other techniques shows that PNP arrays achieve superior results to pinhole cameras and only slightly inferior to URAs [87].

Modified Uniformly Redundant Array (MURA), introduced with a change to URA's encoding algorithm, enabled new arrays to be created in linear, hexagonal and square configurations. The design method for URAs was modified, so that the new arrays were based on quadratic residues rather than PN sequences [88]. Consequently, hexagonal MURA patterns differ significantly from the previously developed HURAs. The hexagonal MURAs can now be formed by mapping of the linear MURAs in exactly the same way as proposed before by Finger and Prince [83]. Linear MURA can now be built in any length L that is a prime number and satisfies the condition $L = 4m + 1$, where $m = 1,2,3\ldots$. Similarly, linear MURAs use quadratic residue modulo L to establish locations of transparent and opaque elements in the coding array A. It was also shown that apertures can be formed in dimensions satisfying not only $p - q = 2$, but also $p - q = 0$ [88]. The square option proved to be particularly popular due to a good balance between design complexity and the high resolution achieved.

3.4 Coded-aperture based X-ray imaging

Development of large scale X-ray imaging systems was mainly motivated by the space exploration missions SuperAGILE [63, 64], SWIFT [60], EXIST [89, 61, 90] and INTEGRAL [91]. As a result, there exists a number of readily available X-ray imagers, where coded-aperture imaging is the dominant technique adopted. Different types of coded-aperture X-ray cameras and telescopes were implemented. Some systems utilise CdZnTe sensors for direct detection of the signals projected through the aperture [60, 61, 62]. Other examples make use of sensitive silicon microstrip detectors [63, 64], where X-ray photons interact directly with the sensitive elements of the detector. Kinetic energy of photons is transformed into electrons, which can be processed by dedicated electronic circuitry.

A comprehensive account of coded-aperture applications in X-ray imaging for space exploration was presented by Caroli et al. [86]. A set of experiments was conducted to compare the coded-aperture based devices with other approaches. The advantages of using URA based coded masks, as opposed to fresnel pinhole or random masks, are clear when the angular resolution of the reconstruction is considered. Decreasing the hole size results in higher angular resolution - SNR is not affected as the increased number of holes can provide up to 50% aperture transparency. As the dimensions of the aperture elements are kept small, the overall size of the aperture may also be small and reduce the field of view (FOV) of the device. However, multiple devices can be built (in e.g. 2×2 configuration), which will compensate for FOV reduction at the cost of greater number of signals required to be processed on the output. This may in turn affect the detection speed as signals from the position sensitive detector require decoding to localise the source of radiation in the coded-aperture imaging systems.

A coded-aperture based X-ray camera, which utilises CCD as the position sensitive detector, was tested with a ^{241}Am source and the results confirmed the improvement in sensitivity when compared to a pinhole camera [92]. In the experiment a device was built comprising a mask, CsI(Tl) scintillator, image intensifiers, CCD, lead shield and high voltage insulation. Different combinations of hole sizes and thicknesses were tested for two types of masks, namely single pinhole and coded-aperture mask based on HURA design. Sensitivity increase of up to four times was observed when images obtained by coded-aperture mask were contrasted with those generated by a single pinhole mask [92].

For comparison a 5 mm thick brass disk was used for both the HURA coded aperture and the pinhole plate. Pinhole diameter was also kept the same for both tests at 2 mm. Images created using both techniques are presented in Figure 3.2. The top four images shown in Figure 3.2 are corresponding to the single hole plate case, and the bottom four images to the coded-aperture disk. It is clear that coded-aperture based reconstruction of the circular ^{241}Am source shows superior spatial resolution, when compared to the single hole plate.

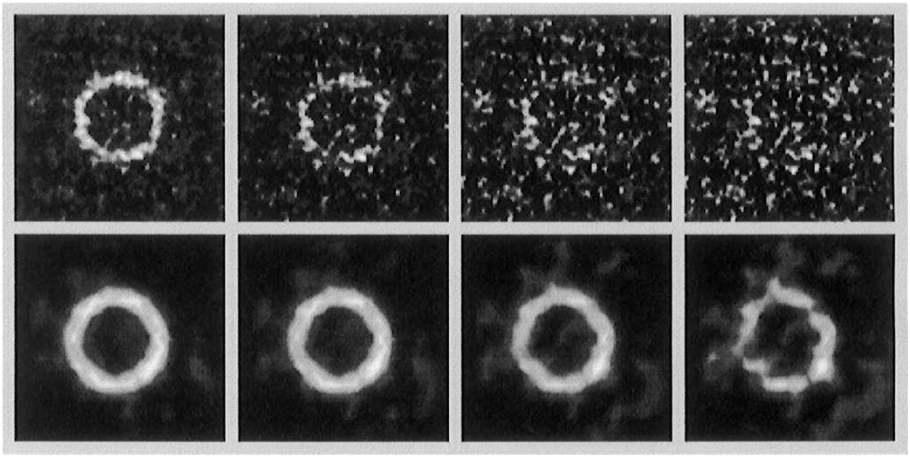

Figure 3.2: Results of experiments carried out with a circular ^{241}Am source by Ivanov et al. [92]. Detection time is equal to 8, 4, 2 and 1 of relative units (from left to right).

3.5 Coded-aperture based gamma imaging

Since gamma-rays are released in a form of high energy photons, X-ray imaging methods can also be exploited for gamma-ray detection. Therefore, coded apertures, as well as pinhole collimators have been implemented into scintillator based devices for gamma-ray detection and localisation. The primary application of coded-aperture based gamma-ray detectors in far-field high energy cameras for space exploration formed a basis for the study of near-field radiation detection in medicine and nuclear decommissioning. A very thorough investigation of coded-aperture approach as compared to pinhole camera collimator, for medical applications, was presented by Accorsi [93]. Results of the study are presented in Table 3.1. These findings highlighted the advantages of employing coded-mask in place of a pinhole aperture when resolution and sensitivity are considered.

Table 3.1: Resolution and sensitivity comparison for collimator, pinhole and coded aperture with ^{99m}Tc used as gamma source [93].

Optics (^{99m}Tc)	**Collimator**		**Pinhole**	**Coded Aperture**
	High Sensitivity	**Ultra-high resolution**		
Hole diameter (mm)	2.54	1.16	4	1.11
Geometric resolution @ 10 cm (mm)	14.6	4.6	6.2	1.45
System resolution @ 10 cm (mm)	15.2	6.3	6.6	1.67
Sensitivity @ 10 cm (cpm/μCi)	1063	100	123	$\sim$ 10000

An often quoted disadvantage of coded-aperture approach is its limited FOV [94]. Moreover, coded-aperture imagers are claimed to perform better than pinhole collimators only when point source localisation is performed. In spite of these potential weaknesses for large scale applications, recent research suggests that large horizontal FOV can be achieved by combining multiple coded apertures into a single hexagonal device [95]. In this particular case a system with 360° horizontal FOV presented angular resolution of average 3.5° when tested with standard calibration source of ^{137}Cs with energy of 662 keV. The system was also able to detect multiple sources in 360 ° FOV.

Detectors of such scale may sometimes be impractical for decommissioning applications as portability plays a key role during deployment. Therefore the overall dimensions are frequently decreased and, as a result, the FOV is reduced. Scanning collimator, for example RadScan, can be used to perform the analysis of greater area alleviating the problem of the limited FOV [96, 97]. Exact location of radionuclides in nuclear decommissioning and environment characterisation applications is often unknown; hence the detection efficiency is of greater significance than the extended FOV.

A recent experiment performed by Gmar et al. [69] presents a strong correlation between the thickness of the mask used and the detection efficiency of a coded-aperture imaging system. During the study two MURA based masks were used - a rank 11, 4 mm thick mask and a rank 13, 2 mm thick mask. The rank number specifies the number of elements (pixels) comprising one side of a basic square MURA pattern, and coded apertures are conventionally built by 2 × 2 arrangement of the basic pattern, following the cyclic permutation of rows and columns [88]. Therefore, the total number of pixels for the rank 13 and the rank 11 aperture are 625 and 441 respectively. When both masks were tested with lower energy gamma-ray emitter (^{241}Am), the rank 13, 2 mm thick mask provided higher resolution than the rank 11, 4 mm thick aperture. However, when the system was exposed to relatively higher energy gamma sources (^{137}Cs and ^{60}Co), the rank 13, 2 mm thick mask performed distinctly inferior to the lower rank mask. In the latter case (^{60}Co) the configuration with rank 13, 2 mm thick aperture was found unable to detect the source [69].

3.6 Neutron detection and coded-aperture imaging approach

The radioactive waste streams can contain neutron-emitting radioactive materials, hence localisation of neutron sources plays an important part in nuclear decommissioning. It is of vital importance that personnel working on a nuclear site are also not exposed to neutron radiation. For many years, neutron detection systems were largely based on techniques involving ^{3}He as the primary detector, for example ^{3}He proportional counters were used extensively by security organisations to identify potential terrorist threats [98]. Despite its popularity and efficiency, an alternative system capable of neutron detection in real-time must be considered as ^{3}He supply has decreased sharply in the aftermath of September 2001 attacks.

Devices based on ^{3}He are preferred due to higher thermal neutron capture cross-section, in comparison to detection systems based on BF_3 gas-filled detectors [19]. Their absolute efficiency depends greatly on the thickness of the moderation material, which is used to slow down fast neutrons. Generally, detectors with the thicker moderation layer provide better response for higher energy neutron detection. However, if the moderator layer is too thick, lower energy neutrons may be captured by the moderator before reaching the sensitive part of the detector.

Also, as the higher energy neutrons lose some of their energy before hitting the detector surface, the information about the neutron origin is lost. Consequently, the detection efficiency of the system is reduced [19]. Moreover, moderation thickness can limit the portability of the device, since significantly thicker moderation layer may be required for higher energy neutrons [99].

Four alternative methods have been tested by Kouzes et al. [10] identifying their absolute neutron efficiency and gamma-ray sensitivity. Each option was tested according to the specification of radiation portal monitoring (RPM) systems for national security in the United States. Only a set of three BF_3 tubes and a B-lined detector met the RPM absolute neutron detection efficiency requirement, as well as intrinsic gamma-ray efficiency requirement. Although BF_3 tubes proved to be effective for detection of slow neutrons, it would not be a feasible solution for fast neutron localisation due to significant efficiency reduction for higher energy neutrons (>100 eV) and moderation requirement in the same way as ^{3}He [19].

Collimators coupled with B- and Gd-doped microchannel plates (MCP) present an interesting option for low energy neutrons. Neutrons are absorbed by B or Gd atoms inside the glass mixture plates, and electrons are emitted as a consequence of the absorbtion [100]. Each of the electrons emitted is then multiplied inside an individual microchannel. This approach offers a very high spatial resolution, due to the dimensions of individual elements in the range of micrometers. As a result, the collimator size is also small. The weakness of the system lies in the requirement of stacking multiple MCPs to detect higher energy neutrons which are otherwise limited to thermal energy neutron detection.

An analogous method to Compton scattering for gamma-rays can be employed to image high energy neutrons. The neutron scatter camera method measures the energy of the recoil proton and time of flight (TOF) of the scattered neutron [101]. Experiments performed showed that these two measurements are not sufficient to undoubtedly distinguish gamma photons from neutron events in mixed-field environment. It was essential to add a PSD module, so the signals can be reliably separated [102].

A release of a neutron, following a nuclear reaction, is often accompanied by an emission of high energy gamma photons. Therefore, an efficient technique is required to distinguish between gamma-rays and neutron events in mixed radiation fields. Undoped organic liquid scintillators, such as EJ-301 and EJ-309, are regularly used to separate fast neutrons from gamma rays in mixed radiation fields, due to their excellent PSD capabilities. The light pulses triggered by the neutron interactions, within the organic scintillator, decay more slowly as compared to those triggered by gamma ray interactions. The difference in the decay time is caused by greater energy loss rate for neutron than for gamma ray interactions within the scintillator [27]. Consequently, PSD can be performed to establish the type of the event detected. Various algorithms have been considered by the researchers in the time domain, as well as in the frequency domain [27, 103].

The aforementioned liquid scintillators (EJ-301 and EJ-309), were developed with capability of detecting fast neutrons, whereas they are not sensitive to thermal neutrons. They require doping with large thermal neutron capture cross-section isotopes to allow the detection of thermal neutrons. An example of such a detector is BC-523A, which is loaded with 4.4% of ^{10}B. As such, it presents greater detection efficiency when compared with the undoped EJ-309. In an experiment performed by Peerani et al. [98] both detectors were irradiated with ^{252}Cf and AmBe sources. Both detectors were 5 inch × 5 inch cylinders with a total detection volume of approximately 1600 cm^3. In each case detection efficiency was approximately 15% better for BC-523A than EJ-309. Moreover, PSD applied to organic liquid scintillators is insufficient to distinguish gamma photons from neutrons perfectly. A partial overlap between the gamma and neutron clouds is recorded suggesting an inevitable degree of misclassification of the events [98]. Recently developed plastic and crystal scintilltors, such as EJ-299-33 [14] and stilbene [104], promise a very good separation characteristics for neutrons and gamma-rays. However, the signals emitted by the plastic scintillators are faster compared to liquid scintillators making the application of PSD more challenging [98].

Despite the challenges, PSD has been established as a standard method of separating neutron events from gamma-rays in radiation detectors based on organic scintillators. Development of fast ADCs and field programmable gate arrays (FPGAs) enabled PSD algorithms to be implemented reliably in the digital domain [105, 27]. A well-established in the laboratory setting Charge Comparison Method

(CCM) for example [106], relies on the comparison of two time integrals of the detected pulse. The first integral is associated with the entire pulse, whereas the second one can be calculated as the area under the tail of the pulse. Hence, they are often described as the long and the short integral, respectively. The light pulse resulting from a gamma-ray photon interaction in the scintillator decays faster than the pulse corresponding to a neutron event. Consequently, the short integral is smaller for gamma-rays than for neutrons, when compared to the same magnitude long integral [106, 107]. Alternatively, CCM can be defined as follows: the short integral as the peak of the pulse, and the long integral as the whole pulse. Regardless of the CCM definition, integration can be performed digitally by the summation of the areas under the pulse corresponding to each sample taken by the ADC.

3.6.1 Coded-aperture based approach

A large energy spectrum of neutron events complicates the employment of the coded-mask approach for neutron imaging. Therefore systems developed to date, focus on a specific energy range of neutrons. One of the implementations of the MURA based coded aperture for thermal neutron detection was studied with a ^{3}He ionisation chamber [47]. High angular resolution obtained by coded-aperture based X- and gamma-ray imagers was maintained, when the same method was employed for thermal neutron localisation. Nevertheless the shortage of ^{3}He supply, as well as the limitations in portability of such a device makes the developments of ^{3}He based coded-aperture detection systems undesirable.

A fast neutron detector design based on the linear MURA using liquid scintillator EJ-301 revealed promising results when tested in security applications [108]. Both the mask as well as the detector plane were built using EJ-301 filled aluminium tubes [72]. This enabled the mask to scatter the fast neutrons rather than block them. As a result the neutrons detected in the mask were removed from the reconstructed image. The results showed high spatial resolution for two AmBe sources placed simultaneously in front of the aperture. The normally opaque elements of the coded-mask are replaced with neutron detectors. Consequently, neutron scattering occurs within the coded-mask, when the system is exposed to a fast neutron source. The scattered neutron will then disperse again (double scattering) when it causes another scattering event with the actual detector plane. Thus, the energy spectrum of the source can be determined by measuring the TOF between scatters. While the primary application of the system developed was fast neutron detection, it also exhibits potential for detecting gamma sources when PSD is applied. In an analogous test to the one performed for AmBe neutron source, a high energy gamma source ^{60}Co was placed 6.7 meters away from the detector. The results presented support the claim of comparable detection efficiency for neutron and gamma-ray sources [108].

Another implementation of a fast neutron and gamma-ray imaging system based on coded-aperture MURA pattern was developed at the U.S. Naval Research Laboratory (NRL) to support maritime security in the US [73]. The system tested comprises a square (13 × 13), 11.2 cm thick aperture made of Pb and high density polyethylene (HDPE) and an array of 30 liquid scintillation detectors (EJ-301). Each element of the aperture, as well as the detector is a 5.1 cm × 5.1 cm square. The detector array was placed 76 cm behind the coded aperture. The system in this arrangement was tested with ^{252}Cf gamma/neutron source and ^{137}Cs gamma source placed 5.1 m away from the aperture plane. Since the lower energy threshold was set to > 2.5 MeV neutron energy in each detector, there was no misclassifications recorded between gamma-ray and neutron events. An angular resolution of up to 4.6° was reported for the reconstructed images.

Further research conducted by the NRL led to a development of a large-scale, coded-aperture imager for fast neutrons [109]. In comparison to the work reported in the above paragraph, a 12 × 12 elements coded aperture made of pure HDPE was built using psedudorandom pattern. EJ-301 scintillators were replaced with bigger EJ-309 detectors. The size of the individual detector was increased to 15 cm × 15 cm × 15 cm and the number of detectors to 32. The system was tested with two ^{252}Cf sources of different activities - 13 μCi (481 kBq) and 1.8 μCi (66.6 kBq) - located at various distances from the aperture. Similarly to the previous work, 4.5° angular resolution was reported in the reconstructed images. However, when the lower activity source was placed 26 m away from the aperture, it was not detected due to the high level of noise detected. Additional shielding around the detector array was necessary to improve the SNR and hence localise the lower activity source. Neutron and gamma PSD was implemented using digital CCM algorithm for each of 32 single channel PMTs.

MURA based coded-aperture fast neutron detection system was also tested for measurement of plutonium holdup at fuel cycle facilities [74]. This system was a result of improvements to the previous work performed at Oak Ridge National Laboratory (ORNL), which used liquid scintillators as sensitive detectors and utilised Pb shielding to block gamma-rays [110, 111]. The new system utilised modulating properties of HDPE to slow down the high energy neutrons, as the rank-11 MURA based aperture was built entirely from this material. In this experiment a new PSD capable plastic scintillator (EJ-299-34) was tested as a replacement to a fragile and susceptible to leaks liquid detector (EJ-309). The detector was built as a 8 × 8 array of individual plastic scintillator pixels with 1.35 × 1.35 × 5 cm^3 making the total volume of the detector to be 10.8 × 10.8 × 5 cm^3. The detector was positioned behind the 53.4 × 53.4 × 2.54 cm^3 coded-aperture pattern machined in a 81 × 81 × 2.54 cm^3 piece of HDPE. Multiple apertures can be joined together to increase the thickness of the HDPE if required. Several scenarios were tested with single and multiple ^{252}Cf sources placed in various location with the reference to the detection system. The main focus of the study was sensitivity rather than spatial resolution. The results suggest that the location of the neutron source in three dimensions can be inferred with a high level of accuracy [74]. Nonetheless, the large scale of the system may present difficulties when attempting to incorporate such a system in nuclear decommissioning environment.

A different implementation of coded-masks to fast neutron localisation was presented by Brennan et al. [112]. In contrast to spatial modulation of a particle flux, normally used in coded-aperture imaging, time modulation of the particle flux was introduced. Time-encoded imaging (TEI) technique adapted in this study, relies on a small number of time-sensitive detectors, as opposed to position-sensitive detectors normally used in the coded-aperture imaging systems. Two time-sensitive detectors were built of two 1 inch diameter aluminium tubes filled with EJ-309 scintillator, coupled with two 2 inch diameter cylindrical PMT. The detectors were placed in the centre of a rotating circular mask made of HDPE. The mask had a

30% open fraction and the thickness chosen such that the fission neutrons were sufficiently moderated. The complete system was moved by a stepper motor which enabled the data from the motor encoder to be synchronised with the incidents detected by the PMTs. An angular resolution of 2° was achieved for two ^{252}Cf point sources after 12 hours exposure time [112]. Due to the rotational operation of the system a 360° horizontal FOV can be realised. However, long exposure time required may prevent the employment of such systems where real or near real-time radiation detection is desired.

More recent attempts of utilising the coded-aperture approach for neutron detection also show promising results. If the coded aperture is made of a neutron absorbing material, its thickness affects the overall performance of the detector. Recently performed Monte Carlo simulations used an 8 cm thick MURA based coded-aperture model (made of ^{10}B, ^{113}Cd and ^{157}Gd), EJ-426 - a thermal neutron scintillator - and ^{241}AmBe as the neutron source. The results present high spatial resolution for the neutron source located near the central point of the aperture. However, a decrease in spatial resolution is observed when the source is placed nearer the edges of the aperture. The decrease is caused by a greater number of neutrons being absorbed by the shielding implemented around the edges of the coded aperture. Since fewer neutrons reach the detector surface, the accuracy of the source reconstruction decreases [113].

Despite the high angular resolution achieved across the coded-aperture based neutron imagers presented in this section, their adaptation for nuclear decommissioning remains to be demonstrated. None of the systems described performs neutron localisation in real-time. Moreover, the large scale systems [102, 74, 112] would be difficult to deploy or maneuver within a nuclear decommissioning environment. They would be impractical in the environment where portability of radiation imaging systems is crucial.

3.7 Potential improvements to coded-aperture based neutron imaging

The currently employed techniques for neutron imaging do not offer sufficient sensitivity across the energy spectrum between thermal and fast neutrons (up to 15 MeV). Existing research suggests adding moderation materials or building apertures of greater thicknesses to solve the problem. These solutions may substantially increase the weight and limit the portability of the complete imaging system.

In this work a novel portable, real-time neutron imaging system is proposed which will be of great benefit to nuclear decommissioning and security applications. Authors simulated an innovative coded-aperture model considering the practicality of such a device. The shape and the dimensions of the aperture are also chosen such that a scintillator and a position sensitive photo multiplier tube (PSPMT) can be matched. Since an organic scintillating material which is sensitive to a range of neutron energies between thermal and fast (up to 15 MeV) is not available, focus was placed on developing a system suitable for the digital PSD implementation. Modern organic liquid scintillators offer discrimination between neutron and gamma incidents down to approximately 40 keVee, which corresponds to 450 keV energy neutrons [114, 28]. Improvements into methods of growing single stilbene crystals led to a development of a scintillator, which claims better PSD for lower energy neutrons than previously mentioned EJ-309 liquid scintillator [115]. Hence, the prospect of utilising the stilbene scintillator will be explored. The system could then be paired with a multi-channel, FPGA based signal processing electronic circuitry, making real-time detection, localisation and discrimination of neutron and gamma sources in a mixed radiation field possible.

3.7.1 Design of MURA based coded aperture

The model created in this work comprises a square rank 7 coded aperture with 169 elements, a scintillator and a neutron source. The coded aperture was designed using original MURA algorithm [88]. The design of the coded-aperture based system involves construction of both an encoding and a decoding array. The encoding array A is placed in front of a source of radiation S resulting in an encoded image being projected on the detector surface D. Considering the practicality of the simulated system, a 13 × 13 aperture - the encoding array A - was designed through a 2 × 2 arrangement of the basic rank 7 pattern. Location of opaque and transparent elements in the encoding array A was determined by following equations 3.1 and 3.2 [88].

$$A_{ij} = \begin{cases} 0 & \text{if } i = 1, \\ 1 & \text{if } j = 0, i \neq 0, \\ 1 & \text{if } C_i C_j = +1, \\ 0 & \text{otherwise,} \end{cases} \tag{3.1}$$

where

$$C_i, C_j = \begin{cases} +1 & \text{if } i \text{ is a quadratic residue modulo L,} \\ -1 & \text{otherwise.} \end{cases} \tag{3.2}$$

The quadratic residue modulo L calculation stems from the number theory and identifies which elements in each row *C_i* and each column *C_j* should be open (+1) or closed (-1). As the case *L=0* is normally excluded from the lists, quadratic residue lists typically range from *1* to *L-1* [116]; from 1 to 6 for the system considered in this work.

Equation 3.1 is then applied to include the row and column when i and j are equal to zero. The resulting encoding array A is obtained by simply replacing *+1* terms with *1* and *-1* terms with *0*. In accordance with equation 3.1, the row with i equal to zero contains all zeros, whereas the column with j equal to zero contains all ones apart from the case when i is zero. Such an aperture can be easily rearranged into a symmetrical form by a cyclic permutation of rows and columns [88]. The basic array in this form can be simply made into 2 × 2 version as presented in Figure 3.3.

In order to decode the image projected by the aperture, equation 3.3 is applied to the array A resulting in the decoding array G. In this case all *0* terms are changed to *-1* and all *1* terms to *+1* except for the situation when the *0* term for *i,j=0* is replaced with *+1*. In the 2 × 2 arrangement of the basic array, it is the middle element that changes its value in comparison to the encoding array A [88].

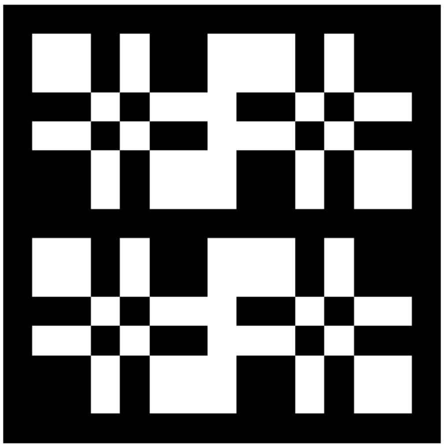

Figure 3.3: Rank 7 coded aperture. Transparent and opaque elements are presented in white and black, respectively. With 84 transparent and 85 opaque elements, the modelled aperture yields 49.7% transparency. A frame of 5 mm was added around the 13 × 13 aperture to represent clear boundaries.

$$G_{ij} = \begin{cases} +1 & \text{if } i + j = 0; \\ +1 & \text{if } A_{ij} = 1, (i + j \neq 0); \\ -1 & \text{if } A_{ij} = 0, (i + j \neq 0); \end{cases} \tag{3.3}$$

The reconstructed image R is obtained by applying the convolution theorem to the image projected on the detection plane D and the decoding array G as presented in equation 3.4. The detection plane array D was obtained by running a simulation in MCNPX [117].

$$R = D * G; \tag{3.4}$$

3.8 MCNPX modelling and simulation

As creation of complicated geometry models in MCNPX can be troublesome and error-prone, MCAM CAD-based software was used for the design of the aperture and detector plane [118]. Models can be built in 3D and converted to commonly used radiation transport codes e.g. MCNP, Geant4. The model of the aperture created in MCAM is shown in Figure 3.4. It was created by closely following the equations presented in the previous subsection.

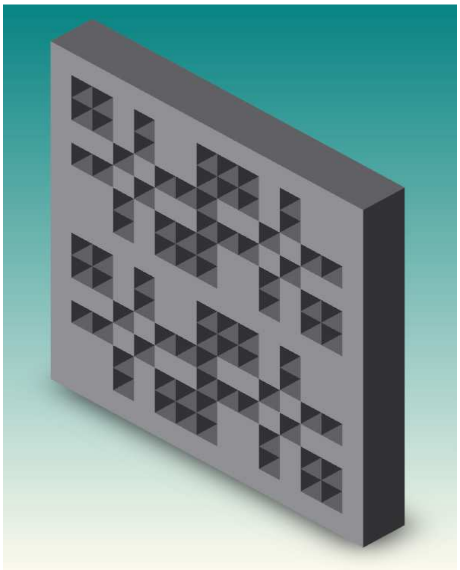

Figure 3.4: Aperture with the 5 mm frame constructed in MCAM

^{113}Cd and naturally occurring W were tested as potential materials for the coded-mask considering their neutron modulating and reflecting properties [119]. ^{113}Cd was chosen due to its relatively high thermal neutron absorption cross-section (26719 barns). High atomic number of natural W, and its low thermal neutron absorption cross-section (23.86 barns) provide marginal moderation of neutrons but adequate reflection for high energy neutrons, due to its high density (19.3 g/cm^3). Moreover, mean free path was calculated for each material for thermal and 15 MeV neutrons (maximum neutron energy of ^{252}Cf as specified in [30]). Results presented in Table 3.2. support the assumption that ^{113}Cd is a better choice for thermal neutron absorption than natural W. However, high density of the natural W is reflected in the comparison between the mean free path values for the two materials at 15 MeV. In both cases, an increase in detection sensitivity is to be expected when the aperture thickness is increased. Therefore, aperture models of two thicknesses were tested - 10 mm and 25 mm. Each square element of the aperture was set to 5 mm × 5 mm. The size of each detector element is identical to the thinner aperture in terms of area as well as thickness of a single element.

Table 3.2: Neutron mean free path calculation results for ^{113}Cd and Natural W based on ENDF/B-VII.1 library from [120].

Material	**Neutron mean free path (cm)**	
	Thermal	**15 MeV**
^{113}Cd	8.112×10^{-4}	4.78
Natural W	0.664	2.954

Commercially available liquid scintillators, for instance EJ-301, present good PSD characteristics. But their implementation in systems targeted for nuclear decommissioning can be hindered by some of their properties: for example, EJ-301 consists of highly toxic, flammable and volatile aromatics. Recently developed plastic scintillators have proven to achieve similar results to organic liquid scintillators with regard to PSD [121]. As these detectors are not manufactured from dangerous substances, they present a potential for use in neutron detection application in nuclear decommissioning.

Recent research into methods of obtaining single stilbene crystals suggests that their light output can be two times higher than that of commonly used liquid scintillator (EJ-309) [122, 19]. Furthermore, a comparison performed between EJ-309 and stilbene crystal scintillators shows that stilbene has superior PSD and energy resolution [115]. These developments in stilbene manufacture made it a viable candidate for the work undertaken. Therefore a stilbene crystal scintillator ($C_{14}H_{12}$) with density of (1.15 g/cm^3) was modelled in the MCNPX environment [104]. According to the technical data sheet, the crystal offers excellent neutron gamma separation, while being non-hygroscopic, non-flammable and non-hazardous [104]; features of great importance in industrial applications.

As the primary interest of this work lies in localisation of neutron sources, ^{252}Cf was modelled as the radiation source. It was defined in the MCNPX code based on the characteristics specified in the BS ISO 8529-1:2001 standard [30]. ^{252}Cf spontaneous fission source releases approximately four fast neutrons as a result of each fission event [19], which makes it a viable choice for the requirements of the work described in this paper.

MCNPX geometries were set up with the ^{252}Cf point source, represented as a red sphere in Figure 3.5, located either 5 cm or 10 cm away from the aperture. The coded aperture and the detector plane - shown in grey and yellow in Figure 3.5, respectively - were arranged to be 10 cm apart. The midpoint of the aperture was located at the origin of the geometry regardless of its thickness. As a result, the coordinates of the source in space were changing, as the thickness of the aperture was altered.

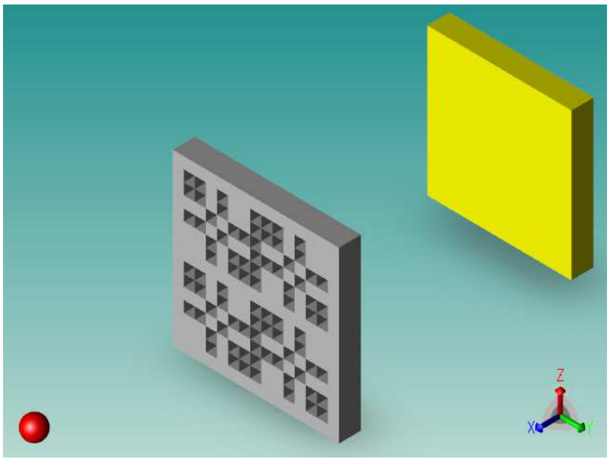

Figure 3.5: 3D image of the complete MCPNX geometry

A pulse height tally was recorded for each detector cell. The pulse height tally (F8) was chosen as the data recorded offers the closest representation of a physical detector cell [117]. Special treatment of the pulse height tally was utilised (FT8 CAP), which transforms it to a neutron capture tally [123]. Once MCNPX completed each simulation, number of neutrons captured within each detector cell were read through a MATLAB script and then stored as a 13 × 13 array. The array obtained is equivalent to the detector plane array D described in section 3.6.1. Using MATLAB, the detector plane array D was convoluted with the decoding array G and the resultant was utilised to find the reconstructed array R.

3.8.1 Simulation Results

For each simulation scenario cell particle activity table - table 126 in MCNPX output file - was analysed and compared for the two aperture materials modelled.

Table 3.3: Detection error for the distance of 5 cm between the source and the aperture

Material	**Detection error(%)**	
	10 mm thick	**25 mm thick**
^{113}**Cd**	18.45	18.45
Natural W	25.32	21.13

Across all arrangements tested, number of neutron collisions in the aperture was on average 40 % higher in the natural W than in ^{113}Cd. Additionally, average neutron mean free path was greater (approx. 3.78 cm) for ^{113}Cd than for W (approx. 2.32 cm). These results are comparable with the values presented in Table 3.2, given the theoretical analysis was performed for the maximum energy of the specified source rather than the average.

Detection errors were calculated based on the results obtained. The errors presented in Table 3.3. and Table 3.4. took into account the difference between the actual source position and the location obtained through the reconstruction process described. The results are presented as 2D images with a scale between -3 and +3 cm in Y and Z directions. Given the rank of the aperture and the dimensions of the detector simulated, the centre of each cell is located every 0.5 cm. Hence the maximum error (100%) in one direction is associated with the situation, when a hot-spot is detected 6 cells away from the actual location of the source. For example Figure 3.6b, presents the reconstructed source at Y = 3 cm i.e. 6 cells away from the actual source in Y direction - maximum error 100%. In the Z direction the difference is only 1/6 cells (Z = 0.5 cm) - approximate error 16.67%. Using trigonometry the resultant error can be calculated to be 25.32% (accounting for the fact that only one quarter of the whole graph is considered).

In the first modelled set-up, the source was located at (5.5 cm, 0.0 cm, 0.0 cm) with the front of the 10 mm thick aperture, exactly 5 cm behind. Images of the reconstructed arrays R were plotted for each simulated scenario. Figure 3.6a and 3.6b present plots of the filtered neutron capture results for ^{113}Cd and natural W, respectively. It can be observed that both materials provide relatively

Table 3.4: Detection error for the distance of 10 cm between the source and the aperture

Material	**Detection error(%)**	
	10 mm thick	**25 mm thick**
^{113}Cd	0.00	0.00
Natural W	18.34	13.12

poor localisation performance when the source is placed only 5 cm away from the aperture and neutron capture tallies are considered. The following two plots - Figure 3.6c and 3.6d - represent the reconstruction of the sources for the aperture of 25 mm thickness with the neutron source located 5 cm away. Although the localisation performance increases marginally in the case of natural W when the aperture thickness is increased, it is not sufficient to provide reliable localisation data.

Results of the simulation for the source located at the distance of 10 cm from the aperture front present a significant improvement in detection sensitivity, when compared to the previously discussed case. Regardless of the thickness ^{113}Cd aperture provides an ideal reconstruction of the source. The improvement for the mask made of natural W is not as prominent as in the case of ^{113}Cd. It should also be noted that a weighted error calculation was applied for all the images presented. Hence, the detection error is greater for 10 mm thick W mask, as contrasted with the 25 mm thick W mask; multiple hot-spots suggest lower confidence in the results obtained. The reason for image splitting can be associated with the neutron reflective properties of natural W. As the aperture is placed farther away from the source, a higher number of particles can be reflected through the internal surfaces of the aperture's open elements. These in turn lead to false neutron events being detected within scintillator cells.

Since the main focus of this study was to assess a workable neutron localisation solution for nuclear decommissioning an isotropic ^{252}Cf source was used. It was found that ^{113}Cd aperture absorbed lower number of neutrons than natural W, which supports the calculated and achieved neutron mean free path values for each

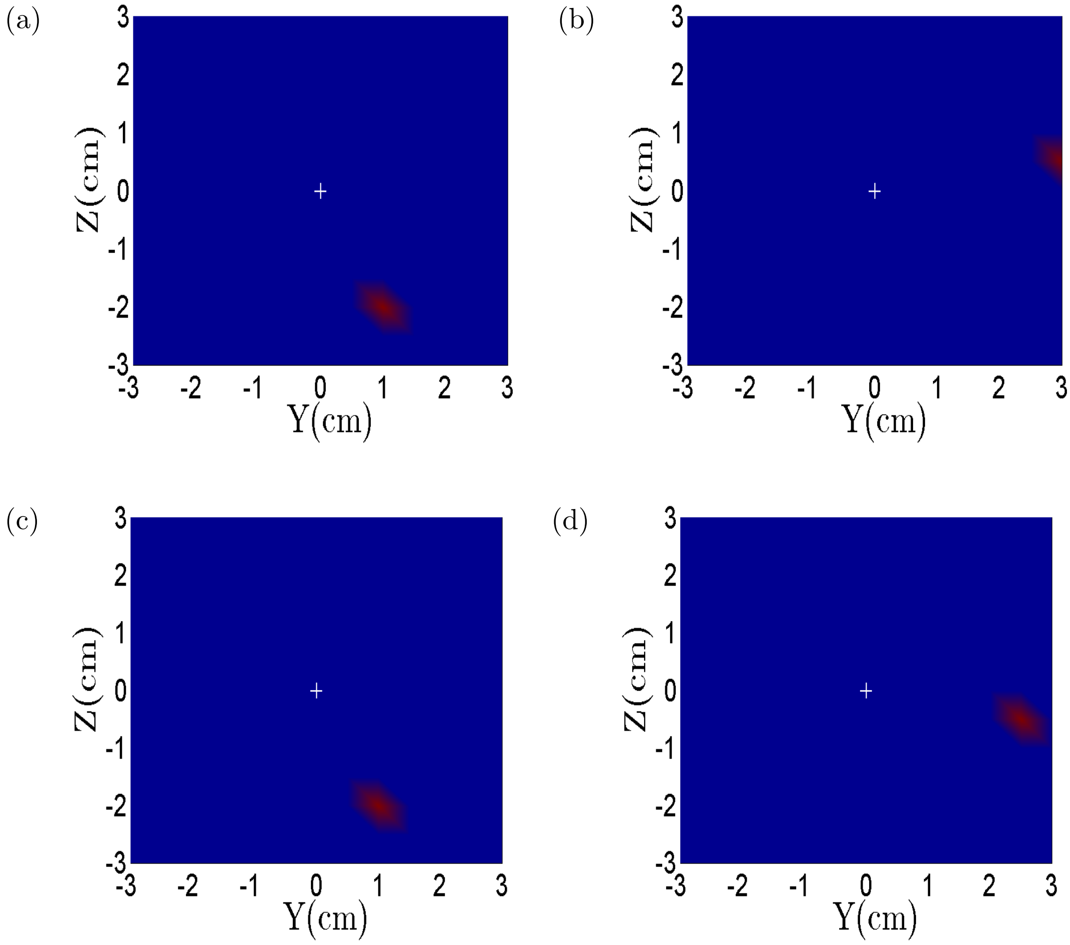

Figure 3.6: MATLAB plots of MCNPX simulation results with ^{252}Cf source located 5 cm away from the aperture: (a) ^{113}Cd aperture, thickness - 10 mm (b) W aperture, thickness - 10 mm, (c) ^{113}Cd aperture, thickness - 25 mm and (d) W aperture, thickness - 25 mm. White cross marks the actual location of the source.

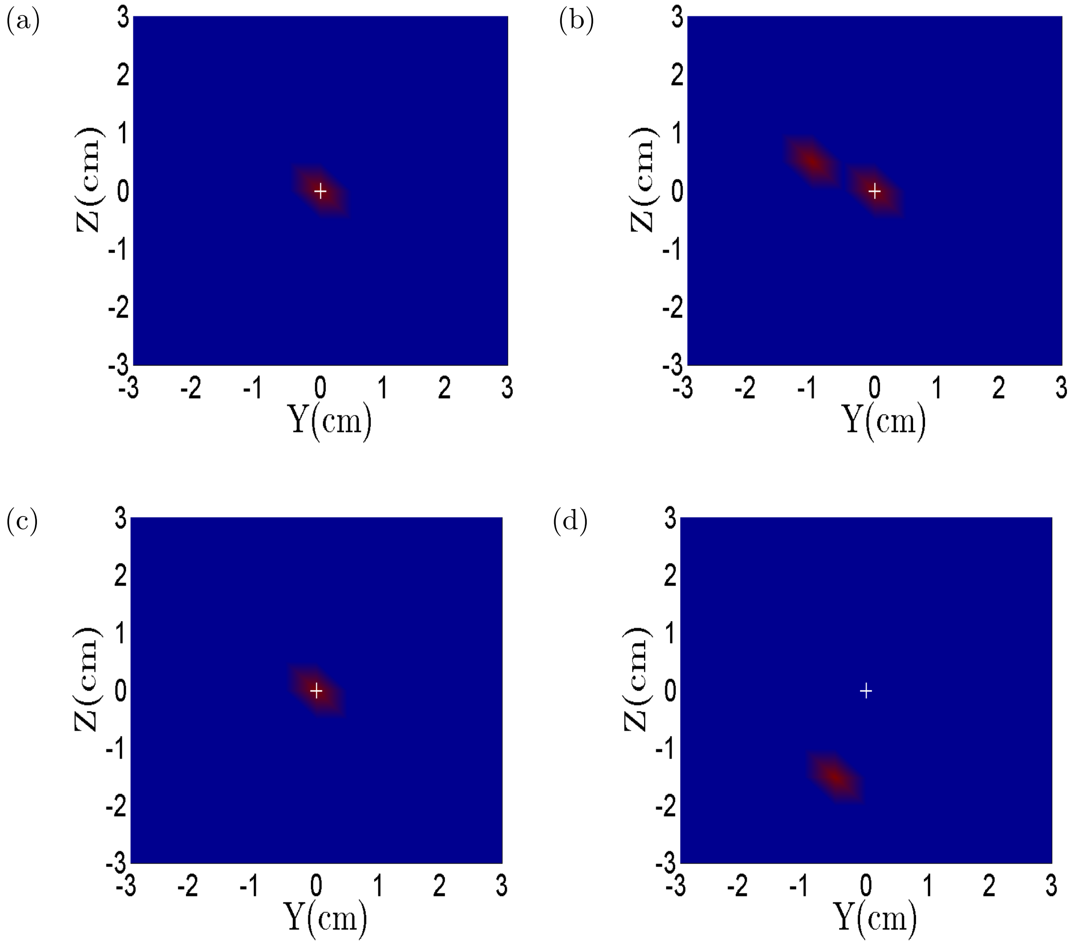

Figure 3.7: MATLAB plots of MCNPX simulation results with ^{252}Cf source located 10 cm away from the aperture: (a) ^{113}Cd aperture, thickness - 10 mm (b) W aperture, thickness - 10 mm, (c) ^{113}Cd aperture, thickness - 25 mm and (d) W aperture, thickness - 25 mm. White cross marks the actual location of the source.

material. In both cases the statistical uncertainty of the results did not exceed 0.01% for the neutron capture tally. The detectors response in the relevant energy ranges did not exceed the statistical uncertainty of 0.05%. This level of statistical accuracy was achieved with 10^8 particle histories simulated.

The modelled stilbene scintillator performed well in the simulated environment, despite its small thickness (1 cm), which makes it a possible solution for practical implementation of the system. Moreover, initial results suggest that even with a relatively large element size (5 mm × 5 mm) and small thickness of 10 mm, ^{113}Cd coded aperture can achieve good localisation performance as shown in Figure 3.7a and 3.7c. It should also be noted that with doubling of the distance between the aperture and the neutron source, an improvement in detection sensitivity was observed. The importance of this is that neutron localisation from a distance would be of great benefit for nuclear decommissioning applications, as access to the areas of nuclear power plants requiring characterisation is often limited.

3.9 Discussion

Existing coded-aperture imaging systems have been reviewed and potential improvements for a practical coded-aperture based neutron imaging system have been discussed and simulated. Scintillator based coded-aperture radiation imaging has been previously well documented by researchers with reference to X- and gamma-ray detection. Coded-aperture neutron imaging systems have shown encouraging results for fast neutron detection in security applications, as well as in nuclear material instrumentation. Neutron detection and localisation in nuclear decommissioning, on the other hand, relies largely on commercially available collimator based pinhole detectors. Many of these systems employ liquid scintillation detectors, which are not favourable in sensitive decommissioning environment, due to their hazardous properties. In this study, an organic stilbene crystal scintillator has been identified, which claims excellent PSD, and provided promising results in the fast neutron environment modelled. In contrast to liquid scintillators, it is not hazardous, easy to transport and not susceptible to leaks. Furthermore, the results obtained from an MCNPX simulation also suggest that using higher density material, such as ^{113}Cd, for the mask enables it to reliably stop fast neutrons from reaching the scintillator through the opaque elements of the mask, without increasing its thickness to impractical dimensions.

The theoretical model proposed holds potential for a portable coded-aperture neutron detection system if paired with a commercially available PSPMT, such as Hamamatsu H9500. It is a square 256 channel PSPMT with pixel size of 2.8 mm × 2.8 mm. The size of a single coded-aperture element can be matched to that of the PMT pixel increasing the overall resolution of the system. As the location of the interaction in the scintillator can be extracted via readout electronic system, the detection sensitivity could also be potentially increased. However, in order to reliably distinguish neutron from gamma interactions within organic scintillator, not only the interaction location but also the shape of the pulse must be retrieved. Hence, a bespoke readout electronic system for the PSPMT would be required. Pulses extracted from the PSPMT would necessitate digitisiation using high sampling rate ADCs before being processed on a fast FPGA chip (up to 500 MHz) to perform ditial PSD. With a correctly characterised scintillator, real-time mixed field characterisation could be achieved.

The modelling work completed, proposes one of the implementations of the scintillator based coded-aperture neutron imaging systems. In comparison to the coded-aperture neutron imaging systems reviewed, the model proposed in this paper is a relatively small scale system. It aims to present an adaptation of the proven advantages of the larger coded-aperture imaging systems for neutron localisation in nuclear decommissioning, where portability and detection efficiency play vital roles. Hence, the system is intended to perform initial scanning of a larger area from a distance of several meters and then gradually focus on the specific location of the radioactive source. Alternatively, multiple modules can be arranged into square arrays avoiding the need for initial scanning of larger areas.

As scintillator based coded-aperture neutron imagers are continuously being explored and improved, owing to technological advancement, coded-aperture based neutron imagers can be adapted in new application fields, such as nuclear decommissioning. Hence, a careful selection of hardware elements, a novel design approach, as well as innovative digitised PSD implementation will play a key role in the performance of an imaging system suitable for this application.

Chapter 4

Critical review of scintillating crystals for neutron detection

Cieslak, M.J., Gamage, K.A.A., Glover, R.

Published in Crystals, 13th September 2019

4.1 Abstract

There exists an ongoing need to develop and improve methods of detecting radioactive materials. Since each radioactive isotope leaves a mark in a form of particles emitted, new materials capable of detecting these particles are constantly sought. Neutrons and their detectors play a significant role in areas such as nuclear power generation, nuclear decommissioning and decontamination, border security, nuclear proliferation and nuclear medicine. Owing to the complexity of their detection, as well as scarcity of ^{3}He, which used to be the preferred choice for neutron detection in many application fields, new sensitive materials are sought. Systems utilising organic and inorganic scintillating crystals have been recognised as particularly good alternative methods of neutron detection. Since they enable a detailed investigation of the neutron spectra, in-depth information about the radioactive source can be inferred. Therefore, in this article an extensive review of scintillating crystals used for neutron detection is presented. Going through the history of scintillating crystals and discussing changes that occurred in their uses and development methods for radiation detection, the authors present a com-

prehensive overview of the current situation. Supported by a practical example, possible future directions of the research area are also presented.

4.2 Introduction

Radiation detection plays an important role in many application fields such as nuclear medicine, power generation, border control and nuclear decommissioning. Regardless of the application field, radiation detectors are primarily deployed to ensure safety of the personnel either working with, or in the close proximity, of the radioactive substances [124]. Further, they are essential to border and security control, where they are used to prevent illegal transportation of dangerous items [125]. Irrespective of the way they are used, a sensitive material is required that interacts directly with the targeted or expected radiation field. Large number of these devices use scintillating materials as radiation sensitive medium.

History of the scintillating materials used for radiation detection goes back to the work by Röntgen and his famous discovery of X-rays [126]. In his experiment, Röntgen was placing barium platinocyanide plates in the close vicinity of the vacuum tubes with $CaWO_4$ powder that were previously discovered by Crookes [127]. He discovered that materials such as lead are opaque to the X-rays, whereas other materials such as aluminium are transparent. Most famously, he discovered that X-rays can be used to image bones of a human body, because calcium absorbs the X-rays owing to its relatively high atomic number, while tissues in other body parts are built of elements characterised by lower density. As such, they are more transparent to the rays.

The discovery was embraced by large scientific community as it allowed to investigate previously unknown properties of materials. One of the materials investigated was crystal, as described by Friedrich et al., where they discovered X-ray diffraction within the crystal [128]. Around the same time, the structure of crystals was described based on the X-ray diffraction [129]. What became apparent as a result of these experiments was that crystals are capable of scintillating X-rays, and thus their interactions in crystals could be observed.

Initially, the fluorescence produced by scintillators was observed by the naked eye, which made it difficult to conduct a suitable investigation. An obvious requirement of a suitable photodetector resulted in the discovery of a photomultiplier tube (PMT). There exists some controversy related to the discovery of PMT, but the first electrostatic PMT (similar to the devices still produced and used today) was presented in 1936 by Zworykin et al. [130]. Nonetheless, discovery of PMTs opened up a new chapter in the history of scintillating crystals, as it made the investigation of the new materials easier and enabled new properties to be found.

In this article, a review of the available crystal scintillators for radiation detection, with particular focus placed on neutron detection, is presented. In the following sections, an overview of types of crystals used for radiation detection with regard to their chemical structure and particle sensitivity is presented. Further, both organic and inorganic crystals used for neutron detection are discussed in detail, as well as their growing importance given the scarcity of ^{3}He and limitations of other detection methods. The discussion is supported through numerous examples from the literature, as well as practical example of a response of an organic crystal to mixed neutron/gamma field provided by ^{252}Cf. The article is concluded with a discussion about possible future directions and expectations of where crystals may be used to further support neutron detection capabilities.

4.3 Scintillating Crystals used in Radiation Detection Applications

Regardless of the chemical type of a scintillating material, the process of extracting information from an interaction occurring within a scintillator is largely the same. When an incident particle enters the scinitllator, it undergoes numerous interactions with the scintillant particles and, by doing so raises atoms to exited states. These emit fluorescence that is transformed into photoelectrons at the surface of a photodetector such as PMT or a silicon photomultiplier (SiPM). Phtotodetectors multiply the weak photoelectrons and form an electrical pulse which carries important information about the incident radiation [131]. These can be easily detected through a combination of analogue and digital electronics.

Characteristics of pulses observed on the outputs of a photodetector, such as their length, height, rise time, decay time, are measured and used to infer the origin of the interaction within the scintillator. These characteristics differ between scinatillators and incident particles, owing to distinctive interactions that govern the scintillation process. The differences can be observed and analysed, enabling the information about the incident particles to be inferred. The most basic distinction related to crystals is between organic and inorganic crystals.

4.3.1 Operation Principle of Inorganic Crystals

One of the most frequently used crystals in radiation detection is NaI. This single crystal of alkali halide is characterised by very good spectrometric response to gamma-ray photons. Pure NaI crystal is an example of an insulating material. As such, its energy band structure consists of *valence band*, which is normally full, and *conduction band*, which is normally empty. The two are separated by *gap band*, which is also known as *forbidden gap* or *energy gap*. In pure NaI crystal electrons cannot be observed in this region [131, 19]. When exposed to ionising radiation, the electrons from the valence band can be excited and move onto the conduction band. Hole in the valence band is filled when the electron returns from the conduction band. This process is accompanied by the release of a photon. However, the width of the energy gap means that the energy of the photon released is too high to be in the visible region, making pure NaI crystal inefficient [19].

In order to alleviate this problem, impurities are introduced to inorganic crystals. These are called *activators* and are introduced to increase the likelihood of emitting a visible photon, when electron is returning to the valence band. The energy band structure is changed when an activator is added, and as its energy is less than that of the energy gap in the pure crystal, visible photon can be emitted. One of the most common activators is Tl, which shifts the maximum emission wavelengths from 303 nm to 450 nm between NaI and NaI(Tl) crystals, respectively [131]. Activators create new regions within the crystalline structure of a scintillator, which are sometimes referred to as *luminescence centres* or *recombination centres*. These enable the scintillators emitted wavelengths to be more closely matched with the sensitivity regions of the PMTs.

Depending on the application different properties of the inorganic crystals may be sought. However, there exists a basic set of requirements that is desirable across many application fields which includes a fast response, high light yield, high density and high atomic number [132]. Excellent gamma-ray sensitivity and energy resolution should naturally lie above the mentioned characteristics. A material meeting all of these criteria does not exist. For instance, NaI(Tl) and CsI(Tl) are characterised by the high light yield, but relatively slow response time. In contrast, pure CsI crystal exhibits very fast response at the cost of low light yield, which is caused by the lack of activator. One of the inorganic crystals that was utilised in varied application areas due to its unique combination of the specified characteristics is $Lu_2SiO_5(Ce)$ (LSO) [133]. As such, it was successfully exploited, together with its modified version containing yttrium - e.g. $Lu_{1.8}Y_{0.2}SiO_5(Ce)$ LYSO in e.g. nuclear medicine for Positron Emission Tomography (PET) applications.

Inorganic crystals were primarily developed for application in gamma-ray detection and characterisation applications, due to their suitability in areas requiring excellent energy resolution. Nonetheless, when exposed to neutron field almost any scintillation material will also react to those particles. Depending on application incident neutrons may give rise to unwanted noise, as a result of nuclear reactions that are accompanied by the release of gamma-ray photons, leading to inaccurate gamma-ray measurements. However, there have been numerous inorganic crystals developed, which are directly aimed at thermal neutron detection. This is possible because the crystals contain a high thermal neutron cross-section material such as Li [19].

4.3.2 Inorganic Crystals Capable of Neutron Detection

Due to their uncharged nature neutrons, as well as gamma-ray photons, do not undergo Coulomb interactions. Therefore, in order to detect neutrons it is necessary to convert them into charged particles. For low-energy neutrons, this is achieved through the nuclear reactions resulting in the release of a proton or alpha particle. These can be subsequently detected through their interactions with matter via Coulomb forces. Given their high cross-section for thermal neutrons, the most commonly used isotopes are ^{10}B, ^{6}Li and ^{3}He.

The most common nuclear reaction with ^{3}He used for neutron detection is defined in Equation 4.1. It is accmpanied by the release of 0.764 MeV of kinetic energy, and cross-section for this particular reaction is 5330 barns [19]. Fast neutron detectors based on ^{3}He have also been implemented, where appropriate moderating material was added to thermalize the fast neutrons [134]. However, scarcity of ^{3}He, caused by the decline in tritium production for nuclear weapons maintenance, requires that other alternatives be sought [10].

$$ {}^{3}_{2}\mathrm{He} + {}^{1}_{0}\mathrm{n} \longrightarrow {}^{3}_{1}\mathrm{H} + {}^{1}_{1}\mathrm{p} + 0.764MeV \tag{4.1} $$

4.3.3 Detectors Utilising ^{6}Li Neutron Reaction

Out of the remaining two isotopes, ^{6}Li has been most widely adapted in inorganic crystals. One of the examples of a scintillating crystal capable of neutron detection, which contains Li, is another alkali halide - LiI(Eu). Detectors containing Li represent a group of potential candidates for detection of low-energy neutrons owing to the ^{6}Li(n,α) reaction, as defined in Equation 4.2. Relatively recent study investigating the doping of the pure LiI crystal with Eu^{2+} show that appropriate doping level, as well as heat treatment may hold an answer to the light yield problem, when used for neutron detection. It should be noted that the heat treated LiI:Eu^{2+} scintillator examined by Boatner et al. [135] also shows excellent spectral response to gamma-rays from ^{137}Cs calibration source.

$$ {}^{6}_{3}\mathrm{Li} + {}^{1}_{0}\mathrm{n} \longrightarrow {}^{3}_{1}\mathrm{H} + {}^{4}_{2}\alpha + 4.78\,MeV \tag{4.2} $$

Another detector utilising the high thermal neutron cross-section of ^{6}Li isotope is Ce^{3+} doped LiCaAlF$_6$ inorganic crystal. When experimentally tested, this detector's performance was compared to that of a commercially available Li-glass scintillator [136]. Samples of two different sizes of LiCaAlF$_6$ were manufactured, and tested in regard to the light yield, neutron/gamma (n/g) separation capabilities and neutron detection efficiency. Regardless of the sample size the light yield was considerably lower than measured for Li-glass detector. However, n/g separation capabilities were deemed as high, and the intrinsic neutron detection efficiency (for the large size sample - 50.8 mm × 2 mm) was estimated to 80% of the Li-glass counterpart.

When a scitnillator is sensitive to both neutrons and gamma-ray photons, it is necessary to separate the two particle types. This phenomena is often referred to as pulse shape discrimination (PSD), and is very common in the domain of organic scintillators. However, PSD methods have also been applied to successfully separate neutrons from gamma-ray photons in crystals such as $LiAlO_2$ and $LiGaO_2$ [137]. In this case, Cherenkov radiation can be used to distinguish between neutrons and gammas, as it provides a cut-off point between the fast and slow component in the pulse decay. As tested with ^{252}Cf, the researchers show that scintillators are capable of detecting fast neutrons. It is believed that detector's sensitivity could potentially be extended to thermal energy region.

A very good potential for neutron detection via PSD methods is presented by detectors utilising $LiBaF_3$ crystal doped with Ce. The discrimination between various particles, across broad energy spectrum, is possible due to the occurrence of core-valence luminescence (CVL). It is a very short pulse (sub-nanoseconds) resulting from a hole in the conduction band of an ionic crystal that is being filled by an electron travelling from the valence band [132]. It appears alongside the self-trapped-exciton (STE) luminescence, when the crystal is exposed to gamma-ray field. When it is exposed to the neutron field, only the STE luminescence is observed. It is reported to have a high energy resolution, and as such be suitable for spectroscopy applications where isotopes can be identified based on the energy spectrum observed. It is also capable of discriminating between gammas, thermal and fast neutrons [138].

Another group of crystals capable of neutron detection are elpasolites, which inlucde scinitllators such as Cs_2LiYCl_6 (CLYC) and $Cs_2LiLa(Br,Cl)_6$ (CLLBC). When doped with Ce, these crystals can separate neutron and gamma-rays with a low level of misclassification probability. They are also characterised by the high energy resolution [139]. Fast neutron detection can also be facilitated by growing the crystals using ^{7}Li, rather than the traditionally used ^{6}Li to maximise thermal neutron sensitivity. Moreover, a number of composite detectors has been developed, consisting of CLYC crystal incorporated into an organic plastic, to further extend the sensitive spectrum to fast neutrons [140, 141].

Further example of an inorganic scintillator for neutron detection that is popularly used is ^{6}LiF/ZnS:Ag [142]. At the heart of this scintillator lies ZnS crystalline powder, which was famously used by Rutherford in his work on the stability of atoms [143]. ZnS:Ag powder is characterised by a very good light yield of 75000 photons/MeV and relatively slow decay time of 1.4 μs [144]. In the same study, the author attempts to characterise pure ZnS single crystal. The analysis presented suggests that due to the absence of the Ag dopant, the light yield is reduced significantly. It is therefore clear that a scintillator in this form would not be capable of detecting neutrons. However, when ^{6}LiF is added to the mix it becomes an efficient thermal neutron detector with low gamma-ray sensitivity. It is commercially available from Eljen Technology as EJ-426 [145].

4.3.4 Detectors Utilising Other Properties of Inorganic Crystals

The ongoing research into finding an appropriate ^{3}He alternative has resulted in new ways of using well established inorganic crystals. One of such examples is $YAlO_3$:Ce3+ which was successfully used for gamma radiation detection. Neutron sensitivity was in this case facilitated by adding *converter* in a form of a powder to the surface of the scintillator. Depending on the energy group of neutrons targeted possible candidates are lithium, boron, gadolinium (thermal neutrons) and thorium, hydrogen (fast neutrons).

The discrimination between gamma-ray and neutron interactions is performed via pulse height discrimination (PHD), and has been successfully presented with PuBe source [146]. A detector utilising $YAlO_3$:Ce3+ with neutron *converter* would benefit from the intrinsic properties of the perovskite detector such as fast decay time, high light yield and good stopping power. Simultaneously, the size of the detector could be kept small which is often desired in applications such as nuclear medicine. However, as with all inorganic scintillation crystals it is characterised by very high gamma-ray sensitivity which makes the analysis and discrimination process difficult.

One of the materials mentioned in the preceding paragraph (gadolinium) is characterised by the highest thermal neutron cross-section known. Apart from being used as a *conveter*, gadolinium based detectors form another group of good fast neutron detecting crystals. $Gd_3Al_2Ga_3O_{12}$:Ce (GAGG:Ce) crystal is characterised by excellent light yield and good stopping power. Neutron interactions with gadolinium are primarily driven by ^{155}Gd(n,γ) and ^{157}Gd(n,γ) reactions, for which the cross-sections are 60900 and 255000 barns, respectively. The reactions are defined in Equation 4.3 and Equation 4.4, where the unstable products return to the ground state with a release of gamma-rays.

The resulting neutron and gamma-ray induced pulses must be separated via appropriate method. However, there is no need for material enrichment due to exceptional neutron sensitivity of gadolinium. Moreover, it is possible to retrieve incident kinetic energy of a neutron interacting within the crystal which opens up the possibility of performing neutron spectroscopy. Recent study performed with AmBe source showed a superior performance of this crystal, when compared with an established ^{6}Li-glass detector [147]. Given the fast response of the crystal to gamma-ray photons, it is also feasible to explore time-of-flight based discrimination. Therefore, it comes at no surprise that a lot of research effort is currently going into the improvement of this detector. However, as with most of inorganic crystals high cost, and long growing time may be unacceptable in many applications.

$$^{155}_{64}\mathrm{Gd} + ^{1}_{0}\mathrm{n} \longrightarrow ^{156}_{64}\mathrm{Gd}^{*} \longrightarrow ^{156}_{64}\mathrm{Gd} + 8.54\,MeV \tag{4.3}$$

$$^{157}_{64}\mathrm{Gd} + ^{1}_{0}\mathrm{n} \longrightarrow ^{158}_{64}\mathrm{Gd}^{*} \longrightarrow ^{158}_{64}\mathrm{Gd} + 7.94\,MeV \tag{4.4}$$

Detection of thermal neutrons using ^{10}B reactions is well established in the domain of organic scintillators [148]. Doping with ^{10}B enables the sensitivity spectrum of organic scintillators, which is a very good fast neutron detector, to be extended to the thermal region. ^{10}B(n,α) reactions, as defined in Equation 4.5 and Equation 4.6, are probably most widely used mechanism for detection of thermal neutrons, owing to high thermal neutron cross-section (3840 barns) [19]. The reaction can lead to a stable or an unstable ^{7}Li isotope, and is accompanied by the release of α particle that can be easily detected using conventional methods.

$$^{10}_{5}\mathrm{B} + ^{1}_{0}\mathrm{n} \longrightarrow ^{7}_{3}\mathrm{Li}^{*} + ^{4}_{2}\alpha + 2.79\,MeV \tag{4.5}$$

$$^{10}_{5}\mathrm{B} + ^{1}_{0}\mathrm{n} \longrightarrow ^{7}_{3}\mathrm{Li} + ^{4}_{2}\alpha + 2.31\ MeV \tag{4.6}$$

Although popular in the domain of organic scintillators, there are not many examples of inorganic crystals utilising ^{10}B based reactions. However, $Li_6Y(BO_3)_3$:Ce has been computationally and experimentally tested showing good potential for thermal neutron detection. It is reported to be a relatively fast scintillator with a decay time for thermal neutrons of 37.8 ± 17.8 ns, and to show a greater thermal neutron detection efficiency than Li-glass scintillator. However, its α/γ ratio is ten times lower than than that of Li-glass, and its light yield is estimated to be six times lower than NaI:Tl [149]. Another potential area of application for boron doped crystals capable of neutron detection is considered to be space instrumentation, with initial experiments showing reasonable results in regard to thermal neutron detection efficiency [150].

Total neutron cross-section for the discussed elements is presented in Figure 4.1. It can be observed that gadolinium (shown in yellow) has the highest overall cross-section for the low energy regions. In agreement with the quoted barn values lithium (shown in orange) has the lowest cross-section out of the three considered candidates. However, there is a noticeable spike between 100 keV and 1 MeV that could be exploited in a specific application targeting this energy region. Boron (shown in grey) appears to be the most stable, out of the three thermal detector options, across the energy spectrum. For comparison, hydrogen's cross-section (shown in blue) is considerably lower than the other three elements in the thermal energy region. It is expected since hydrogen is primarily used for fast neutron detection in organic scintillators.

It is also worth noting that as early as 1968, it was attempted to perform neutron detection using NaI(Tl) crystal [151]. The experiment was performed with ^{127}I to observe crystal's response to low energy neutrons (via radiative capture) and fast neutrons (inelastic scattering). When tested in mono-energetic field of 1 MeV neutrons, overall efficiency was measured as 0.5 %, considerably lower than that obtained for organic scintillators. As a result, research into suitable fast neutron detection was pursued within the organic scintillators' domain.

Heavy oxide scintillator crystals represent another group of detectors showing

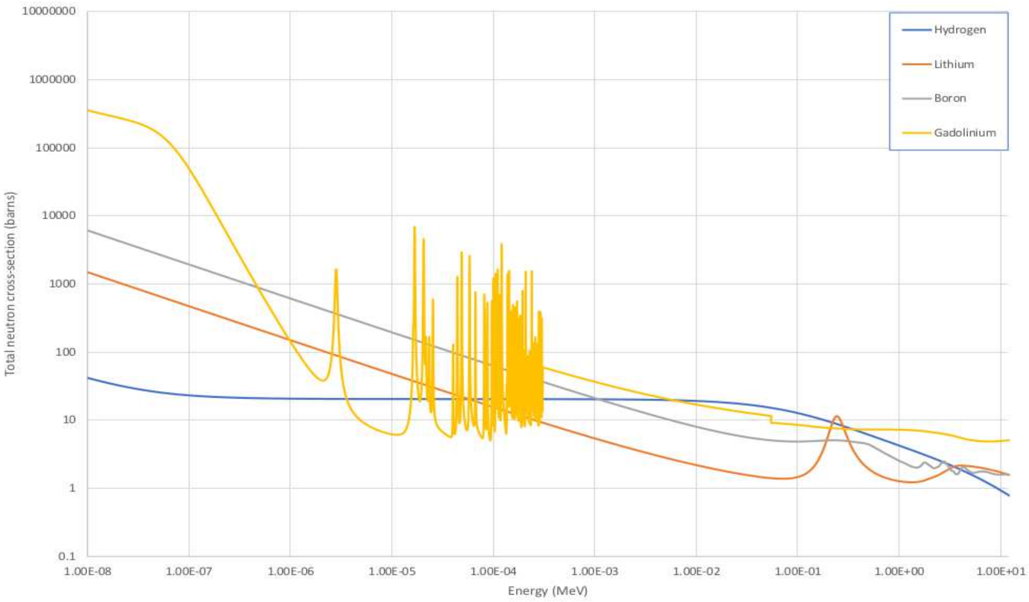

Figure 4.1: Total neutron cross-sections for the discussed elements: hydrogen, lithium, boron and gadolinium using ENDF/B-VIII.0 libraries.

potential of neutron detection. Most commonly used examples of this group are $CdWO_4$ and $PbWO_4$ crystals. $CdWO_4$ is capable of providing a very good spectral response to fast neutrons, but there exist handling issues in some places (e.g. UK) related to this crystal due to toxicity of Cd [152]. Similarly, has been tested for its fast neutron sensitivity [153]. Despite relatively good response in comparison to other counterparts tested, its low light yield makes it unsuitable for many applications [139].

4.3.5 Organic Crystals Operation

Regardless of their state (solid or liquid), organic scintillators are generally sensitive to both fast neutrons and gamma-ray photons. Therefore, many PSD methods have been investigated to facilitate low misclassification probability. The difference between the two particles can be inferred from the varying rate of energy loss of the particle, when scattered in the scintillation medium. Fast neutrons primarily undergo *elastic scattering* with a proton, while gamma-ray photons interact with the atoms of the scintillant via *Compton scattering*. These result in *fluorescence*, whose decay time is proportional to the rate of energy loss of the incident particle. Appropriate photodetector is then capable of detecting the *fluorescence*, and gives rise to a proportional electronic pulse. The rate of energy loss is greater for Compton electrons (resulting from gamma-ray interactions), when compared to protons (resulting from neutron interactions). This difference is reflected in the tail of the electronic pulse produced by the detector [19].

There are only two pure organic crystals that have been widely exploited in radiation detection applications: anthracene and stilbene. Anthracence was popularly used due to its scintillation efficiency, which is the greatest of all organic scintillators [19]. Scintillation efficiency of organic scintillators is often quoted as a percentage of anthracence's outputs. Stilbene on the other hand, was characterised by an excellent neutron/gamma separation capabilities, and was originally used by Brooks [106] when investigating PSD methods in the analogue domain. However, due to the issues related to growing of these crystals in greater dimensions, they have been left aside for many years. In the first decade of the 21st century, an interest has grown back due to new growing methods developed by the team at Lawrence Livermore National Laboratory (LLNL) in the US led by Natalia Zaitseva [154].

Given its excellent light yield anthracene still remains as the material that is characterised by the best scintillation efficiency available and is often used as a reference when developing new crystals. It was also tested for its PSD capabilities, and even though inferior to stilbene decent separation was observed [154]. One of the disadvantages of using organic crystals is their anisotropic response to incident radiation, which affects the performance when the orientation of the detector changes. However, this property can also be exploited to infer the location of the interaction via the angle of the scattered proton. It was successfully used by Brubaker and Steele [155] to perform neutron imaging.

Traditionally, *trans-stilbene* crystals were grown using the melt growth method. Growth process was associated with both high complexity of the growth process and high cost. Hence, they were only grown in sizes not exceeding 10 cm. However, when new solution growth method was applied, the growth time was reduced and samples of greater sizes were grown. It also partially adresses the well-recgnised issue of high misclassification between neutrons and gamma-ray photons in the low energy region. Furthermore, when tested in regard to its light yield and PSD capabilities, solution grown stilbene crystal performed considerably better than equivalent melt grown stilbene and organic liquid scintillator - EJ-309 [122]. It also shows better PSD characteristics than other PSD plastic scintillators [156].

As a solid, non-hygroscopic, not hazardous material, light-weight stilbene crystal is suitable for many applications such as nuclear decommissioning and portable security devices [157]. Although it is now possible to grow these crystals in larger sizes, the cost of manufacturing is still relatively high suggesting that organic liquids may still be more cost effective for large scale detectors. Nevertheless, the continuous interest in the field of organic crystals has led to the development of a new stilbene crystal, where hydrogen is replaced with deuterium. This deuterated stilbene is reported to have even better PSD capabilities than the standard stilbene [12]. Another organic crystal that should be mentioned at this stage is rubrene crystal, that is also grown from solution and is reported to show clear response to α particles, and a moderate response to fast neutrons [158].

Based on the presentation of the scintillating crystals currently utilised in neutron detection applications, it can be noticed that there is no single choice that would account for all the requirements of a neutron detector. Therefore, it is essential to carefully analyse the requirements of a detector and choose the sensitive material accordingly. In the following section, a practical example of an organic stilbene crystal tested in the mixed field of ^{252}Cf, in regard to its pulse shape discrimination capabilities is presented. This particular scintillator was chosen, as it illustrates the feature of lower misclassification probability at lower neutron energies. Results obtained are then analysed, and the article is concluded with the future outlook for scintillating crystals in neutron detection field.

4.4 Methodology

In order to illustrate the capabilities of organic scintillators in regard to fast neutron detection, two solid state organic detectors have been tested in the mixed-field (n,γ) environment provided by ^{252}Cf at Lancaster University, UK. A single stilbene organic crystal scintillator was obtained from Inrad Optics in 2016. PSD performance of this cylindrical crystal (20 cm × 20 cm) was compared with that of an organic plastic cylindrical sample (25.4 cm × 25.4 cm) obtained from Lawrence Livermore National Laboratory (LLNL) in the US, with LLNL sample number 5706. Samples have been covered with reflective coating on the side and back to minimise the change of photons escaping the scintillator without being detected. Each scintillator was then in turn attached to a single channel ET Enterprises 9107B PMT using EJ-550 silicon grease. The PMT anode signals were collected via FPGA based signal digitiser operating at the sampling frequency of 500 MS/s with 12-bit resolution.

Combined scintillator and PMT assembly was places in a cylindrical light proof box and placed in front of the water tank, where the radioactive isotope is normally stored. The radioactive source is normally located in the centre of a water-filled tank, as shown in Figure 4.2. For experiments the source is pneumatically moved to the edge of the tank, which stops approximately 20 cm away from the edge. The detector assembly was placed 15 cm away from the edge of the tank, resulting in the total distance of 35 cm between the source and the detector front. Each scintillator was exposed for the duration of 1 hour. The FPGA based digitiser collected raw data, with each sample collected every 2 ns. Detection window consisted of 128 samples, collected over 256 ns trigger period.

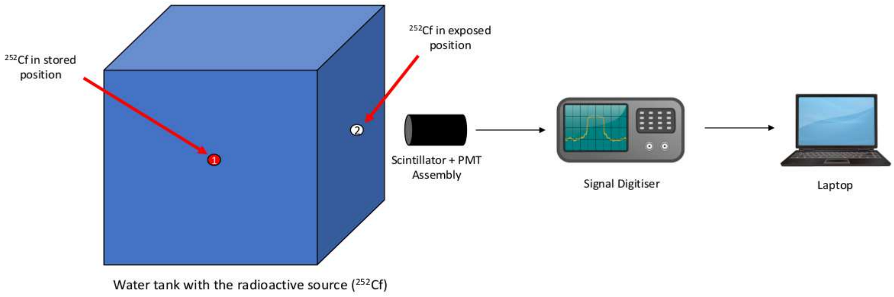

Figure 4.2: Diagram presenting the experimental set-up, with the radioactive isotope in the centre of a water-filled steel tank (position 1), where it is normally stored. For experiments the source is pneumatically moved to the edge of the tank (position 2).

Before any further analysis was performed each pulse was processed via bespoke pile-up rejection algorithm, where a pulse was rejected if two peaks within one trigger window, which covered 256 ns, were detected. Also baseline subtraction was performed by calculating the average over the periods before and after the pulse within the trigger window. Given that the pulse was detected between sample no. 50 and 100, baseline was calculated over samples 1-45 and 105 - 128. Charge Comparison Method (CCM) was applied in the digital domain to assess neutron/gamma-ray separation capabilities of the scintillator samples.

The CCM is the most popularly used method, where the pulse is analysed by calculating integrals over two different time intervals [106]. As the difference between the neutron and gamma-ray induced interactions is most prominent in the tail of the pulse, the *short integral* is calculated between a point some time after the peak of the pulse and the end of the pulse, as specified in Figure 4.3. The *long intergal* is calculated over the entire duration of the pulse. These can then be plotted on the same plot exploiting the PSD capabilities of the detector, as shown in the following section.

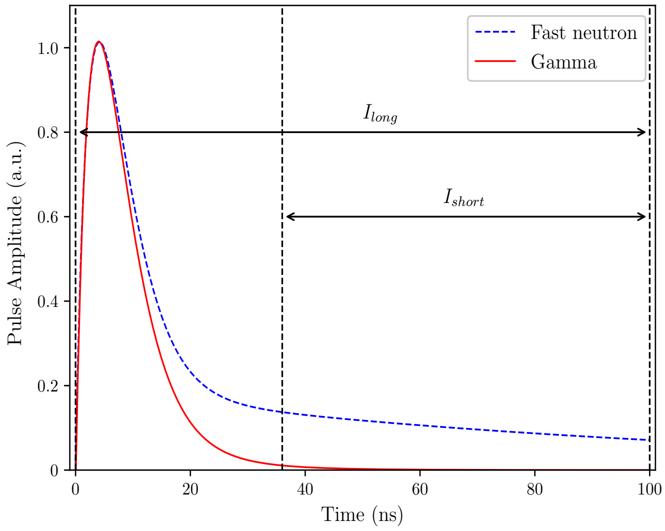

Figure 4.3: Illustration of the implementation of the pulse shape discrimination method used in this study. Long and short integrals used in CCM calculations are clearly marked on the plot. Theoretical fast neutron and gamma-ray pulses were obtained based on the data from Knoll [19] and Zaitseva et. al [159].

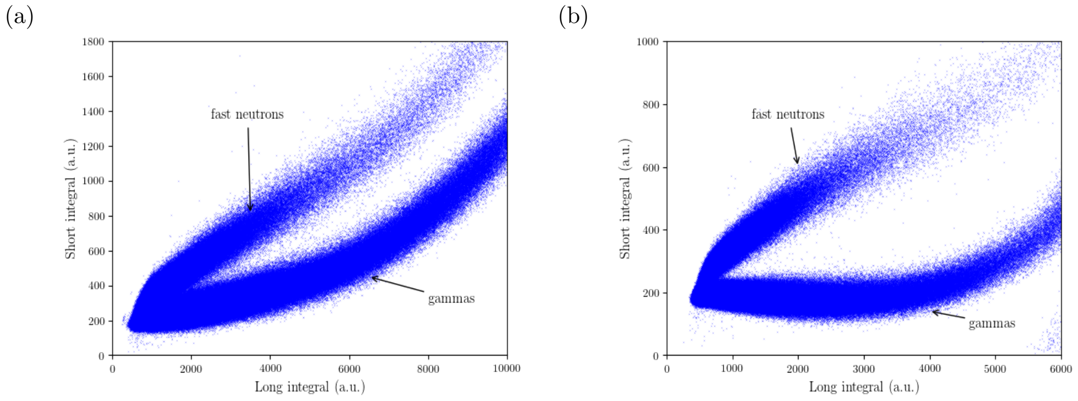

Figure 4.4: Comparison of CCM plots for the two organic scintillator samples when exposed to ^{252}Cf and data were collected with 500 MS/s digitiser: a) Cylindrical PSD Plastic from LLNL, and b) Single Stilbene Crystal.

4.5 Results

Each scintillator was in turn exposed to the mixed-field environment provided by ^{252}Cf for the duration of 60 min. There were 902,564 pulses accepted for the plastic scintillator sample, and 840,583 pulses for the organic crystal sample. PSD scatter plots for each sample are presented in Figure 4.4a (plastic) and Figure 4.4b (crystal). Short integral values, as defined in previous sections, have been plotted against the long integral values. The resulting plumes represent the neutron and gamma-ray photon interactions, as marked on the PSD plots with gamma-rays depicted by the lower plume and neutrons by the upper plume.

Following that, PSD separation quality was assessed for each scintillator using figure-of-merit (FOM) calculation. The concept of FOM as a measure for particle separation quality was originally introduced by Winyard et al. [160]. In order to estimate the FOM, the data needs to be presented in a form of a plot, where the distribution of the particles is illustrated. For neutrons and gamma-ray photons it is expected that they will show normal distribution spread. One of the methods used to obtain the distribution is to draw a separation line between the particle plumes, as judged by the naked eye. The distribution can then be drawn by measuring the distance between each particle and the line [156, 27]. This method was used to estimate the FOM in the current study, with the resulting values of 0.637 for the plastic and 0.892 for the crystal scintillator sample.

4.6 Discussion and Conclusions

Given the increasing need for reliable neutron detection alternatives for ^{3}He detectors, the authors attempted to present a review of the most viable options available among the crystal scintillators. Given the complexity of neutron detection, various methods are required to target specific neutron energy range. Both organic and inorganic options were considered. Each group presents advantages for certain application areas.

It appears that inorganic crystals utilising isotopes with high thermal neutron cross-section (lithium, boron, gadolinium) provide a very good alternative for low energy neutron detectors. However, the manufacturing cost is still high, and the growing process is long. Fast neutron region, on the other hand, has been targeted by organic scintillators for a long time, due to ^{1}H content, which allows elastic scattering of neutrons with a proton. Stilbene crystal is arguably the best available scintillator detector capable of neutron/gamma separation. Nonetheless, growing large size detectors using stilbene crystals is expensive in comparison to organic plastics and liquids.

There have been attempts to develop a neutron detector targeting a larger energy spectrum. However, due to different mechanisms governing neutron interactions with matter at various energy levels, this is not possible with a single material detector. Up to date literature reports on multi-detector systems, where different detectors are used independently to detect specific group of neutrons. Readout electronics attached to such system can combine the results into one system. Another method, stemming from the multi-detector approach described, is based on composite detectors, where a detector such as CLYC is incorporated into plastic scintillator to detect gammas, and thermal and fast neutrons. Regardless of the target energy range, it is clear that scintillating crystals will continue to play a key role in neutron detectors.

4.6.1 Example of Neutron Detection Capabilities Using Single Stilbene Crystal

An example of detecting neutrons originating from ^{252}Cf using organic solid state scintillators is presented in Figure 4.4. Due to scintillators' sensitivity to both neutrons and gamma-ray photons, both particle types are detected resulting in two corresponding plumes. These tend to overlap slightly in the region of low I_{short} and I_{values}. A significant overlap in that region leads to higher probability of particle misclassification. Since the overlap is most prominent in the region of low I_{short} and I_{values}, which correspond to the region of low energy neutrons, plots presented in Figure 4.4 only focus on that part of the graph.

Based solely on the observation of two graphs presented in Figure 4.4, it is clear that the single stilbene crystal (Figure 4.4b) provides superior PSD, when compared with the LLNL plastic sample (Figure 4.4a). Given that similar number of pules were accepted by the system for each scintillator, the shape and intensity of the plumes are very similar. Most importantly, the separation angle between the neutron and gamma-ray plumes appears greater for the single stilbene crystal. Moreover, the overlap in the low energy area is smaller for the single stilbene than it is for plastic.

These general observations agree with the quantitative analysis performed. The FOM was estimated for each detector, where 0.637 was observed for the plastic, and 0.892 for the single stilbene crystal. Despite various unique considerations required in the process of FOM estimation, presented results strongly support the claim that stilbene crystal is characterised by significantly superior PSD for fast neutron detection. The FOM estimated for stilbene crystal is considerably higher than the FOM value calculated for the plastic.

Chapter 5

Pulse shape discrimination characteristics of stilbene crystal, pure and ^{6}Li loaded plastic scintillators for a high resolution coded-aperture neutron imager

Cieslak, M.J., Gamage, K.A.A., Glover, R.

Published in Journal of Instrumentation, 25th July 2017

5.1 Abstract

Pulse shape discrimination performances of single stilbene crystal, pure plastic and ^{6}Li loaded plastic scintillators have been compared. Three pulse shape discrimination algorithms have been tested for each scintillator sample, assessing their quality of neutron/gamma separation. Additionally, the digital implementation feasibility of each algorithm in a real-time embedded system was evaluated. Considering the pixelated architecture of the coded-aperture imaging system, a reliable method of simultaneous multi-channel neutron/gamma discrimination was sought, accounting for the short data analysis window available for each individual channel. In this study, each scintillator sample was irradiated with a ^{252}Cf neutron source and,

a bespoke digitiser system was used to collect the data allowing detailed offline examination of the sampled pulses. The figure-of-merit was utilised to compare the discrimination quality of the collected events, with respect to various discrimination algorithms. Single stilbene crystal presents superior neutron/gamma separation performance, when compared to the plastic scintillator samples.

5.2 Introduction

Pulse shape discrimination (PSD) is a well-established method of separating fast neutron and gamma-ray interactions within an organic scintillation medium. The method is based on the difference in the decay time of fluorescence emitted within an organic scintillator as a result of an interaction between the ionising particle and the scintillant. The fluorescence decay time observed for heavy ionising particles, such as protons, is longer when compared to electrons [106]. Fast neutrons and gamma-ray photons interact with an organic scintillant predominantly through elastic scattering with a proton and Compton scattering, respectively. Consequently, the fluorescence decay rate exhibited by recoil protons and recoil electrons (Compton scattering) can be compared to infer the origin of the interaction [19].

Fluorescence emission is linked to the kinetic energy of the incoming particle. When it interacts with the organic molecules, the particle excites π-electrons within the structure of the scintillation medium [19]. Thus, the π-electrons are raised to one of the exited electronic states. Depending on the initial energy of the radiating particle, it can be lifted to a singlet S_S or triplet T_S state. Prompt fluorescence (also known as *fast component* of the scintillation process) is emitted when the particle in the S_S state returns to the ground electronic state. The lifetime of a S_S state is measured in nanoseconds and is short when compared to that of a T_S state which can be up to 1 millisecond. The longer de-excitation time of the T_S state is often associated with the π-electron transferring to one of S_S states before returning to the ground state. Hence, fluorescence emission is delayed resulting in the occurrence of the *slow component* of the scintillation process.

The fraction of light in the *slow component* of the scintillation can be used to infer the origin of the interacting particle. The decay rate of the *slow component* varies for the incoming particles of different nature but equal kinetic energy. When heavy particles interact with the scintillation medium, they demonstrate greater rate of energy loss. Therefore, the fluorescence decay time of recoil protons (resulting from neutron interactions) is longer, when compared to the fluorescence decay time of recoil electrons (resulting from gamma-ray photon interactions) [19]. Thus, the difference in the fluorescence decay rate forms a basis for neutron/gamma PSD techniques in organic scintillators. Fluorescence decay characteristics for a theoretical neutron and a gamma-ray, are shown in Figure 5.1. Various PSD techniques have been developed in analogue and digital domains to separate neutron events from gamma-rays effectively and efficiently.

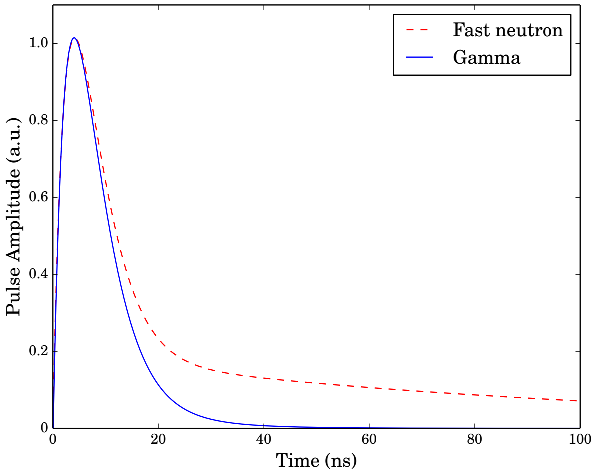

.

Figure 5.1: Theoretical fast neutron and gamma-ray scintillation pulses induced in an organic solid scintillation medium based on the information from Knoll [19] and Zaitseva et al. [159]

When the research into neutron/gamma discrimination was at its origins, the techniques developed were intended for liquid scintillator detectors [106, 19, 161, 107]. As a result, many liquid scintillators have been developed and accurately characterised [162, 163, 164, 165, 166]. However, due to flammable properties of some liquid scintillators and their susceptibility to leaks, these were not suitable for many industrial applications. An alternative in a form of solid scintillation detectors was perceived inferior to liquid counterparts, with regards to neutron/gamma separation (plastic scintillators) and light output (organic crystals) [19]. Recent progress into techniques of developing solid organic scintillators shows that their PSD performance improved significantly with stilbene crystal aspiring to outperform widely used EJ-309 liquid scintillator [121, 74, 122, 167, 115, 168]. Hence, only solid scintillation samples were selected for testing.

In this paper, a succinct review of selected PSD methods is presented, aiming to identify the most suitable candidate for a real-time scintillation based coded-aperture neutron imaging system. Three chosen techniques are then experimentally tested and the results compared for three different scintillator types. Additionally, performance assessment of the PSD method and scintillator combinations was examined. Online data processing was adopted in this study for the investigation of the three selected methods. Computational complexity of each method was also considered with regards to the real-time operation feasibility. A brief review of the existing organic scintillator characterisation methods, which was performed prior to the characterisation work undertaken in this study, is also presented.

5.3 Pulse shape discrimination methods in organic scintillators

5.3.1 Analogue PSD methods

Discovery of the pulse shape variation between neutron and gamma-ray induced incidents triggered a long search for the most effective separation method. Around the time of its discovery, PSD was dominated by two algorithms implemented in the analogue domain; zero-crossing and charge comparison method (CCM). The former method transforms the photo-detector output pulse into bipolar signal. The time between the trigger and the zero-crossing point is then used as benchmark for neutron and gamma discrimination [169]. Although less often used nowadays, mainly due to the implementation practicality of the digital approaches, the zero-crossing method shows very good PSD performance when implemented in organic scintillator studies [170, 171].

The latter method is based on the ratio between the charge integrated over the duration of the entire pulse (*long integral*) and the charge integrated over the tail of the pulse (*short integral*). Analogue CCM (also known as charge integration method) was first described by Brooks and utilised various RC circuit combinations to perform the integration of the entire pulse and its tail [106]. A comprehensive investigation of these two analogue methods has been performed by Nakhostin [169].

5.3.2 Digital Charge Comparison Method

The advent of digital electronics enabled complicated analogue circuits to be replaced by a few lines of a computer code. Therefore, both analogue methods were successfully employed in the digital domain, with CCM becoming one of the most powerful PSD algorithms [172]. Recent study, which compared PSD performance of the digital CCM and the analogue zero-crossing method, reports that the estimated figure-of-merit (FOM) for the digital CCM is on average 20% greater than that obtained for the analogue zero crossing method [173]. However, similar investigation conducted over two decades earlier indicates superior performance of the zero-crossing method over the digital CCM which illustrates the progress of the digital approaches [174].

The arrival of fast high resolution analogue-to-digital converters (ADC) enabled integration to be calculated as an area under the digitised pulse. There are three integration algorithms that can be easily employed; running sum, trapezoidal rule and Simpson's rule. The running sum is the simplest algorithm where the integral is calculated as a sum of the digitised samples. The trapezoidal rule estimates the area between two digitised samples by taking an average of the two adjacent samples, whereas the Simpson's rule approximates the integral by calculating quadratic polynomials for specific intervals. Since previous research suggests that all three integration algorithms provide identical PSD results when used in the digital CCM implementation, the running sum algorithm was used in this research [169].

5.3.3 Simplified Digital Charge Comparison

Different decay rates of the slow scintillation components for neutron and gamma-ray events define the separation capability of an organic scintillator. The simplified digital charge comparison (SDCC) method focuses on the period between the peak amplitude sample and the final sample of the digitised signal. As the difference in the decay rate between the gamma-ray photon and neutron induced pulses can be observed some time after the peak, an interval was identified when the difference is most prominent [175]. The start sample and the end sample of the interval are defined by a and b parameters, respectively in Equation 5.1. These parameters specify the interval of the *short integral*.

$$D = log(\sum_{n=a}^{n=b} {x_n}^2) \tag{5.1}$$

Generally, a parameter corresponds to three-sixteenths and b to one half of the pulse length where the peak amplitude is considered as the first sample. The discrimination parameter D is then plotted against the magnitude of the peak amplitude to separate the particles. Preceding work advocates a superior discrimination performance of this method in comparison to other digital discrimination algorithms [27].

5.3.4 Pulse Gradient Analysis

Digital signal processing implemented using advanced field-programmable gate arrays (FPGA) and high sampling rate ADCs provided a way of performing PSD faster than it was ever possible in the analogue domain. However, the aforementioned CCM and SDCC algorithms require the whole pulse to be digitised before the discrimination can be performed. Pulse Gradient Analysis (PGA) can be performed with only two samples taken at the early stages of a scintillation pulse [34]. The magnitudes of the *peak amplitude* and the sample amplitude (known as the *discrimination amplitude*) recorded a specific time period after the peak amplitude are plotted against each other to separate neutrons from gamma-rays. Since only the magnitudes of the specific samples are considered the discrimination process can be completed faster in comparison to other methods. Hence, this method was successfully implemented in a multi-channel real-time Mixed Field Analyser (MFA) [75].

5.3.5 Other Pulse Shape Discrimination methods

There exist other digital discrimination methods implemented in the time and frequency domains [28]. Generally, methods not mentioned in the previous sections require more complex and resources-exhausting analysis of the digitised pulses. Some algorithms, such as Neutron Gamma Model Analysis (NGMA), compare digitised signals with neutron and gamma pulses modelled prior to the analysis [27]. Such methods are not desirable for a high resolution real-time neutron imaging system where the discrimination results are to be fed to an image reconstruction algorithm.

5.4 Existing characterisation techniques of organic scintillation detectors

5.4.1 Digitiser selection

The digital CCM is one of the most powerful and hence has become one of the most often utilised neutron/photon separation methods in organic scintillator characterisation studies. Due to clear advantages of the digital methods over the analogue counterparts, such as implementation practicality and performance superiority [173], the latter are only rarely used. Thus, an appropriate digitiser must be selected, so that the information contained in the analogue signal is truthfully transferred into the digital domain. Generally, the higher the sampling rate and the resolution of the digitiser's ADC, the more accurate the representation of the analogue signal. However, the ADC's resolution normally decreases as the sampling rate increases.

Previous study performed by Flaska et al. [37] reports that at least 250 MHz sampling frequency is required to obtain good PSD results. Nonetheless, another study conducted two years after the study by Flaska, successfully carried out crystal scintillator characterisation using 14-bit resolution, 200 MS/s digitiser [122].

A digitiser of equal resolution and even lower sampling frequency (150 MS/s) was effectively utilised to perform PSD for a neutron survey meter [176].

5.4.2 Performance assessment methods of organic scintillators

With the light output of the scintillator detector adequately represented in the digital domain further analysis of the pulse shape can be performed. Since liquid PSD scintillation detectors have become a preferred choice in many nuclear facilities, there exist various performance assessment criteria which can be easily adopted for solid organic scintillators. Furthermore, with the continuous development of the new solid organic scintillation materials, they are often contrasted with liquid organic scintillators [177, 168].

The most important characteristic of any PSD scintillator is the FOM. It is utilised to compare the separation quality, based on the number of detected particles of different types. The FOM can be obtained by plotting a histogram of the ratio of the maximum and the minimum amplitudes of the digitised pulses [19, 28]. Another approach exploits the concept of discrimination line where the histogram is plotted as a function of the orthogonal distance from each particle to the discrimination line [27].

A decent quality PSD with a sufficiently good FOM enables further analysis of the identified particles. Based on the number of neutron events and gamma-ray photons accepted by the digitiser system it may be feasible to identify the differences between radioactive isotopes detected [178]. One of such methods is R-factor which computes the ratio of neutron and gamma-ray interactions within the scintillator. The FOM, as well as the R-factor, are described in detail in the following sections. These characteristics are used to perform quality assessment of the chosen samples with regards to PSD.

5.5 Experimental method

Three different organic solid scintillator samples were in turn irradiated with ^{252}Cf (half-life of 2.64 years) source located at Lancaster University, Lancaster, UK. A pure PSD plastic scintillator sample (25 mm diameter, 25 mm thick) and a ^{6}Li loaded PSD plastic scintillator sample (40 mm diameter, 25 mm thick) were both provided by the Lawrence Livermore Laboratory (LLNL), USA - denoted by the LLNL numbers 5706 and 9023, respectively. A single stilbene crystal (20 mm diameter, 20 mm thick) was obtained from Inrad Optics [104]. The experimental set-up is shown in Figure 5.2 where the radioactive source was in a water tank. The detector front was placed 15 cm away from the source and 10 cm away from Pb shielding. The Pb shielding was utilised to reduce the number of gamma-rays reaching the scintillator detector.

The back of each scintillator sample was covered with EJ-510 reflective coating. Each sample was then coupled to an ET Enterprises 9107B photomultiplier tube (PMT) with EJ-550 silicone grease, used to maximise the light transmission properties between scintillator and the PMT. The PMT was supplied in a B2/RFI housing with a 637BFP tapered distribution voltage divider. The PMT module supplied by ET Enterprises was enclosed in a light-proof tube. Depending on the scintillator type the positive high voltage supply, connected to the cathode of the PMT, was varied between 850 V and 900 V. The PMT anode was connected to a bespoke digitiser system which utilises a Analog Devices AD9254 150 MS/s, 14-bit amplitude resolution ADC directly linked to a Altera Cyclone IV EP4CE115 FPGA. The system recorded 28 raw samples (taken approximately every 6.67 ns) per each triggered pulse. The registered data were transferred to a laptop running Linux via universal asynchronous receiver/transmitter (UART) configured to transfer data at 8 Mbits/s. The received data were further processed by a bespoke script developed in Python.

5.6 Results

Prior to PSD implementation each digitised pulse was run through a bespoke pulse pile-up rejection algorithm. The algorithm simply rejected any pulse where two peaks were detected. Since each scintillator sample was exposed to ^{252}Cf neutron field for approximately 1 hour many thousands of pulses were collected, with the number of pulses accepted by the pulse pile-up rejection algorithm varying between

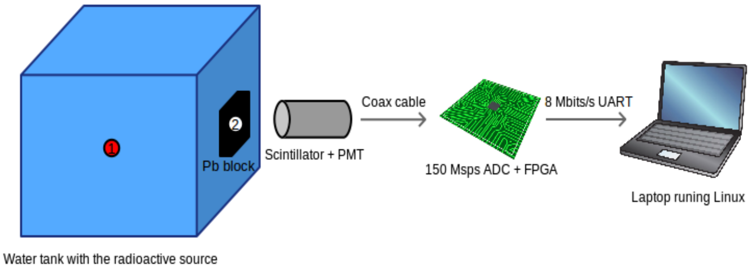

Figure 5.2: Schematic diagram of the experimental set-up. ^{252}Cf source is in the centre of a water filled, metal tank (position 1). During the experiments the source is moved to the edge of the tank (position 2).

approximately 60,000 and 80,000 pulses for the three samples tested.

Reconstructed analogue pulses are often affected by high frequency noise which may lead to misclassification of a pulse when PSD is performed. Moving average filter was applied to each digitised pulse, to smooth out the high frequency component [27]. Given the relatively low number of recorded samples per triggered pulse a 7-point moving average filter was used with the digitised input samples placed symmetrically around the filtered output point. Thus, each filtered sample is replaced with an average which leads to the 'raw' digitised samples being lost in the computation. Although the filter removes the 'raw' components from the signal to be discriminated, reduction in the high frequency components in the processed signal results in lower neutron/gamma misclassification probability [179]. Following that, PSD was performed on each pulse using the methods specified earlier. For each method implemented the neutron and the gamma-ray plumes were separated using a discrimination line (where possible) [180]. In each case, shown in Figure 5.4 to Figure 5.6, plume above the discrimination line is corresponding to neutrons and the plume below the line to gamma-rays.

Based on PSD results obtained for each scintillator sample FOM was calculated (using Equation 5.2) to compare their performance in particle separation. *Peak separation* in Equation 5.2 represents the difference between the peak distances from a normal distribution fitting of neutron and gamma-ray plumes; FWHM is the full-width at half-maximum for each particle distribution. Further, Equation 5.3 was utilised to calculate R-factor values. The R-factor is a ratio of the number gamma-rays over the number of neutrons which is often utilised to quantify the gamma-ray rejection efficiency in neutron detectors. Results are presented in Table 1. where Poisson approximation of the distribution was assumed to determine the corresponding uncertainty.

$$FOM = \frac{Peak\ separation}{FWHM_g + FWHM_n} \tag{5.2}$$

$$R = \frac{\sum_g}{\sum_n} \tag{5.3}$$

In order to calculate FOM it is required to obtain particle distribution plots. In this case, the distribution is presented as a function of the perpendicular distance of each point to the discrimination line. This is shown graphically on an example scatter plot in Fig. 5.3. The distance between each point and the discrimination line is recorded. If the particle point is located below the discrimination line (its y-axis value is lower than that of the discrimination line at the crossing point), the distance is assumed to be negative. Conversely, all points with the y-axis value higher than that of the discrimination line at the crossing point are assumed positive. In this case, these correspond to gamma-rays and neutrons, respectively.

5.6.1 CCM implemented in the digital domain

Scatter plots of the *short integral* against the *long integral* for the three samples are shown in Figure 5.4. There is no discrimination line plotted for ^{6}Li loaded plastic scintillator sample, as there is no clear separation between fast neutrons and gamma-ray photons, when irradiated with ^{252}Cf radioactive source. Hence, it was not possible to estimate the FOM for this scintillator sample. Estimated FOM values for the plastic scintillator sample and single stilbene crystal were 0.649 and 0.867, respectively. It can be clearly noticed that the stilbene crystal presents superior PSD performance, when compared to the two plastic scintillation samples tested.

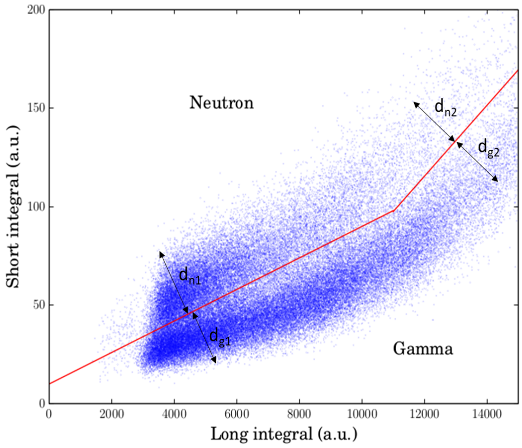

Figure 5.3: Example PSD scatter plot with sample distances to the discrimination line marked in black. Perpendicular projections were implemented for each point and distance to the discrimination line calculated. These were then used to present particle distribution plots as a function of distance to the discrimination line.

5.6.2 SDCC implemented in the digital domain

Figure 4. shows scatter plots of PSD performed using SDDC method; in this case discrimination parameter D is plotted versus the peak amplitude. The results obtained show similar characteristics to those obtained with CCM algorithm. The FOM value for single stilbene crystal estimated at 1.033 was far higher than 0.761 obtained for the plastic scintillator sample. Similarly to the results of the PSD using CCM algorithm, SDDC method was also unsuccessful in discriminating between fast neutron events and gamma-ray photons in ^{6}Li loaded plastic scintillator.

5.6.3 PGA implemented in the digital domain

Results of PSD implemented using PGA method are shown in a form of scatter plots in Figure 5.6 and they are comparable to those obtained using the other two methods. In this instance *discrimination amplitude* was plotted against *peak amplitude* with the estimated FOM values of 0.631 for the plastic scintillator sample and 0.823 for single stilbene crystal. In the same way as for the CCM and SDDC algorithms, it was not possible to draw a discrimination line between fast

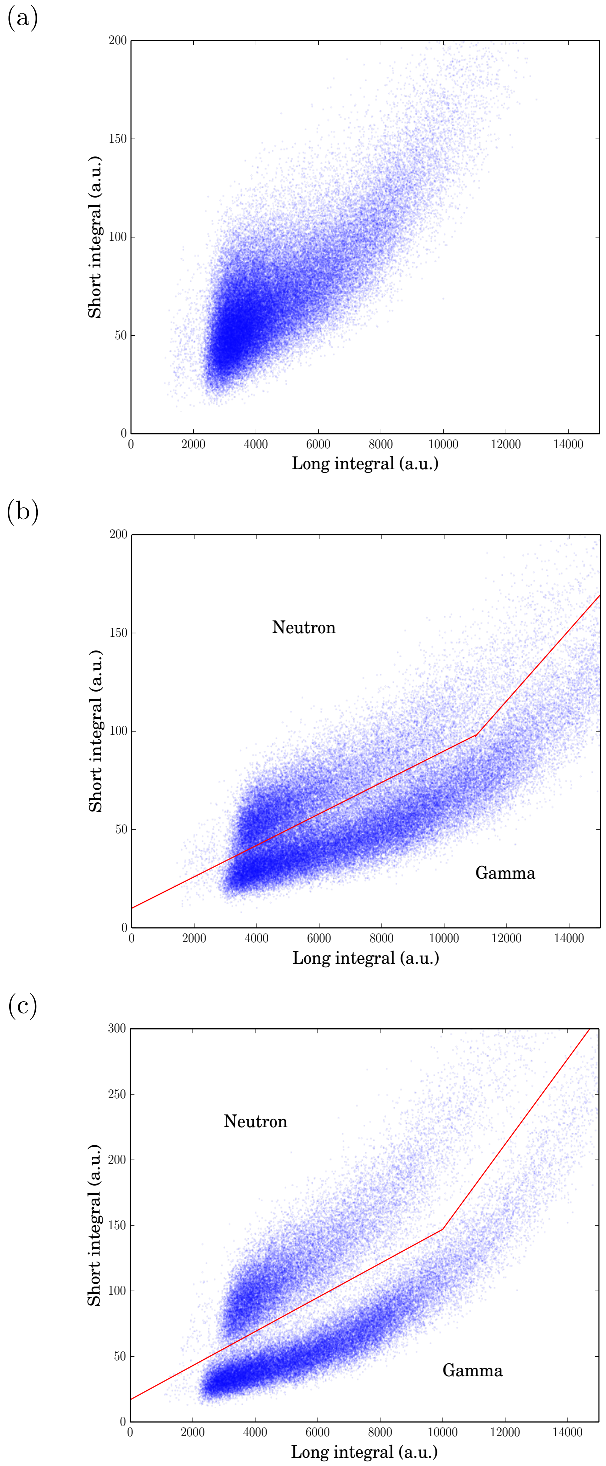

Figure 5.4: PSD discrimination plots using CCM method: (a) ^{6}Li loaded plastic scintillator, (b) Plastic scintillator and (c) Single stilbene crystal.

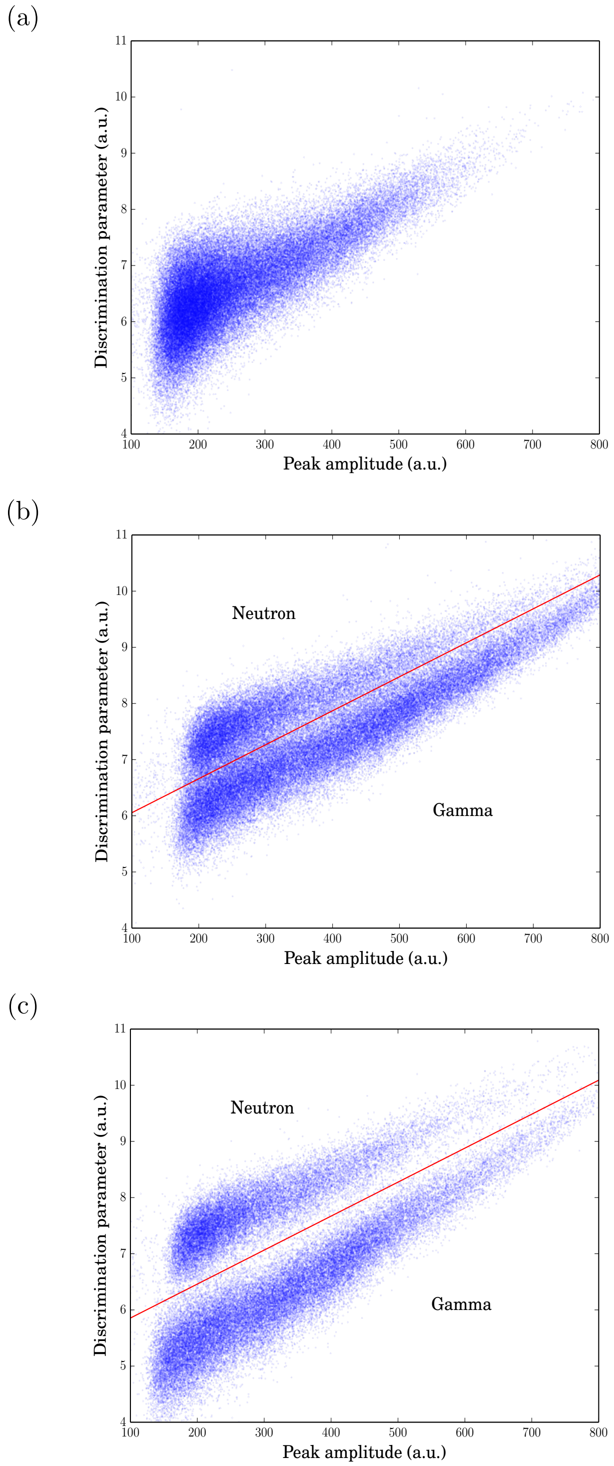

Figure 5.5: PSD discrimination plots using SDCC method: (a) ^{6}Li loaded plastic scintillator, (b) Plastic scintillator and (c) Single stilbene crystal.

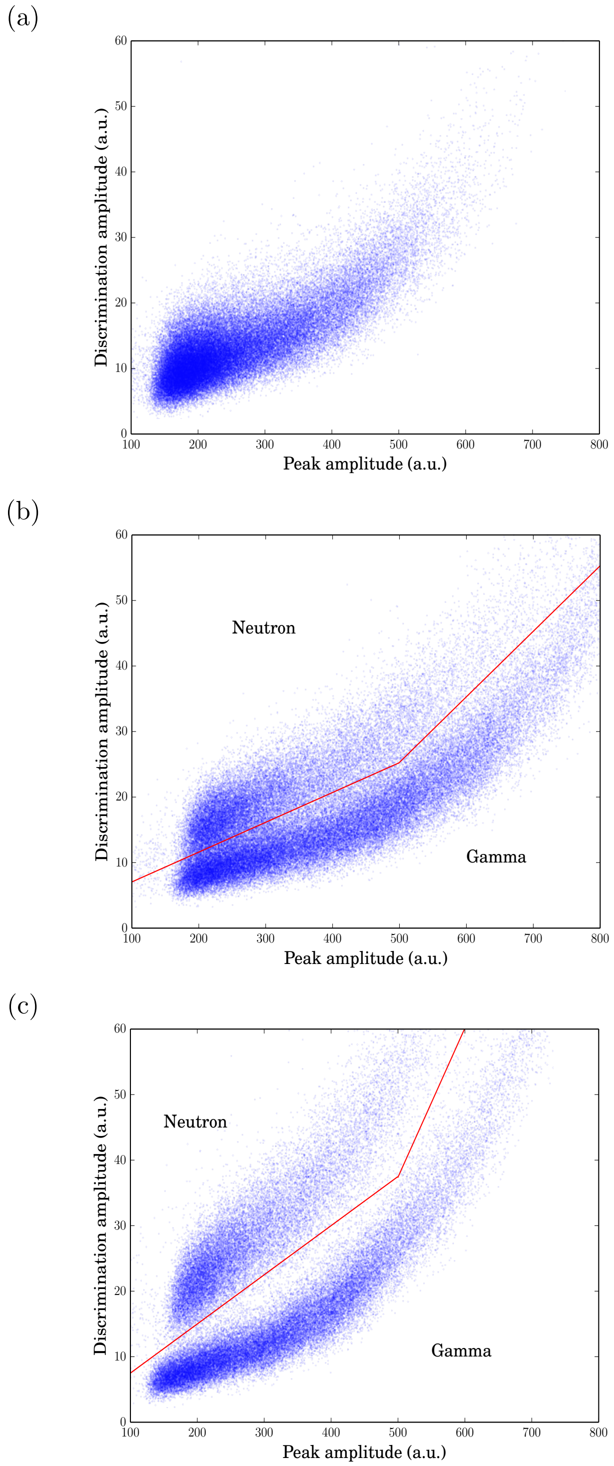

Figure 5.6: PSD discrimination plots using PGA method: (a) ^{6}Li loaded plastic scintillator, (b) Plastic scintillator and (c) Single stilbene crystal.

neutrons and gamma-rays for ^{6}Li loaded plastic scintillator.

5.6.4 Separation quality assessment

Distribution of each point from the discrimination line plots are shown in Figure 5.7 for all scintillator/PSD method combinations. The distribution plots are corresponding to the cases with the highest FOM value estimated for each of the scintillator samples. Based on the distributions presented a good agreement can be observed across the three methods tested with regards to PSD performance of the two scintillation samples compared. Statistical analysis of the distributions shows that 95% confidence level in the results can be assumed for stilbene crystal using CCM and SDCC. The data generated for these two methods was further validated by chi-square test against the normal distribution hypothesis. It follows that 95% of the detected particles will be correctly discriminated in this specific experimental scenario.

For the remaining scintillator/PSD method combinations a clear separation can only be observed within one standard deviation of the mean. Hence, the resulting confidence interval is considerably smaller than for the aforementioned cases. Although the stilbene PGA combination still claims reasonably good separation (approximately 90% confidence level), the plastic scintillator separation performance is significantly inferior as evidenced by the results on the left in Figure 5.7. Although chi-square normality test validated the normal hypothesis for all the distribution fits considered, within their respective confidence intervals, it must be noted that the test was performed against single Gaussian distributions (separately for each neutron and gamma-ray distributions). This was necessary to ensure that FWHM correctly represents the fluctuations of Gaussian distribution. Neutron and gamma-ray distribution fit lines were only plotted to the zero point (discrimination line) in order to clearly show the difference in misclassification quality between stilbene and plastic scintillator samples.

A general consistency across the three separation methods can be found, as presented in Table 5.1. with the single stilbene crystal providing results of supreme quality when compared to the pure plastic scintillator sample. Since there is a clearer separation between the neutron and gamma-ray normal distribution fits in

Figure 5.7b, 5.7d and 5.7f than in Fig 5.7a, 5.7c and 5.7e, there is a lower chance of particle misclassification for the single stilbene crystal than for the pure plastic scintillator.

Optimisation of the estimated FOM values was performed, as shown in Figure 5.8. The length of the *short integral* was varied for CCM method by adjusting the starting sample number. Samples investigated range between sample number 4 and sample number 12, with the peak amplitude being considered as sample number 1. The optimal sample numbers for the pure plastic and the stilbene crystal scintillators were 10 and 8, as presented in Figure 5.8a and Figure 5.8b, respectively. These sample numbers correspond to 66.70 and 53.36 ns after the sample of the peak amplitude. With the peak amplitude usually occurring within first 20 ns of the pulse, the shortest window inspected was approximately 86.71 ns. This specific interval was considered because outside this range no clear separation between neutron and gamma-ray plumes was observed.

The length of the *short integral* was also varied for SDCC method where the value of parameter a was adjusted. In this case the optimal values were found approximately 53.36 and 46.69 ns (sample numbers 8 and 7) after the peak amplitude for the pure plastic and stilbene crystal scintillators, respectively. Similarly to CCM algorithm, sample numbers outside the range presented in Figure 5.8c and Figure 5.8d were excluded because of the two particle plumes not being distinguishable.

The *discrimination amplitude* sample number was inspected for PGA algorithm. Since PGA method only considers magnitudes of two samples there is no need to specify a window to be considered with reference to the *peak amplitude*. Both scintillators exhibit the optimal PSD performance when sample number 10 (occurring 66.70 ns after sample number 1) is plotted against the *peak amplitude*. The results of PGA algorithm optimisation are presented in Figure 5.8e and Figure 5.8f.

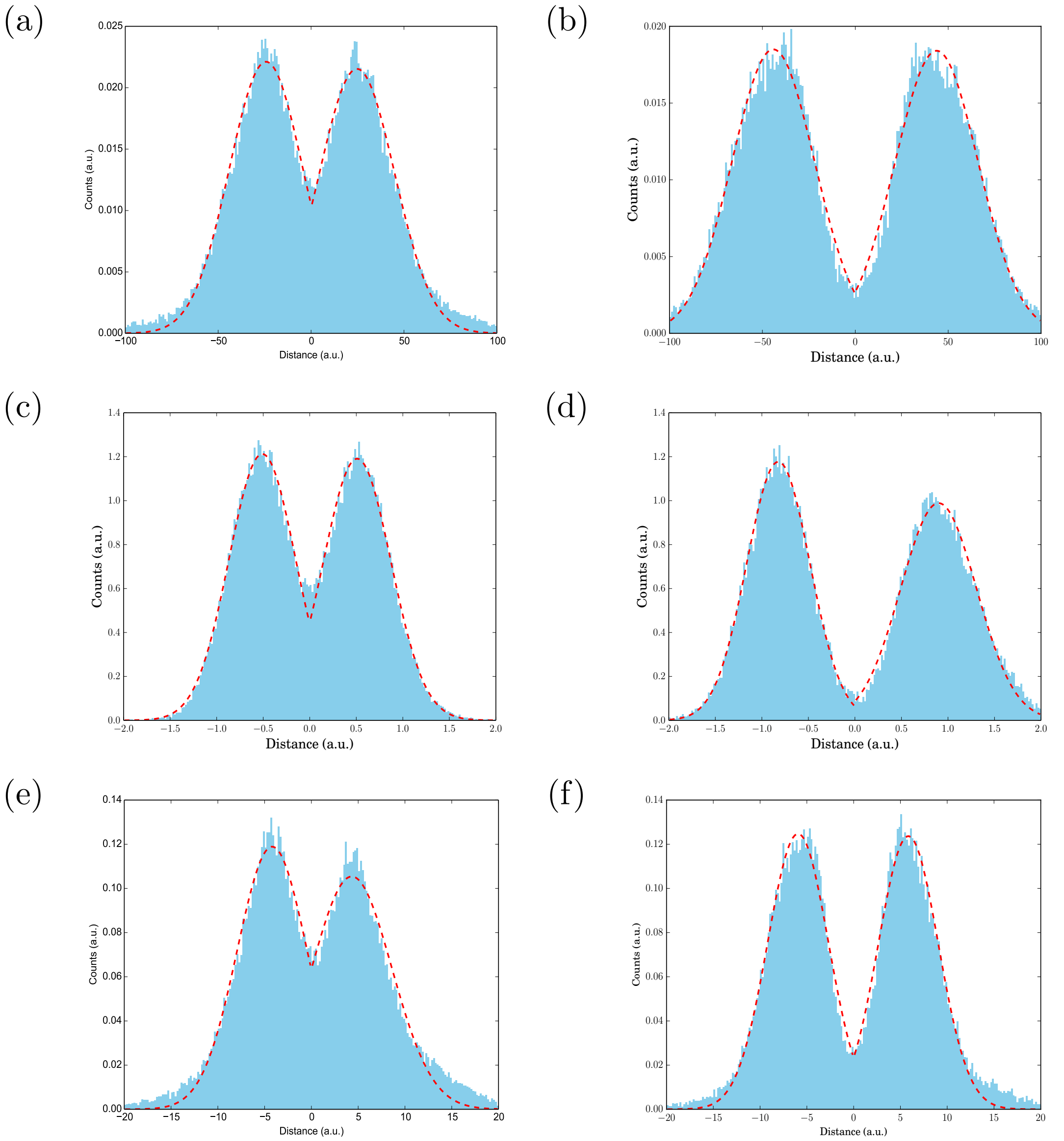

Figure 5.7: Distribution of each point from the discrimination line for all scintillator sample/PSD method combinations: (a) plastic CCM, (b) stilbene CCM, (c) plastic SDCC, (d) stilbene SDCC, (e) plastic PGA and (f) stilbene PGA.

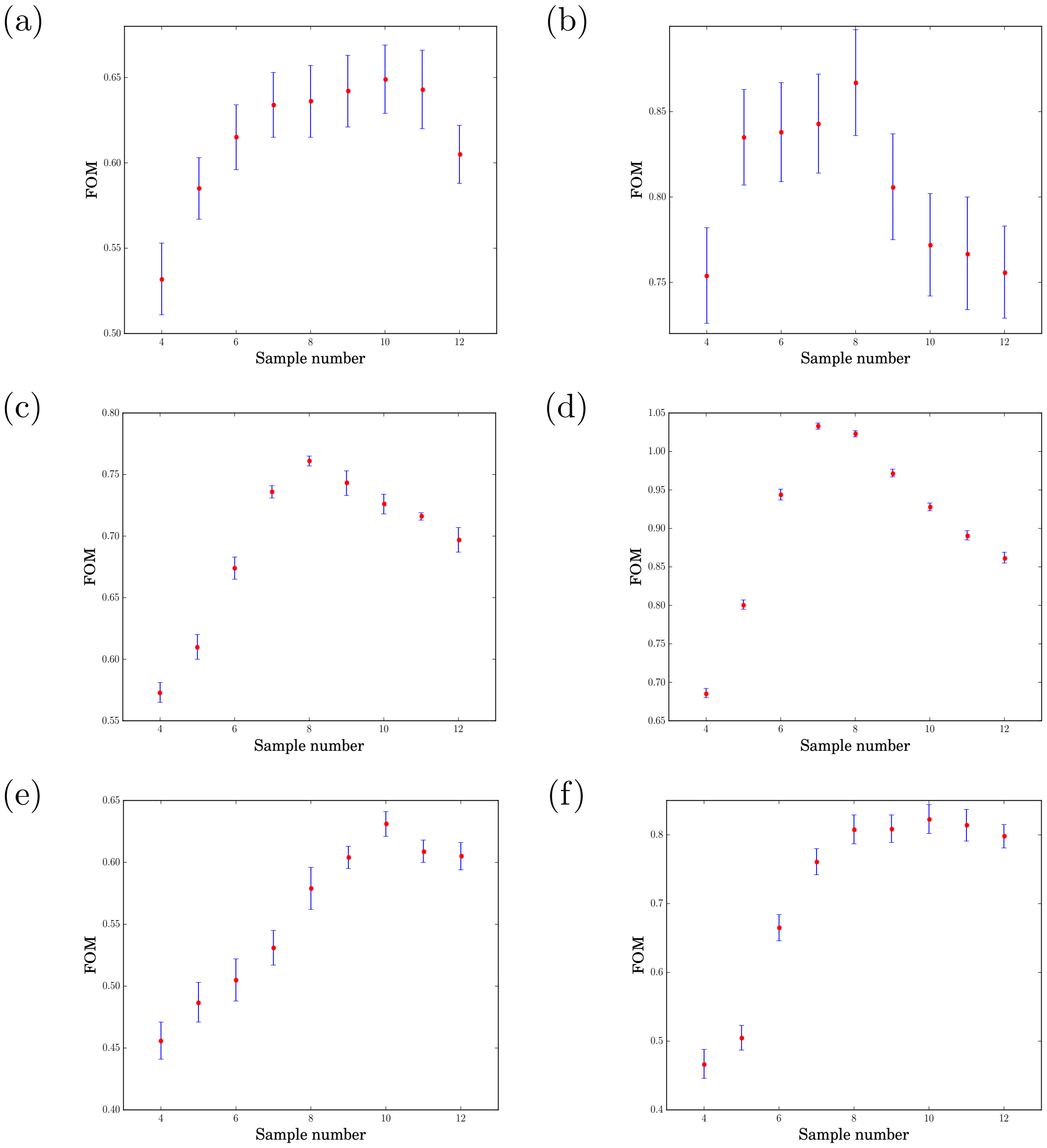

Figure 5.8: FOM optimisation plots for all scintillator sample/PSD method combinations: (a) plastic CCM, (b) stilbene CCM, (c) plastic SDCC, (d) stilbene SDCC, (e) plastic PGA and (f) stilbene PGA.

Table 5.1: FOM and R-factor values determined for the pure plastic and stilbene crystal scintillator samples for the three PSD algorithms compared in this study.

Sample	Method	gamma-rays	neutrons	FOM	R-factor
Pure plastic	CCM	38790	36696	0.649 ± 0.020	1.057 ± 0.002
	SDCC	38936	37492	0.761 ± 0.004	1.038 ± 0.002
	PGA	39784	36229	0.631 ± 0.010	1.098 ± 0.002
Stilbene crystal	CCM	30747	29450	0.867 ± 0.030	1.044 ± 0.003
	SDCC	34368	26026	1.033 ± 0.005	1.321 ± 0.003
	PGA	30460	29628	0.823 ± 0.020	1.028 ± 0.003

5.7 Discussion

Three solid organic scintillation samples were exposed to ^{252}Cf fission source, and the collected data discriminated between neutrons and gamma-rays using three different PSD techniques. Results obtained show agreement across the three algorithms implemented with single stilbene crystal showing superior neutron/gamma separation performance. All three algorithms failed to separate fast neutrons from gamma-rays within ^{6}Li loaded plastic scintillator, whereas the FOM values estimated for the pure plastic scintillator suggest relatively good discrimination performance. This difference in discrimination quality is associated with the doping of the former which enables neutrons thermalized within the organic detector to be captured by the high neutron capture cross-section ^{6}Li.

Since the neutron energy spectrum of ^{252}Cf averages at approximately 2.1 MeV, a large number of neutrons emitted would fall below the 1 MeV threshold. Previous studies support the claim that PSD performance of organic plastic scintillators increases when exposed to higher energy neutron fields (>1 MeV). When exposed to ^{241}AmBe neutron field ^{6}Li loaded plastic sample tested in this study performed considerably better in terms of fast neutrons and gamma separation [28]. Moreover, ^{252}Cf source at Lancaster University, UK is in a water tank where neutrons are thermalized as a result of their interaction with H atoms. It can therefore be concluded that ^{6}Li loaded plastic can be beneficial for certain applications but neutron capture events are difficult to separate from gamma-ray photons in relatively lower energy fields, such as from a moderated ^{252}Cf source, as presented in this and previous studies [28].

R-factor measurements show reasonable consistency across the algorithms tested for the two scintillator samples where neutron events and gamma-ray photons were successfully separated. However, the average R-factor value of approximately 1.098 is lower than the expected 2.118 based on the average number of neutrons and gamma-rays per fission event of 3.767 and 7.980, respectively [31] [32]. It is thought that the difference is associated with a Pb block placed adjacent to the water tank, which was used to reduce the number of gamma-rays reaching the detector, as shown in Figure 5.2.

One of the aims of this study was to find a suitable scintillation material for a scintillator based coded-aperture neutron imager to potentially extend the neutron detection range. A preceding study identified single stilbene crystal as a suitable solution for the imaging system [11]. The results obtained do not only support the claim of the preceding study but also show that neutrons and gamma-ray photons can be clearly separated within the stilbene crystal. As such, stilbene crystal can be perceived as an ideal candidate from the performance point of view for applications where neutron/gamma separation is required to extend to below the 1 MeV neutron energy threshold.

The FOM values obtained for CCM and PGA algorithms are comparable, whereas the FOM values estimated for SDDC method are significantly higher. These results are resembled most clearly in the scatter graph presented in Figure 5.5c where the results of PSD performed using SDDC for the stilbene crystal are plotted. An evident separation between neutron and gamma-ray plumes enables a reduction in misclassification of particles which may sometimes occur in lower energy areas.

The neutron/photon misclassification problem in lower energy regions ($<$ 1 MeV) for CCM has been thoroughly investigated. The method proposed by Polack et al. [181] enables misclassification reduction when there is a clear overlap of the neutron and gamma-ray plumes in the lower energy ranges. However, in this study, there is a clear distinction between the two plumes for PSD using CCM for the stilbene crystal as shown in scatter plot in Figure 5.4. Therefore, no further method of plume separation was sought. While SDCC method transpired to be the most effective, it is also the most computationally exhaustive which may be of concern for real-time applications. However, continuous advancement in the FPGA technology makes this matter a less prevailing factor.

It is worth noting that a relatively low speed digitiser (i.e. 150 MS/s) was used throughout this research which could contribute to the misclassification of the digitised pulses. Prior study, which investigated the influence of the sampling properties on the PSD performance, claims that 250 MHz digitiser would be a sensible choice when good PSD performance is required [37]. Nonetheless, successfully implemented PSD is consistent with the claim of the preceding work where the same digitiser was tested with simulated neutron and gamma-ray pulses [182]. The digitiser was also utilised in a novel neutron survey meter which further advocates the statement that good PSD results can be obtained with 150 MS/s system [176].

5.8 Conclusion

As evidenced by the results of the three PSD methods single stilbene crystal outperforms the plastic scintillators when neutron/gamma separation capabilities are considered. In spite of that, relatively large machining costs and fragility of stilbene (in comparison with plastics) hinder widespread adaptation of the single stilbene crystal scintillator in nuclear decommissioning applications. Plastic scintillators on the other hand, such as EJ-299-34 from Eljen Technology, are easily machined to build scintillator arrays as required for the coded-aperture imaging system described [14].

Although SDCC method exhibits the best FOM out of the three methods tested, its computational overhead, when tested using online processing, may be too high for a real-time application. PGA method offers the fastest response out of the three algorithms tested. However, its estimated FOM is the lowest. Moreover, since it only considers values of the digitised pulse at two separate points part of the information contained may be missed. This information may be crucial when the system is required to operate in multi-channel configuration due to the levels of high frequency noise expected. Despite the highest error associated with its FOM results of neutron/gamma separation using CCM present a good compromise between the digital implementation difficulty and PSD performance for the application described in the paper.

Three digital methods were employed to compare neutron/gamma discrimination performance of the chosen solid organic scintillators. Observed consistency in PSD quality for the three methods tested can be discerned as a cross validation of the test dataset collected in this study. Furthermore, the results obtained in this work are consistent with the previous studies conducted with similar organic solid scintillators [121, 177]. Hence, it can be surmised with a sufficient level of confidence that the results obtained represent a valid PSD performance of the tested samples.

Chapter 6

Investigation into a suitable scintillator and coded-aperture material for a mixed-field radiation imaging system

Cieslak, M.J., Gamage, K.A.A., Glover, R.

Published in Journal of Instrumentation, 6th December 2017

6.1 Abstract

Monte-Carlo modelling (MCNPX) methods have been employed to conduct an investigation into a suitable scintillator and coded-aperture material for a scintillator based mixed-field radiation imaging system. Single stilbene crystal, pure and ^{6}Li-loaded plastic scintillators were simulated and their neutron/gamma detection performance compared when exposed to the spontaneous fission spectrum produced by ^{252}Cf. The most suitable candidate was then incorporated into a scintillator based mixed-field coded-aperture imaging system. Coded-aperture models made of three W and ^{113}Cd compositions were tested in different neutron/gamma environments with a square W collimator modelled around the aperture. Each simulation involved recording the interactions of neutron events in organic solid scintillator, whose neutron/gamma detection performance was assessed prior to

the coded-aperture material investigation. Three coded-aperture material compositions have been tested with the simulated ^{252}Cf spontaneous fission as well as ^{241}AmBe neutron sources. Results generally claim very good detection sensitivity and spatial resolution for the radioactive sources located in the centre of the aperture.

6.2 Introduction

6.2.1 Scintillator detector

Over the years, organic liquid scintillators have become the preferred choice for neutron detection and imaging instruments [183, 119, 184, 185]. Although organic liquid scintillators are sensitive to both neutrons and gamma-ray photons, the difference in the fluorescence decay rate of heavily-ionising particles such as protons (resulting from neutron interactions) and electrons (resulting from gamma-ray photons interactions) can be utilised to infer the origin of the interaction [106]. As such, organic liquid scintillators provide a viable solution for mixed-field characterisation, when pulse-shape discrimination (PSD) methods are employed to reliably separate neutron events from gamma-ray interactions within the organic liquid scintillator [186].

Properties of some organic liquid scintillators, such as low flashpoint and susceptibility to leaks, make them unsuitable for certain industrial applications. However, the same discrimination methods can be exploited to separate particles within less flammable and less hazardous organic solid scintillators [154, 121]. Owing to continuous development, organic plastics and crystals have shown a significant improvement in their PSD capabilities in recent years. While plastics currently remain inferior to their liquid counterparts, solution-grown stilbene crystal claims better PSD performance in comparison to one of the most widely used organic liquid scintillator EJ-309 [187, 168].

In this study, a scintillation material suitable for mixed-field characterisation in nuclear decommissioning applications was sought. Due to the safety concerns related to the nuclear decommissioning sites low flammability and non-hazardous nature of the sensitive detectors were required. Thus, only organic plastic and crystal scintillators were investigated. Pure plastic, ^{6}Li-loaded plastic and single stilbene crystal scintillation samples were tested within a simulated spontaneous fission spectrum of heavily shielded ^{252}Cf. Perfect neutron/gamma PSD was assumed, and the three samples comparison performed based on the neutron/photon flux recorded within the scintillator as well as number of neutron and photon interactions within each scintillator sample based on PTRAC card implementation in MCNPX. MCNPX version 2.7.0 was utilised to perform all the simulations described in this paper [123].

6.2.2 Coded-aperture material

Many of the mixed-field characterisation systems utilise a sensitive detector in a form of an organic scintillator [186, 188, 189, 190]. These can be found in collimated single pinhole cameras utilised in many branches of nuclear instrumentation engineering to facilitate radiation imaging requirements. Despite their limitations, primarily related to the interdependence between spatial resolution and signal to noise ratio (SNR), collimator based radiation imaging systems have been successfully implemented in gamma-ray and neutron imaging systems [191, 192, 119, 193]. Development of multi-hole cameras with aperture patterns based on uniformly redundant arrays (URAs) and modified URAs (MURAs) allowed the development of high resolution radiation cameras without affecting SNR [59, 88]. Consequently, coded-aperture imaging (CAI) was favourably adopted in X- and gamma-ray localisation applications [63, 194]. Authors' previous work presents a detailed review of CAI systems [11].

Research into coded-aperture based neutron imaging system has been recently revived due to continuous development of the PSD capable organic scintillators and the advancements in digital signal processing on Field Programmable Gate Arrays (FPGAs). The difficulty arises, when PSD is required to be performed simultaneously on multiple channels, which is the case for scintillator based coded aperture neutron imaging systems (CANIS). Moreover, CANIS requires image reconstruction to be performed, once PSD is completed. Reconstruction algorithm does not only increase the computational overhead, but also requires that the incoming particles are effectively prevented, via coded aperture's opaque elements, from reaching the sensitive detector.

It follows that the coded-aperture material must be carefully chosen, so that the likelihood of misclassification of the particles reaching the elements of the sensitive detector is reduced to minimum. Owing to the characteristics of neutron interactions with matter, detectors tend to be focused on a specific energy range, such as thermal or fast neutron systems. Systems targeting fast neutron detection can utilise either *active* or *passive* coded-aperture system.

Active CAI is performed, when the aperture is built of neutron detectors and double scattering (in the aperture and the sensitive detector) is utilised to infer the time-of-flight and the direction of the incident neutron [108]. *Passive* CAI relies either on the high neutron absorption cross-section materials, such as polyethylene, or neutron reflecting materials, such as natural W. In contrast to the *active* coded-aperture approach, neutron interaction within the aperture is not directly used to perform localisation [109].

The most advanced example of the application of CAI techniques into neutron imaging and localisation has been presented by Hausladen et al. [74]. This scintillator based CANIS is aimed at fast neutron detection and utilises rank-11 MURA design for the coded aperture, which was built from high-density polyethylene (HDPE) to modulate the fast neutron field. The most recent implementation of the work reports on the use of an array of sensitive detectors built of the EJ-299-34 plastic scintillators [14]. Each scintillator element has a PMT attached to it, which allows for an easy localisation of the particle interaction. Experiments performed with multiple neutron sources of similar strength present a capability of distinguishing multiple sources, without the need for complicated analysis.

Based on author's preceding work, in this paper, MCNPX code was used to investigate the suitability of three W-^{113}Cd compositions for a portable scintillator based coded-aperture neutron imaging system. Each material was examined with ^{252}Cf and ^{241}AmBe radiation sources to observe its behaviour in different environments with varied neutron energy spectra. In each case neutron and photon energy spectra were manually defined for the sources specified. As a result, the potential of simultaneous neutron and gamma-ray sources identification was examined. In contrast to the aforementioned CANISs an array of small scintillation detector bars was constructed, whose each detector bar is to be linked to a single pixel of H9500 Hamamatsu MAMPT [195], in order to infer the location of the interaction.

6.3 Simulation based comparison of solid organic scintillators

6.3.1 Geometry and Physics

Real-life experimental scenario geometry - as available at Lancaster University, Lancaster, UK - has been used for the simulation based investigation performed in this study. Spontaneous fission source ^{252}Cf of 2.65 years half-life and average neutron energy spectrum of 2.1 MeV is stored in the centre of a water-filled metal tank. During experiments the source is pneumatically released and moved towards the edge of the side of the tank (for the purposes of this simulation based study the source is retained in the released position). Detectors are normally placed in closed vicinity to the edge of the tank as shown in Figure 6.1. There is also a 5 cm thick Pb block placed adjacent to the tank in order to reduce the number of gamma-ray photons reaching the sensitive detector. Similar approach has been previously adopted by Zaitseva et al. [121], where 5.1 cm of Pb reduced the number of gamma-ray photons to the same number as neutrons.

Fast neutrons are most likely to undergo elastic scattering with a proton, as a result of an interaction with nuclei in matter. In a similar way, gamma-ray photons will interact with the organic scintillant through Compton scattering with an electron [19]. These neutron and photon collisions in matter were examined for three different organic scintillation detectors. Mixed-field detector assembly comprising cylindrical scintillator sample and a PMT enclosed in an aluminium housing was placed 15 cm away from the side of the tank, where the radiation source is located during experiments.

For the purposes of the simulation work carried out in this study, neutron energy spectrum was defined using Watt fission spectrum. Gamma spectrum was defined based on the information presented by Valentine [32] and Gehrke et al. [31].

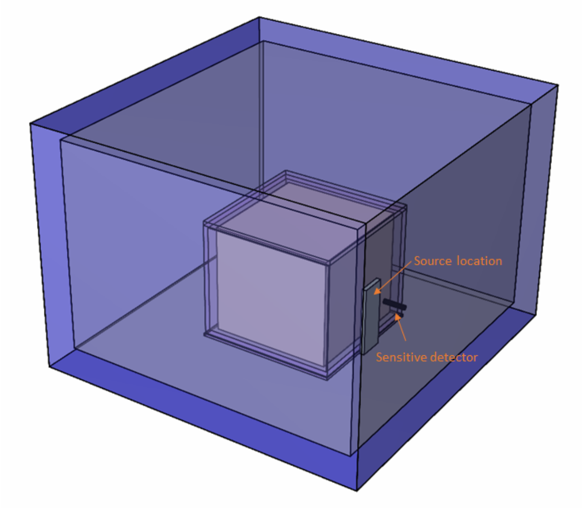

Figure 6.1: Geometry of the water-filled metal tank, where the ^{252}Cf fission source is kept at Lancaster University. Orange arrows point to the source location, when it is released for experiments, and to the placement of the sensitive detector.

Energy spectra of both neutron and gamma-ray photons yielded by the unshielded ^{252}Cf were recorded in MCNPX using a small volume (cylindrical) stilbene detector. These are used for reference, and are contrasted with the flux measurement at the location within the experimental geometry, where the scintillator samples were later placed. Particle flux measurements, as shown in Figure 6.2., illustrate the scale of moderation provided by the water tank where the source is normally kept.

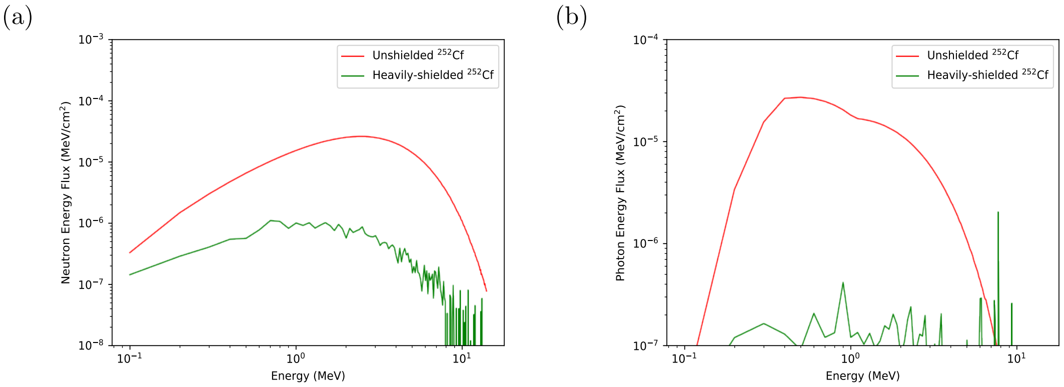

Figure 6.2: Unshielded and heavily-shielded (by means of water) particle energy spectra of ^{252}Cf for: a) neutrons and b) gamma-ray photons.

Solid plastic scintillator sample was modelled based on the information provided in EJ-299-33/34 data sheet from Eljen Technology [14]. In a similar way, single stilbene crystal was modelled using the information provided by Inrad Optics [104], whereas ^{6}Li-loaded plastic scintillator was modelled based on the data obtained from Balmer et al. [28]. Each scintillator sample, placed in a cylindrical Al enclosure, was in turn irradiated with the ^{252}Cf source. Walls surrounding the water tank were built of concrete completing the model of the neutron laboratory. The laboratory was filled with air to resemble the factual experimental environment.

6.4 Coded-aperture optimisation

6.4.1 Geometry and Physics

Based on the authors' preceding work, coded-aperture model examined in this work, was rank-7 MURA design. Detailed description of the design process and initial feasibility study can be found here [11]. It is worth noticing at this point that there is a correlation between the rank of the aperture and the resolution of the reconstructed image. Generally, the resolution increases with the growing rank of the aperture. However, higher rank apertures can be difficult to manufacture in materials, such as W and ^{113}Cd, due to fragility of very small elements. Moreover, it is the thickness of the aperture that contributes in a greater way to the performance of the imaging system, as shown by Gmar et al. [69], when the aperture is required to successfully block the incoming particles in the opaque elements.

Due to neutron source localisation issues identified in the initial work, a tungsten square collimator was added to the original design, aiming to prevent particles from escaping the geometry around the aperture. The new geometry is presented in Figure 6.3. Further, gamma-ray photon spectrum was added in order to reflect the real-life scenario more closely. The dimensions of a single aperture cell, as well as the dimensions of an individual detector cell were adjusted to the dimensions of a single anode of Hamamatsu's H9500 MAPMT.

The coded-aperture model - shown in green in Figure 6.3 - was in turn exposed to unshielded ^{252}Cf (spontaneous fission) and ^{241}AmBe neutron source. In each

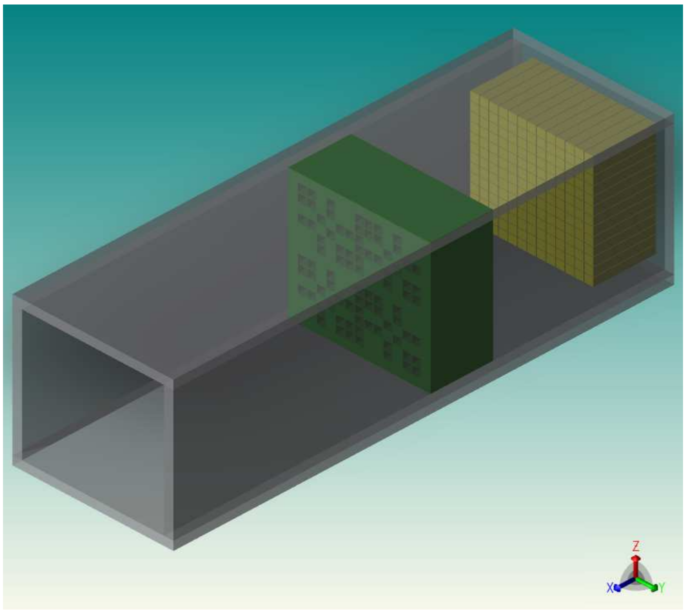

Figure 6.3: Geometry modelled in SuperMC was translated to MCNPX particle transport code [118]. Collimator is shown in grey, coded aperture in green and sensitive detector in yellow.

case, the radiation source was located 18 cm away from the aperture front. The sensitive detector thickness was set to 15 mm and was placed 50 mm behind the aperture; 10 mm thick square collimator encloses the modelled set-up as presented in Figure 3. Geometry presented in Figure 6.3 is a not to scale representation of the testing environment generated in SuperMC software. Properties such as thickness and materials were then manually adjusted to a specific simulation scenario in MCNPX input files. The presented MCNPX geometry was placed in an air-filled sphere.

Single stilbene crystal showed a very good neutron detection performance, when tested with neutron spectrum of ^{252}Cf in the previous study [11]. Its neutron/gamma detection performance was further investigated in the first part of this work. It also presents best neutron/gamma sensitivity out the three samples tested as evidenced by the results presented in section 6.3. Thus, single stilbene crystal was used to build the pixelated sensitive detector, as represented in yellow in Figure 6.3.

With the various radiation sources placed in turn 18 cm away from the aperture front neutron and gamma-ray photon fluxes, as well as energy deposited in the individual sensitive detector cells were recorded for each coded-aperture material composition and thickness investigated in this study. Three different W and ^{113}Cd compositions (25% W, 75% ^{113}Cd; 50% W, 50%^{113}Cd; 75% W, 25% ^{113}Cd) were examined. Based on the authors' initial study the thickness selected for testing was 25.4 mm [11].

6.5 Results

6.5.1 Comparison of the three scintillation samples

Three plastic scintillator samples were in turn exposed to the heavily-shielded ^{252}Cf fission source and their relative neutron and gamma-ray photon fluxes compared. The resulting plots against neutron and photon energy are presented in Figure 6.4a and 6.4b, respectively. A single simulation run consisted of 10^9 particle histories generated from the source and particle flux in a cell was recorded for each scintillation sample. Uncertainty for each simulation run was below the confidence level of 0.05%.

Relative neutron and gamma-ray photon energy spectra measured from the unshielded fission spectrum of ^{252}Cf (Figure 6.2a) can be compared to the results obtained for individual scintillator cell when the source energy is shielded through the water in the tank (Fig 6.4a). While it can be observed that the measured neutron flux is greatly reduced, the neutron energy spectrum resembles the distribution of the unshielded source for all three samples.

Gamma-ray photon spectrum of the unshielded source (Figure 6.2b) on the other hand is significantly altered through the metal tank and Pb shielding provided (Figure 6.4b). Based on the dissimilarity it can be concluded that most of gamma-ray photons produced by spontaneous fission ^{252}Cf have been successfully shielded by the Pb block located between the tank and the sensitive detector. The resulting peaks between 6-10 MeV are the result of neutron interactions with water in the tank, as well as neutron interactions with air around the detector, which are both accompanied by gamma release. There is also very little fluctuations between the photon flux measurements for different scintillators eliminating the scintillator from being the source of these species.

Additionally, the particle tracking card (PTRAC) was utilised to investigate 10^4 entries to the scintillator cell in order to estimate the highest neutron detection efficiency. Neutron interactions such as elastic scattering, inelastic scattering and capture events were recorded. The ^{252}Cf spontaneous fission source was defined as a point isotropic source, placed in a small Al capsule, as it is stored in real-life conditions at Lancaster University. The highest number of neutron interactions was recorded in the ^{6}Li-loaded plastic scintillator - 9905, which was followed by the single stilbene crystal - 8503 and the pure plastic sample - 8442. The highest neutron efficiency of the ^{6}Li-loaded sample is in this case associated with the loading of the scintillator, which allows thermal neutron detection due to high neutron absorption cross-section of the ^{6}Li. In this case, the plastic scintillator was loaded with 0.14% fractional mass of ^{6}Li.

The remaining 100-1500 interactions detected using PTRAC card within the scintillator cell were associated with gamma-ray induced Compton scattering events. Such results would suggest an unrealistic ratio between neutron and gamma-ray events detected. However, further investigation revealed that many thousands of neutron events detected within the scintillator do not originate in the ^{252}Cf source. In contrast to gamma-ray photons, which are successfully moderated through the Pb block and then further through the concrete walls of the neutron laboratory, neutrons are scattered by H molecules within the concrete walls. Hence, a large number of neutrons undergo elastic scattering interaction with H in the surrounding walls and can re-enter the scintillator cell, falsely increasing the number of neutron counts in the scintillator.

6.5.2 Coded-aperture optimisation

Neutron and photon flux measurements recorded for the individual cells of the sensitive detector have been utilised to investigate neutron blocking properties of the chosen material compositions as described in section 6.3. Total flux detected, as well as energy deposited, in a single detector cell were read via bespoke Matlab scripts to build a projection of the source, as seen through the coded aperture. These unprocessed images were expected to closely reflect transparent and opaque elements of the coded-aperture pattern. For clarity the coded-aperture pattern

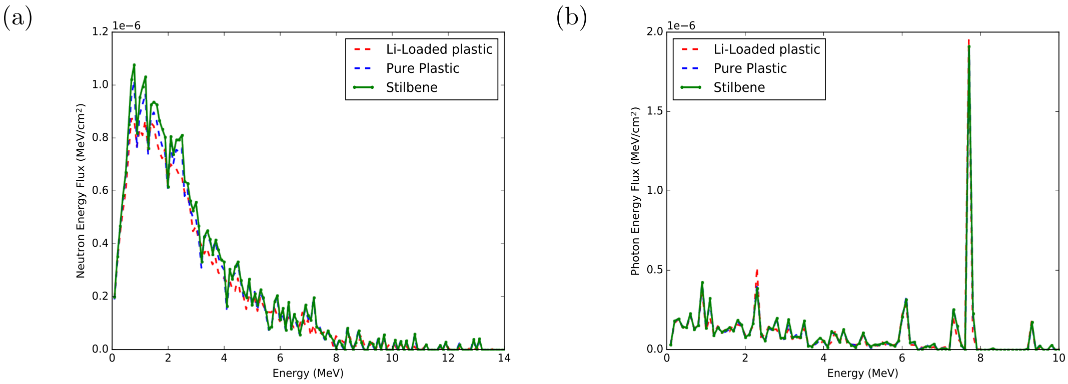

Figure 6.4: Relative particle fluxes for the three scintillator samples simulated and plotted against 100 keV energy bins for a) neutrons and b) gamma-ray photons

exploited in this study is shown in Figure 6.5., which is then further compared to the projections obtained.

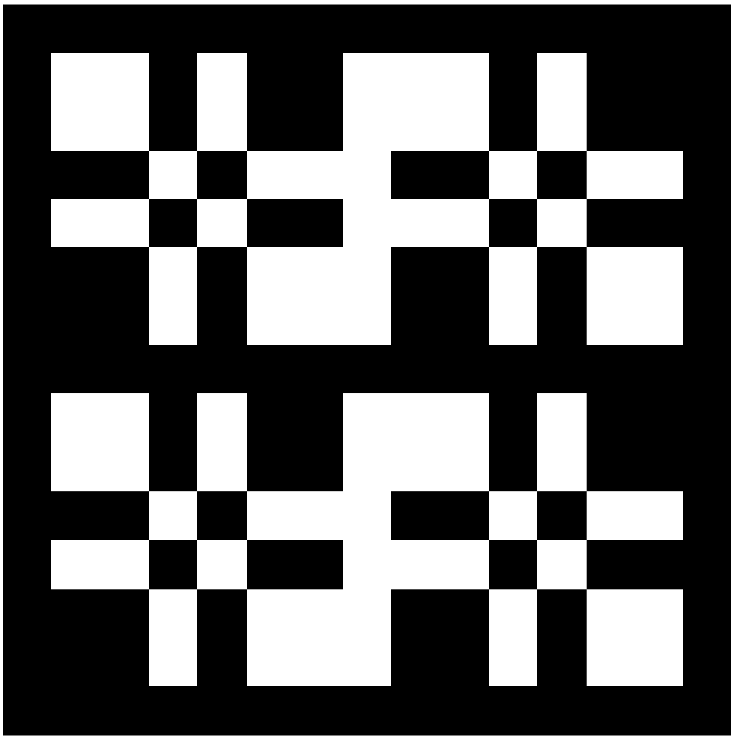

Figure 6.5: Rank 7 coded aperture. Transparent and opaque elements are presented in white and black, respectively. With 84 transparent and 85 opaque elements, the modelled aperture yields 49.7% transparency. A frame of 2.8 mm was added around the 13 × 13 aperture to represent clear boundaries which yielded the total length of 42 mm. Taken from [11].

Results of the relative neutron flux passing through a detector cell in Figure 6.6 present a good resemblance of the pattern from Figure 6.5. The central opaque horizontal line in Figure 6.5 can be identified with a strip of low neutron flux crossing the projections around zero on the y-axis. Furthermore, the transparent elements of the pattern from Figure 6.5 can be matched with the areas of the higher flux; the main vertical line crossing the images around zero on the x-axis. Although the three different compositions yield a very similar performance, the images presented in Figure 6.6i and Figure 6.6j claim the clearest separation between the areas of high and low neutron flux, which is of vital importance when coded-aperture decoding algorithm is applied in order to obtain the location of the radiation source. Despite the difference in the neutron fluxes measured for the different radiation sources investigated, as evidenced by the difference of the colour intensity in Figure 6.6, coded-aperture patterns are distinguishable for both simulated sources.

In a similar way, gamma-ray photon flux was measured in the sensitive detector (Figure 6.7). As expected, the images reconstructed with regards to the gamma-ray flux passing through the sensitive detector show an even greater resemblance to the rank-7 coded-aperture pattern used. It is predominantly due to the very good gamma-ray shielding properties of the high Z element - W. It interacts with gamma-rays of energies up to approximately 1.5 MeV through Compton scattering and photoelectric effect. Hence, the difference between the modulation of the particle fields between ^{241}AmBe and ^{252}Cf is not as evident as for neutrons.

In addition to neutron and gamma-ray fluxes passing through a detector cell, energy deposition in a cell was also investigated. Pulse height tally (F8) scores in the detector's cells were mapped on to a square array to reconstruct the projections. In the case of neutron energy deposition (Figure 6.6 columns 3 and 4), source reconstruction may be difficult due to unclear pictures, when contrasted with the coded-aperture pattern from Figure 6.5. The vertical line of transparent elements crossing through the coded-aperture centre, which was easily identifiable in particle flux figures, can only be discerned with difficulty energy deposition distributions. There is a tendency that can be observed across gamma-ray measurements, where the increase of W content in the composition is proportional

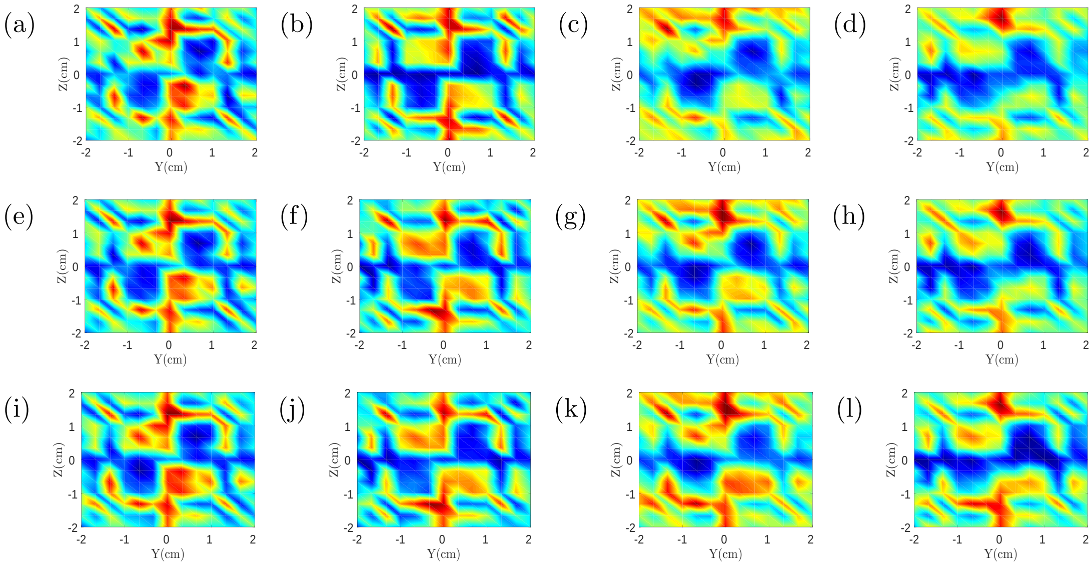

Figure 6.6: Neutron flux and energy deposition projected on the sensitive detector through the coded aperture of three W-^{113}Cd compositions. Columns 1 and 2 shown neutron flux and columns 3 and 4 energy deposition for two different sources a) & c) W-25%, ^{113}Cd-75% with ^{241}AmBe b) & d) W-25%, ^{113}Cd-75% with ^{252}Cf e) & g) W-50%, ^{113}Cd-50% with ^{241}AmBe f) & (h) W-50%, ^{113}Cd-50% with ^{252}Cf i) & k) W-75%, ^{113}Cd-25% with ^{241}AmBe and j) & l) W-75%, ^{113}Cd-25% with ^{252}Cf. Intensity scale was normalised for all images to between 1e^{-7} and 1e^{-3} MeV/cm^2.

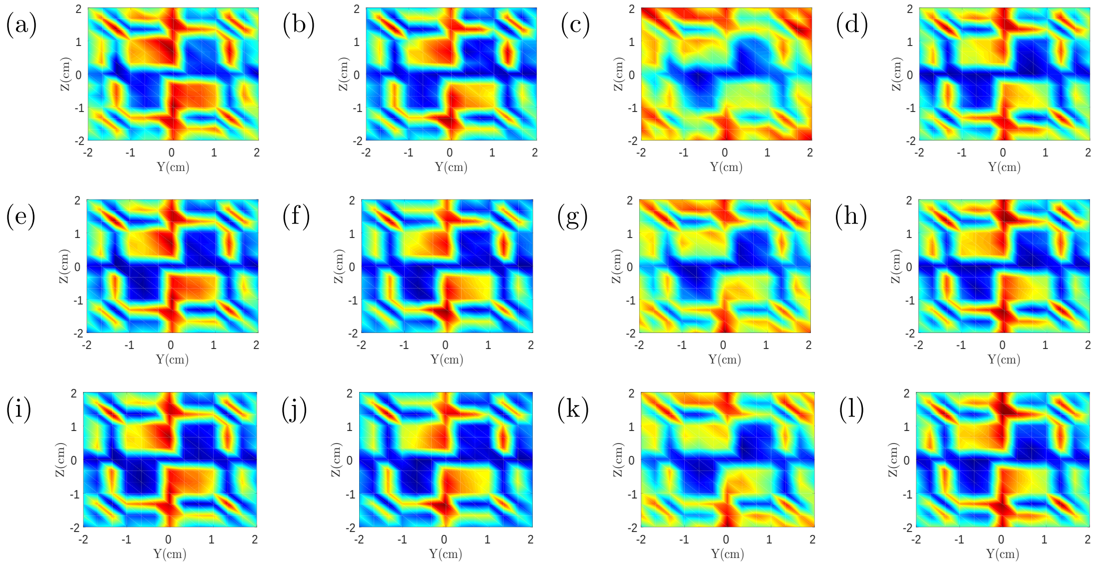

Figure 6.7: Gamma-ray photon flux and energy deposition projected on the sensitive detector through the coded aperture of three W-^{113}Cd compositions. Columns 1 and 2 shown neutron flux and columns 3 and 4 energy deposition for two different sources a) & c) W-25%, ^{113}Cd-75% with ^{241}AmBe b) & d) W-25%, ^{113}Cd-75% with ^{252}Cf e) & g) W-50%, ^{113}Cd-50% with ^{241}AmBe f) & (h) W-50%, ^{113}Cd-50% with ^{252}Cf i) & k) W-75%, ^{113}Cd-25% with ^{241}AmBe and j) & l) W-75%, ^{113}Cd-25% with ^{252}Cf. Intensity scale was normalised for all images to between 1e^{-7} and 1e^{-3} MeV/cm^2.

to the increase of the projections' quality. Furthermore, there is a clear difference in particle modulation quality between the projections obtained in Figure 6.7 (Columns 3 and 4) for ^{241}AmBe and ^{252}Cf. When compared with the corresponding results of gamma-ray flux measurement (Figure 6.7 Columns 1 and 2) the quality of the image is significantly lower. It suggests that a large number of gamma-ray photons passes through the detector cells without depositing energy.

6.5.3 Source reconstruction

The results presented in the previous subsection were further processed via deconvolution algorithm implemented in a custom Matlab script. The process involves deconvolution of the input array (raw projections presented in the previous subsection) with the decoding array. It results in an array, whose expected outcome is a single impulse response, marking the location of the source. The decoding array is specific for a coded-aperture design of a set rank. Further details about the decoding process are presented here [11].

Reconstruction plots presented in Figure 6.8 - 6.9 show a good agreement with the results of the 'raw' data - before the decoding algorithm was applied. In the same way as the 'raw' data images, particle flux measurements (Figure 6.6 and Figure 6.7 Columns 1 and 2) present the most accurate exemplification of the location of the radiation source. Single hotspots can be clearly distinguished for neutron and gamma-ray images for both sources simulated. Moreover, the hotspot location in the middle of the reconstructed image claims 100% accuracy with the source coordinates specified as (0.0,0.0,0.0).

Images in Figure 6.9 (Columns 3 and 4) present the source reconstruction based on the measurement of the energy deposition in a cell. A significant drop in the localisation accuracy, caused by the identification of multiple hotspots, is observed in many cases, with W-25%, ^{113}Cd-75% composition being mostly affected. There is also a general tendency that can be discerned across all the reconstructed images; the localisation accuracy is proportional to the increased W content in the composition. Furthermore, the images in Figure 6.9 (Columns 3 and 4) suggest a considerably greater detection accuracy for ^{252}Cf than for ^{241}AmBe.

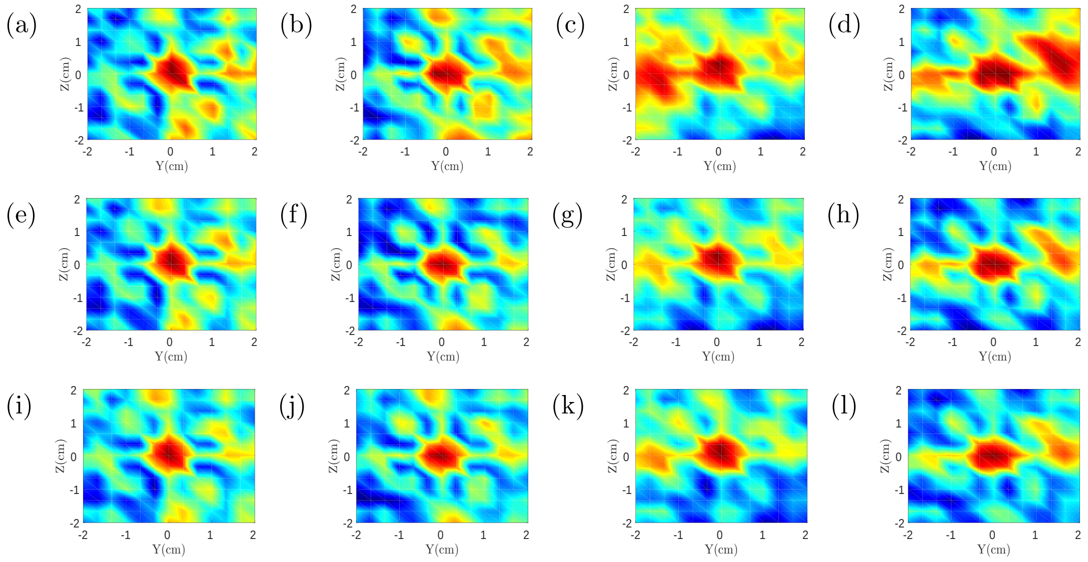

Figure 6.8: Neutron source reconstruction results based on particle flux measurements (Columns 1 and 2) and energy deposition (Columns 3 and 4) for W-^{113}Cd compositions a) & c) W-25%, ^{113}Cd-75% with ^{241}AmBe b) & d) W-25%, ^{113}Cd-75% with ^{252}Cf e) & g) W-50%, ^{113}Cd-50% with ^{241}AmBe f) & (h) W-50%, ^{113}Cd-50% with ^{252}Cf i) & k) W-75%, ^{113}Cd-25% with ^{241}AmBe and j) & l) W-75%, ^{113}Cd-25% with ^{252}Cf. Intensity scale was normalised for all images to between 1e^{-7} and 1e^{-3} MeV/cm^2.

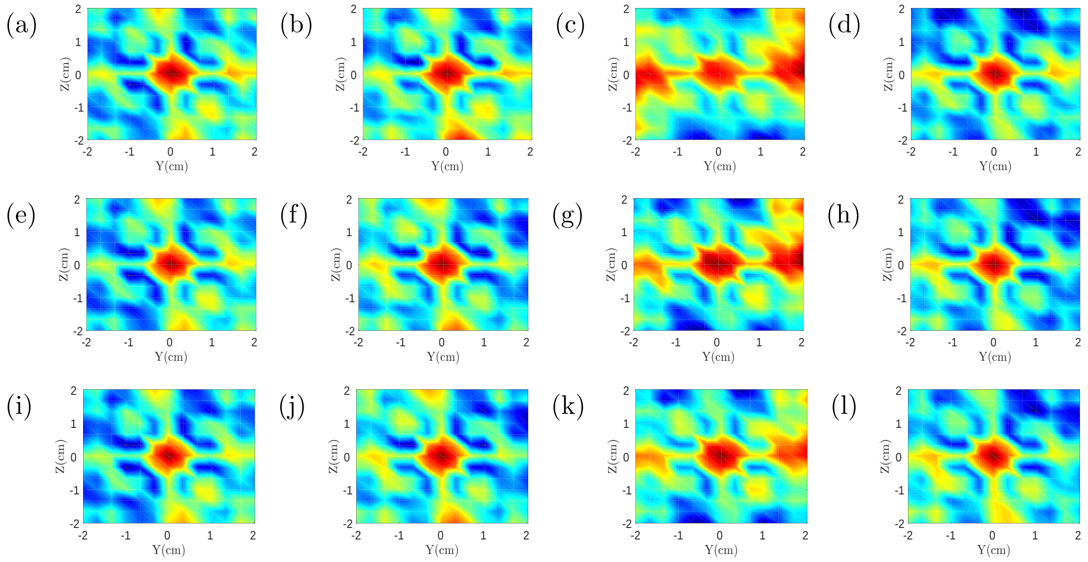

Figure 6.9: Gamma-ray source reconstruction results based on particle flux measurements (Columns 1 and 2) and energy deposition (Columns 3 and 4) for W-^{113}Cd compositions a) & c) W-25%, ^{113}Cd-75% with ^{241}AmBe b) & d) W-25%, ^{113}Cd-75% with ^{252}Cf e) & g) W-50%, ^{113}Cd-50% with ^{241}AmBe f) & (h) W-50%, ^{113}Cd-50% with ^{252}Cf i) & k) W-75%, ^{113}Cd-25% with ^{241}AmBe and j) & l) W-75%, ^{113}Cd-25% with ^{252}Cf. Intensity scale was normalised for all images to between 1e^{-7} and 1e^{-3} MeV/cm^2.

6.6 Discussion

Based on the results presented in section 6.5.1. the most suitable candidate for the mixed-field imaging system for nuclear decommissioning applications would be the single stilbene crystal. Relative neutron energy flux measured was the highest in the crystal out of the three samples tested. The number of PTRAC interactions recorded, which was limited to 10,000 revealed that due to neutron capture events there were more neutron interactions in ^{6}Li-loaded plastic scintillator than in pure plastic or crystal. Devices used for mixed-field characterisation necessitate better neutron to gamma detection ratio, if these are to be used to simultaneously identify neutron and gamma-ray sources. Previous experimental study of ^{6}Li-loaded plastic scintillator shows good thermal neutron detection performance. However, it also reveals that fast neutrons and gamma-ray photons are difficult to separate using PSD with this scintillator, especially when exposed to ^{252}Cf field [28].

Another study investigating ^{6}Li-loaded plastic scintillators claims even better PSD separation performance [196]. In a similar way to Balmer et al.[28] Cherepy et al. [196] uses figure-of-merit (FOM) for PSD applications to estimate neutron/gamma separation performance of the scintillator [19]. The Cherepy et al. study claims the FOM of 1.4 in the 350 to 450 keVee energy range, which is approximately twice as high as in Balmer et al. The difference between the two studies lies most likely in the amount of ^{6}Li doping. Moreover, both of these experiments were performed in a controlled environment, enabling the neutrons from ^{252}Cf to be sufficiently thermalized for the neutron capture on ^{6}Li. However, authors' recent experimental study of the ^{6}Li-loaded scintillator shows that it fails to separate fast neutrons and gamma-ray photons from ^{252}Cf fission source, when the energy spectrum is modulated by means of water (in exactly the same way as simulated in this study) [156].

Furthermore, the absence of sufficient moderation (by means of Bonner Sphere or Polyethylene layer, as in the studies by Balmer et al. and Cherepy et al., respectively) relates to the lack of the peak resulting from ^{6}Li neutron capture interaction around 400 keVee in Figure 6.4. Neutron energy spectrum from the heavily-shielded ^{252}Cf at Lancaster University peaks at approximately 0.7-0.9 MeV, as shown in Figure 6.2a. This is further supported by the aforementioned authors' experimental work, where thermal neutron peak was not detected and the ^{6}Li-loaded scintillator did not discriminate between neturons and gamma-ray photons at this energy level [156].

Although the single stilbene crystal presents the best neutron/gamma detection performance out of the three samples tested in this study its practical implementation can be prevented by the high manufacturing cost and little performance gain. Pure plastic scintillator sample shows only slightly inferior neutron/gamma detection performance, which relates to the neutron energy detection spectrum. Moreover, crystal scintillators are more susceptible to mechanical damage during transportation. Pure plastic scintillator such as EJ-299-34 does not only claim good PSD performance, even with relatively low neutron energy spectrum of ^{252}Cf but can also be machined to high precision for small imaging arrays [121, 14].

There is a general trend that can be observed across the results of the second part of the study. In all the cases considered the higher W content in the aperture material composition provides the most effective neutron/gamma field modulation. Thus, the W-75%, ^{113}Cd-25% composition offers the most accurate reconstruction of the simulated radiation source. However, the modulation performance of each material (and the source localisation as a result) is affected by the energy spectrum of the source.

With the average neutron energy spectrum of ^{241}AmBe higher than ^{252}Cf, the corresponding reconstructed source localisation images in Figure 6.8 and Figure 6.9 show greater intensity of the former. Despite the difference in the level of intensity, the localisation efficiency is comparable for both sources with only one clear neutron hotspot identified in the mentioned cases. There is a good agreement between the results based on neutron flux and energy deposited, as far as single hotspot identification is considered.

Gamma-ray source localisation on the other hand, is more efficient when particle flux is considered for the reconstruction. Figure 6.9 (Columns 1 and 2) presents an ideal source reconstruction with a single hotspot easily-identifiable in the centre of the image. In contrast, the energy deposited based images of ^{241}AmBe in Figure 6.9 (Column 3) show poor source detection performance. In line with the previously made claim, the performance increases with the increased W content.

This is observed due to a very high number of 4.4 MeV gamma-ray photons emitted form ^{241}AmBe. Therefore, the higher W content enables greater absorption of these gamma-rays in the aperture which in turn results in higher quality reconstruction. Nonetheless, multiple gamma-ray hotspots identified for ^{241}AmBe in Figure 6.9 (Column 3) prevent reliable gamma-ray source detection and localisation. As the average gamma-ray spectrum of spontaneous fission ^{252}Cf source is much lower, even the lowest W content allows for the radiation source to be effectively reconstructed.

Based on the results presented the most suitable composition for the coded-aperture material would be W-75%, ^{113}Cd-25%. However, the W-50%, ^{113}Cd-50% composition claims only marginally inferior neutron/gamma field modulation performance. For practical application factors such as machining difficulty and the specific energy spectra would need to be considered. Since this study is aimed at mixed-field detection and characterisation of the radioactive sources with energy spectra similar to ^{252}Cf, one of the identified compositions could be considered for implementation.

Chapter 7

Gamma-ray modulation properties of tungsten coded apertures for a novel mixed-field imaging system

Cieslak, M.J., Gamage, K.A.A., Glover, R., C. James Taylor

Published in Journal of Instrumentation, 8th February 2019

7.1 Abstract

An investigation into the gamma-ray modulation properties of a tungsten coded aperture, whose design is based on the mathematical principles of Modified Uniformly Redundant Arrays (MURA), has been performed. Due to the small size of the individual cells, the aperture was built using additive manufacturing methods. The gamma-ray field was produced by a ^{137}Cs radioactive isotope at Lancaster University, UK. An organic plastic scintillator sample, which is capable of pulse shape discrimination, has been used to detect the gamma-ray field modulated by a tungsten aperture. Prior to the investigation of the aperture modulation properties, energy calibration of the scintillator was performed. Its pulse shape discrimination capabilities were verified using a ^{252}Cf fission source. In this study, each of 169 coded aperture cells were investigated by collimating the modulated

gamma-ray field of ^{137}Cs through a 25.4 mm thick supporting plate, made of lead due to its gamma absorption capabilities. The supporting plate has one opening in the centre, of the same dimensions as the single aperture cell, i.e. 2.5 mm × 2.5 mm. The number of pulses detected for every aperture location was recorded in an array. The array was subsequently used to create a two-dimensional image of the source, which was encoded through the coded aperture pattern. Finally, the image was decoded using deconvolution techniques to reveal the actual source location. The new results obtained in this study indicate that sufficient gamma-ray modulation properties of the aperture can be determined, despite the relatively small footprint and thickness of the coded aperture.

7.2 Introduction

Coded-aperture imaging is a well-established and widely applied concept of optics, and is frequently incorporated into a range of other research fields [197]. Radiation detection is one of the examples, where there is a particular focus on X-ray and gamma-ray imaging systems [198, 199]. In recent years, however, coded-aperture based neutron imaging has seen considerably increased attention [200, 201]. A detailed account of coded-aperture based systems for radiation detection, including discussion of design and implementation methods, has been previously presented [11].

The main advantage of coded-aperture imaging is the increased signal-to-noise-ratio (SNR), when compared to single opening pinhole devices. In the latter case, there is always a trade-off between the resolution and SNR. An ideal pinhole device would require an infinitely small opening in the aperture, to achieve the highest resolution. At the same time, the opening would need to be infinitely large to obtain the highest SNR. Development of scatter-hole, and later coded-aperture techniques offer a form of a compromise between SNR and resolution [58, 59]. Due to multiple small sized openings of the aperture, it has become possible to increase the overall opening percentage of the aperture to approximately 50%.

Studies of neutron imaging systems based on coded masks that utilise organic scintillators as sensitive detectors are primarily designed as large scale detectors.

For instance, Griffith et al. [200] use 15 × 15 × 10 cm^3 blocks of high-density polyethylene as single cells of a 144 element coded aperture. The detector array in the study comprises of 64 cubic liquid scintillation detectors (EJ-309) of 15 × 15 × 10 cm^3 each. Another study conducted by Newby et al. [202] reports a system where a single block of the detector has dimensions 13.5 × 13.5 × 50 mm^3. In this case, the single blocks are combined into 8 × 8 arrays. These are further combined into a 3 × 3 array to build a 33.7 × 33.7 cm^2 detector.

Such devices are neither easily portable nor easily deployable in the field. Therefore, they are not suitable for nuclear decommissioning applications, where the detectors are often required to survey small enclosed areas. These areas are often difficult to access by people, let alone by large machinery. Hence, the present article considers a small scale coded aperture, for which the single opening dimensions are 2.8 × 2.8 × 25 mm^3. When complemented by a suitably sized sensitive organic detector, such a system could be packaged into a portable device for nuclear decommissioning applications.

7.2.1 Design considerations

Depending on the application of a coded aperture in a system, a number of key features of the aperture require careful consideration at the design stage. Thickness and material type define the stopping power of the coded aperture. The aperture is expected to block the incoming particles on its opaque elements. Hence, the distance that a particle can travel in a specific material before an interaction occurs necessitates close investigation. High density chemical elements, such as lead and tungsten, are known for their good gamma-ray stopping capabilities, whereas neutron stopping properties are more complex and closely related to neutron's kinetic energy (defined by cross-sections for specific energy ranges). Isotopes such as ^{10}B, ^{7}Li, ^{113}Cd and ^{157}Gd exhibit large thermal neutron cross-sections, while ^{1}H shows a greater fast neutron cross-section.

Therefore, for the requirements of an empirical study, a material capable of blocking both neutrons and gamma-ray photons was sought. Our earlier Monte-Carlo simulation study revealed that a W-^{113}Cd composition (75%-25% ratio) provides optimal results [203]. However, due to safety concerns related to the handling of ^{113}Cd, a pure tungsten coded aperture was built for the present study and only tested in relation to gamma-ray modulation properties. The model drawing used for simulation and the manufactured tungsten coded apertures for the experimental work are presented in Figure 7.1a and 7.1b, respectively.

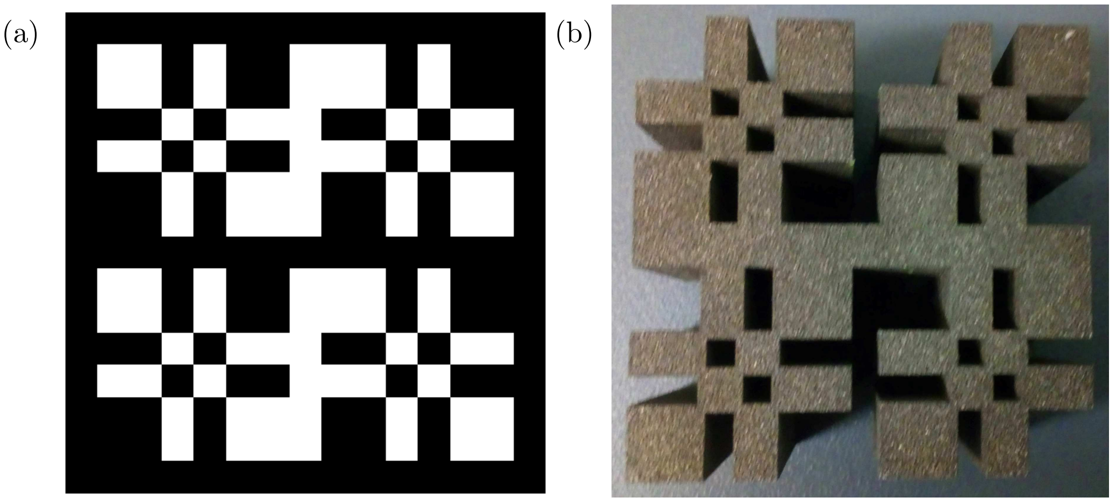

Figure 7.1: Coded aperture designed for the requirements of this study, including a) initial simulated design with a single cell dimensions of 2.8 × 2.8 mm, and b) manufactured in tungsten by M&I Materials Ltd. with a single transparent cell dimensions adjusted to 2.5 × 2.5 mm.

Another key feature that needs to be carefully considered is the pattern of the array to be used as the coded aperture. The most extensively used patterns are Uniformly Redundant Arrays (URAs) and Modified Uniformly Redundant Arrays (MURAs) [59, 88]. In both cases, the rank of the aperture defines the number of pixels in the particular pattern. For instance, the rank-7 aperture utilised in the present study comprises 169 cells (arranged into a 13 × 13 array). For an extensive review of array patterns as applied to coded apertures, as well as their design rules and associated mathematical calculations, the reader is referred to the authors' previous work [11].

Generally, the higher the rank of the aperture, the higher the resolution of the reconstructed image. However, as the rank of the aperture becomes higher, the associated pixel size decreases. As a result, the sensitive detector and accompanying photodetector would have to be of very small dimensions to provide the required one-to-one interface. Therefore, in this work, a rank-7 MURA based coded aperture with a $2.8 \times 2.8 \times 25.4$ mm^3 cell size was built. In this manner, it will be feasible to match the cell with a similarly sized sensitive detector and photodetector in the future.

7.2.2 Sensitive detectors

Regardless of the application, coded-aperture imaging requires a sensitive detector, whose task is to detect the image that is modulated through the transparent and opaque elements of the aperture. The detector's efficacy with regard to the identification of specific particle types is vital for the accurate acquisition of the modulated "image". This is subsequently used for the reconstruction of an actual image, in line with conventional image reconstruction techniques [11]. A requirement of the present study is that the detector provides good energy resolution, as well as pulse shape discrimination (PSD) potential. Therefore, a PSD capable organic plastic scintillator sample was chosen for the experiments.

Hence, the research contributions of this article relate to an experimental study of the gamma-ray modulation properties of a tungsten coded aperture using a PSD capable sensitive detector. The key novelty is the relatively small footprint and thickness of the coded aperture. To the authors knowledge, this represents the first time that a tungsten coded aperture of this scale has been tested with regard to its gamma-ray modulation capabilities. The following section 7.3 describes the methodology. The results and discussion are presented in sections 7.4 and 7.5 respectively, followed by the conclusions in section 7.6, where potential future improvements to the system are also presented.

7.3 Methodology

The present section considers methods for detector calibration, PSD and the modulation capabilities of the coded aperture.

7.3.1 Detector calibration

Before the assessment of the modulation properties of tungsten coded aperture commenced, it was required to conduct energy calibration of the scintillation detector. The scintillator used in this study was an organic plastic PSD sample (25mm diameter, 25mm thick) provided by Lawrence Livermore National Laboratory (LLNL), U.S.A. - denoted by the LLNL number 5706. The sample was previously compared to two other solid organic scintillators in regard to its neutron/gamma discrimination properties [156]. However, no information about its energy calibration was provided.

In this study, the back and side of the scintillator sample was covered with EJ-510 reflective coating. The sample was subsequently coupled to an ET Enterprises 9107B photomultiplier tube (PMT) with EJ-550 silicone grease. A light-proof enclosure was placed around the scintillator-PMT assembly. The PMT was connected to a positive high voltage power supply of 860 V. Finally, an FPGA based 12-bit resolution, 500 MS/s “raw data” digitising system was used to collect the detected pulses. It collected 128 samples (every 2 ns) for every triggered pulse.

The assembly was exposed in turn to ^{137}Cs and ^{22}Na gamma-ray sources of 319 kBq and 1.68 kBq current activity, respectively. The sources were placed 15 cm away from the front of the detector while measurements were being taken. Given the respective activities of the sources, 120,950 ^{137}Cs pulses and 36,548 ^{22}Na pulses were accepted. Each detected pulse was digitally verified against pile-up by a custom rejection algorithm. Here, a pulse was rejected if there were two peaks detected within the same triggered window.

Recorded pulse height spectra were plotted for both gamma-ray emitters to compute the corresponding Compton edges. Pulse height spectra are presented in Figure 7.2a. These were subsequently used to convert the pulse height values to electron equivalent energy for both calibration sources. ^{137}Cs produces a Compton edge of 477 keV, and ^{22}Na produces two Compton edges of 341 keV and 1062 keV gamma-ray interactions. A linear relationship between the pulse height values and corresponding electron equivalent energy is assumed, as suggested by Figure 7.2b. However, for the case when the number of interactions in a cell is counted, slight deviations from the linearity are of lesser importance.

(a)

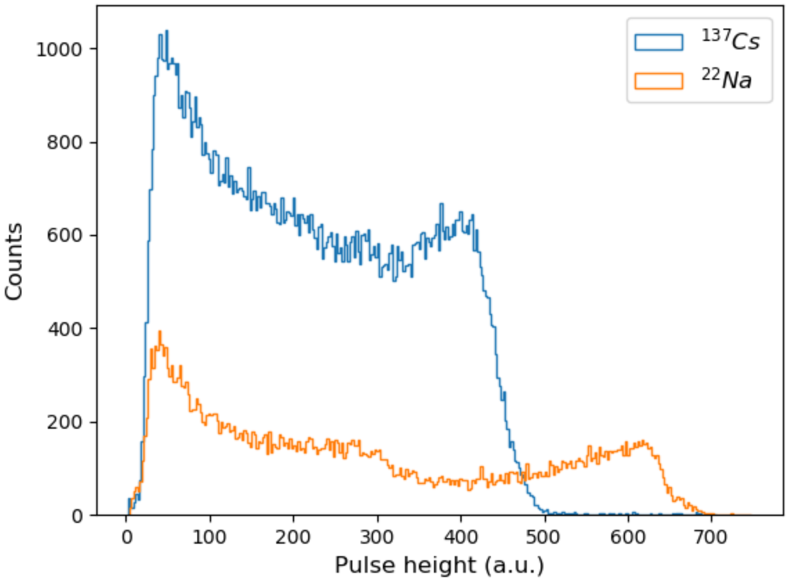

(b)

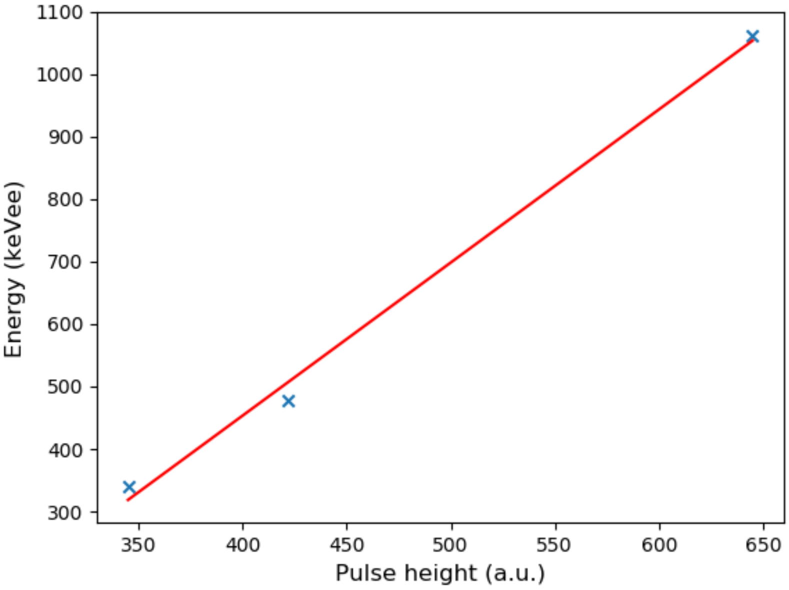

Figure 7.2: Energy calibration performed with ^{137}Cs and ^{22}Na showing a) pulse height spectra and b) the relationship between the pulse height and electron equivalent energy. Compton edge was calculated at 75% of the Compton peaks.

7.3.2 Pulse shape discrimination performance of the detector

Pulse shape discrimination performance of the plastic scintillator sample was previously investigated in comparison to other organic scintillator samples [156]. However, a relatively low sampling rate digitiser was utilised and the low energy limit was not investigated. In the present work, the charge comparison method (CCM) was used to perform PSD, and the low energy discrimination limit (in terms of electron equivalent energy) was sought [106]. The discrimination factor D_f was calculated using Equation 7.1, in which I_{long} denotes the integral calculated over the entire tail of the pulse, with the peak of the pulse represented by the first sample, and I_{short} is calculated as an integral between the first sample being taken 32 ns after the peak and the last sample of the entire window.

$$D_f = 1 - \frac{I_{short}}{I_{long}} \tag{7.1}$$

A mixed field environment was provided by the ^{252}Cf source located at Lancaster University, UK. The aforementioned assembly comprising the PMT and the organic plastic scintillator sample was exposed to the ^{252}Cf radioactive isotope. The source is normally stored in the centre of a water tank and is pneumatically moved to the edge of the tank, when required to be exposed for taking measurements. The detector assembly was placed 15 cm away from the edge of the tank, where the source is located when in exposed position. Very good pulse separation can be observed for the chosen sample, with an illustrative PSD scatter plot shown in Figure 7.3. Here, the upper plume depicts the gamma-ray photon interactions and the lower plume the neutron interactions.

7.3.3 Modulation capabilities of tungsten coded aperture

Before the coded aperture was manufactured, the part was first designed in Computer-Aided Design (CAD) software and subsequently translated into Monte-Carlo code for simulation. Following completion of the simulation study, the model was built into a part using additive manufacturing techniques by M&I Materials Ltd, Manchester, UK.

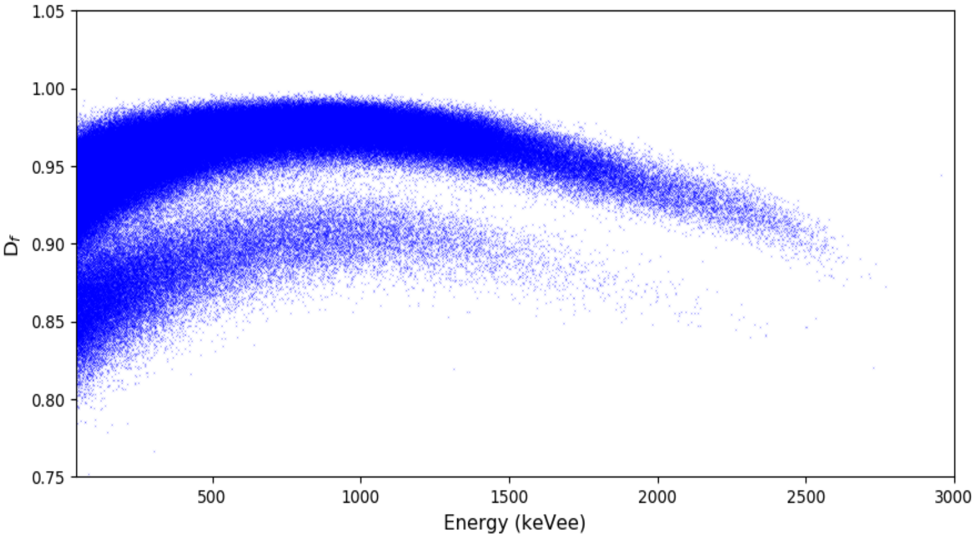

Figure 7.3: Scatter plot of PSD performed using CCM for the plastic scintillator sample exposed to the neutron/gamma-ray field of ^{252}Cf. There were 908,037 samples accepted in the process. Lower discrimination level was set to 40 keVee.

Due to the complexity and small dimensions of the coded aperture, the design used for simulation work (shown in Figure 7.1a), with each cell of 2.8 × 2.8 × 25.4 mm^3, was revised somewhat (Figure 7.1b). This is due to the fragility of the links between single opaque cells and other parts of the coded aperture. As a result, the single transparent cell of the coded aperture was reduced to 2.5 × 2.5 × 25.4 mm^3, so that the thickness of the link to a single opaque element of the aperture could be at least 0.8 mm.

The experimental setup is presented in Figure 7.4a. The green holder is used to place the plastic disk with the radioactive source. The tungsten coded aperture is placed 10 cm below the radioactive source holder – directly on top of the supporting lead plate. The CAD image of the lead supporting plate, the purpose of which was to collimate the gamma-ray photons on to the front of the detector, is shown in Figure 7.4b. The front of the detector assembly is placed directly underneath the bottom of the lead supporting plate. The total distance between the bottom of the source holder and the top of the detector assembly is 15 cm.

The experiment was performed by placing the ^{137}Cs radioactive point source in the green holder. The top surface of the lead supporting plate was covered with a 2.5 × 2.5 mm grid, which was used to aid the movement of the coded aperture across the supporting plate. Each location of the 169 cell tungsten aperture was examined by moving the aperture across the grid, where each location was exposed to the radioactive source for 5 minutes, before moving on to the next cell.

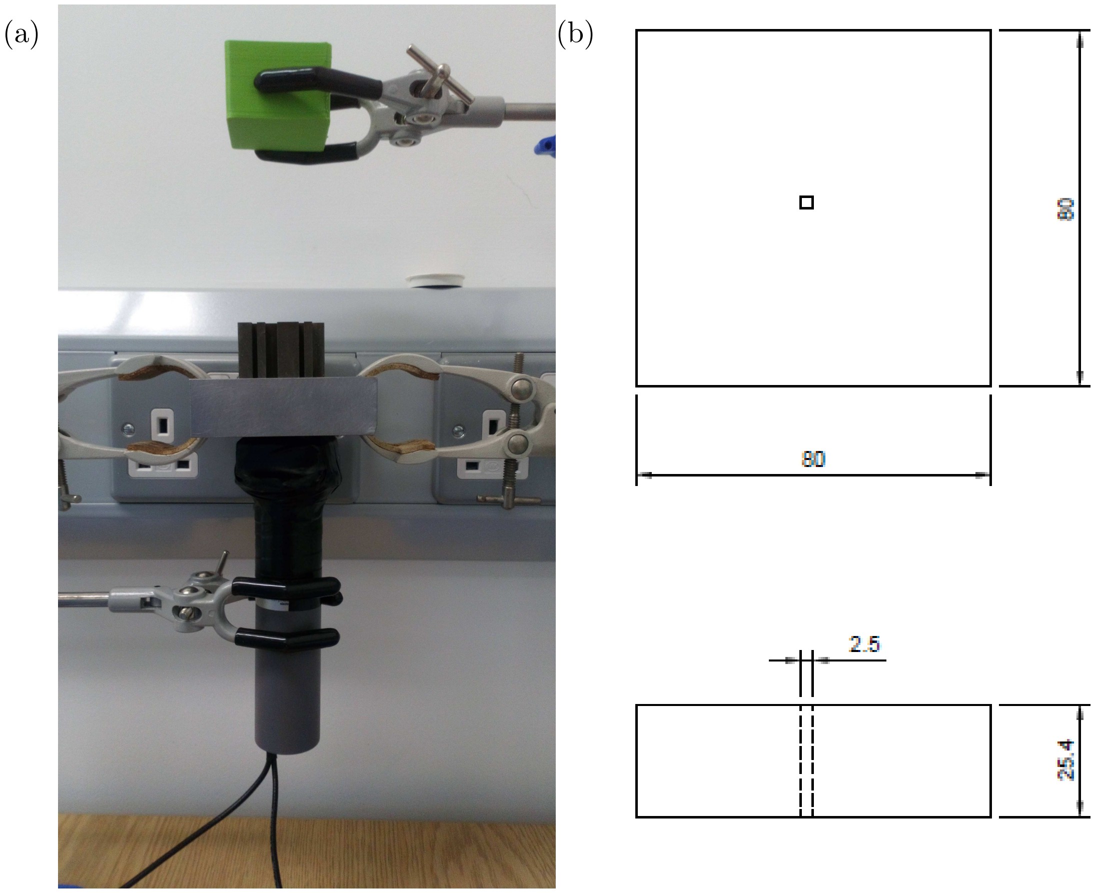

Figure 7.4: Equipment used in the experiment showing a) the entire experimental set-up comprising PMT and scintillator assembly, supporting lead plate, tungsten coded aperture, and source holder, and b) perspective CAD drawing of the supporting plate, with dimensions specified (mm).

7.4 Results

Before the first measurements of the ^{137}Cs modulated gamma-ray field were taken, the complete experimental set-up was tested without the coded aperture on top of the lead plate. This was used as an example to verify the energy spectrum obtained after 5 min exposure. Figure 7.5 shows that the ^{137}Cs Compton edge can be clearly identified. In this 5 minute exposure window, 9315 pulses were detected. When completed, the aperture was placed back on top of the supporting plate and the measurement of the first location of the coded aperture was taken. The detector set-up was exposed for 5 minutes in this location, before the aperture was in turn moved to each of the remaining 168 locations.

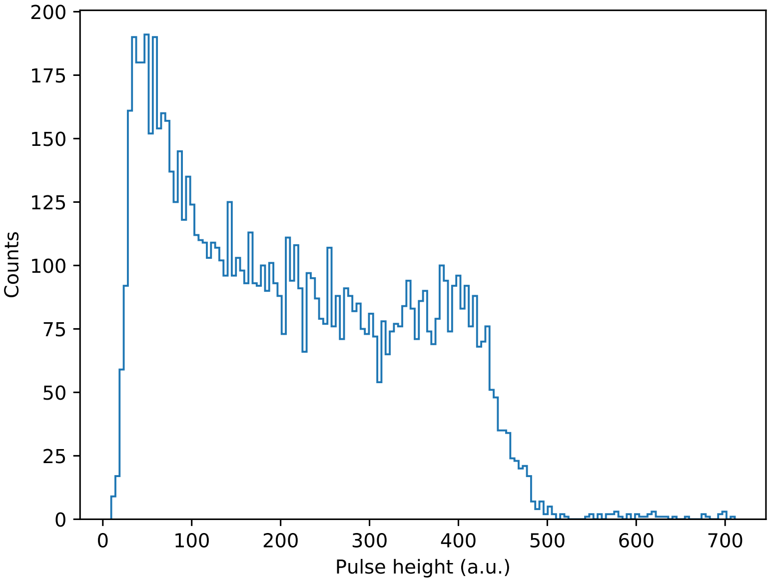

Figure 7.5: Pulse height spectra of ^{137}Cs, obtained by exposing of the source in the experimental set-up, but without the coded aperture in place. Measurements were taken over a 5 min exposure window.

7.4.1 Modulation properties of tungsten coded aperture

The collected data were arranged into a two dimensional array. Overall, 613,998 pulses were accepted through the pile-up rejection algorithm. The lowest count was around 1500 pulses, and the highest count over 9000 pulses. The lowest count corresponds to the area of the aperture where the cell under investigation is surrounded by opaque cells. The highest count was recorded in a clear area in the corner of the aperture where the transparent cell is also surrounded by transparent cells. The modulation image of the data is shown in Figure 7.6b in comparison to the manufactured coded aperture shown in Figure 7.6a.

It can be noticed that the modulation image in Figure 7.6 does not fully correspond to the aperture design presented in Figure 7.1. Opaque and transparent

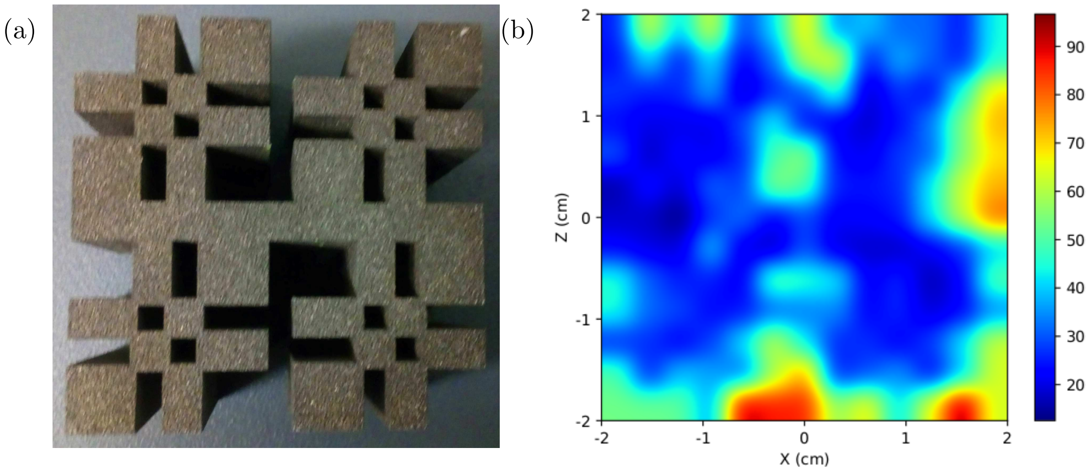

Figure 7.6: Comparison of a) the manufactured coded aperture with the overall dimensions of 39.52 × 39.52 mm^2, and b) Image obtained based on the data received when the coded aperture was exposed to ^{137}Cs and moved across the supporting plate to access its modulation properties. Colourbar values correspond to number of counts.

elements of the aperture are very difficult to distinguish and the overall pattern is equally difficult to recognise. However, some trends can be noticed. The areas of the image with the highest number of counts, i.e. approximately between 7000 and 9000 counts, are accumulated around the area where the single open aperture cells are not bounded by closed cells.

Counts between approximately 4000 and 6000 are associated with the areas of the aperture where there are only single cell or larger opening areas, for instance the area very close to the centre of the image, but these areas are surrounded by closed spaces. This indicates that the modulation provided by the closed areas of the coded aperture affects the neighbouring open spaces, as a result of gamma-ray interactions with the tungsten aperture blocks. Finally, the lowest count numbers (<4000) can be linked to the closed areas of the aperture. Hence, despite the fact that a quick visual inspection does not seem to resemble the design, closer examination does allow us to recognise useful patterns, including parts of the main body of the aperture.

7.4.2 Coded-aperture image reconstruction

According to the rules of designing a coded aperture based on MURAs, an image detected by the sensitive detector is encoded through the aperture pattern. Therefore, the reconstruction process takes longer, when compared to other imaging methods, such as single pinhole collimator based detectors. However, the advantage is that the resolution of the reconstructed image is higher. The method responsible for encoding the image in MURA based apertures is convolution. Consequently, the decoding of the image is achieved by deconvolution methods. A response for such analysis is expected to approximate the delta function [11].

Localisation of the ^{137}Cs source has been performed using a customised square deconvolution script implemented in Python. Initial inspection of the reconstructed image in Figure 7.7 clearly indicates that the source was recognised in the centre of the aperture. This result has been obtained despite the imperfect modulation provided by the aperture indicated by Figure 7.6. However, there is a noticeable spread of the reconstructed source over three cells of the aperture located in the centre of the reconstructed image. This suggests that the response is not in a form of a perfect delta function, as there are three impulses normalised to unity. This result is also indicated by the colourbar in Figure 7.7.

It should also be noted that the illustrative results presented above have been obtained using a very specific experimental set-up, which was primarily designed for the analysis of aperture modulation properties. An additional aim was to verify the operation of the decoding algorithm. Given the basic assumptions of the design and implementation of the coded-aperture imaging systems based on MURAs, a nearly perfect response, following the decoding, can be expected. A response approximating a delta function can only be obtained, if nearly perfect encoding occurs. Also the source must be reconstructed through the specific algorithm, which accounts for the pattern of the aperture used. In this work, the encoding of the radioactive source was of acceptable quality. However, the arrangement was sufficient for the deconvolution algorithm to place the reconstructed image in the centre of the aperture, as required.

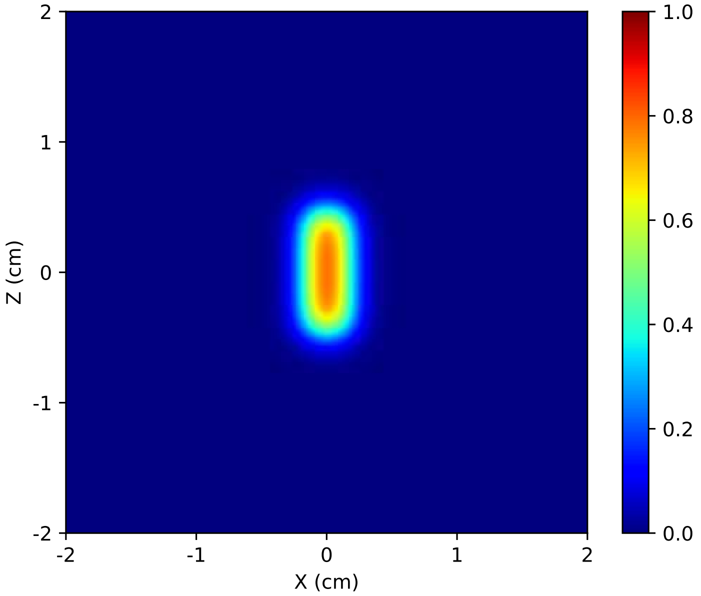

Figure 7.7: Reconstructed location of the source using deconvolution encoding. The image was obtained based on the data collected for each aperture location and arranged into a 13 × 13 array.

7.5 Discussion

The results presented in the previous section suggest that a pure tungsten coded aperture, with a small cell size $2.8 \times 2.8 \times 25$ mm^3, provide sufficient modulation of the gamma-ray field to reconstruct the source location. It could be argued that the localisation is not ideal, even though the the aperture was tested cell by cell, enabling the highest gamma-ray yield to be produced for every investigated cell directly. However, the results show the source on the expected location, and the spread over the three cells lies within standard statistical error boundaries.

Given the set-up chosen for this particular study, there is a small chance of some gamma-ray photons interacting with lead atoms in the supporting block. These can travel from the source, through any open area of the coded aperture, even those that are not investigated at a specific time. Hence, they could be accidentally detected by the scintillator detector. In a similar way, particles modulated through the aperture could still travel through the Pb block, and contribute to adding misclassified counts to specific cells. It is believed such interference caused the image in Figure 7.6 to not fully represent the shape of the coded aperture.

Although the coded aperture examined in this study is eventually aimed for operation in mixed radiation fields, it was decided to initially examine the system in a single particle radiation field, as reported in this article. Since the ^{137}Cs radioactive isotope is widely used for detector calibration, it was used in this study to determine if the results of 5 min exposures of a single aperture cell were sufficient to reconstruct the expected gamma-ray spectrum. If this was not achieved, the experiment for the specific cell was repeated.

7.6 Conclusions

Given the results and discussion presented, it can by deduced that the tungsten coded aperture investigated in this work provides a sufficient level of gamma-ray modulation. As such, it offers the possibility of incorporating the aperture into a portable mixed-field radiation imaging system, owing to the small size of the part. Moreover, in comparison with the part designed for simulation work (Figure 7.1a), the manufactured tungsten aperture does not have a bracket around its main body (Figure 7.1b). This change was dictated by the possibility of placing the aperture in an enclosure [203], which would allow for adjustment of the field of view (FOV) depending on the specific requirements of an application.

The plastic organic scintillator used in this study offers a very good neutron/gamma separation down to 40 keVee. This provides an opportunity to use the system as a single- or dual-particle detection device. The second particle type could be either ignored or included, and secondary imaging provided for the other particle type. It would also become possible to have more coded apertures manufactured using different materials, such as the aforementioned ^{113}Cd, to target other particle types, given the replaceable character of the aperture. Finally, it would also be advantageous to test the tungsten coded aperture in a mixed-field environment, to appraise if the neutron modulation level is sufficient.

In future work, it is also intended to replace the single block scintillation detector with a pixelated form of an organic plastic scnitillator. Such a scintillator has already been manufactured and is currently being characterised [44]. Moreover, various photodetectors and the accompanying readout electronics options are being considered, ranging from the standard mutli-anode photomultiplier tubes (PMTs) to pixelated Silicon Photomultipliers (SiPMs). As a general rule, the former option offers better noisy immunity, whereas the latter offers a small footprint and is easier to implement in the system, since it does not require high voltage supply to operate. Both options have been extensively compared with regard to time resolution and PSD capabilities [183, 204].

Chapter 8

Pulse shape discrimination performance of a pixelated plastic scintillator (EJ-299-34) for a coded-aperture based dual particle imaging system

Cieslak, M.J., Gamage, K.A.A., Glover, R., Taylor C.J.

Published in Journal of Instrumentation, 31st July 2019

8.1 Abstract

The pulse shape discrimination performance of a pixelated organic plastic scintillator has been investigated. The scintillator has been built using 169 plastic scintillator blocks (arranged into a 13 × 13 square array) of 2.8 × 2.8 × 15 mm^3 each. The scintillator was coupled with a single-channel photomultiplier tube. The scintillator was exposed to a mixed-field environment provided by ^{252}Cf and its pulse shape discrimination capabilities are presented in this paper. Initial results revealed that a 150 MS/s digitising system was insufficient to separate neutrons from gamma-ray photons. Therefore, the experiment was repeated with a 500 MS/s system, which provided improved pulse shape discrimination perfor-

mance. In order to validate the performance of the pixelated plastic scintillator, it was compared to that of a cylindrical plastic sample. Tests were also carried out in moderated neutron and gamma-ray fields of ^{252}Cf. The results indicate that acceptable levels of pulse shape discrimination are obtained for the case of a pixelated scintillator, when the higher sampling rate digitiser was used.

8.2 Introduction

Efficient and effective methods of radiation detection and imaging are highly desirable in numerous application areas, such as nuclear medicine, nuclear power generation, nuclear proliferation, nuclear decontamination and decommissioning. Depending on the information that is sought, different detection methods can be applied. For instance, X-ray imaging can be utilised for detecting the metallic parts of an item under investigation. However, if neutron imaging is applied to investigate the same item, the plastic parts of the item can be explored [205]. This is because distinctive targets interact in different ways as a result of exposure to varying radiation fields. Hence, combined X-ray and neutron imaging could provide a complementary solution for border control systems.

In a similar way, various radiation types are used in medicine e.g. ^{99m}Tc can be used to detect cancerous cells in a patient's body. As ^{99m}Tc is a human made gamma-ray emitter, it produces a specific gamma-ray field (photon energy of 140 keV) that can be detected using an appropriate gamma-ray imaging system. As its half-life is only 6.0058 hours, this approach allows enough time to produce an image of a patient's body and to track cancerous cells. Furthermore, its exposure time is short enough to keep the patient's absorbed dose low [206]. This is an example of a very specific application of radiation imaging i.e. when the produced radiation field is known.

For the application areas described above, in most cases the expected radiation field to be detected is known, whereas for nuclear decontamination and decommissioning applications it is generally unknown. During this final stage of a nuclear power plant's life, the local infrastructure, as well as the surrounding grounds, are required to be characterised in order to restore the area to a safe state. It is often difficult to judge what type of radiation, or specific spectrum of a certain radiation type, would be envisaged in a particular area. The information required to infer the type of radioactive isotope is often found in its gamma-ray or neutron spectrum [19]. Hence, it is beneficial to understand whether traces of these radiation types are present in the area of investigation.

8.2.1 Scintillator based detectors used in nuclear decommissioning applications

Particle detectors suitable for nuclear decommissioning applications of mixed-field characterisation are required to be sensitive to both neutrons and gamma-ray photons. Over the years, organic liquid scintillators have been established as one of the most popular choices for mixed-field applications [184, 207]. This is primarily due to their good neutron/gamma-ray separation quality and reasonable spectroscopic response. However, they are only sensitive to fast neutrons. Moreover, liquid scintillators are characterised by high toxicity, and some cocktails also have a low flashpoint [164]. Hence, they are often inappropriate for use in sensitive industrial environments, such as nuclear decommissioning facilities.

Such limitations have been gradually addressed by research into plastic organic scintillators. These detectors are not toxic and the risk of spillage is fully alleviated. However, only recently has a plastic scintillator been developed whose pulse shape discrimination (PSD) performance is comparable to an EJ-309 liquid detector [13]. Furthermore, in a similar manner to organic liquids, plastic scintillators have been doped with ^{10}B and ^{6}Li to allow thermal neutron detection [208, 159]. Plastic scintillators can also be straightforwardly formed into array blocks. However, in regard to PSD performance, stilbene crystal is far superior when compared to liquid and plastic scintillators.

Stilbene and anthracene represent some of the oldest scintillation crystals that have been widely used. Stilbene has been broadly recognised as the preferred choice in neutron/gamma separation applications, due to its high particle discrimination quality. However, the crystal was difficult to grow and its production was only viable in small sizes ($<$ 10 cm) until recently [19]. A relatively new method of growing the crystal has enabled researchers to go beyond the 10 cm limit and improve its light output [122]. Continuous improvements have led the stilbene crystal to offer far superior PSD performance when compared to plastic and liquid counterparts [12]. The manufacturing cost is however still high which makes building large stilbene detectors very expensive.

In order to improve the sensitivity of the detector across a greater energy spectrum, new methods of particle detection are sought. One of the recently proposed methods is a composite detector, where Cs_2LiYCl_6(CLYC), which is characterised by an excellent energy response and thermal neutron detection, is incorporated into a PSD capable plastic scintillator [209]. Such a scintillator is capable of separating thermal and fast neutrons, as well as gamma-ray events, that are induced in both the plastic and CLYC scintillators [141]. The downside of this approach lies in the detector size, as the composite is required to be sufficiently large so as to incorporate the inorganic scintillator inside.

Unfortunately, a large detector size is often a problem when nuclear decommissioning applications are considered. The areas to be interrogated are likely to be difficult to access and the space available for equipment deployment is scarce. Therefore, in the present article, we present some initial characterisation results of a small scale pixelated organic plastic scintillator (EJ-299-34). The overall dimensions of the scintillator, $39.52 \times 39.52 \times 15$ mm^3, make it suitable for the intended application. Furthermore, the pixelated design, as well as a single pixel size of $2.8 \times 2.8 \times 15$ mm^3, allows the scintillator to be matched to readily available pixelated photo detectors; in particular, a Position Sensitive Photomultiplier Tube (PSPMT) or a Silicon Photomultiplier (SiPM) can be utilised. Given the dimensions of the scintillator's single pixel, a one-to-one match can be found for the plastic scintillator. This characteristic is of vital importance when a sensitive detector is considered for coded-aperture based applications, as here.

8.2.2 Coded-aperture based radiation detectors

Coded-aperture based imaging is used to enhance the resolution of the reconstructed image, in comparison to conventional radiation imaging approaches, such as use of single opening collimators. As evidenced through extensive research conducted with gamma-ray detectors, higher lateral resolution allows the exposure time to be reduced [93]. However, in order to exploit the potential of a coded-aperture based approach, the location of the interaction within the scintillator must be reliably inferred. In particular, the direct matching of the pixel size between the scintillator and the photodetector can improve the process of interaction localisation.

Single particle detectors (X-ray and gamma-ray) utilising coded-aperture imaging methods have been thoroughly investigated [63, 210, 211]. A range of readily available pixelated inorganic scintillators, such as the CsI(Tl) scintillator, provide excellent energy resolution and can also be used to improve the spatial resolution due to their pixelated design [212]. There have been attempts to use pixelated detectors for fast neutron detection [74, 200]. However, the latter designs are based on a large scale approach and are not practical for nuclear decommissioning applications, which require more easily portable and deployable systems. Moreover, the systems described by references [74, 200] do not follow a one-to-one approach in regard to scintillator pixel and photodetector pixel dimensions.

8.2.3 Organic pixelated plastic scintillator EJ-299-34

The present article considers the suitability of the EJ-299-34 (produced by Eljen Technology) scintillator for neutron/gamma detection using PSD, based on experimental work performed with a ^{252}Cf radioactive source. Various digitising systems are used to comprehensively investigate the requirements of this novel scintillator. In particular, following on from previously performed work with FPGA based 150 MS/s and 500 MS/s digitising systems [203], these two devices were similarly used to analyse PSD performance here. To the authors knowledge, this is the first time that an analysis of the PSD performance of an organic pixelated plastic scintillator of this size scale has been reported. The scintillator was designed so that it can match currently available pixelated photodetectors, such as the Hamamatsu H9500 PSPMTs or SensL series-J SiPMs. It was further customised to address a previously performed MCNP based simulation study of the coded-aperture based neutron/gamma imaging system [156]. The pixelated scintillator comprises 169 scintillator blocks arranged into a 13 × 13 array, as shown in Figure 8.1. All the scintillator blocks are optically isolated from one another through ^{TM}ESR reflective tape to provide up to 98% isolation.

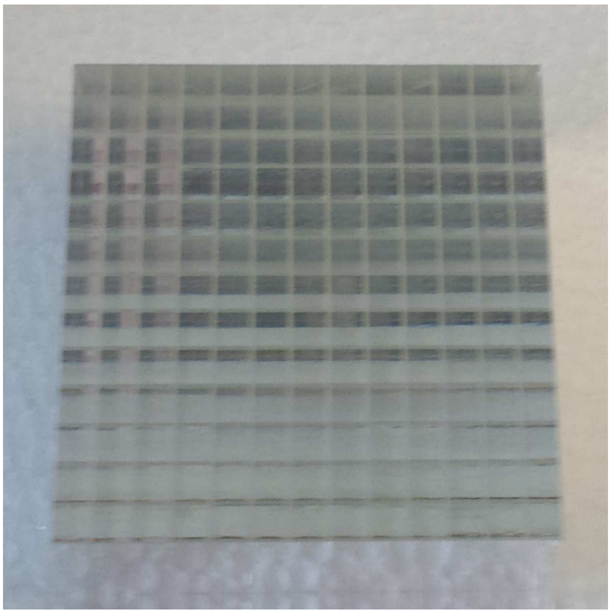

Figure 8.1: Organic pixelated plastic scintillator (EJ-299-34). There are 169 scintillator blocks of 2.8 × 2.8 × 15 mm^3, arranged into a 13 × 13 array.

Hence, a key objective of the present work is to assess the particle separation capability of the pixelated plastic scintillator (EJ-299-34), based on experimental work performed at Lancaster University, UK. A second contribution is the comparison of the scintillator's PSD performance in regard to the sampling frequency of the digitiser. For this purpose, FPGA based digitiser systems of different sampling frequency were used – 150 MS/s and 500 MS/s. In each case, the performance of the digitiser was verified with a cylindrical PSD plastic scintillator sample obtained from LLNL in 2016, which was previously tested [203]. Section 8.3 describes the methodology and materials utilised in this work. This is followed in section 8.4 by presentation of the results. The findings are discussed in section 8.5, with the conclusions presented in section 8.6.

8.3 Methodology

Both neutrons and gamma-ray photons are examples of uncharged particles. Hence, they do not undergo Coulomb interactions with electrons in materials. In organic scintillators, they interact primarily with ^{1}H atoms through elastic scattering with a proton (neutrons), and Compton scattering with an atomic electron (gamma-ray photons). Each of these interactions result in a fluorescence emitted in the scintillator that is proportional to the rate of energy loss of the interacting particle. The fluorescence emitted can be subsequently detected via a suitable photodetector, which produces pulses that reflect the particle's rate of energy loss. The difference in the pulse shape can be exploited to separate gamma-ray interactions from neutron events via PSD techniques [203].

There are numerous PSD methods that can be implemented in the digital domain [27, 213]. However, the most popularly used technique is a charge comparison method (CCM) that was originally implemented in the analogue domain [106]. It relies on the integration of the pulse over two specific intervals. The first integral (I_{long}) is calculated over the entirety of the pulse, and the second integral (I_{short}) is calculated over a specific period of the tail of the pulse, as the difference between the pulses is most pronounced in this region. Graphical illustration of this method is presented in Figure 8.2.

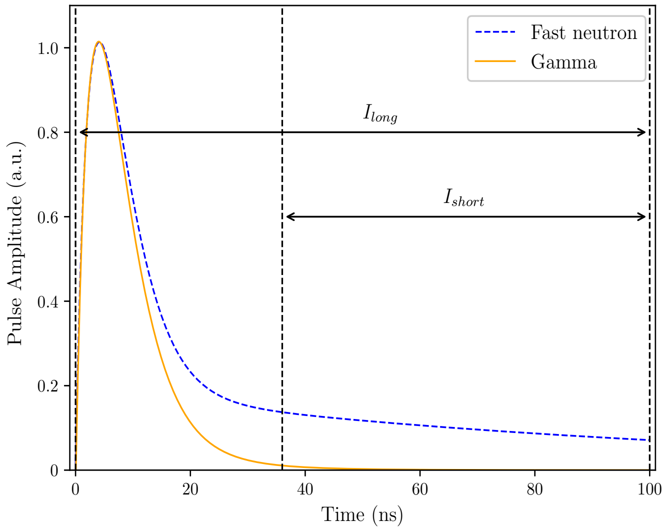

Figure 8.2: Illustration of the implementation of the pulse shape discrimination method used in this study. Long and short integrals used in CCM calculations are marked on the plot. Theoretical fast neutron and gamma-ray pulses were obtained based on the data from Knoll [19] and Zaitseva et. al [159].

The scintillator used in this study was based on organic pixelated plastic provided by Eljen Technology. The outer dimensions of the scintillator are 39.52 × 39.52 × 15 mm^3. The scintillator was subsequently coupled to an ET Enterprises 9107B photomultiplier tube (PMT). As the diameter of the PMT (25 mm) is smaller the outer dimensions of the pixelated plastic, appropriate light guide and EJ-550 silicone grease were used to provide optimal photon transfer. The PMT's sensitive area was placed at the centre of the pixelated plastic sample. A light-proof enclosure was placed around the scintillator-PMT assembly. The PMT was connected to a positive high voltage power supply of 850 V.

The assembly comprising the scintillator and the PMT was connected in turn to two FPGA based digitisers to infer its PSD potential. The first experiment was performed with a 14-bit resolution, 150 MS/s "raw data" digitiser. This collected 28 samples for every triggered pulse (every 6.67 ns). It was subsequently replaced with a 12-bit resolution, 500 MS/s "raw data" digitiser, which collected 128 samples (every 2 ns) for every triggered pulse.

The PSD capabilities of the scintillator were assessed using a ^{252}Cf fission source that is normally stored in the centre of a water filled steel tank. The source is pneumatically moved to towards the edge of the tank and is placed approximately 20 cm away from the edge, when in an exposed position. The detector assembly (scintillator-PMT) was placed 15 cm away from the edge of the water tank, resulting in a total distance of 35 cm between the source and the front of the detector.

The same equipment (PMT, digitisers) and facilities were used to take measurements using the cylindrical plastic PSD sample. The sample (25 mm diameter, 25 mm thickness) was developed at the Lawrence Livermore National Laboratory (LLNL), U.S.A. – denoted by the LLNL number 5706. The results obtained with this sample were contrasted with those of the pixelated scintillator. Further information about this research sample can be found in authors' preceding work [214].

In subsequent experiments, three different modulation scenario were tested. Firstly, a 5 cm thick modulation block made of lead was placed adjacent to the tank (as illustrated in Figure 8.3), so that the single particle sensitivity of the detectors could be evaluated. The thickness of the lead block was then increased to 10 cm to further block the gamma-ray field of ^{252}Cf. The final experiment was performed with a 9 cm thick high density polyethylene (HDPE) block placed adjacent to the tank in order to modulate the neutron field. In each case, the detector was exposed to the radioactive field for 30 minutes.

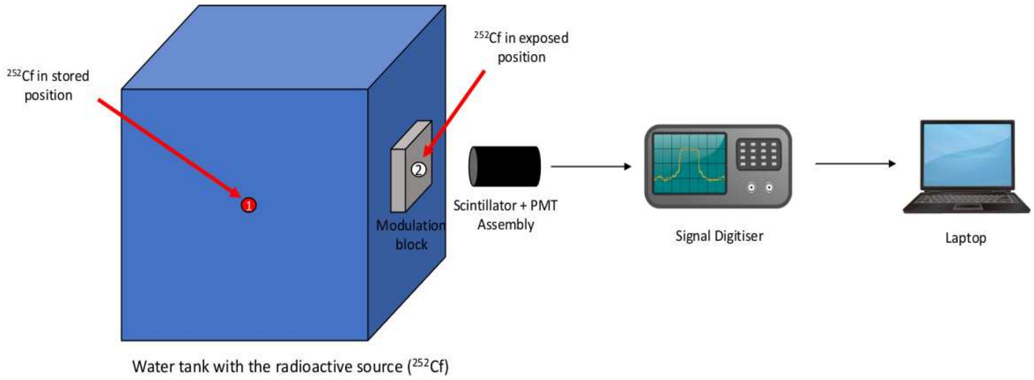

Figure 8.3: Schematic diagram of the experimental set-up. ^{252}Cf source is in the centre of a water-filled steel tank (position 1). During the experiments the source is moved to the edge of the tank (position 2).

8.4 Results

Initially both plastic scintillators were linked to the FPGA based 150 MS/s signal digitiser to collect the data. Each triggered pulse was processed through a bespoke pile-up rejection algorithm, where pulses with two peaks occurring within the same trigger window were rejected. There were 68,368 pulses accepted for the pixelated plastic sample and 80,955 for the cylindrical sample. Accepted pulses were used to plot CCM scatter plots as presented in Figure 8.4, where (I_{short}) is depicted on the y-axis and (I_{long}) is depicted on the x-axis.

It can be noticed that only the PSD plastic sample (Figure 8.4b) is capable of separating the neutron events from gamma-ray photons interactions. Therefore, further quality assessment of particle separation is only considered for the PSD plastic sample, since the pixelated plastic scintillator sample is deemed not capable of performing neutron/gamma discrimination when the 150 MS/s digitiser is used for data collection.

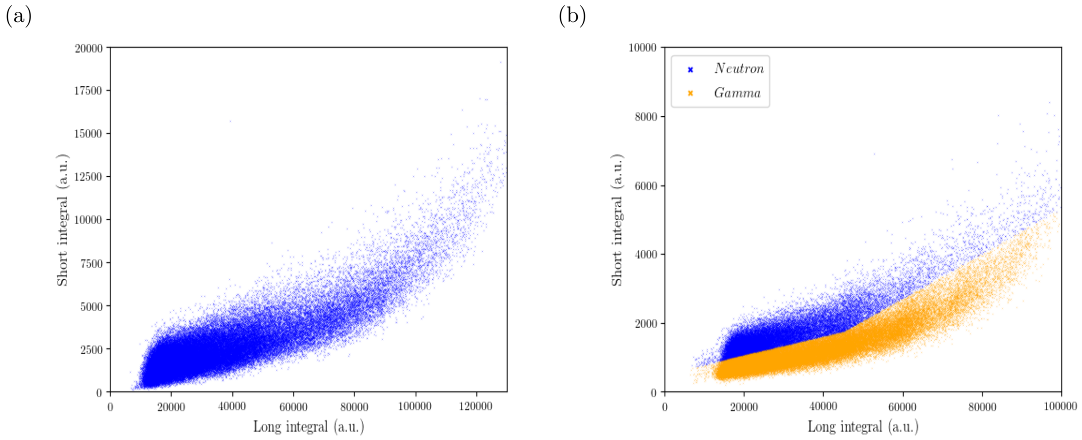

Figure 8.4: Comparison of CCM plots for the two plastic samples when exposed to ^{252}Cf and data were collected with 150 MS/s digitiser: a) Pixelated plastic and b) Cylindrical PSD Plastic from LLNL.

Following a similar procedure, the scintillator and PMT assemblies were subsequently tested with the FPGA based 500 MS/s digitiser. Each triggered pulse was processed through the same rejection algorithm. There were 70,485 pulses accepted for the pixelated plastic scintillator, and 120,213 accepted for the cylindrical sample. Particle separation was also performed using CCM, as described above, and the resulting scatter plots are presented in Figure 8.5.

In comparison to the results presented for the 150 MS/s digitiser (Figure 8.4a), a significant improvement of PSD performance can be observed for the corresponding pixelated plastic scintillator plot when the 500 MS/s digitiser was used (Figure 8.5a). However, it is still far inferior to the results obtained with the cylindrical sample. Nonetheless, it is deemed sufficient to be included in the separation quality analysis discussed in the following subsection.

8.4.1 Separation quality of each detector

The same data (i.e. as used to compose the scatter plots in Figure 8.4 and Figure 8.5) were used to assess the separation quality of each detector and signal digitiser arrangement. The figure-of-merit (FOM), as defined by Equation 8.1, was calculated for each case where the apparent separation quality was sufficient to meaningfully compare their performance. Neutron and gamma-ray events were separated through a discrimination line, as visible to the naked eye [27, 203], and

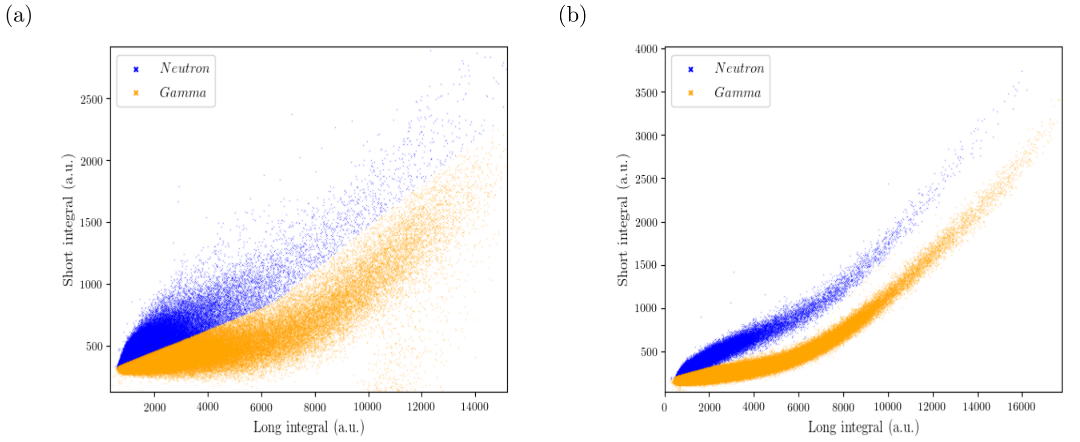

Figure 8.5: Comparison of CCM plots for the two plastic samples when exposed to ^{252}Cf and data were collected with 500 MS/s digitiser: a) Pixelated plastic and b) Cylindrical PSD Plastic from LLNL.

were subsequently used to compose the coloured scatter PSD plots.

$$\text{FOM} = \frac{\text{Peak separation}}{FWHM_g + FWHM_n} \tag{8.1}$$

Peak separation in Equation 8.1 represents the distance between the peaks of the normal distribution fitting of neutron and gamma-ray plumes, while FWHM represents the full-width at half-maximum for each particle distribution. A Poisson approximation of the distribution was assumed in order to determine the corresponding uncertainty. Illustrative neutron and gamma-ray distribution plots in regard to the discrimination line are presented in Figure 8.6, where the peak separation and FWHM for gamma-rays ($FWHM_g$) and neutrons ($FWHM_n$) are also shown.

The normal distribution fittings of neutron and gamma-ray plumes for the plots presented in Figure 8.5, where data were collected using 500 MS/s digitiser, are presented in 8.7. As expected, the distributions in 8.7a are more widely spread across the distance from the distribution line when compared to the corresponding distribution in 8.7b. As a result, the number of counts for the PSD plastic is considerably higher, as the distribution is more condensed. This is in contrast to the lower number of counts for the pixelated plastic where the distance between the separation line and coordinates of the particle pulse is more varied. Moreover, there is always a level of misclassification probability which needs to be assumed

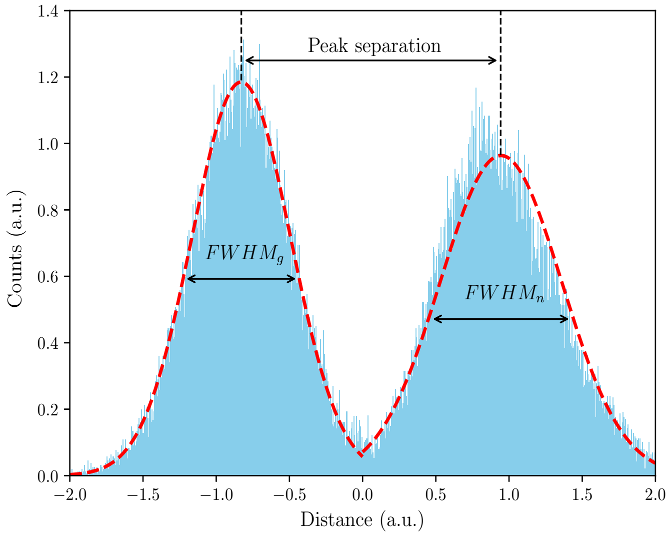

Figure 8.6: Example neutron and gamma-ray distribution in relation to the discrimination line, with the components of Equation 8.1 highlighted. Data taken from 5.7 in Chapter 5.

for the lower energy region.

The FOM values, together with corresponding statistical uncertainties calculated at the 95% confidence level, are presented in Table 8.1. As the performance of the pixelated plastic scintillator with the 150 MS/s digitiser was insufficient to assume particle separation, FOM for this arrangement was not estimated. The FOM estimation results presented in Table 8.1 reflect the relative quality of particle separation, as indicated qualitatively in Figure 8.4 and Figure 8.5. Despite the considerably lower FOM value in comparison to that of the cylindrical sample, the pixelated plastic scintillator in fact represents reasonable PSD performance in absolute terms. It should be noted that the pixelated scintillator was built in 2017 using Eljen Technology's old type PSD plastic EJ-299-34.

8.4.2 Pixelated scintillator performance with modulated neutron and gamma-ray fields

Based on the results presented above, it is apparent that the pixelated plastic scintillator (EJ-299-34) does not provide a clear neutron/gamma separation and

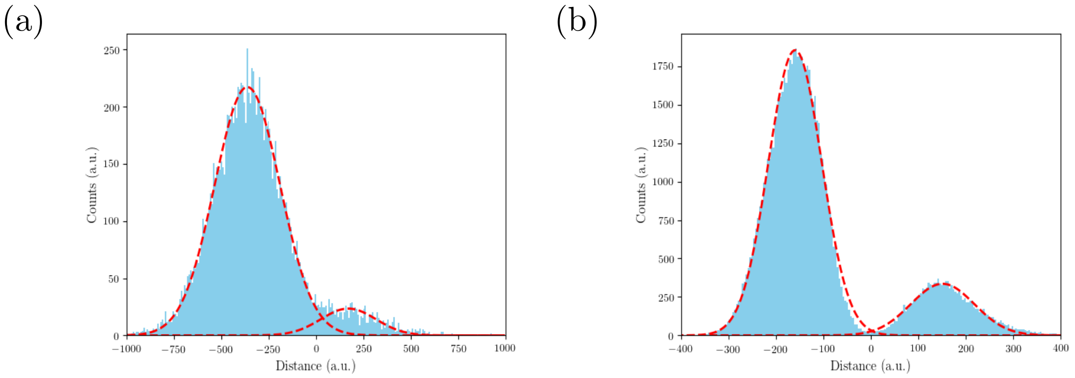

Figure 8.7: Comparison of neutron and gamma-ray distribution plots for the two plastic scintillators when exposed to ^{252}Cf and data were collected with 500 MS/s digitiser: a) Pixelated plastic and b) Cylindrical PSD plastic from LLNL.

Table 8.1: FOM values determined for each scintillator for the two digitisers used in this study.

Sample	Digitiser	FOM
PSD Plastic	150 MS/s	0.592 ± 0.001
	500 MS/s	0.637 ± 0.002
Pixelated plastic	150 MS/s	-
	500 MS/s	0.479 ± 0.010

the misclassification probability can be relatively high. Many factors can contribute to the overall PSD performance of a scintillator based detector, such as the energy spectrum of the radioactive isotope, the digitising electronics and photodetector type. These issues will be further considered in the following section 8.5. However, in order to first illustrate the particle separation performance of the pixelated scintillator in more depth, the mixed-field environment provided by ^{252}Cf was modulated.

The following three scenarios were considered to observe the detector's response to the modulated neutron and gamma-ray fields. In the first scenario, a 5 cm thick lead block was placed adjacent to the tank, between the source and the detector assembly, to reduce the number of gamma-ray photons reaching the scintillator. The thickness of the lead modulating block was subsequently doubled to 10 cm. The results of each scenario in the form of PSD scatter plots are presented in Figure 8.8a and Figure 8.8b, respectively. In the final arrangement, the neutron field was modulated by placing a HDPE block, of thickness 9 cm, adjacent to the tank between the radioactive source and the detector. Figure 8.8c illustrates the results obtained for this scenario. Distribution of neutron and gamma-ray photons in relation to the discrimination line, for the case of HDPE modulation, is presented in Figure 8.8d. It can be observed that a negligible number of neutrons was able to pass through the HDPE block. For each scenario, the detector was exposed to the radioactive field of ^{252}Cf for a duration of 30 mins.

8.5 Discussion

The PSD potential of a bespoke pixelated scintillator was experimentally tested. Building on the authors' prior work, the particle separation capability of the scintillator was first investigated using a FPGA based 150 MS/s digitiser [203, 28]. However, in this case, the pixelated plastic sample failed to separate neutrons from gamma-ray photons (Figure 8.4a). Therefore, the performance of the digitiser was verified with a cylindrical PSD plastic scintillator sample, obtained from LLNL in 2016 and previously tested by the authors [203]. Results obtained with this cylindrical sample (Figure 8.4b) indicate considerably superior performance,

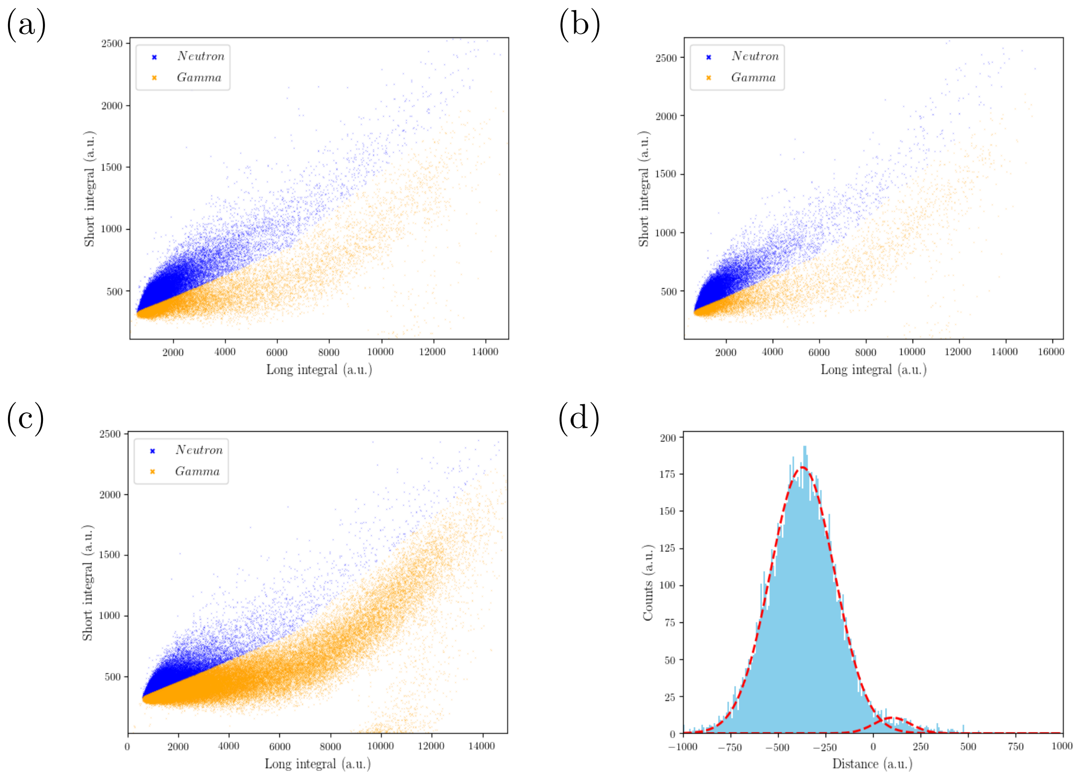

Figure 8.8: PSD scatter plots resulting from the exposure of the pixelated plastic scintillator detector to ^{252}Cf source with the following modulation type in place: (a) lead 5 cm, (b) lead 10 cm, (c) HDPE 9 cm and (d) neutron and gamma-ray distribution for HDPE modulated scenario.

when compared with the pixelated plastic.

Similar observations can be made for the experiments performed with a 500 MS/s digitiser. The pixelated plastic scintillator (EJ-299-34) shows considerably improved PSD performance when compared to the results obtained with the lower sampling rate digitiser. Although the estimated FOM of 0.479 is far from optimal, it was nonetheless possible to estimate FOM in this scenario, and the results demonstrate the promising PSD potential of the scintillator despite its small size and pixelated arrangement. As expected, the cylindrical research sample again shows improved PSD performance at this higher sampling rate, in comparison to the pixelated plastic sample, as evidenced by the FOM of 0.637 as well as Figure 8.5b and 8.7b.

Dependence of PSD performance on the sampling rate of the digitising electronics has been previously discussed in literature [37]. Furthermore, new methods applied in the frequency domain suggest that digitisers of relatively low sampling frequency may be sufficient to separate neutrons from gamma-rays, when the digital data is considered in the frequency domain [29]. The results presented in the present article suggest that there is a correlation between the sampling frequency of the digitiser and PSD performance measured using FOM, when PSD is performed in the time domain.

8.5.1 FOM as a measure of PSD performance

Particle separation performance between two particle types is often characterised by the FOM. It was first introduced by Winyard et al. [160], and further discussed by Knoll [19]. Although FOM is potentially a good measure of the separation quality, its value should be used with caution since its value depends on the experimental context. It depends strongly on the low energy threshold, at which point the energy gate is defined [215]. The majority of organic scintillators present the highest misclassification probability in the low energy regions, and this decreases as the energy rises. In the present study, the energy gating was not considered, as the FOM estimation was performed across the whole energy spectrum.

Another important factor, which emerges as a part of this work, is the dependence of the FOM on the sampling frequency of the digitiser, when PSD analysis is performed in the time domain. It appears that if the intrinsic particle separation of a scintillator is sufficient, even the low sampling digitiser can be capable of performing satisfactory PSD. This is evidenced by comparing the PSD plots shown for the cylindrical sample in Figure 8.4b and Figure 8.5b. However, when the inherent PSD capabilities of a scintillator are not sufficient, as in the case of the pixelated EJ-299-34 scintillator, increased sampling rate provides significant improvement in terms of particle separation (Figure 8.5a).

The estimated FOM value is also significantly impacted by the type of radioactive source used in a specific study, which is particularly important for organic scintillators aimed at fast neutron detection. The average energy of neutrons produced by the ^{252}Cf source is approximately 2.1-2.5 MeV, whereas neutrons produced by ^{241}AmBe average approximately 4.5 MeV. Moreover, the mixed field environment created by a radioisotope can be affected by the way it is stored. Since the neutron source used for the present work is stored in a water tank, the average energy spectrum of ^{252}Cf has been reduced to approximately 0.7-0.9 MeV [156]. This has further impact on the neutron/gamma separation in the low energy region.

Given the large number of factors contributing to the calculations of FOM, its value should always be interpreted on a case by case basis for specific research work or research environments. Many of the factors mentioned previously differ between research environments, and hence comparisons based purely on FOM do not reflect absolute differences between the quality of the results obtained.

8.5.2 Further assessment of the PSD quality in the pixelated plastic

As evidenced by the results presented in Figure 8.5a, there exists a misclassification probability between neutrons and gamma-ray photons in the pixelated plastic scintillator. In contrast to the equivalent results obtained with the cylindrical PSD sample (Figure 8.5b), there is no clear separation between the two particle types. There is noise present between the two plumes and the area of the lowest noise level was chosen to draw the separation line between the two particle types. As a single channel photodetector was used to collect the emitted fluorescence from a pixelated scintillator (where each block is optically isolated from one another), it is possible that the light collected in the photodetector is affected by interactions in more than one block of the scintillator.

Given the levels of noise present, the experiments performed with the pixelated plastic were repeated for three different scenarios when the ^{252}Cf mixed field environment was modulated. Firstly, the gamma-ray spectrum was modulated by placing 5 cm and 10 cm thick lead blocks adjacent to the tank between the source and the detector. The resulting plots are presented in Figure 8.8a and Figure 8.8b, respectively. As expected, the gamma-ray plume, which is presented in yellow, is significantly reduced in 8.8a and even more so in 8.8b.

Subsequently, 9 cm HDPE was used to modulate the neutron field, with the results presented in Figure 8.8c. This time, the concentration of neutrons in the area of low integral values ($I_{long} \sim 2000$, $I_{short} \sim 750$) is noticeably reduced. The neutron concentration is higher in this region for the plot presented in Figure 8.5a, where the results obtained with an unmodulated source are presented. With HDPE modulation, lower rates of neutron occurrences are also noticeable in the area of higher integral values ($I_{long} \sim 10000$, $I_{short} \sim 1500$). In a similar way the reduction of neutron count rate can be observed by the comparison of the distribution plots presented in 8.7a and 8.8d. There is a noticeable difference between the spread of neutron incidents across the distance axis as well as the number of counts, when the two plots are contrasted. The results discussed in this section further support the claim that the designed pixelated scintillator presents good PSD potential despite the intrinsically low PSD performance of the scintillator, when tested in this specific environment.

The neutron/gamma separation performance of EJ-299-34 has been previously assessed for larger scintillator blocks [216, 217]. The values of the estimated FOM quoted in these studies ($\sim$ 1.4–1.5) are considerably higher than the 0.479 reported in the present work. It should be noted that the testing conditions (radioactive source, digitiser, etc.) were different from one another, and from the scenario described in this paper. These earlier studies both utilised larger size scintillator blocks and the ratio of the number of photodetector channels to the number of pixels attached was smaller i.e. either 1:1 [200] or 1:16 [216].

It should also be mentioned that EJ-299-34 was originally described by Eljen Technology as a scintillator that was easier to form into array blocks due to the specific plastic content. Its PSD performance was deemed inferior to the EJ-299-33 plastic that was also available from Eljen at the same time, but not recommended for array applications. However, numerous studies have since shown that its PSD performance is relatively poor (especially in the low energy region) [218, 219], and remained inferior to equivalent liquid PSD capable scintillators [177]. It is, therefore, believed that the development of new plastics, whose PSD performance is comparable to liquid equivalents, would directly improve the performance of a small pixelated plastic scintillator, similar to the one presented in this work [13].

8.6 Conclusions

This article has reported on new experiments to investigate the PSD performance of a pixelated plastic scintillator. To the authors knowledge, this represents the first time that experimental results for the PSD of a pixelated plastic scintillator of this size have been presented. Despite the small size of individual pixels, the scintillator exhibits promising PSD results. It is believed that with improved inherent PSD for the scintillator material, the overall performance of a similarly designed scintillator would be further improved. In future research, therefore, it would be of great interest to test similar arrays built of the new plastic available from Eljen Technology (EJ-276).

It is also apparent that the photodetector used in this study does not provide optimal fluorescence collection for the pixelated plastic. As a single channel is responsible for light collection from the complete 13 × 13 array, there is a high probability of signal noise, due to interference from neighbouring pixels. It is, therefore, expected that replacing a single channel PMT with readily available pixelated photodetectors (PSPMT, SiPM) would help to alleviate these issues.

Moreover, with the advancement in the development of high speed digitisers, devices of 1 GS/s to 5 GS/s are now becoming available. Given the results obtained with the digitisers in this study, it is anticipated that an improved PSD would be observed, if higher sampling rate digitisers were used. It would also be advisable to gain more insight into the relationship between the particle separation quality and energy spectrum of the radioactive source. This could be tested by exposing the pixelated scintillator to other mixed-field environments, which provide different energy spectra, such as an unmoderated ^{252}Cf or ^{241}AmBe.

Chapter 9

Discussion and conclusions

9.1 Summary

In this thesis a new approach to coded aperture based neutron imaging has been designed, and the proof-of-concept instrument has been built and tested. To author's knowledge, it is the first time that pixelated plastic scintillator of this size has been successfully tested in regard to neutron detection through digital PSD techniques in near real-time.

During the literature review stage (chapter 3) of this project, several coded-aperture based neutron imaging systems have been identified [74, 41, 200] which are capable of neutron/gamma discrimination. Some of these devices utilise organic scintillators to detect fast neutrons via PSD methods [74, 200]. However, these are examples of large scale machines which would pose significant difficulties when attempting to deploy such devices on nuclear decommissioning sites. The small scale devices, as presented by Whitney et al. [41], are often based on inorganic crystal scintillators such as CLYC, which exploit the large thermal cross-section of ^{6}Li to detect thermal neutrons. Therefore, it is necessary to provide a moderator to detect fast neutrons. It should also be noted that inorganic crystals are considerably more expensive than organic plastics. Based on the experimental and simulation studies, presented in chapters 5, 6 and 8, it was shown that pixelated plastic scintillator provides reasonable PSD response.

Another area that was closely investigated at the beginning of the project was the material of the coded aperture. In accordance with the design rules, it is required that the material is chosen such that it either stops or reflects the incident particles. Tugsten collimators have been efficaciously used in similar applications for gamma-ray shielding purposes [220]. In the past, neutron shielding has been traditionally provided by high neutron cross-section isotopes such as ^{113}Cd, ^{154}Gd or HDPE. In this project, author has simulated (using MCNP code) various compositions of W-^{113}Cd as the potential candidate for the coded-aperture material. However, it proved impossible to have a coded aperture which would be built with ^{113}Cd, due to safety concerns related to handling of cadmium. Therefore, the aperture tested in this study was made purely of tungsten and results are presented in chapter 7.

Following the simulation work, as well as extensive literature review of possible sensitive detectors presented in chapters 3 and 4, experimental techniques have been employed to test block and pixelated solid organic scintillators, as described in chapters 5 and 8, respectively. Given the available solid organic scintillators and the testing performed, it was concluded that pure plastic scintillator from chapter 5 provides sufficient PSD performance for neutron detection. However, it was not possible to build a small scale pixelated detector using this material, as it was only a research sample at the time. Therefore, the pixelated scintillator was built of EJ-299-34. The results showing its PSD performance are presented in chapter 8.

Given the investigation of the main parts of the system, an overall potential of coded-aperture based approach to neutron detection has been presented. The main outcome of the thesis is the design of the small-scale pixelated plastic scintillator, which proposes a real advantage over more expensive, inorganic based devices, despite its relatively poor PSD performance.

Although only performed within gamma-ray field, the result of image reconstruction performed in chapter 7 is deemed to provide satisfactory outcome. The coded aperture constructed during this project was exposed to effectively constant gamma-ray field provided by ^{137}Cs. Given the rules of deconvolution filtering, the resulting image estimates the source to be spread over three aperture cells in centre of the aperture. Also, theoretical highest achievable resolution for this system could be estimated to 2.8 mm, dictated by the single aperture and scintillator cell dimensions.

9.2 Outlook

Existing coded-aperture imaging systems are primarily aimed at gamma-ray detection, due to established techniques and available scintillation materials. When compared with traditional single opening collimators, coded-aperture based devices not only improve the resolution of the image, but also allow to reduce the exposure time [94]. Devices used for neutron detection are either large scale [74] or relatively expensive, when focused around inorganic crystal such as CLYC [41] and semiconductor devices [201]. Another important aspect that needs to be taken into consideration is the aperture material, which is often decided by the incident particle type or energy spectrum of the targeted particle. Incident thermal neutrons may produce secondary radiation as a result of interaction with the coded aperture when, for instance, the aperture is made of ^{113}Cd. The overall gamma-ray count will be increased due to (n,γ) reaction in ^{113}Cd. Reliable PSD techniques allow gamma-ray background to either be rejected or utilised for dual-particle imaging [111, 41].

Nuclear imaging used in medical applications requires that the images produced are of highest possible resolution in order to, for instance, distinguish which parts of a human body are affected by cancer. Therefore, coded-aperture based gamma-ray imaging systems are often used in this setting to enhance spatial resolution [221]. Furthermore, traditional single opening collimators tend to require long time to perform scanning of large areas, especially in nuclear decommissioning applications, due to the limited FOV. Coded-aperture based approach allows FOV to be improved by increasing the number of small openings in the aperture. It can be also increased by implementing an adjustable coded aperture, where the aperture built as a part of this project can be moved within the enclosure. As such, the highest FOV can be achieved when the aperture is placed at the farthest point of the enclosure. It can then be gradually moved backwards to increase the FOV, when the overall system gets closer to the hot-spot.

The amount of radioactive waste at reprocessing plants such as Sellafield Ltd is constantly increasing. Therefore, the ability to reduce the time required to characterise the storage facilities would be highly beneficial. It is often unknown whether traces of specific radioactive isotopes are present in the waste. The ability to perform dual-particle imaging with a small-scale device could further reduce the time required to characterise the area under investigation, as the deployment time could be reduced. When complemented with appropriate photodetector and readout electronics, the system proposed in this thesis would meet these criteria.

In a similar way, neutron based cancer treatments such as Fast Neutron Therapy (FNT) and Boron Neutron Capture Therapy (BNCT) are gaining importance. They are capable of attacking tumours that are normally resistant to radiotherapy [222]. Unfortunately, it is often impossible to avoid affecting the healthy surrounding tissues. Therefore, small-scale, high resolution device capable of imaging the affected area of patient's body would be highly required to estimate the damage to healthy cells. A proof-of-concept study documented in this thesis presents a partial solution that could be easily adapted for such application.

Chapter 10

Future work

The proof-of-concept study of the scintillator based coded-aperture approach to neutron imaging presented in this thesis shows a good potential for adaptation in nuclear decommissioning applications. There are, however, areas where this concept system would benefit from improvements. These areas, together with suggested recommendations, are presented in this chapter.

10.1 Design changes

The system has been designed to utilise standard rank-7 MURA based coded-aperture pattern. The main reason behind this design was the ability to match the size of the aperture cell to the single pixel of the photodetector. However, with the advent of the latest commercially available SiPMs the pixel size can be reduced to an active area of 1 mm, and subsequently the theoretical spatial resolution increased. Furthermore, SiPMs offer the advantage of requiring considerably lower bias voltage to operate in comparison with PMTs, which reduces the overall volume of the detector system.

Although the changes outlined above would have profound effect on the overall resolution of the system, further reduction of the aperture dimensions may not be currently plausible. It would be beneficial from the viewpoint of the spatial resolution of the system to increase the rank of the aperture, which effectively increases the number of aperture cells. These could be designed to provide very high resolution, but manufacturing the aperture in tungsten using currently available techniques with very small elements can be problematic.

As the ^{113}Cd content of the aperture has not been realised due to safety issues, the thickness of the aperture could be further investigated. Currently implemented thickness of 25.4 mm could possibly be reduced, and a layer of HDPE could be added. This addition would provide neutron modulation layer that could realistically reduce the number of fast neutrons reaching the scintillator through the opaque elements of the aperture. However, further simulation work is required to decide the exact thickness of the aperture.

10.2 Scintillation detector

As the key element of the system, dimensions as well as material of the scintillation detector could be revised. The choice of the solid organic scintillator was restricted to commercially available plastics from Eljen Technology. Research sample obtained from LLNL was tested in 2016, and compared in terms of its PSD performance to other available solid organic options. This scintillator has now become a commercially available plastic scintillator EJ-276, whose PSD performance is comparable to that of the well-established EJ-309 liquid scintillator. It is therefore expected that replacing the material of the pixelated plastic scintillator would significantly improve system's ability to provide dual-particle detection operation.

Even though there are possibilities to reduce the dimensions of an individual pixel of the photodetector, it is unlikely that it would be feasible to make the dimensions of the scintillator cells smaller. This is primarily dictated by neutron mean free path, which decides how far a neutron needs to travel in a material before it undergoes an interaction. Therefore, it is likely that there would not be a direct match between the dimensions of the detector cell and the photodetector pixel. As a result, single scintillator dimensions could be maintained, but additional computational techniques may need to be required at the readout stage to infer the location of the interaction. Increasing the size of the scintillator would undoubtedly reduce the overall cost of the scintillator, but would introduce additional computational overhead.

10.3 Readout electronics

Readout electronics for the system has been also developed during this project. The development completed has been presented at two topical conferences and, the articles documenting the accomplished work have been published in the conference proceedings. Theses publications are attached to this thesis in appendix A and appendix B.

The work completed consisted of electronic simulation stage performed in LT-Spice and TINA simulation packages, where the resistive network capable of reducing the expected number of 169 pixels to four (two for each axis) signals was tested. Further reduction could be achieved in either analogue or digital domain which would enable to have one signal for each axis, and those signals could then be digitised to infer the location of the interaction within the 13 × 13 array. A double channel readout electronics based on an FPGA and two 150 MS/s ADC has been implemented, which would be capable of interpreting the signals obtained from the resistive network.

In line with the discussion section presented in chapter 8, 150 MS/s digitiser may not be able to provide sufficient PSD performance for the system. However, with the availability of the latest digitising solutions, it is now possible to obtain multi-channel (4) systems with up to 5 GS/s sampling rate. As such, the final reduction stage from 4 to 2 signals of the resistive network could be easily implemented in the digital domain without having an effect on the overall timing operation of the system.

10.4 Complete instrument testing

Key parts of the system have been tested, and provided strong support for the possibility of implementing a scintillator based coded-aperture small-scale pixelated approach to neutron and gamma-ray detection. It would be beneficial to perform further testing of the coded aperture presented in an unmoderated mixed-field environment (^{252}Cf, ^{241}AmBe). The final stage would see the complete instrument being tested in a real-life location such as Sellafield Ltd.

10.5 Medical applications

As previously hinted in chapter 9, small-scale devices capable of performing high resolution neutron detection could be relatively easily adopted in medical applications. With the increasing necessity of being able to observe the impact of BNCT and FNT on healthy tissues in human body, a device such as the one proposed could be customised (by changing the scintillation detector) to either target thermal or fast neutrons.

Appendix A

Design and development of a real-time readout electronics system to retrieve data from a square multi-anode photomultiplier tube for neutron gamma pulse shape discrimination.

Conference Paper presented at 20th IEEE-NPSS Real Time Conference 2016 - Padova, Italy, 5-10 June 2016

Design and Development of a Real-time Readout Electronics System to Retrieve Data from a Square Multi-anode Photomultiplier Tube for Neutron Gamma Pulse Shape Discrimination

Michal Cieslak, *Student Member, IEEE,* Kelum Gamage, *Member, IEEE,*

***Abstract*—Pulse Shape Discrimination (PSD) algorithms can reliably separate neutrons and gamma-ray photons interacting in a scintillation detector. When implemented in the digital domain, the PSD algorithms allow real-time discrimination between neutron and gamma sources. This paper presents a design of a readout electronics system to retrieve data from a multi-anode photomultiplier tube (MAPMT) for a scintillator based coded-aperture neutron imager. The scintillator is to be coupled with Hamamatsu H9500, a square MAPMT, where each anode of the MAPMT is linked to a resistor network to infer the position of incidence of radiation within the scintillant. Additionally, the resistor network output signals are to be filtered through a novel noise reduction circuit to preserve the data corresponding to each pulse. Localised pulses are digitised using high sampling rate Analogue to Digital Converter (ADC). Sampled signals are temporarily stored in a local ping-pong buffer, before being processed on a field programmable gate array (FPGA). Initial results suggest that 150 MSPS rate provides sufficient information for neutron gamma source discrimination using PSD. Parallel real-time signal processing, implemented on the FPGA, enables multi-channel functioning to generate an array of interactions within the scintillator in terms of gamma rays and neutrons.**

***Index Terms*—Pulse shape discrimination, Readout electronics, Coded-aperture, Neutron detection, Analogue to digital conversion.**

I. INTRODUCTION

SCINTILLATOR based radiation detectors have been successfully employed in application fields, such as nuclear medicine [1], [2], homeland security [3] and nuclear decommissioning [4], [5]. In each case, accurate localisation of the radioisotopes is of vital importance, since failing to do so would pose a threat to human lives. Although specific requirements may differ between implementations, each of the above application fields necessitates high signal-to-noise ratio (SNR), as well as spatial resolution of the results.

In a typical single anode scintillation counter the scintillator is optically coupled to a photomultiplier tube (PMT). The photocathode of the PMT transforms photons emitted by the scintillator to photoelectrons. The photoelectrons can then be counted via electronic systems connected to the anode of the PMT. These systems do not account for the position of interaction within the scintillator [6].

Recent research into anisotropic properties of crystalline scintillation materials suggest that some positional information can be inferred from the scintillator response [7]. The localisation of a particle interaction with the scintillant can also be achieved by replacing the PMT with a multi-anode photomultiplier tube (MAPMT).

Flat panel MAPMTs from Hamamatsu Photonics, such as H8500 [8] and H9500 [9], have replaced old type of cross-wire MAPMTs, substantially increasing the sensitive area of the similar size device. If coupled to a correct scintillator, they have shown superior spatial resolution performance, when used in gamma cameras [1], [2], [10], [11] and neutron detectors [12]. However, due to a high number of anodes, readout electronics circuits are required to provide sufficient filtering of the extracted signal, as well as cross-talk avoidance.

In this paper a design of a new readout electronics circuit for H9500 MAPMT aimed at neutron/gamma pulse shape discrimination (PSD) is discussed. The event localisation is based on resistive network approach [13] requiring a novel signal filtering implementation to preserve the data corresponding to each interaction within the scintillator. The X and Y coordinates are to be recorded and individual pixels identified. Signal from the inferred location is to be filtered through a band pass filter and amplified before connecting to a high speed analogue to digital converter (ADC).

II. RESISTIVE CHARGE DIVISION NETWORK

Flat panel MAPMT H9500 from Hamamatsu photonics has been successfully applied in high resolution gamma imaging systems, such as positron emission tomography (PET) and single photon emission computed tomography (SPECT) scanners [14]. The MAPMT's high number of pixels offers exceptional angular resolution when coupled to appropriately selected sensitive detector. However, multiple anodes present a challenge associated with retrieving a high number of signals simultaneously. The challenge has been directly addressed by the development of readout electronics for H8500 and H9500 MAPMTs [11], [15] in gamma cameras.

Each of H9500 MAPMT's 256 anodes is a 2.8 x 2.8 mm^2 square, offering a high resolution results when incorporated in gamma-rays and neutron localisation systems [12], [15]. The sensitive area of H9500 is built of 16 x 16 matrix of individual pixels and is equal to 49 x 49 mm^2. If the signal appearing

M. Cieslak and K. Gamage are with the Engineering Department, Lancaster University, Lancaster, LA1 4YW, UK, e-mail: (m.cieslak@lancaster.ac.uk and k.gamage@lancaster.ac.uk).

978-1-5090-2014-0/16$31.00 © 2016 IEEE

on the individual MAPMT's anode was to be processed independently, 256 ADC channels would be required to perform full analysis. The standard readout electronics circuit proposed by Popov and Majewski [15] reduces the number of required channels to 32. Additional circuitry can also be added to the standard readout electronics to further reduce the number of the output channels to 4 (2 channels in X direction and 2 channels in Y direction). A schematic diagram of the standard readout electronics is presented in Fig. 1.

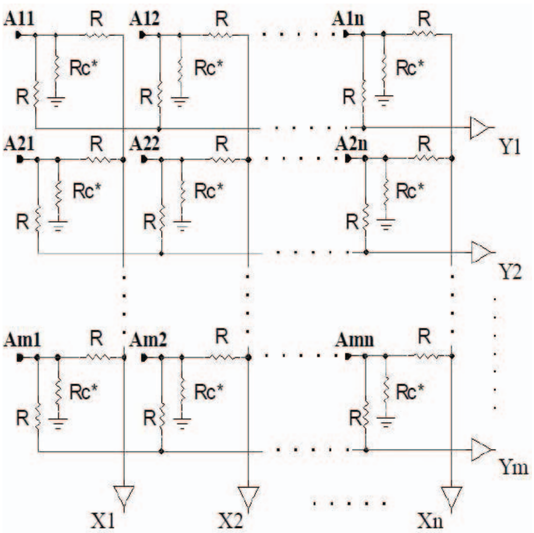

Fig. 1. Readout electronics circuit for 256 channels Hamamatsu H9500 MAPMT proposed by Popov and Majewski [15]

This method of positional data extraction has been successfully adapted in scintillator based high resolution gamma cameras. As crystal scintillators, such as NaI(Tl) and CsI(Tl), are sensitive exclusively to gamma-rays, number of interactions in a specific 2-D position can be counted, when light photons are detected on the anode of the MAPMT. Consequently, location of the gamma source can be detected with very high accuracy. It has been shown, that when tested with NaI(Tl) block scintillator, gamma ray interaction within an area of the single anode can be differentiated [15]. However, adaptation of the system for fast neutron imaging poses difficulties, as the scintillation detectors available are generally sensitive to both gamma-rays and neutrons.

Despite the difficulties, it was attempted to adopt the readout electronics circuit proposed by Popov and Majewski [15] for fast neutron radiography [12]. However, the system tested utilised EJ-200 plastic scintillator as a sensitive detector and was tested with D-D 2.5 MeV neutron generator. Although it showed accuracy of better than 0.5 mm in X and Y directions, its behaviour in mixed radiation environment cannot be assessed, as single radiation type environment was generated. Hence, further investigation and testing in mixed radiation fields would be required to fully evaluate the performance of the system.

In both cases (gamma and neutron detectors), the presented systems are only capable of detecting one type of radiation. Modern methods of fast neutron detection utilise PSD capable organic scintillators, which are sensitive to both gamma-ray and neutrons. A lack of detector sensitive exclusively to fast neutrons prevents the direct adaptation of the system from Fig. 1. for neutron localisation. Since organic plastic scintillator, such as EJ-299-33, detects fast neutrons as well as gamma-rays PSD would need to be performed on each individual channel to reliably class an event detected as neutron or gamma. For high resolution system based on one H9500, PSD would be required for all 256 channels.

III. LTSPICE SIMULATION OF THE READOUT ELECTRONICS

One way to reduce the number of channels would be to ensure that the signal extracted via readout electronics carries not only the positional data but also maintains the shape of the pulse, so that the origin of the interaction detected within the scintillator can be correctly identified. For testing purposes a schematic similar to the circuit shown in Fig. 1. was built in LTSpice simulation package for all 256 anodes of H9500 MAPMT. Simulated gamma and neutron pulses presented in Fig. 2. were connected to randomly chosen anodes in order to evaluate the signal appearing directly on 32 outputs.

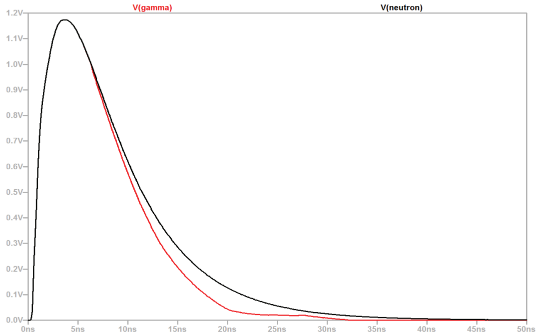

Fig. 2. Simulated gamma and neutron pulses connected to the resistive network

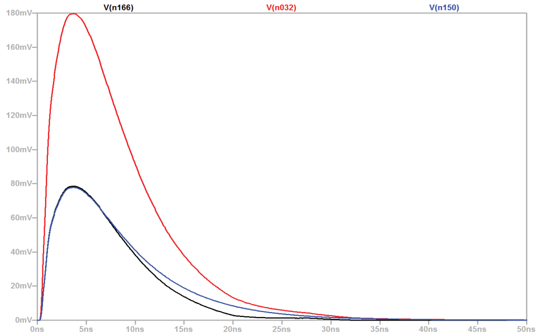

Fig. 3. Resistive network output signals probed at chosen locations

Simulated pulses were connected to two anodes and then probed at the two corresponding X outputs (black and blue traces) and single Y output (red trace) as reflected in Fig. 3. It shows that the pulses appear attenuated on the outputs. Amplification would be required before connecting to the ADC, as lower resolution ADCs may not be capable of differentiating between very low sample values. Moreover, a way of separating pulses reaching multiple anodes simultaneously must also be addressed in the design of the filtering circuit. Finally, a development of an additional circuitry targeting noise, which appears within a resistive charge division readout methods [16], is required.

IV. ANALOGUE TO DIGITAL CONVERSION FOR PSD

Digital PSD has become a standard method of neutron identification in organic scintillation detectors, with Charge Comparison Method (CCM) algorithm being one of the most popular techniques implemented in the digital domain. It has proved superior to analogue zero crossing method [17]. On average, digital CCM performed 20% better than the zero crossing method implemented in the analogue domain.

The crucial part of a digital system implementing PSD is its ADC. Resolution and sampling frequency of an ADC determine the accuracy of the digitised signal, as well as discrimination precision between gamma-rays and neutron events. Generally, the higher the sampling rate the lower the resolution. Although the current state-of-the-art ADCs offer very high sampling rates, PSD has been successfully performed using 14-bit, 150 and 200 MSPS ADCs [18], [19]. Moreover, a recent research performed by Ruch et al. [20] suggest that 12-bit, 250 MSPS ADC provides sufficient accuracy for good PSD performance.

As a proof of concept, two Analog Devices AD9254 14-bit, 150 MSPS ADCs on TERASIC AD/DA Data Conversion Card, were utilised. The data conversion card was connected to an Altera Cyclone IV EP4CE115 FPGA. As the data conversion card also contains a fast digital to analogue converter (DAC), 200 ns neutron and gamma pulses were generated for testing purposes. Pulses generated by the DAC were connected to the inputs of the two AD9254 ADCs. Outputs of the ADC channels were handled by a pair of ping-pong buffers implemented on the FPGA. Digitised samples were sent via 12Mbits/s universal asynchronous receiver/transmitter (UART) to a computer running Linux. A Python script allowed for the implementation of high speed UART, resulting in a throughput of approximately 6000 samples/s.

Off-line analysis of the recorded samples was performed and reconstructed pulses plotted. These were analysed in order to assess their suitability for the digital CCM implementation. The digital CCM can be easily performed by the summation of all the ADC samples (long integral) and a number of samples associated with the tail of the pulse (short integral) [21]. Based on the ratio between the short and the long integral it can be determined if the pulse resulted from gamma or neutron interaction within the scintillator. The difference between the two generated pulses can be clearly recognised with the ADCs used. However, higher sampling rate ADC would be necessary for scintillation detectors producing faster light pulses than those generated in the simple test performed.

V. CONCLUSION AND FUTURE PERSPECTIVE

The work completed to date focused mainly on the development of FPGA code to extract sufficient number of ADC samples for digital PSD using CCM algorithm. Two ADCs present on the data conversion card allowed simultaneous processing of two channels. Although the shape of the reconstructed pulses suggests that higher sampling rate will be required, the outputs of two concurrently operating ADCs can be linked to the inputs of the rows and columns summing amplifiers to infer the location of the interaction. Furthermore, if the filtering circuit preserves sufficient information about the origin of the interaction in the scintillant, it should be possible to perform PSD for individual anode of the MAPMT.

Future work will be focused on the development of the filtering circuit for the positional PSD implementation. Also, emphasis will be placed on replacing AD9254 ADC with a 500 MSPS, 12-bit Texas Instruments ADS5463, which would enable input signal to be sampled every 2 ns. As it will have a significant impact on the accuracy of neutron/gamma discrimination, a faster FPGA may need to be introduced to provide reliable operation with the ADC of the higher sampling rate. When identified and localised, counted pulses will be combined with coded-aperture decoding algorithm to perform real-time source localisation. Once completed, the system is expected to combine high spatial resolution achieved in coded-aperture imaging systems with accurate neutron/gamma discrimination within organic plastic scintillator.

ACKNOWLEDGEMENTS

The authors would like to acknowledge the funding support from EPSRC via Faculty of Science and Technology, Lancaster University, UK and Sellafield Ltd., UK. We also acknowledge the help and advise of Mr Matthew Balmer at Lancaster University, UK.

REFERENCES

[1] C. Trotta, R. Massari, G. Trinci, N. Palermo, S. Boccalini, F. Scopinaro, and A. Soluri, “High-Resolution Imaging System (HiRIS) based on H9500 PSPMT,” *Nuclear Instruments and Methods in Physics Research, Section A: Accelerators, Spectrometers, Detectors and Associated Equipment*, vol. 593, no. 3, pp. 454–458, 2008.

[2] P. Musico, E. Cisbani, F. Cusanno, F. Garibaldi, M. L. Magliozzi, S. Torrioli, G. Marano, M. Musumeci, M. Baiocchi, L. Vitelli, G. De Vincentis, S. Majewski, Tsui, and B, “A powerful readout system for high resolution and high efficiency molecular imaging studies of cardiovascular diseases in mice,” pp. 1–3, 2009.

[3] L. Sinclair, P. Saull, D. Hanna, H. Seywerd, A. MacLeod, and P. Boyle, “Silicon photomultiplier-based compton telescope for safety and security (scotss),” *IEEE Transactions on Nuclear Science*, vol. 61, pp. 2745–2752, Oct 2014.

[4] S. Sun, Z. Zhang, L. Shuai, D. Li, Y. Wang, Y. Liu, X. Huang, H. Tang, T. Li, P. Chai, X. Jiang, B. Ma, M. Zhu, X. Wang, Y. Zhang, W. Zhou, F. Zeng, J. Guo, L. Sun, M. Yang, Y. Zhang, C. Wei, C. Ma, and L. Wei, “Development of a panorama coded-aperture gamma camera for radiation detection,” *Radiation Measurements*, vol. 77, no. 0, pp. 34–40, 2015.

[5] S. Shifeng, Z. Zhiming, S. Lei, L. Daowu, W. Yingjie, L. Yantao, H. Xianchao, T. Haohui, L. Ting, C. Pei, Z. Yiwen, Z. Wei, Y. Mingjie, W. Cunfeng, M. Chuangxin, and W. Long, “Far field 3D localization of radioactive hot spots using a coded aperture camera,” *Applied Radiation and Isotopes*, vol. 107, pp. 177–182, 2016.

[6] E. Kowalski, *Nuclear electronics [by] E. Kowalski*. Springer-Verlag Berlin, New York, 1970.

[7] E. Brubaker and J. Steele, "Neutron imaging using the anisotropic response of crystalline organic scintillators," *IEEE Nuclear Science Symposium Conference Record*, pp. 1647–1652, 2010.

[8] Hamamatsu Photonics, *Flat Panel Multianode Photomultiplier Tube*, July 2011.

[9] Hamamatsu Photonics, *Flat Panel Multianode Photomultiplier Tube*, April 2015.

[10] J. T. Harris, P. M. Grudberg, and W. K. Warburton, "Digital electronics for 256 anode Hamamatsu H9500 PSPMT arrays in full-volume Compton imagers," *Journal of Instrumentation*, vol. 9, no. 07, pp. C07005–C07005, 2014.

[11] P. D. Olcott, J. A. Talcott, C. S. Levin, F. Habte, and A. M. K. Foudray, "Compact readout electronics for position sensitive photomultiplier tubes," *IEEE Transactions on Nuclear Science*, vol. 52, no. 1 I, pp. 21–27, 2005.

[12] V. Popov, P. Degtiarenko, and I. Musatov, "New detector for use in fast neutron radiography," *Journal of Instrumentation*, vol. 6, no. 01, pp. C01029–C01029, 2011.

[13] V. Popov, "Advanced data readout technique for Multianode Position Sensitive Photomultiplier Tube applicable in radiation imaging detectors," *Journal of Instrumentation*, vol. 6, no. 01, pp. C01061–C01061, 2011.

[14] J. Proffitt, W. Hammond, S. Majewski, V. Popov, R. R. Raylman, and A. G. Weisenberger, "Implementation of a high-rate USB data acquisition system for PET and SPECT imaging," *IEEE Nuclear Science Symposium Conference Record*, vol. 5, pp. 3063–3067, 2007.

[15] V. Popov and S. Majewski, "A compact high performance readout electronics solution for H9500 Hamamatsu 256 Multianode Photomultiplier tube for application in gamma cameras," *IEEE Nuclear Science Symposium Conference Record*, vol. 5, pp. 2981–2985, 2007.

[16] J. C. Vermeulen, "Noise in resistive charge-division position-sensing methods," *Nuclear Instruments and Methods*, vol. 185, no. 1-3, pp. 591–593, 1981.

[17] C. Sosa, M. Flaska, and S. Pozzi, "Comparison of analog and digital pulse-shape-discrimination systems," *Nuclear Instruments and Methods in Physics Research Section A: Accelerators, Spectrometers, Detectors and Associated Equipment*, vol. 826, pp. 72–79, 2016.

[18] M. Balmer, K. Gamage, and G. Taylor, "Neutron assay in mixed radiation fields with a ^{6}Li-loaded plastic scintillator," *Journal of Instrumentation*, vol. 10, no. 08, pp. P08012–P08012, 2015.

[19] N. Zaitseva, A. Glenn, H. Paul Martinez, L. Carman, I. Pawe??czak, M. Faust, and S. Payne, "Pulse shape discrimination with lithium-containing organic scintillators," *Nuclear Instruments and Methods in Physics Research, Section A: Accelerators, Spectrometers, Detectors and Associated Equipment*, vol. 729, pp. 747–754, 2013.

[20] M. L. Ruch, M. Flaska, and S. A. Pozzi, "Pulse shape discrimination performance of stilbene coupled to low-noise silicon photomultipliers," *Nuclear Instruments and Methods in Physics Research, Section A: Accelerators, Spectrometers, Detectors and Associated Equipment*, vol. 793, pp. 1–5, 2015.

[21] K. Gamage, M. Joyce, and N. Hawkes, "A comparison of four different digital algorithms for pulse-shape discrimination in fast scintillators," *Nuclear Instruments and Methods in Physics Research Section A: Accelerators, Spectrometers, Detectors and Associated Equipment*, vol. 642, no. 1, pp. 78–83, 2011.

Appendix B

Localised Response Retrieval from Hamamatsu H9500 for a Coded-aperture Dual-particle Imaging System Based on an Organic Pixelated Plastic Scintillator (EJ-299-34).

Conference Paper presented at 21st IEEE Real Time Conference (RT2018), Williamsburg, VA, USA, 9-15 Jun 2018

Localised response retrieval from Hamamatsu H9500 for a coded aperture neutron-gamma imaging system based on an organic pixelated plastic scintillator (EJ-299-34)

Michal J. Cieslak
Engineering Department
Lancaster University
Lancaster, LA1 4YW
United Kingdom
Email: m.cieslak@lancaster.ac.uk

Kelum A.A. Gamage
School of Engineering
University of Glasgow
Glasgow, G12 8QQ
United Kingdom
Email: kelum.gamage@glasgow.ac.uk

***Abstract*—Localised response of a sensitive light detector, such as Hamamatsu H9500 multi anode photomultiplier tube (MAPMT), is of vital importance for coded-aperture imaging systems. When coupled with a suitable sensitive detector (e.g. EJ-299-34 plastic scintillator), output signals of the MAPMT can be retrieved to infer the interaction location in the pixelated scintillator. Given the number of anodes in H9500 (256), significant processing power would be necessary to handle each pulse individually. Therefore, a readout electronics system was developed, based on resistive network approach, which reduces the number of output signals to individual X and Y coordinates, and subsequently allows particle identification. Coordinates retrieved in this manner can be analysed in real time and used to infer the two-dimensional location. Particle type can be also exploited by pulse shape discrimination (PSD) application to the scintillator's response. In this study, 169 anodes were used (due to coded-aperture design rules), and reduced to two X and Y output signals. These have been digitised using a bespoke FPGA based two channel 14-bit 150 MSPS digitiser. The digital data are transferred to a host application using UART to USB converter operating at 12 Mbits/s. Promising results have been observed when the scintillator's response was tested in single particle field of ^{137}Cs. However, further tests performed in the mixed-field environment of ^{252}Cf suggest that faster digitiser may be required to obtain the required PSD performance.**

I. INTRODUCTION

Neutron radiation is an example of highly penetrating radiation, which if not controlled, can pose a significant threat from nuclear safety and security viewpoint. Therefore, effective neutron detection it is of vital importance in areas, such as medicine [1], border control [2] and nuclear decommissioning [3]. Moreover, the localisation of neutron emitting isotopes can be particularly challenging in nuclear decommissioning applications, where large areas may be contaminated and exact location of the radioactive substance unknown. Collimator based imaging systems with a single opening in the aperture, can be used to scan the large areas and create an image identifying the location of the neutron emitters [4]. However, the drawbacks of such system include the fact that process of image creation can be time consuming (due to scanning requirement) and the effective field-of-view much limited.

Coded-aperture neutron imaging systems show promising results when considered as an alternative to the single opening collimators. Relatively large scale neutron detectors utilising coded-aperture approach have been previously tested and characterised [5], [6]. Both examples exploit pulse shape discrimination (PSD) capabilities of organic liquid (EJ-309) and plastic (EJ-299) scintillators. Small scale implementation of the coded-aperture imaging was previously realised with CLYC (Cs2LiYCl6:Ce) inorganic scintillation block as the radiation sensitive detector [7].

In this study a pixelated organic plastic scintillator (Fig. 1) was coupled to Hamamatsu H9500 MAPMT. The size of the single pixel has been matched to the size of a single anode of Hamamatsu H9500 (2.8mm x 2.8 mm) to reduce the risk of crosstalk between the anodes. Also, each scintillator block (2.8 mm x 2.8 mm x 15 mm) has been covered with 3M reflective tape to avoid interference between adjoining blocks. Given the sensitivity of the scintillator to both neutrons and gamma-ray photons, such configuration requires a bespoke readout electronics system. It is required that the readout electronics can not only infer the location of the interaction, but also enable particle classification (either neutron or gamma-ray photon).

II. METHODOLOGY

The readout electronics system, consists of resistive network and pulse shaping circuit followed by Field Programmable Gate Array (FPGA) based signal digitiser. The resistive network, first proposed by Popov [8], splits the voltage incurred as a result of an interaction in the specific pixel into equal parts on X and Y axis. This is then passed on to the weighted pre-amp pulse shaping stage, where based on the voltage detected, X and Y coordinates of the interaction can be computed.

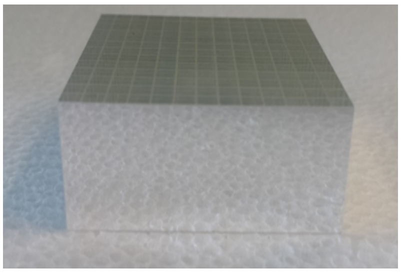

Fig. 1. Solid pixelated organic plastic scintillator (EJ-299-34).

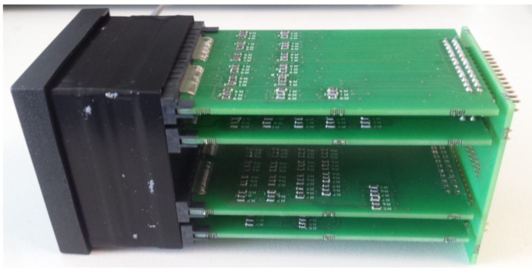

Fig. 3. A network of 507 resistors that reduces the number of output signals from 169 to 26 (13 on X and 13 in Y axis).

This stage has been simulated using TI-TINA (SPICE based) simulation package. Simulated neutron pulses were applied to three adjoining anodes and transient response recorded at the relative outputs of the pre-amp stage. Fig. 2 presents the proportional response of the simulated circuit at selected outputs, which advocates the claim that two-dimensional coordinates of the interaction can be inferred using this method. Furthermore, the resistive network does not appear to distort the shape of the applied pulse, presenting the potential of PSD techniques application for particle identification.

Following the successful simulation of the circuit, resistive network was designed and built into a printed circuit board (PCB). It contains 507 surface-mount resistors in 803 and 605 packages, split onto four printed circuit boards (PCBs), which are directly attached to the output connectors of the Hamamatsu H9500 MAPMT. Complete assembly attached to the MAPMT is presented in Fig. 3. It reduces the number of output signals from 169 to 26. This is further reduced to 2 signals (X and Y coordinates) through the shaping pre-amp and summing op-amp circuitry.

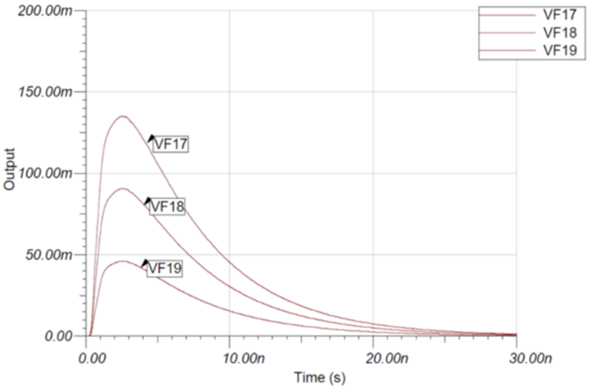

Fig. 2. Proportional response of the circuit simulated in TI-TINA software package for pulses connected to three adjoining anodes on one axis. VF17-VF19 correspond to transient response to the simulated neutron pulse connected to the three adjoining anodes.

Analogue pulses present at the output stage of the summing op-amp circuitry are digitised utilising two Analog Devices AD9254 150 MSps, 14-bit amplitude resolution ADCs directly linked to Altera Cyclone IV EP4CE115 FPGA. Verilog VHDL code has been developed that reads the outputs of the two 14-bit ADCs and transfers the data at 12 Mbits/s to a host application (such as Python application on a Laptop running Linux) via USB to UART converter. Each sample is transmitted to the host application with a channel identifier (A or B), e.g. A4087, B6743.

In order to further assess PSD capability of the pixelated scintillator, the anode of the PMT was directly linked to a 10-bit, 500 MSps "raw" data digitizer where the data were transferred from the digitizer to a host PC using Ethernet protocol. The drawback of this system is single channel operation. However, much higher sampling rate is expected to allow more accurate pulse reconstruction despite the reduced ADC resolution.

III. RESULTS AND CONCLUSIONS

Simulation of the resistive network deem a result (Fig. 2) that is proportional to the location of the interaction of the incoming particle, suggesting localised response of the MAPMT can be obtained in this way. Additionally, pulse shape analysis of the response of the pixelated scintillator to single particle field of ^{137}Cs proposes PSD as a viable technique for particle identification, given the comparison to modelled pulses, as presented in Fig. 4.

Initial simulation and experimental results obtained, based on the single particle type detection, present a potential for good localisation and particle separation capabilities of the complete system. Given the neutron-gamma separation potential of the scintillator, the complete system was also tested in dual-particle environment of the spontaneous fission field of ^{252}Cf.

Two different digitizer systems were tested, as initial results obtained using the FPGA based 150 MSps digitizer system failed to discriminate neutrons from gamma-ray photons. Results obtained from the 500 MSps "raw" data digitizer (Fig. 5) show somewhat promising PSD potential, given the modulated energy spectrum of ^{252}Cf at Lancaster University. However, the estimated figure-of-merit (FOM) of 0.337 suggests considerably poorer performance when compared with the FOM of 0.649 previously quoted in the literature for the cylindrical

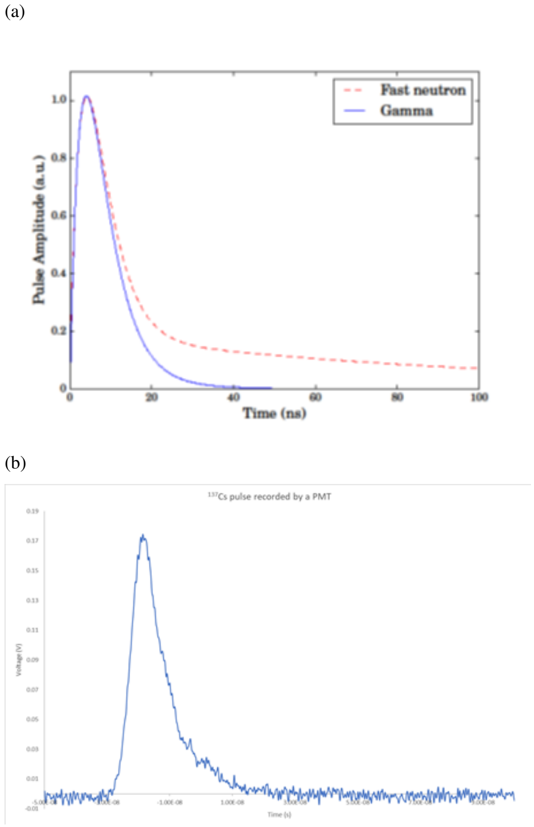

Fig. 4. A comparison of a) A mathematical model of gamma-ray photon and neutron induced pulses from organic scintillator, b) A recoded gamma-ray pulse from ^{137}Cs.

plastic scintillator samples tested in the same environment [9]. Additional tests and analysis with "bare" mixed-field sources would also be advantageous to further assess the suitability of the system for similar applications.

ACKNOWLEDGMENT

The authors would like to acknowledge the funding support from EPSRC via Faculty of Science and Technology, Lancaster University, U.K. and Sellafield Ltd.

REFERENCES

[1] S. D. Clarke, E. Pryser, B. M. Wieger, S. A. Pozzi, R. A. Haelg, V. A. Bashkirov, R. W. Schulte. A scintillator-based approach to monitor secondary neutron production during proton therapy A scintillator-based approach to monitor secondary neutron production during proton therapy *Medical Physics*, vol. 5915, no. 11, pp. 5915–5925, 2016, https://doi.org/10.1118/1.4963813.

[2] R. T. Kouzes, E. R. Siciliano, J. H. Ely, P. E. Keller, R. J. McConn. Passive neutron detection for interdiction of nuclear material at borders *Nuclear Instruments and Methods in Physics Research, Section A: Accelerators, Spectrometers, Detectors and Associated Equipment*, 584(2–3), 383–400, https://doi.org/10.1016/j.nima.2007.10.026.

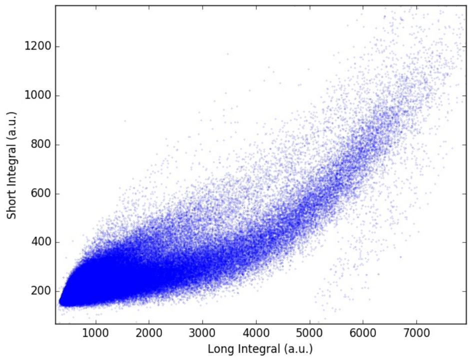

Fig. 5. PSD scatter plots using CCM for Pixelated EJ-299-34 plastic scintillator).

[3] F. Jallu, A. Reneleau, P. Soyer, J. Loridon. Dismantling and decommissioning: The interest of passive neutron measurement to control and characterise radioactive wastes containing uranium *Nuclear Instruments and Methods in Physics Research Section B: Beam Interactions with Materials and Atoms*, 271, 48–54. https://doi.org/10.1016/j.nimb.2011.09.018.

[4] K. A. A. Gamage, M. J. Joyce, G. C. Taylor. A digital approach to neutron-γ imaging with a narrow tungsten collimator aperture and a fast organic liquid scintillator detector *Applied Radiation and Isotopes : Including Data, Instrumentation and Methods for Use in Agriculture, Industry and Medicine*, 70(7), 1223–7, https://doi.org/10.1016/j.apradiso.2012.01.021.

[5] P. Hausladen, J. Newby, F. Liang, M. Blackston. The Deployable Fast-Neutron Coded- Aperture Imager : Demonstration of Locating One or More Sources in Three Dimensions Oak Ridge National Laboratory Report, ORNL/TM-2013/446, September 2013.

[6] C. V. Griffith, R. S. Woolf, B. F. Phlips. 64-Element Fast-Neutron, Coded-Aperture Imager. *IEEE International Symposium on Technologies for Homeland Security (HST)*, pages 1–5, 2017, https://doi.org/10.1109/THS.2017.7943453.

[7] C. M. Whitney, L. Soundara-Pandian, E. B. Johnson, S. Vogel, B. Vinci, M. Squillante, J. F. Christian. GammaâĂŞneutron imaging system utilizing pulse shape discrimination with CLYC *Nuclear Instruments and Methods in Physics Research Section A: Accelerators, Spectrometers, Detectors and Associated Equipment*, 784, 346–351, https://doi.org/10.1016/j.nima.2014.09.022.

[8] V. Popov. Advanced data readout technique for Multianode Position Sensitive Photomultiplier Tube applicable in radiation imaging detectors *Journal of Instrumentation* , 6(1), C01061–C01061, https://doi.org/10.1088/1748-0221/6/01/C01061.

[9] M. J. Cieślak, K. A. A. Gamage, R. Glover, Pulse shape discrimination characteristics of stilbene crystal, pure and ^{6}Li loaded plastic scintillators for a high resolution coded-aperture neutron imager, *Journal of Instrumentation*, 12 (2017).

Glossary

ADC	Analogue-to-Digital Converter
AI	Artificial Intelligence
BNCT	Boron Neutron Capture Therapy
CCD	Charge Coupled Device
CCM	Charge Comparison Method
CVL	Core-valence luminescence
DSP	Digital Signal Processor
FNT	Fast Neutron Therapy
FIR	Finite Impulse Filter
FOM	Figure-of-Merit
FOV	Field of View
FPGA	Field Programmable Gate Array
HDPE	High Density Polyethylene
HURA	Hexagonal Uniformly Redundant Array
MAPMT	Multi-anode Photomultiplier Tube
MCP	Microchannel Plate
MURA	Modified Uniformly Redundant Array

PGA	Pulse Gradient Analysis
PHD	Pulse Height Discrimination
PMT	Photomultiplier Tube
PN	Pseudo-Noise
PNP	Pseudo-Noise Product
PSD	Pulse Shape Discrimination
PSPMT	Position Sensitive Photomultiplier Tube
RPM	Radiation Portal Monitoring
SDCC	Simplified Digital Charge Comparison
SNR	Signal-to-Noise Ratio
SiPM	Silicon Photomultiplier
STE	Self-Trapped Exciton
TOF	Time of Flight
URA	Uniformly Redundant Array

References

[1] International Atomic Energy Agency, "Nuclear power reactors in the world," tech. rep., 2018. 1

[2] World Nuclear Association, "Nuclear power in the united kingdom," 2018. Accessed: 2018-09-04. 1

[3] M. Laraia, *Nuclear decommissioning : planning, execution and international experience*. Woodhead Publishing in energy ; no. 36, Oxford: Woodhead Publishing, 2012. 1, 2

[4] Nuclear Decommissioning Authority, "Strategy," Tech. Rep. April, 2016. 2

[5] J. A. Heathcote, "Characterisation of radioactively contaminated land at dounreay, an area with a high natural background," in *Environmental Radiochemical Analysis V*, pp. 1–14, The Royal Society of Chemistry, 2015. 2

[6] Department for Business Energy & Industrial Strategy and Nuclear Decommissioning Authority, "Radioactive waste in the uk, a summary of the 2016 inventory." urlhttps://ukinventory.nda.gov.uk/wp-content/uploads/sites/18/2017/03/High-Level-Summary-UK-Radwaste-Inventory-2016.pdf, 2016. Accessed: 2018-09-24. 2

[7] P. Martin, J. Moore, J. Fardoulis, O. Payton, and T. Scott, "Radiological assessment on interest areas on the sellafield nuclear site via unmanned aerial vehicle," *Remote Sensing*, vol. 8, no. 11, 2016. cited By 4. 2

[8] M. Nancekievill, A. R. Jones, M. J. Joyce, B. Lennox, S. Watson, J. Katakura, K. Okumura, S. Kamada, M. Katoh, and K. Nishimura,

"Development of a radiological characterization submersible rov for use at fukushima daiichi," *IEEE Transactions on Nuclear Science*, vol. 65, pp. 2565–2572, Sept 2018. 2

[9] A. M. Arkharov, I. A. Arkharov, D. A. Dolgopyatov, and V. L. Bondarenko, "3He supply crisis: Reasons and challenges," *Chemical and Petroleum Engineering*, vol. 49, no. 1-2, pp. 41–45, 2013. 4

[10] R. T. Kouzes, J. H. Ely, L. E. Erikson, W. J. Kernan, A. T. Lintereur, E. R. Siciliano, D. L. Stephens, D. C. Stromswold, R. M. Van Ginhoven, and M. L. Woodring, "Neutron detection alternatives to ^{3}He for national security applications," *Nuclear Instruments and Methods in Physics Research Section A: Accelerators, Spectrometers, Detectors and Associated Equipment*, vol. 623, no. 3, pp. 1035–1045, 2010. 4, 22, 38, 48, 72

[11] M. Cieślak, K. Gamage, and R. Glover, "Coded-aperture imaging systems: Past, present and future development – A review," *Radiation Measurements*, vol. 92, 2016. 4, 105, 110, 114, 115, 116, 118, 122, 129, 131, 132, 140

[12] F. Becchetti, R. Torres-Isea, A. D. Fulvio, S. Pozzi, J. Nattress, I. Jovanovic, M. Febbraro, N. Zaitseva, and L. Carman, "Deuterated stilbene (stilbene-d12): An improved detector for fast neutrons," *Nuclear Instruments and Methods in Physics Research Section A: Accelerators, Spectrometers, Detectors and Associated Equipment*, vol. 908, pp. 376 – 382, 2018. 4, 79, 147

[13] N. Zaitseva, A. Glenn, A. Mabe, M. Carman, C. Hurlbut, J. Inman, and S. Payne, "Recent developments in plastic scintillators with pulse shape discrimination," *Nuclear Instruments and Methods in Physics Research Section A: Accelerators, Spectrometers, Detectors and Associated Equipment*, vol. 889, pp. 97 – 104, 2018. 5, 146, 162

[14] Eljen Technology, *Neutron/Gamma PSD Plastic Scintillator EJ-276 (formerly EJ-299-33A and EJ-299-34)*, October 2017. Data sheet. 5, 49, 106, 111, 114, 126

[15] International Agency for Research on Cancer, "IARC Working Group on the Evaluation of Carcinogenic Risk to Humans.," 2012. 14

[16] R. D. Evans, *The Atomic Nucleus*. New York: McGraw-Hill Book Company Inc., 1955. 15, 16

[17] G. Nelson and D. Reilly, "Gamma-ray interactions with matter," *Passive Nondestructive Analysis of Nuclear Materials*, no. I, pp. 27–42, 1991. 16

[18] P. Schuster and E. Brubaker, "Investigating the anisotropic scintillation response in anthracene through neutron, gamma-ray, and muon measurements," pp. 1–11, 2015. 16, 37

[19] G. F. Knoll, *Radiation Detection and Measurement*. Hoboken: John Wiley & Sons, 4th ed., 2010. 16, 21, 22, 23, 40, 47, 48, 58, 70, 71, 72, 75, 78, 81, 86, 87, 88, 92, 112, 125, 146, 150, 159

[20] N. Carron, *An Introduction to the Passage of Energetic Particles through Matter*. Boca Raton: CRC Press, 2006. 18

[21] M. Luszik-Bhadra, F. D'Errico, O. Hecker, and M. Matzke, "A wide-range direction neutron spectrometer," *Nuclear Instruments and Methods in Physics Research Section A: Accelerators, Spectrometers, Detectors and Associated Equipment*, vol. 476, pp. 291–297, January 2002. 23

[22] S. Tavernier, *Experimental Techniques in Nuclear and Particle Physics*. Springer Berlin Heidelberg, 2010. 23

[23] S. Pospisil, B. Sopko, E. Havránková, Z. Janout, J. Konicek, I. Mácha, and J. Pavlu, "Si Diode as a Small Detector of Slow Neutrons," *Radiation Protection Dosimetry*, vol. 46, pp. 115–118, 02 1993. 23

[24] C. Petrillo, F. Sacchetti, O. Toker, and N. Rhodes, "Solid state neutron detectors," *Nuclear Instruments and Methods in Physics Research Section A: Accelerators, Spectrometers, Detectors and Associated Equipment*, vol. 378, pp. 541–551, August 1996. 23

[25] L. Bao, G. Zha, J. Li, L. Guo, J. Dong, and W. Jie, "CdZnTe quasi-hemispherical detector for gamma-neutron detection," *Journal of Nuclear Science and Technology*, vol. 56, no. 5, pp. 454–460, 2019. 23

[26] R. T. Kouzes, A. T. Lintereur, and E. R. Siciliano, “Progress in alternative neutron detection to address the helium-3 shortage,” *Nuclear Instruments and Methods in Physics Research Section A: Accelerators, Spectrometers, Detectors and Associated Equipment*, vol. 784, pp. 172–175, June 2015. 23

[27] K. Gamage, M. Joyce, and N. Hawkes, “A comparison of four different digital algorithms for pulse-shape discrimination in fast scintillators,” *Nuclear Instruments and Methods in Physics Research Section A: Accelerators, Spectrometers, Detectors and Associated Equipment*, vol. 642, no. 1, pp. 78–83, 2011. 23, 49, 82, 90, 91, 92, 94, 150, 153

[28] M. Balmer, K. Gamage, and G. Taylor, “Neutron assay in mixed radiation fields with a ^{6}Li-loaded plastic scintillator,” *Journal of Instrumentation*, vol. 10, no. 08, p. P08012, 2015. 23, 54, 91, 92, 104, 105, 114, 125, 157

[29] M. Nakhostin, “Digital discrimination of neutrons and gamma-rays in liquid scintillation detectors by using low sampling frequency ADCs,” *Nuclear Instruments and Methods in Physics Research Section A: Accelerators, Spectrometers, Detectors and Associated Equipment*, vol. 916, pp. 66–70, February 2019. 23, 159

[30] International Organization for Standardization, “Reference neutron radiations — Part 1: Characteristics and methods of production,” Standard, BS ISO 8529-1:2001, British Standards Institution, London, UK, August 2001. 24, 57, 58

[31] R. Gehrke, R. Aryaeinejad, J. Hartwell, W. Yoon, E. Reber, and J. Davidson, “The γ-ray spectrum of 252Cf and the information contained within it,” *Nuclear Instruments and Methods in Physics Research Section B: Beam Interactions with Materials and Atoms*, vol. 213, pp. 10–21, 2004. 25, 105, 112

[32] T. E. Valentine, “Evaluation of prompt fission gamma rays for use in simulating nuclear safeguard measurements,” *Annals of Nuclear Energy*, vol. 28, no. 3, pp. 191 – 201, 2001. 25, 105, 112

[33] J. Scherzinger, R. A. Jebali, J. Annand, K. Fissum, R. Hall-Wilton, S. Koufigar, N. Mauritzson, F. Messi, H. Perrey, and E. Rofors, "A comparison of untagged gamma-ray and tagged-neutron yields from 241ambe and 238pube sources," *Applied Radiation and Isotopes*, vol. 127, pp. 98 – 102, 2017. 26

[34] B. D'Mellow, M. Aspinall, R. Mackin, M. Joyce, and A. Peyton, "Digital discrimination of neutrons and γ-rays in liquid scintillators using pulse gradient analysis," *Nuclear Instruments and Methods in Physics Research Section A: Accelerators, Spectrometers, Detectors and Associated Equipment*, vol. 578, no. 1, pp. 191–197, 2007. 29, 90

[35] M. Flaska and S. A. Pozzi, "Digital pulse shape analysis for the capture-gated liquid scintillator BC-523A," *Nuclear Instruments and Methods in Physics Research, Section A: Accelerators, Spectrometers, Detectors and Associated Equipment*, vol. 599, no. 2-3, pp. 221–225, 2009. 29

[36] R. M. Preston and J. R. Tickner, "Fast-Neutron Survey With Compact Plastic Scintillation Detectors," *Radiation Protection Dosimetry*, vol. 175, pp. 406–412, 01 2017. 29

[37] M. Flaska, M. Faisal, D. D. Wentzloff, and S. A. Pozzi, "Influence of sampling properties of fast-waveform digitizers on neutron−gamma-ray, pulse-shape discrimination for organic scintillation detectors," *Nuclear Instruments and Methods in Physics Research Section A: Accelerators, Spectrometers, Detectors and Associated Equipment*, vol. 729, pp. 456 – 462, 2013. 30, 91, 106, 159

[38] C. Hellesen, M. Skiba, G. Ericsson, E. Andersson Sundén, F. Binda, S. Conroy, J. Eriksson, and M. Weiszflog, "Impact of digitization for timing and pulse shape analysis of scintillator detector signals," *Nuclear Instruments and Methods in Physics Research Section A: Accelerators, Spectrometers, Detectors and Associated Equipment*, vol. 720, pp. 135–140, August 2013. 30

[39] M. Balmer, *Design and testing of a novel neutron survey meter*. PhD thesis, Lancaster University, 2016. 30, 31

[40] D. Cester, M. Lunardon, G. Nebbia, L. Stevanato, G. Viesti, S. Petrucci, and C. Tintori, "Pulse shape discrimination with fast digitizers," *Nuclear Instruments and Methods in Physics Research Section A: Accelerators, Spectrometers, Detectors and Associated Equipment*, vol. 748, pp. 33–38, June 2014. 30

[41] C. M. Whitney, L. Soundara-Pandian, E. B. Johnson, S. Vogel, B. Vinci, M. Squillante, J. Glodo, and J. F. Christian, "Gamma–neutron imaging system utilizing pulse shape discrimination with CLYC," *Nuclear Instruments and Methods in Physics Research Section A: Accelerators, Spectrometers, Detectors and Associated Equipment*, vol. 784, pp. 346–351, 2015. 30, 164, 166

[42] M. D. Aspinall, M. J. Joyce, A. Lavietes, R. Plenteda, F. D. Cave, H. Parker, A. Jones, and V. Astromskas, "Real-Time Capabilities of a Digital Analyzer for Mixed-Field Assay Using Scintillation Detectors," *IEEE Transactions on Nuclear Science*, vol. 64, no. 3, pp. 945–950, 2017. 30

[43] Z. Szadkowski, D. Głas, K. Pytel, and M. Wiedeński, "Optimization of an FPGA Trigger Based on an Artificial Neural Network for the Detection of Neutrino-Induced Air Showers," *IEEE Transactions on Nuclear Science*, vol. 64, no. 6, pp. 1271–1281, 2017. 30

[44] M. J. Cieslak and K. A. A. Gamage, "Localised response retrieval from Hamamatsu H9500 for a coded aperture neutron-gamma imaging system based on an organic pixelated plastic scintillator (EJ-299-34)," pp. 8–10, 2018. 31, 142

[45] K. Akurugoda Gamage, L. Evans, and M. Cieslak, "Signal noise filtering techniques in radiation detection applications for neutron gamma pulse shape discrimination," in *2016 European Nuclear Conference (ENC-2016)*, pp. 256–258, European Nuclear Society, 10 2016. 32

[46] K. Jahoda, C. B. Markwardt, Y. Radeva, A. H. Rots, M. J. Stark, J. H. Swank, T. E. Strohmayer, and W. Zhang, "Calibration of the rossi x-ray

timing explorer proportional counter array," *The Astrophysical Journal Supplement Series*, vol. 163, pp. 401–423, 2006. 37

[47] P. E. Vanier, "Improvements in coded aperture thermal neutron imaging," *Proceedings SPIE, Penetrating Radiation Systems and Applications V*, vol. 5199, pp. 124–131, 2004. 37, 50

[48] J. Tous, J. Blazek, J. Zemlicka, and J. Jakubek, "Evaluation of a YAG:Ce scintillation crystal based CCD X-ray imaging detector with the Medipix2 detector," *Journal of Instrumentation*, vol. 6, no. 11, pp. C11011–C11011, 2011. 37

[49] M. Woodring, D. Beddingfield, D. Souza, G. Entine, M. Squillante, J. Christian, and A. Kogan, "Advanced multi-dimensional imaging of gamma-ray radiation," *Nuclear Instruments and Methods in Physics Research Section A: Accelerators, Spectrometers, Detectors and Associated Equipment*, vol. 505, no. 1-2, pp. 415–419, 2003. 37, 39

[50] T. Nakamura, E. Schooneveld, N. Rhodes, M. Katagiri, K. Sakasai, and K. Soyama, "Evaluation of the performance of a fibre-coded neutron detector with a ZnS^{10}/B_2O_3 ceramic scintillator," *Nuclear Instruments and Methods in Physics Research Section A: Accelerators, Spectrometers, Detectors and Associated Equipment*, vol. 600, no. 1, pp. 164–166, 2009. 37

[51] J. Lilley, *Nuclear physics: principles and applications*. Manchester physics series, J. Wiley, 2001. 38, 40

[52] M. Hirota, C. Takada, K. Takasaki, T. Momose, O. Kurihara, T. Saze, S. Ito, and K. Nishizawa, "Feasibility of in vivo measurement of ^{239}Pu distribution in lungs using an imaging plate.," *Applied radiation and isotopes*, vol. 69, no. 5, pp. 808–813, 2011. 38, 40

[53] K. Masumoto, A. Toyoda, K. Eda, and T. Ishihara, "Measurement of the spatial distribution of neutrons in an accelerator room by the combination of activation detectors and an imaging plate," *Radiation Safety Management*, vol. 1, no. 1, pp. 12–16, 2002. 38

[54] R. Mortimer, H. Anger, C. Tobias, and U. A. E. Commission, *The gamma-ray pinhole camera with image amplifier*. U.S. Atomic Energy Commission. UCRL, University of California Radiation Laboratory, 1954. 38

[55] O. Gal, B. Dessus, F. Jean, F. Laine, and C. Leveque, "Functioning of the cartogam portable gamma camera in a photon counting mode," in *Nuclear Science Symposium Conference Record, 2000 IEEE*, vol. 1, pp. 6/308–6/312 vol.1, 2000. 38

[56] O. Gal, B. Dessus, F. Jean, F. Laine, and C. Leveque, "Operation of the cartogam portable gamma camera in a photon-counting mode," *IEEE Transactions on Nuclear Science*, vol. 48, pp. 1198–1204, Aug 2001. 38

[57] B. A. Cattle, A. S. Fellerman, and R. M. West, "On the detection of solid deposits using gamma ray emission tomography with limited data," *Measurement Science and Technology*, vol. 15, no. 7, pp. 1429–1439, 2004. 38

[58] R. H. Dicke, "Scatter-hole cameras for x-rays and gamma rays," *The Astrophysical Journal*, vol. 153, pp. 101–106, June 1968. 38, 41, 42, 129

[59] E. E. Fenimore and T. M. Cannon, "Coded aperture imaging with uniformly redundant arrays," *Applied optics*, vol. 17, no. 3, pp. 337–347, 1978. 39, 42, 110, 129, 131

[60] N. Gehrels, G. Chincarini, P. Giommi, K. O. Mason, J. A. Nousek, A. A. Wells, N. E. White, S. D. Barthelmy, D. N. Burrows, L. R. Cominsky, K. C. Hurley, F. E. Marshall, P. Meszaros, P. W. A. Roming, L. Angelini, L. M. Barbier, T. Belloni, S. Campana, P. A. Caraveo, M. M. Chester, O. Citterio, T. L. Cline, M. S. Cropper, J. R. Cummings, A. J. Dean, E. D. Feigelson, E. E. Fenimore, D. A. Frail, A. S. Fruchter, G. P. Garmire, K. Gendreau, G. Ghisellini, J. Greiner, J. E. Hill, S. D. Hunsberger, H. A. Krimm, S. R. Kulkarni, P. Kumar, F. Lebrun, N. M. Lloyd Ronning, C. B. Markwardt, B. J. Mattson, R. F. Mushotzky, J. P. Norris, J. Osborne, B. Paczynski, D. M. Palmer, H. Park, A. M. Parsons, J. Paul, M. J. Rees, C. S. Reynolds, J. E. Rhoads, T. P. Sasseen, B. E. Schaefer, A. T. Short, A. P. Smale, I. A. Smith, L. Stella, G. Tagliaferri, T. Takahashi, M. Tashiro, L. K. Townsley,

J. Tueller, M. J. L. Turner, M. Vietri, W. Voges, M. J. Ward, R. Willingale, F. M. Zerbi, and W. W. Zhang, “The Swift Gamma Ray Burst Mission,” *The Astrophysical Journal*, vol. 611, no. 2, pp. 1005–1020, 2004. 39, 43, 44

[61] J. Hong, S. V. Vadawale, M. Zhang, E. C. Bellm, A. Yousef, J. Noss, J. E. Grindlay, and T. Narita, “Laboratory coded aperture imaging experiments: radial hole coded masks and depth-sensitive CZT detectors,” *Proceedings SPIE, Hard X-Ray and Gamma-Ray Detector Physics VI*, vol. 5540, pp. 1–10, 2004. 39, 43, 44

[62] T. Tumerl, T. J. O. Neilll, K. Hurley, H. Ogelman, R. J. Paulos, R. C. Puettefl, I. Qpniss, W. J. Hamilton, and R. Proctor, “All-sky X-ray & Gamma-ray Astronomy Monitor (AXGAM),” *IEEE Transactions on Nuclear Science*, vol. 44, no. 3, pp. 572–576, 1997. 39, 44

[63] E. Del Monte, E. Costa, G. Di Persio, I. Donnarumma, Y. Evangelista, M. Feroci, M. Frutti, I. Lapshov, F. Lazzarotto, M. Mastropietro, E. Morelli, L. Pacciani, G. Porrovecchio, M. Rapisarda, A. Rubini, P. Soffitta, M. Tavani, and A. Argan, “An X-ray imager based on silicon microstrip detector and coded mask,” *Nuclear Instruments and Methods in Physics Research Section A: Accelerators, Spectrometers, Detectors and Associated Equipment*, vol. 576, no. 1, pp. 191–193, 2007. 39, 43, 44, 110, 148

[64] M. Feroci, E. Costa, P. Soffitta, E. Del Monte, G. Di Persio, I. Donnarumma, Y. Evangelista, M. Frutti, I. Lapshov, F. Lazzarotto, M. Mastropietro, E. Morelli, L. Pacciani, G. Porrovecchio, M. Rapisarda, a. Rubini, M. Tavani, and a. Argan, “SuperAGILE: The hard X-ray imager for the AGILE space mission,” *Nuclear Instruments and Methods in Physics Research Section A: Accelerators, Spectrometers, Detectors and Associated Equipment*, vol. 581, no. 3, pp. 728–754, 2007. 39, 43, 44

[65] M. Alnafea, K. Wells, N. M. Spyrou, M. I. Saripan, M. Guy, and P. Hinton, “Preliminary results from a Monte Carlo study of breast tumour imaging with low-energy high-resolution collimator and a modified uniformly-redundant array-coded aperture,” *Nuclear Instruments and Methods in*

Physics Research Section A: Accelerators, Spectrometers, Detectors and Associated Equipment, vol. 563, no. 1, pp. 146–149, 2006. 39

[66] M. Alnafea, K. Wells, N. Spyrou, and M. Guy, "Preliminary Monte Carlo study of coded aperture imaging with a CZT gamma camera system for scintimammography," *Nuclear Instruments and Methods in Physics Research Section A: Accelerators, Spectrometers, Detectors and Associated Equipment*, vol. 573, no. 1-2, pp. 122–125, 2007. 39

[67] A. L. Damato, B. K. P. Horn, and R. C. Lanza, "Coded source imaging for neutrons and X-rays," *IEEE Nuclear Science Symposium Conference Record*, vol. 1, pp. 199–203, 2007. 39

[68] A. A. Faust, R. E. Rothschild, P. Leblanc, and J. E. McFee, "Development of a coded aperture X-Ray backscatter imager for explosive device detection," *IEEE Transactions on Nuclear Science*, vol. 56, no. 1, pp. 299–307, 2009. 39

[69] M. Gmar, M. Agelou, F. Carrel, and V. Schoepff, "GAMPIX: A new generation of gamma camera," *Nuclear Instruments and Methods in Physics Research Section A: Accelerators, Spectrometers, Detectors and Associated Equipment*, vol. 652, no. 1, pp. 638–640, 2011. 39, 46, 47, 114

[70] A. N. Sudarkin, O. P. Ivanov, V. E. Stepanov, A. G. Volkovich, A. S. Turin, A. S. Danilovich, D. D. Rybakov, and L. I. Urutskoev, "High-energy radiation visualizer (HERV): A new system for imaging in x-ray and gamma-ray emission regions," *IEEE Transactions on Nuclear Science*, vol. 43, no. 4, pp. 2427–2433, 1996. 39

[71] A. Sudarkin, O. Ivanov, V. Stepanov, and L. Urutskoev, "Portable gamma-ray imager and its application for the inspection of the near-reactor premises contaminated by radioactive substances," *Nuclear Instruments and Methods in Physics Research Section A: Accelerators, Spectrometers, Detectors and Associated Equipment*, vol. 414, no. 2-3, pp. 418–426, 1998. 39

[72] P. Marleau, J. Brennan, E. Brubaker, N. Hilton, and J. Steele, "Active coded aperture neutron imaging," in *2009 IEEE Nuclear Science Symposium Conference Record (NSS/MIC)*, pp. 1974–1977, October 2009. 39, 50

[73] R. S. Woolf, B. F. Phlips, A. L. Hutcheson, L. J. Mitchell, and E. A. Wulf, "An active interrogation detection system (ACTINIDES) based on a dual fast neutron/gamma-ray coded aperture imager," *2012 IEEE Conference on Technologies for Homeland Security (HST)*, pp. 30–35, 2012. 39, 51

[74] P. Hausladen, J. Newby, F. Liang, and M. Blackston, "The Deployable Fast-Neutron Coded- Aperture Imager : Demonstration of Locating One or More Sources in Three Dimensions," 2013. 39, 52, 53, 88, 111, 148, 164, 166

[75] M. J. Joyce, M. D. Aspinall, F. D. Cave, and A. Lavietes, "A 16-channel real-time digital processor for pulse-shape discrimination in multiplicity assay," *IEEE Transactions on Nuclear Science*, vol. 61, pp. 2222–2227, Aug 2014. 39, 91

[76] R. J. Ott, J. MacDonald, K. Wells, and R. J. Ott, "The performance of a ccd digital autoradiography imaging system," *Physics in Medicine and Biology*, vol. 45, no. 7, p. 2011, 2000. 40

[77] C.-H. Baek, S. J. An, H.-i. Kim, S.-W. Kwak, and Y. H. Chung, "Development of a pinhole gamma camera for environmental monitoring," *Radiation Measurements*, vol. 59, pp. 114–118, 2013. 41

[78] J. Islamian, A. Azazrm, B. Mahmoudian, and E. Gharapapagh, "Advances in Pinhole and Multi-Pinhole Collimators For Single Photon Emission Computed Tomography Imaging," *World Journal of Nuclear Medicine*, vol. 14, no. 1, pp. 3–9, 2015. 41

[79] J. G. Ables, "Fourier transform photography: A new method for x-ray astronomy," *Proceedings of the Astronomical Society of Australia*, vol. 1, pp. 172–173, December 1968. 41

[80] A. Poularikas, *Signals and Systems Primer with MATLAB*. Electrical Engineering & Applied Signal Processing Series, Taylor & Francis, 2006. 42

[81] D. Calabro and J. K. Wolf, "On the synthesis of two-dimensional arrays with desirable correlation properties," *Information and Control*, vol. 11, no. 5-6, pp. 537–560, 1967. 42

[82] F. J. MacWilliams and N. J. A. Sloane, "Pseudo-random sequences and arrays," *Proceedings of the IEEE*, vol. 64, no. 12, pp. 1715–1729, 1976. 42

[83] M. H. Finger and T. A. Prince, "Hexagonal Uniformly Redundant Arrays for Coded-Aperture Imaging," *International Cosmic Ray Conference*, vol. 3, pp. 295 – 298, August 1985. 42, 43

[84] W. R. Cook, M. Finger, T. A. Prince, and E. C. Stone, "GAMMA-RAY IMAGING WITH A ROTATING HEXAGONAL UNIFORMLY REDUNDANT ARRAY," *IEEE Transactions on Nuclear Science*, vol. NS-31, no. 1, pp. 771–775, 1984. 42

[85] A. Goldwurm, K. Byard, A. J. Dean, C. J. Hall, and J. S. J. Harding, "Laboratory images with HURA coded apertures," *Astronomy and Astrophysics*, vol. 227, pp. 640–648, 1990. 42

[86] E. Caroli, J. B. Stephen, G. Di Cocco, L. Natalucci, and A. Spizzichino, "Coded aperture imaging in X- and gamma-ray astronomy," *Space Science Review*, vol. 45, pp. 349–403, September 1987. 43, 44

[87] S. R. Gottesman and E. J. Schneid, "PNP - A new class of coded aperture arrays," *IEEE Transactions on Nuclear Science*, vol. 33, no. 1, pp. 745–749, 1986. 43

[88] S. R. Gottesman and E. E. Fenimore, "New family of binary arrays for coded aperture imaging.," *Applied optics*, vol. 28, no. 20, pp. 4344–4352, 1989. 43, 47, 54, 55, 56, 110, 131

[89] S. V. Vadawale, J. Hong, J. E. Grindlay, and G. Skinner, "Monte-Carlo simulations of the expected imaging performance of EXIST high-energy telescope," in *Proceedings SPIE, Optics for EUV, X-Ray, and Gamma-Ray Astronomy II*, vol. 5900, pp. 590014–12, 2005. 43

[90] J. E. Grindlay and J. Hong, "Optimizing wide-field coded aperture imaging: radial mask holes and scanning," in *Proceedings SPIE, Optics for EUV, X-Ray, and Gamma-Ray Astronomy*, vol. 5168, pp. 402–410, 2004. 43

[91] G. Bélanger, A. Goldwurm, P. Goldoni, J. Paul, R. Terrier, M. Falanga, P. Ubertini, A. Bazzano, M. Del Santo, C. Winkler, A. N. Parmar, E. Kuulkers, K. Ebisawa, J. P. Roques, N. Lund, and F. Melia, "Detection of Hard X-Ray Emission from the Galactic Nuclear Region with INTEGRAL," *The Astrophysical Journal*, vol. 601, pp. L163–L166, February 2004. 43

[92] O. Ivanov, A. Sudarkin, V. Stepanov, and L. Urutskoev, "Portable x-ray and gamma-ray imager with coded mask: performance characteristics and methods of image reconstruction," *Nuclear Instruments and Methods in Physics Research Section A: Accelerators, Spectrometers, Detectors and Associated Equipment*, vol. 422, no. 1–3, pp. 729 – 734, 1999. 44, 45

[93] R. Accorsi, *Design of Near-Field Coded Aperture Cameras for High-Resolution Medical and Industrial Gamma-Ray Imaging.* PhD thesis, Massachusetts Institute of Technology. Dept. of Nuclear Engineering., 2001. 45, 46, 148

[94] R. Accorsi, F. Gasparini, and R. Lanza, "A coded aperture for high-resolution nuclear medicine planar imaging with a conventional Anger camera: experimental results," *IEEE Transactions on Nuclear Science*, vol. 48, no. 6, pp. 2411–2417, 2001. 46, 166

[95] S. Sun, Z. Zhang, L. Shuai, D. Li, Y. Wang, Y. Liu, X. Huang, H. Tang, T. Li, P. Chai, X. Jiang, B. Ma, M. Zhu, X. Wang, Y. Zhang, W. Zhou, F. Zeng, J. Guo, L. Sun, M. Yang, Y. Zhang, C. Wei, C. Ma, and L. Wei, "Development of a panorama coded-aperture gamma camera for radiation detection," *Radiation Measurements*, vol. 77, no. 0, pp. 34–40, 2015. 46

[96] J. T. Santo, M. Maul, Y. Lucero, M. Clapham, B. Battle, D. Sluszka, and B. Carberry, "Application of Remote Gamma Imaging Surveys at the Turkey Point PWR Reactor Facility," 2006. 46

[97] K. A. Hughes, G. Mottershead, D. J. Thornley, A. P. Comrie, and O. Group, "Use of gamma-ray imging instrumentation in support of TRU waste characterization challenges," in *Waste Management Conference, Tucson, AZ*, pp. 1–9, Feb 2004. 46

[98] P. Peerani, A. Tomanin, S. Pozzi, J. Dolan, E. Miller, M. Flaska, M. Battaglieri, R. De Vita, L. Ficini, G. Ottonello, G. Ricco, G. Dermody, and C. Giles, "Testing on novel neutron detectors as alternative to ^{3}He for security applications," *Nuclear Instruments and Methods in Physics Research, Section A: Accelerators, Spectrometers, Detectors and Associated Equipment*, vol. 696, pp. 110–120, 2012. 47, 49

[99] L. B. Rees and J. B. Czirr, "Optimizing moderation of He-3 neutron detectors for shielded fission sources," *Nuclear Instruments and Methods in Physics Research Section A: Accelerators, Spectrometers, Detectors and Associated Equipment*, vol. 691, pp. 72–80, 2012. 48

[100] A. S. Tremsin, D. S. Hussey, R. G. Downing, W. B. Feller, D. F. R. Mildner, D. L. Jacobson, M. Arif, and O. H. W. Siegmund, "Neutron collimation with microchannel plates: calibration of existing technology and near future possibilities," *IEEE Transactions on Nuclear Science*, vol. 54, pp. 1–5, April 2005. 48

[101] N. Mascarenhas, J. Brennan, K. Krenz, J. Lund, P. Marleau, J. Rasmussen, J. Ryan, and J. Macri, "Development of a Neutron Scatter Camera for Fission Neutrons," *2006 IEEE Nuclear Science Symposium Conference Record*, vol. 2, no. 2, pp. 185–188, 2006. 48

[102] P. Marleau, J. Brennan, K. Krenz, N. Mascarenhas, and S. Mrowka, "Advances in Imaging Fission Neutrons with a Neutron Scatter Camera," in *Nuclear Science Symposium Conference Record, 2007. NSS '07. IEEE*, vol. 1, pp. 170–172, October 2007. 48, 53

[103] G. Liu, M. J. Joyce, X. Ma, and M. D. Aspinall, "A digital method for the discrimination of neutrons and γ-rays with organic scintillation detectors using frequency gradient analysis," *IEEE Transactions on Nuclear Science*, vol. 57, no. 3, pp. 1682–1691, 2010. 49

[104] Inradoptics, *Stilbene Single Crystals*. Data sheet. 49, 58, 93, 114

[105] N. P. Hawkes, K. A. A. Gamage, and G. C. Taylor, "Digital approaches to field neutron spectrometry," *Radiation Measurements*, vol. 45, no. 10, pp. 1305–1308, 2010. 49

[106] F. Brooks, "A scintillation counter with neutron and gamma-ray discriminators," *Nuclear Instruments and Methods*, vol. 4, no. 3, pp. 151 – 163, 1959. 50, 78, 81, 86, 87, 89, 109, 135, 150

[107] J. Adams and G. White, "A versatile pulse shape discriminator for charged particle separation and its application to fast neutron time-of-flight spectroscopy," *Nuclear Instruments and Methods*, vol. 156, no. 3, pp. 459 – 476, 1978. 50, 87

[108] P. Marleau, J. Brennan, E. Brubaker, and J. Steele, "Results from the coded aperture neutron imaging system," in *Nuclear Science Symposium Conference Record (NSS/MIC), 2010 IEEE*, pp. 1640–1646, October 2010. 50, 51, 111

[109] R. S. Woolf, B. F. Phlips, A. L. Hutcheson, and E. A. Wulf, "Fast-neutron, coded-aperture imager," *Nuclear Instruments and Methods in Physics Research Section A: Accelerators, Spectrometers, Detectors and Associated Equipment*, vol. 784, pp. 398–404, 2015. 51, 111

[110] P. Hausladen and M. Blackston, "Passive and Active Fast-Neutron Imaging in Support of AFCI Safeguards Campaign Prepared by," *Energy*, no. August, 2009. 52

[111] P. Hausladen, M. Blackston, E. Brubaker, D. Chichester, P. Marleau, and R. Newby, "Fast-Neutron Coded-Aperture Imaging of Special Nuclear Material Configurations," 2012. 52, 166

[112] J. Brennan, E. Brubaker, M. Gerling, P. Marleau, K. McMillan, A. Nowack, N. R.-L. Galloudec, and M. Sweany, "Demonstration of two-dimensional time-encoded imaging of fast neutrons," *Nuclear Instruments and Methods in Physics Research Section A: Accelerators, Spectrometers, Detectors and Associated Equipment*, vol. 802, pp. 76 – 81, 2015. 52, 53

[113] S. Hayes and K. Gamage, "Scintillator based coded-aperture imaging for neutron detection," in *3rd International Conference on Advancements in Nuclear Instrumentation Measurement Methods and their Applications (ANIMMA)*, pp. 1–6, June 2013. 53

[114] C. Yong-Hao, C. Xi-Meng, Z. Xiao-Dong, L. Jia-Rong, A. Li, S. Jian-Xiong, Z. Pu, W. Xin-Hua, Z. Chuan-Xin, H. Tie, and Y. Jian, "Study of n-γ discrimination in low energy range (above 40 keVee) by charge comparison method with a BC501A liquid scintillation detector," *Chinese Physics C*, vol. 38, no. 3, p. 036001, 2014. 54

[115] M. Gerling, P. Marleau, and J. Goldsmith, "Comparison of Stilbene neutron detection performance to EJ-309," 2014. 54, 58, 88

[116] G. H. Hardy and E. M. Wright, *An Introduction to the Theory of Numbers*. Oxford University Press, fifth ed., 1979. 55

[117] T. E. Booth, H. Grady Hughes, A. Zukaitis, F. B. Brown, R. D. Mosteller, M. Boggs, J. S. Bull, R. E. Prael, R. Martz, R. A. Forster, A. Sood, J. T. Goorley, and J. E. Sweezy, *MCNP - A General Monte Carlo N-Particle Transport Code, Version 5*, 2005. User manual. 56, 59

[118] Y. Wu, J. Song, H. Zheng, G. Sun, L. Hao, P. Long, and L. Hu, "CAD-based Monte Carlo program for integrated simulation of nuclear system SuperMC," *Annals of Nuclear Energy*, vol. 82, pp. 161–168, 2015. 56, 115

[119] K. A. A. Gamage, M. J. Joyce, and G. C. Taylor, "A comparison of collimator geometries for imaging mixed radiation fields with fast liquid organic scintillators," *IEEE Transactions on Nuclear Science*, vol. 59, pp. 1432–1437, Aug 2012. 57, 109, 110

[120] M. B. N. Soppera, E. Dupont, *Book of Neutron comparison of evaluated and experimental data*. No. June, Nuclear Energy Agency, 2012. 58

[121] N. Zaitseva, B. L. Rupert, I. Pawełczak, A. Glenn, H. P. Martinez, L. Carman, M. Faust, N. Cherepy, and S. Payne, "Plastic scintillators with efficient neutron/gamma pulse shape discrimination," *Nuclear Instruments and*

Methods in Physics Research Section A: Accelerators, Spectrometers, Detectors and Associated Equipment, vol. 668, pp. 88–93, 2012. 58, 88, 107, 109, 112, 126

[122] N. Zaitseva, A. Glenn, L. Carman, H. P. Martinez, R. Hatarik, H. Klapper, and S. Payne, "Scintillation properties of solution-grown trans-stilbene single crystals," *Nuclear Instruments and Methods in Physics Research Section A: Accelerators, Spectrometers, Detectors and Associated Equipment*, vol. 789, pp. 8 – 15, 2015. 58, 79, 88, 91, 147

[123] D. B. Pelowitz, "MCNPX USER'S MANUAL - Version 2.7.0," no. April 2011. 59, 110

[124] A. Osovizky, D. Ginzburg, A. Manor, R. Seif, M. Ghelman, I. Cohen-Zada, M. Ellenbogen, V. Bronfenmakher, V. Pushkarsky, E. Gonen, T. Mazor, and Y. Cohen, "SENTIRAD-An innovative personal radiation detector based on a scintillation detector and a silicon photomultiplier," *Nuclear Inst. and Methods in Physics Research, A*, vol. 652, pp. 41–44, 2011. 68

[125] R. Seymour, C. D. Hull, T. Crawford, B. Coyne, M. Bliss, and R. A. Craig, "Portal, freight and vehicle monitor performance using scintillating glass fiber detectors for the detection of plutonium in the illicit trafficking radiation assessment program," *Journal of Radioanalytical and Nuclear Chemistry*, vol. 248, pp. 699–705, Jun 2001. 68

[126] W. C. Röntgen, "On a new kind of rays," *Science*, vol. 3, no. 59, pp. 227–231, 1896. 68

[127] W. Crookes, "On The Illumination of Lines of Molecular Pressure and the Trajectory of Molecules," *Philosophical Transactions of The Royal Society of London*, 1878. 68

[128] W. Friedrich, P. Knipping, and M. Laue, "Interferenzerscheinungen bei röntgenstrahlen," *Annalen der Physik*, vol. 346, no. 10, pp. 971–988, 1913. 68

[129] W. H. Bragg, "X-rays and crystalline structure," *Science*, vol. 40, no. 1040, pp. 795–802, 1914. 68

[130] V. K. Zworykin, G. A. Morton, and L. Malter, “The secondary emission multiplier-a new electronic device,” *Proceedings of the Institute of Radio Engineers*, vol. 24, pp. 351–375, March 1936. 69

[131] K. S. Krane, *Introductory nuclear physics.* New York: Wiley, 1988. 69, 70

[132] C. W. Van Eijk, “Development of inorganic scintillators,” *Nuclear Instruments and Methods in Physics Research, Section A: Accelerators, Spectrometers, Detectors and Associated Equipment*, vol. 392, no. 1-3, pp. 285–290, 1997. 71, 73

[133] J. S. Schweitzer, “Cerium-doped Lutetium Oxyorthosilicate:,” vol. 39, no. 4, pp. 502–505, 1992. 71

[134] A. Tomanin, P. Peerani, and G. Janssens-Maenhout, “On the optimisation of the use of 3 He in radiation portal monitors,” *Nuclear Inst. and Methods in Physics Research, A*, vol. 700, pp. 81–85, 2012. 72

[135] L. Boatner, E. Comer, G. Wright, J. Ramey, R. Riedel, G. Jellison, and J. Kolopus, “Improved Lithium Iodide neutron scintillator with Eu 2 + activation II: Activator zoning and concentration effects in Bridgman-grown crystals,” *Nuclear Instruments and Methods in Physics Research Section A: Accelerators, Spectrometers, Detectors and Associated Equipment*, vol. 903, pp. 8–17, September 2018. 72

[136] J. Iwanowska, L. Swiderski, M. Moszynski, T. Yanagida, Y. Yokota, A. Yoshikawa, K. Fukuda, N. Kawaguchi, and S. Ishizu, “Thermal neutron detection with Ce3 doped LiCaAlF6 single crystals,” *Nuclear Instruments and Methods in Physics Research, Section A: Accelerators, Spectrometers, Detectors and Associated Equipment*, vol. 652, no. 1, pp. 319–322, 2011. 72

[137] T. Yanagida, K. Watanabe, G. Okada, and N. Kawaguchi, “Neutron and gamma-ray pulse shape discrimination of LiAlO2 and LiGaO2 crystals,” *Nuclear Instruments and Methods in Physics Research Section A: Accelerators, Spectrometers, Detectors and Associated Equipment*, vol. 919, pp. 64–67, March 2019. 73

[138] P. L. Reeder and S. M. Bowyer, “Fast neutron and alpha detection using LiBaF3 scintillator,” *IEEE Transactions on Nuclear Science*, vol. 48, no. 3 I, pp. 351–355, 2001. 73

[139] J. Glodo, Y. Wang, R. Shawgo, C. Brecher, R. H. Hawrami, J. Tower, and K. S. Shah, “New Developments in Scintillators for Security Applications,” *Physics Procedia*, vol. 90, pp. 285–290, 2017. 73, 77

[140] A. Gueorguiev, E. van Loef, G. Markosyan, L. Soundara-Pandian, J. Glodo, J. Tower, and K. Shah, “Composite neutron gamma detector,” in *2015 IEEE Nuclear Science Symposium and Medical Imaging Conference (NSS/MIC)*, pp. 1–3, Oct 2015. 73

[141] U. Shirwadkar, A. Gueorguiev, E. V. van Loef, G. Markosyan, J. Glodo, J. Tower, K. S. Shah, S. Pozzi, S. Clarke, and M. Bourne, “Multi-Signature Composite Detector System for Nuclear Non-proliferation,” in *2017 IEEE Nuclear Science Symposium and Medical Imaging Conference (NSS/MIC)*, pp. 1–4, IEEE, October 2017. 73, 147

[142] C. W. van Eijk, “Inorganic scintillators for thermal neutron detection,” *Radiation Measurements*, vol. 38, no. 4, pp. 337 – 342, 2004. Proceedings of the 5th European Conference on Luminescent Detectors and Transformers of Ionizing Radiation (LUMDETR 2003). 74

[143] S. E. Rutherford, “The stability of atoms,” *Proceedings of the Physical Society of London*, vol. 33, pp. 389–394, December 1920. 74

[144] T. Yanagida and Y. Fujimoto, “Evaluations of pure zinc sulfide crystal scintillator,” *Japanese Journal of Applied Physics*, vol. 53, p. 032601, February 2014. 74

[145] Eljen Technology, “EJ-426 Thermal Neutron Detector Data Sheet,” 2016. 74

[146] L. Viererbl, V. Klupak, M. Vins, Z. Lahodova, and J. Soltes, “YAP:Ce Scintillator Characteristics for Neutron Detection,” *IEEE Transactions on Nuclear Science*, vol. 63, no. 3, pp. 1963–1966, 2016. 74

[147] M. Korjik, K. T. Brinkmann, G. Dosovitskiy, V. Dormenev, A. Fedorov, D. Kozlov, V. Mechinsky, and H. G. Zaunick, “Compact and Effective Detector of the Fast Neutrons on a Base of Ce-doped Gd3Al2Ga3O12 Scintillation Crystal,” *IEEE Transactions on Nuclear Science*, vol. 66, no. 1, pp. 536–540, 2019. 75

[148] J. Iwanowska, T. Szczeęśniak, and T. Szczęśniak, “New Organic Scintillators for Neutron Detection,” vol. 1204, p. 165, 2010. 75

[149] Z. Fu, S. Pan, F. Yang, S. Gu, X. Lei, Y. Heng, G. Ren, and M. Qi, “Neutron detection properties of Li6Y(BO3)3:Ce crystal,” *Radiation Measurements*, vol. 72, pp. 39–43, January 2015. 76

[150] C. C. T. Hansson, A. Owens, and J. V. D. Biezen, “X-ray, γ-ray and neutron detector development for future space instrumentation $,” *Acta Astronautica*, vol. 93, pp. 121–128, 2013. 76

[151] T. Inada, “Detection of Fast Neutrons with NaI(Tl) Crystal,” *Journal of Nuclear Science and Technology*, vol. 5, no. 6, pp. 287–291, 1968. 76

[152] V. D. Ryzhikov, S. V. Naydenov, G. M. Onyshchenko, L. A. Piven’, T. Pochet, and C. F. Smith, “High efficiency fast neutron detectors based on inorganic scintillators,” in *2014 IEEE Nuclear Science Symposium and Medical Imaging Conference (NSS/MIC)*, pp. 1–6, Nov 2014. 77

[153] M. Lucchini, K. Pauwels, M. Pizzichemi, R. Chipaux, F. Jacquot, H. Mazué, H. Wolff, P. Lecoq, and E. Auffray, “Response of inorganic scintillators to neutrons of 3 and 15 mev energy,” *IEEE Transactions on Nuclear Science*, vol. 61, pp. 472–478, Feb 2014. 77

[154] G. Hull, N. P. Zaitseva, N. J. Cherepy, J. R. Newby, W. Stoeffl, and S. A. Payne, “New organic crystals for pulse shape discrimination,” *IEEE Transactions on Nuclear Science*, vol. 56, no. 3, pp. 899–903, 2009. 78, 109

[155] E. Brubaker and J. Steele, “Neutron imaging using the anisotropic response of crystalline organic scintillators,” *IEEE Nuclear Science Symposium Conference Record*, pp. 1647–1652, 2010. 78

[156] M. J. Cieślak, K. A. Gamage, and R. Glover, "Pulse shape discrimination characteristics of stilbene crystal, pure and6Li loaded plastic scintillators for a high resolution coded-aperture neutron imager," *Journal of Instrumentation*, vol. 12, no. 7, 2017. 79, 82, 125, 126, 133, 135, 148, 160

[157] Inrad Optics, "Stilbene Single Crystals," 2019. 79

[158] L. Carman, H. Paul Martinez, L. Voss, S. Hunter, P. Beck, N. Zaitseva, S. A. Payne, P. Irkhin, H. H. Choi, and V. Podzorov, "Solution-Grown Rubrene Crystals as Radiation Detecting Devices," *IEEE Transactions on Nuclear Science*, vol. 64, no. 2, pp. 781–788, 2017. 79

[159] N. Zaitseva, A. Glenn, H. Paul Martinez, L. Carman, I. Pawełczak, M. Faust, and S. Payne, "Pulse shape discrimination with lithium-containing organic scintillators," *Nuclear Instruments and Methods in Physics Research, Section A: Accelerators, Spectrometers, Detectors and Associated Equipment*, vol. 729, pp. 747–754, 2013. 81, 87, 146, 150

[160] R. Winyard, J. Lutkin, and G. McBeth, "Pulse shape discrimination in inorganic and organic scintillators. I," *Nuclear Instruments and Methods*, vol. 95, pp. 141–153, August 1971. 82, 159

[161] T. Alexander and F. Goulding, "An amplitude-insensitive system that distinguishes pulses of different shapes," *Nuclear Instruments and Methods*, vol. 13, pp. 244 – 246, 1961. 87

[162] H. Klein, "Neutron spectrometry in mixed fields: NE213/BC501A liquid scintillation spectrometers," *Radiation Protection Dosimetry*, vol. 107, pp. 95–109, 11 2003. 87

[163] J. Iwanowska, L. Swiderski, and M. Moszynski, "Liquid scintillators and composites in fast neutron detection," *Journal of Instrumentation*, vol. 7, pp. C04004–C04004, April 2012. 87

[164] L. Stevanato, D. Cester, G. Nebbia, and G. Viesti, "Neutron detection in a high gamma-ray background with EJ-301 and EJ-309 liquid scintillators,"

Nuclear Inst. and Methods in Physics Research, A, vol. 690, pp. 96–101, 2012. 87, 146

[165] C. Bass, E. Beise, H. Breuer, C. Heimbach, T. Langford, and J. Nico, "Characterization of a 6li-loaded liquid organic scintillator for fast neutron spectrometry and thermal neutron detection," *Applied Radiation and Isotopes*, vol. 77, pp. 130 – 138, 2013. 87

[166] A. Tomanin, J. Paepen, P. Schillebeeckx, R. Wynants, R. Nolte, and A. Lavietes, "Characterization of a cubic ej-309 liquid scintillator detector," *Nuclear Instruments and Methods in Physics Research Section A: Accelerators, Spectrometers, Detectors and Associated Equipment*, vol. 756, pp. 45 – 54, 2014. 87

[167] B. Fraboni, A. Fraleoni-Morgera, and N. Zaitseva, "Ionizing radiation detectors based on solution-grown organic single crystals," *Advanced Functional Materials*, vol. 26, no. 14, pp. 2276–2291, 2016. 88

[168] M. M. Bourne, S. D. Clarke, N. Adamowicz, S. A. Pozzi, N. Zaitseva, and L. Carman, "Neutron detection in a high-gamma field using solution-grown stilbene," *Nuclear Inst. and Methods in Physics Research, A*, vol. 806, pp. 348–355, 2016. 88, 92, 109

[169] M. Nakhostin, "Recursive algorithms for digital implementation of neutron/gamma discrimination in liquid scintillation detectors," *Nuclear Instruments and Methods in Physics Research, Section A: Accelerators, Spectrometers, Detectors and Associated Equipment*, vol. 672, pp. 1–5, 2012. 88, 89

[170] J. Iwanowska-Hanke, M. Moszynski, L. Swiderski, P. Sibczynski, T. Krakowski, N. Zaitseva, I. A. Pawelczak, P. Martinez, A. Gektin, and P. N. Zhmurin, "Comparison of various plastic scintillators with pulse shape discrimination (PSD) capabilities based on polystyrene (PS)," *IEEE Nuclear Science Symposium Conference Record*, pp. 1–3, 2013. 88

[171] M. Grodzicka, T. Szczesniak, M. Moszynski, D. Wolski, L. Swiderski, K. Grodzicki, S. Korolczuk, J. Baszak, and P. Schotanus, "Study of n-g

discrimination by zero-crossing method with SiPM based scintillation detectors," *2014 IEEE Nuclear Science Symposium and Medical Imaging Conference, NSS/MIC 2014*, pp. 14–16, 2016. 88

[172] T. Szczesmak, M. Grodzicka, M. Moszyński, D. Wolski, L. Swiderski, M. Szawłowski, and P. Schotanus, "Digital neutron-gamma discrimination methods: Charge comparison versus zero-crossing," in *2014 IEEE Nuclear Science Symposium and Medical Imaging Conference (NSS/MIC)*, pp. 1–4, Nov 2014. 89

[173] C. Sosa, M. Flaska, and S. Pozzi, "Comparison of analog and digital pulse-shape-discrimination systems," *Nuclear Instruments and Methods in Physics Research Section A: Accelerators, Spectrometers, Detectors and Associated Equipment*, vol. 826, pp. 72–79, 2016. 89, 91

[174] D. Wolski, M. Moszyński, T. Ludziejewski, A. Johnson, W. Klamra, and Ö. Skeppstedt, "Comparison of n-γ discrimination by zero-crossing and digital charge comparison methods," *Nuclear Instruments and Methods in Physics Research Section A: Accelerators, Spectrometers, Detectors and Associated Equipment*, vol. 360, no. 3, pp. 584–592, 1995. 89

[175] D. I. Shippen, M. J. Joyce, and M. D. Aspinall, "A Wavelet Packet Transform Inspired Method of Neutron-Gamma Discrimination," *IEEE Transactions on Nuclear Science*, vol. 57, pp. 2617–2624, October 2010. 90

[176] M. J. I. Balmer, K. A. A. Gamage, and G. C. Taylor, "A novel approach to neutron dosimetry," *Medical Physics*, vol. 43, no. 11, pp. 5981–5990, 2016. 92, 106

[177] S. A. Pozzi, M. M. Bourne, and S. D. Clarke, "Pulse shape discrimination in the plastic scintillator EJ-299-33," *Nuclear Instruments and Methods in Physics Research, Section A: Accelerators, Spectrometers, Detectors and Associated Equipment*, vol. 723, pp. 19–23, 2013. 92, 107, 162

[178] M. M. Bourne, J. Whaley, J. L. Dolan, J. K. Polack, M. Flaska, S. D. Clarke, A. Tomanin, P. Peerani, and S. A. Pozzi, "Cross-correlation measurements

with the EJ-299-33 plastic scintillator," *Nuclear Instruments and Methods in Physics Research, Section A: Accelerators, Spectrometers, Detectors and Associated Equipment*, vol. 784, pp. 460–464, 2015. 92

[179] S. W. Smith, *The Scientist and Engineer's Guide to Digital Signal Processing*. 1999. 94

[180] M. D. Aspinall, B. D'Mellow, R. O. Mackin, M. J. Joyce, Z. Jarrah, and A. J. Peyton, "The empirical characterization of organic liquid scintillation detectors by the normalized average of digitized pulse shapes," *Nuclear Instruments and Methods in Physics Research, Section A: Accelerators, Spectrometers, Detectors and Associated Equipment*, vol. 578, no. 1, pp. 261–266, 2007. 94

[181] J. K. Polack, M. Flaska, A. Enqvist, C. S. Sosa, C. C. Lawrence, and S. A. Pozzi, "An algorithm for charge-integration, pulse-shape discrimination and estimation of neutron/photon misclassification in organic scintillators," *Nuclear Instruments and Methods in Physics Research, Section A: Accelerators, Spectrometers, Detectors and Associated Equipment*, vol. 795, pp. 253–267, 2015. 105

[182] M. Cieslak and K. Gamage, "Design and development of a real-Time readout electronics system to retrieve data from a square multi-Anode photomultiplier tube for neutron gamma pulse shape discrimination," in *2016 IEEE-NPSS Real Time Conference, RT 2016*, 2016. 106

[183] T. Szczesniak, M. Moszynski, A. Syntfeld-Kazuch, . Swiderski, D. Wolski, M. Grodzicka, G. Pausch, J. R. Stein, F. Kniest, M. R. Kusner, P. Schotanus, and C. Hurlbut, "Light pulse shapes in liquid scintillators originating from gamma-rays and neutrons," *IEEE Transactions on Nuclear Science*, vol. 57, pp. 3846–3852, Dec 2010. 109, 143

[184] A. Kaplan, M. Flaska, A. Enqvist, J. Dolan, and S. Pozzi, "Ej-309 pulse shape discrimination performance with a high gamma-ray-to-neutron ratio and low threshold," *Nuclear Instruments and Methods in Physics Research*

Section A: Accelerators, Spectrometers, Detectors and Associated Equipment, vol. 729, pp. 463 – 468, 2013. 109, 146

[185] A. Jones and M. Joyce, "The angular dependence of pulse shape discrimination and detection sensitivity in cylindrical and cubic EJ-309 organic liquid scintillators," *Journal of Instrumentation*, vol. 12, no. 01, pp. T01005–T01005, 2017. 109

[186] K. Gamage and G. Taylor, "Neutron gamma fraction imaging: Detection, location and identification of neutron sources," *Nuclear Instruments and Methods in Physics Research Section A: Accelerators, Spectrometers, Detectors and Associated Equipment*, vol. 788, pp. 9 – 12, 2015. 109, 110

[187] Eljen Technology, *Neutron/Gamma PSD Liquid Scintillator EJ-301,EJ-309*, November 2016. Data sheet. 109

[188] M. G. Paff, M. L. Ruch, A. Poitrasson-Riviere, A. Sagadevan, S. D. Clarke, and S. Pozzi, "Organic liquid scintillation detectors for on-the-fly neutron/gamma alarming and radionuclide identification in a pedestrian radiation portal monitor," *Nuclear Instruments and Methods in Physics Research Section A: Accelerators, Spectrometers, Detectors and Associated Equipment*, vol. 789, pp. 16 – 27, 2015. 110

[189] A. Poitrasson-Rivière, J. K. Polack, M. C. Hamel, D. D. Klemm, K. Ito, A. T. McSpaden, M. Flaska, S. D. Clarke, S. A. Pozzi, A. Tomanin, and P. Peerani, "Angular-resolution and material-characterization measurements for a dual-particle imaging system with mixed-oxide fuel," *Nuclear Instruments and Methods in Physics Research Section A: Accelerators, Spectrometers, Detectors and Associated Equipment*, vol. 797, pp. 278 – 284, 2015. 110

[190] "Imaging of fast neutrons and gamma rays from 252cf in a heavily shielded environment," *Nuclear Instruments and Methods in Physics Research Section A: Accelerators, Spectrometers, Detectors and Associated Equipment*, vol. 847, pp. 77 – 85, 2017. 110

[191] O. Gal, C. Izac, F. Lainé, and A. Nguyen, "Cartogam: a portable gamma camera," *Nuclear Instruments and Methods in Physics Research Section A: Accelerators, Spectrometers, Detectors and Associated Equipment*, vol. 387, no. 1, pp. 297 – 303, 1997. New Developments in Photodetection. 110

[192] S. Guru, Z. He, D. Wehe, G. Knoll, R. Redus, and M. Squillante, "Portable high energy gamma ray imagers," *Nuclear Instruments and Methods in Physics Research Section A: Accelerators, Spectrometers, Detectors and Associated Equipment*, vol. 378, no. 3, pp. 612 – 619, 1996. 110

[193] J. Beaumont, B. Colling, M. P. Mellor, and M. J. Joyce, "On the design and test of a neutron collimator for real-time neutron imaging in the mev energy range," in *2013 3rd International Conference on Advancements in Nuclear Instrumentation, Measurement Methods and their Applications (ANIMMA)*, pp. 1–8, June 2013. 110

[194] R. Accorsi and R. C. Lanza, "Near-field artifact reduction in planar coded aperture imaging," *Appl. Opt.*, vol. 40, pp. 4697–4705, Sep 2001. 110

[195] Hamamatsu Photonics, *Flat Panel Type Multianode Photomultiplier Tube Assembly H9500, H9500-03*, April 2015. Data sheet. 112

[196] N. J. Cherepy, R. D. Sanner, P. R. Beck, E. L. Swanberg, T. M. Tillotson, S. A. Payne, and C. R. Hurlbut, "Bismuth- and lithium-loaded plastic scintillators for gamma and neutron detection," *Nuclear Instruments and Methods in Physics Research Section A: Accelerators, Spectrometers, Detectors and Associated Equipment*, vol. 778, pp. 126 – 132, 2015. 125

[197] X. Li, A. Stevens, J. A. Greenberg, and M. E. Gehm, "Single-shot memory-effect video," *Scientific Reports*, vol. 8, p. 13402, December 2018. 129

[198] A. Vella, A. A. Munoz, M. J. Healy, D. W. Lane, and D. Lockley, "An artificial X-ray wire test emitter and calculations on the resolution and field of view of X-ray pinhole optics by simulation," *Nuclear Instruments and Methods in Physics Research, Section A: Accelerators, Spectrometers, Detectors and Associated Equipment*, vol. 905, no. March, pp. 119–128, 2018. 129

[199] T. Lee, S. W. Kwak, and W. Lee, "Investigation of nuclear material using a compact modified uniformly redundant array gamma camera," *Nuclear Engineering and Technology*, vol. 50, no. 6, pp. 923–928, 2018. 129

[200] C. V. Griffith, R. S. Woolf, and B. F. Phlips, "64-element fast-neutron, coded-aperture imager," in *2017 IEEE International Symposium on Technologies for Homeland Security, HST 2017*, pp. 1–5, 2017. 129, 130, 148, 161, 164

[201] C. Lynde, F. Carrel, V. Schoepff, C. Frangville, R. Woo, A. Sardet, J. Venara, M. Ben Mosbah, R. Abou Khalil, and Z. El Bitar, "Demonstration of coded-aperture fast-neutron imaging based on Timepix detector," *Nuclear Instruments and Methods in Physics Research Section A: Accelerators, Spectrometers, Detectors and Associated Equipment*, October 2018. 129, 166

[202] M. A. Blackston, P. Hausladen, J. F. Liang, and J. Newby, "Performance of fast-neutron imaging detectors based on plastic scintillator ej-299-34," 2 2013. 130

[203] M. Cieślak, K. Gamage, and R. Glover, "Investigation into a suitable scintillator and coded-aperture material for a mixed-field radiation imaging system," *Journal of Instrumentation*, vol. 12, no. 12, 2017. 130, 142, 148, 149, 150, 153, 157

[204] M. L. Ruch, C. B. Sivels, S. A. Czyz, M. Flaska, and S. A. Pozzi, "Comparison between silicon photomultipliers and photomultiplier tubes for pulse shape discrimination with stilbene," in *2014 IEEE Nuclear Science Symposium and Medical Imaging Conference (NSS/MIC)*, pp. 1–3, Nov 2014. 143

[205] E. H. Lehmann and W. Wagner, "Neutron imaging at PSI: A promising tool in materials science and technology," *Applied Physics A: Materials Science and Processing*, vol. 99, no. 3, pp. 627–634, 2010. 145

[206] C. W. E. van Eijk, "Inorganic scintillators in medical imaging," *Physics in Medicine and Biology*, vol. 47, no. 8, pp. R85–R106, 2002. 145

[207] M. J. Joyce, M. D. Aspinall, F. D. Cave, and A. D. Lavietes, "Real-time, digital pulse-shape discrimination in non-hazardous fast liquid scintillation detectors: Prospects for safety and security," *IEEE Transactions on Nuclear Science*, vol. 59, no. 4 PART 2, pp. 1245–1251, 2012. 146

[208] F. Pino, L. Stevanato, D. Cester, G. Nebbia, and G. Viesti, "Detecting fast and thermal neutrons with a boron loaded liquid scintillator, EJ-339A," *Applied Radiation and Isotopes*, vol. 92, pp. 6–11, 2014. 146

[209] M. Bourne, C. Mussi, E. Miller, S. Clarke, S. Pozzi, and A. Gueorguiev, "Characterization of the clyc detector for neutron and photon detection," *Nuclear Instruments and Methods in Physics Research Section A: Accelerators, Spectrometers, Detectors and Associated Equipment*, vol. 736, pp. 124 – 127, 2014. 147

[210] O. Gal, M. Gmar, O. P. Ivanov, F. Lainé, F. Lamadie, C. L. Goaller, C. Mahé, E. Manach, and V. E. Stepanov, "Development of a portable gamma camera with coded aperture," *Nuclear Instruments and Methods in Physics Research Section A: Accelerators, Spectrometers, Detectors and Associated Equipment*, vol. 563, no. 1, pp. 233 – 237, 2006. Proceedings of the 7th International Workshop on Radiation Imaging Detectors. 148

[211] M. Gmar, O. Gal, C. L. Goaller, O. P. Ivanov, V. N. Potapov, V. E. Stepanov, F. Laine, and F. Lamadie, "Development of coded-aperture imaging with a compact gamma camera," *IEEE Transactions on Nuclear Science*, vol. 51, no. 4, pp. 1052–1056, 2003. 148

[212] M. Jeong, B. Van, B. T. Wells, L. J. D'Aries, and M. D. Hammig, "Scalable gamma-ray camera for wide-area search based on silicon photomultipliers array," *Review of Scientific Instruments*, vol. 89, no. 3, p. 033106, 2018. 148

[213] M. Nakhostin, "A comparison of digital zero-crossing and charge-comparison methods for neutron/γ-ray discrimination with liquid scintillation detectors," *Nuclear Instruments and Methods in Physics Research Section A: Accelerators, Spectrometers, Detectors and Associated Equipment*, vol. 797, pp. 77 – 82, 2015. 150

[214] M. Cieślak, K. Gamage, R. Glover, and C. Taylor, “Gamma-ray modulation properties of tungsten coded apertures for a novel mixed-field imaging system,” vol. 14, pp. P02007–P02007, February 2019. 151

[215] I. Pawełczak, S. Ouedraogo, A. Glenn, R. Wurtz, and L. Nakae, “Studies of neutron–γ pulse shape discrimination in ej-309 liquid scintillator using charge integration method,” *Nuclear Instruments and Methods in Physics Research Section A: Accelerators, Spectrometers, Detectors and Associated Equipment*, vol. 711, pp. 21 – 26, 2013. 159

[216] R. Newby, P. Hausladen, M. Blackston, and J. Liang, “Performance of fast-neutron imaging detectors based on plastic scintillator ej-299-34,” tech. rep., February 2013. Oak Ridge National Laboratory Report. 161

[217] C. Payne, P. J. Sellin, M. Ellis, K. Duroe, A. Jones, M. Joyce, G. Randall, and R. Speller, “Neutron/gamma pulse shape discrimination in ej-299-34 at high flux,” in *2015 IEEE Nuclear Science Symposium and Medical Imaging Conference (NSS/MIC)*, pp. 1–5, Oct 2015. 161

[218] C. Liao and H. Yang, “Pulse shape discrimination using ej-299-33 plastic scintillator coupled with a silicon photomultiplier array,” *Nuclear Instruments and Methods in Physics Research Section A: Accelerators, Spectrometers, Detectors and Associated Equipment*, vol. 789, pp. 150 – 157, 2015. 162

[219] S. Chung, A. Kacperek, R. Speller, and A. Gutierrez, “Optimisation of pulse shape discrimination using EJ299-33 for high energy neutron detection in proton beam therapy,” *Journal of Instrumentation*, vol. 12, no. 11, 2017. 162

[220] K. A. A. Gamage, M. J. Joyce, and G. C. Taylor, “A digital approach to neutron-γ imaging with a narrow tungsten collimator aperture and a fast organic liquid scintillator detector.,” *Applied radiation and isotopes : including data, instrumentation and methods for use in agriculture, industry and medicine*, vol. 70, no. 7, pp. 1223–7, 2012. 165

[221] I. Kaissas, C. Papadimitropoulos, C. Potiriadis, K. Karafasoulis, D. Loukas, and C. P. Lambropoulos, “Imaging of spatially extended hot spots with coded apertures for intra-operative nuclear medicine applications,” 2017. 166

[222] F. M. Wagner, B. Loeper-Kabasakal, and H. Breitkreutz, “Neutron medical treatment of tumours — a survey of facilities,” *Journal of Instrumentation*, vol. 7, pp. C03041–C03041, March 2012. 167